Fall 10-1-2021

Cosmology and Astrophysics with Dark Matter and Gaseous Halos

Han S. Aung
Yale University Graduate School of Arts and Sciences, hansoeaung9@gmail.com

Abstract

Cosmology and Astrophysics with Dark Matter and Gaseous Halos

Han Aung

2021

Multi-wavelength astronomical surveys promise to provide unprecedented data on dark matter halos from galactic to cluster scales in the coming decade. One of the new frontiers lies in studies of intracluster medium (ICM) and circumgalactic medium (CGM) for cosmology and galaxy formation. In this work, we will combine cosmological and idealized simulations to study the non-linear growth of structures and the effects of small scale astrophysics in the realistic cosmological settings. Specifically, we will investigate the connection between the dark matter halos and the cosmic web structures, focusing on the outer boundaries of dark matter and gaseous halos around cluster-size dark matter halos and the filamentary cold gas accretion feeding high-redshift galaxies. We show that the edge of the phase space structure and accretion shock radii denote the outer boundaries of the halos and have the potential to advance cluster cosmology. We also investigate the roles of hydrodynamic and gravitational instabilities on the survival of cold gas streams feeding high-redshift galaxies. My research highlights the importance of understanding the growth of dark matter halos and their interactions with the cosmic web structures for advancing cosmology and astrophysics in the era of multi-wavelength astronomical surveys.

Cosmology and Astrophysics with Dark Matter and Gaseous Halos

A Dissertation
Presented to the Faculty of the Graduate School
of
Yale University
in Candidacy for the Degree of
Doctor of Philosophy

by
Han Aung

Dissertation Director: Daisuke Nagai

December 2021

Acknowledgements

This dissertation is the product of six years of work with the help and support of many people along the journey. During these six years, I have had the privilege of working with and learning from many brilliant scientists without whom this work would not be possible.

I would like to thank my advisor, Dr. Daisuke Nagai. Your support, encouragement and advice on both academic and professional fronts have helped me developed both as a person and a scholar, and I will forever be grateful for these years. I would also like to thank Dr. Nikhil Padmanabhan, Dr. Priya Natarajan, Dr. Frank van den Bosch, and Dr. Alexie Leauthaud for guiding through my thesis and helpful advice. I am also grateful for the advice and suggestions of my undergraduate research advisor, Dr. Joanne Cohn.

The work is strengthened by the brilliant ideas and suggestions from many colleagues and collaborators. I would like to thank Dr. Eduardo Rozo for the scientific discussions and the hospitality at University of Arizona during my visit. I am forever grateful to Dr. Andrew Hearin, Dr. Erwin Lau, Dr. Nir Mandelker, Dr. Avishai Dekel and Dr. Yuval Birnboim. It has been a pleasure to work and learn from you all.

I am grateful to the Yale Physics Department for funding and support as well as everyone in the department who have created an enjoyable work environment.

Last but not least, I would like to thank my family, especially my mother who has supported me since my childhood, and my father who passed away during my graduate school years. I am also grateful to my high school physics teachers U Aung Soe Win and U Kyaw Myint, whose stories and teachings have inspired me to pursue the research in physics.

Contents

List of Figures

List of Tables

Chapter 1

Introduction

1.1 Cosmology and Galaxy Formation with Dark Matter Halos

1.1.1 Cosmology with Galaxy Clusters

In the concordance ΛCDM model of cosmology, galaxy clusters are the most massive objects and powerful probes of the mysterious dark energy and cold dark matter. The total energy density today consists of 70% from dark energy Ω_Λ, 25% from cold dark matter 25%, and 5% baryonic matter according to the latest constraint (Planck Collaboration et al., 2020), where the latter two is usually combined as matter density Ω_m. The dark energy density Λ acts to expand the space, and is constant in space and time in the ΛCDM model, but extended model introduces additional time dependence where $\rho_\Lambda \propto a^{-3(1+w_0+w_a(1-a))}$, where w_0 can vary from the fiducial value of -1 and w_a can vary from 0 (see Joyce et al., 2016, for review). Cold dark matter particles only interact gravitationally and moves with non-relativistic speed today (see Bertone & Hooper, 2018, for review). In contrast, the baryonic matter such as hydrogen and helium are luminous in electromagnetic spectrum and provide the majority of

observed signals such as visible stars and galaxies.

The abundance of galaxy clusters is a powerful probe for dark matter and dark energy. The standard ΛCDM cosmology postulates that a cosmic inflation period follows the Big Bang. Before the period of recombination, the primordial plasma consists of a mixture of matter and photons in a thermal equilibrium. The Universe gradually cools down as it expands, and the period of recombination occurs when protons and electrons are cold enough to combine and form hydrogen atoms. Once the recombination consumes all the free electrons, the photons decouple, fall out from the thermal equilibrium, and start free streaming. The cosmic microwave background (CMB) captures the snapshot that we have retained from the photons during this period also known as the surface of last scattering at around $z = 1100$. The CMB measured today is consistent with the black body power spectrum of $T = 2.7K$, and reveals that the early Universe is isotropic and homogeneous. The quantum fluctuations that remained at the end of the inflation period seeded small inhomogeneities in the density distribution. The detected anisotropies have amplitudes of only $10^{-5} - 10^{-6}K$, which gives us a constraint on the over or under density of the inhomogeneities at the time of decoupling.

The overdense regions will collapse due to gravity while the underdense regions expand following the expansion of the Universe. This serves as the seed of the large scale structure formation as dark matter and baryons form the halos after collapsing onto the overdensity. Since the growth of the overdensity depends on the cosmology, measuring the abundances of the dark matter provides the constraint on the dark matter and dark energy by halos or galaxy clusters. In fact, the abundance of the dark matter halos is quantified by halo mass function $n(M, t)$, which counts the number density of halos within a given mass bin as a function of time. The halo mass function has been used to successfully constrain the cosmology using galaxy clusters (Vikhlinin et al., 2009), by comparing the halo mass function at two different redshifts

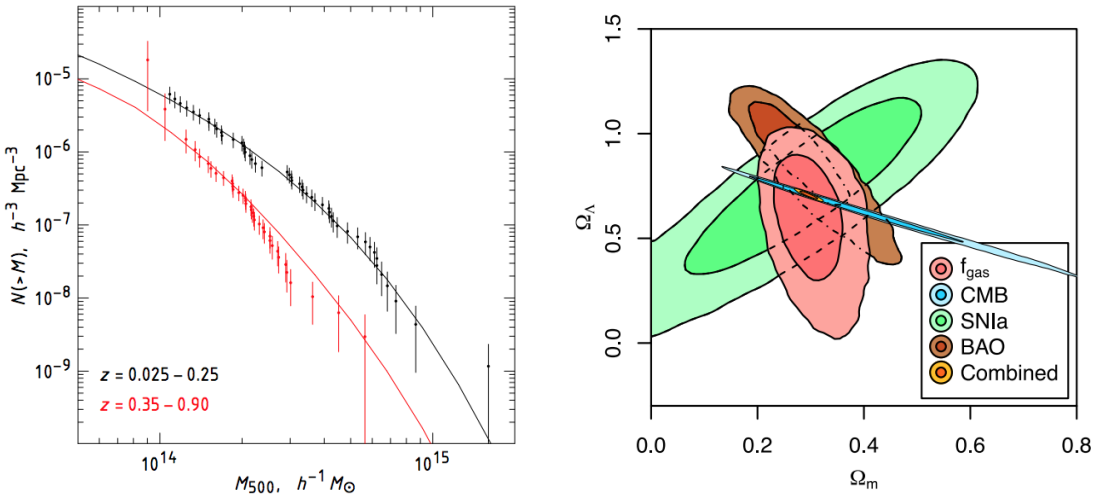

Figure 1.1: *Left panel:* Measurements of the cluster mass function at two different redshift bins, where the masses of the galaxy clusters are estimated using the Chandra X-ray data (Vikhlinin et al., 2009). Solid lines show the mass function models from $\Omega_m = 0.25, h = 0.72$ flat ΛCDM cosmology. The measurement provides the constraint on $\Omega_m h$ using the cluster data alone. *Right panel:* Constraints on ΛCDM models using various observations of dark energy probe where the dark and light shaded regions describe 68.3 and 95.4 per cent confidence regions. The datasets include the Chandra X-ray cluster data set for $f_{\rm gas}$ constraint (red; Mantz et al., 2014), CMB data from WMAP, ACT and SPT (blue), Supernovae 1a , baryon accoustic oscillations. The combined constraint is shown in gold.

to obtain the growth of the abundance of galaxy clusters (see fig. 1.1).

Baryon fraction in galaxy clusters also provides an additional constraint on dark matter and dark energy content (Allen et al., 2002, 2004). The ratio of baryonic mass to total mass is expected to approach cosmic fraction Ω_b/Ω_m at large scales. Thus, measuring gas fraction in clusters provide a constraint on Ω_m if there is a prior on Ω_b from other cosmological probes. In fact, the constraint from the galaxy clusters along with other probes of cosmology provides tight constraint on dark matter and dark energy (fig. 1.1, Mantz et al., 2014). However, when constraining dark energy with cluster galaxies, a prior on Hubble constant or baryon content obtained from other probes must be assumed to reduce degeneracy.

Observations of colliding galaxy clusters provide direct evidences of dark matter. One example of this is Bullet Cluster where a smaller subcluster collides with and

passes through a larger cluster. The multi-wavelength observations using X-ray and optical photometry reveals that while the bulk of mass and the visible galaxies have passed through each other after the collision, the hot gas in the galaxy cluster lags behind, leaving an image of the bulk of hot gas detected by X-ray squashed between the matter distribution detected by weak lensing as seen in fig. 1.2 (Markevitch et al., 2004). This is only possible when the bulk of the mass comes from invisible particles which are not baryons, consistent with the dark matter particles comprising majority of the mass in the universe. The measurements of the offset also put an upper limit on the interaction cross-section of dark matter particles, indicating that the dark matter is only weakly interacting.

1.1.2 The Physics of Galaxy Formation

Galaxies are intimately linked to the properties of dark matter halos and their properties correlate directly with dark matter halo mass. However, baryonic physics directly influences galaxy formation physics and the properties and evolution of the circumgalactic medium (CGM). Thus, CGM provides a powerful laboratory for testing the galaxy formation models and sub-grid physics implemented in cosmological simulations with the next generation multi-wavelength probes (Tumlinson et al., 2017; Battaglia et al., 2019). Inside the massive dark matter halos, the baryons continue to adiabatically cool down as they collapse. Once it is cool and dense in the potential well of the halos, the collapsed hydrogen and helium gases form stars. Galaxies are the collections of stars in the dark matter halos. In the massive dark matter halos into which smaller halos have fallen in, we can see a cluster of galaxies together each of which indicates the remnant of the halo which have merged with the larger halo in which these galaxies belong to. In fact, the cosmic star formation rates peaking at “cosmic noon" at $z \approx 2$ and lower star formation rate at late time is related to declining dark matter accretion rates of the halo (Behroozi et al., 2013b). Thus, we

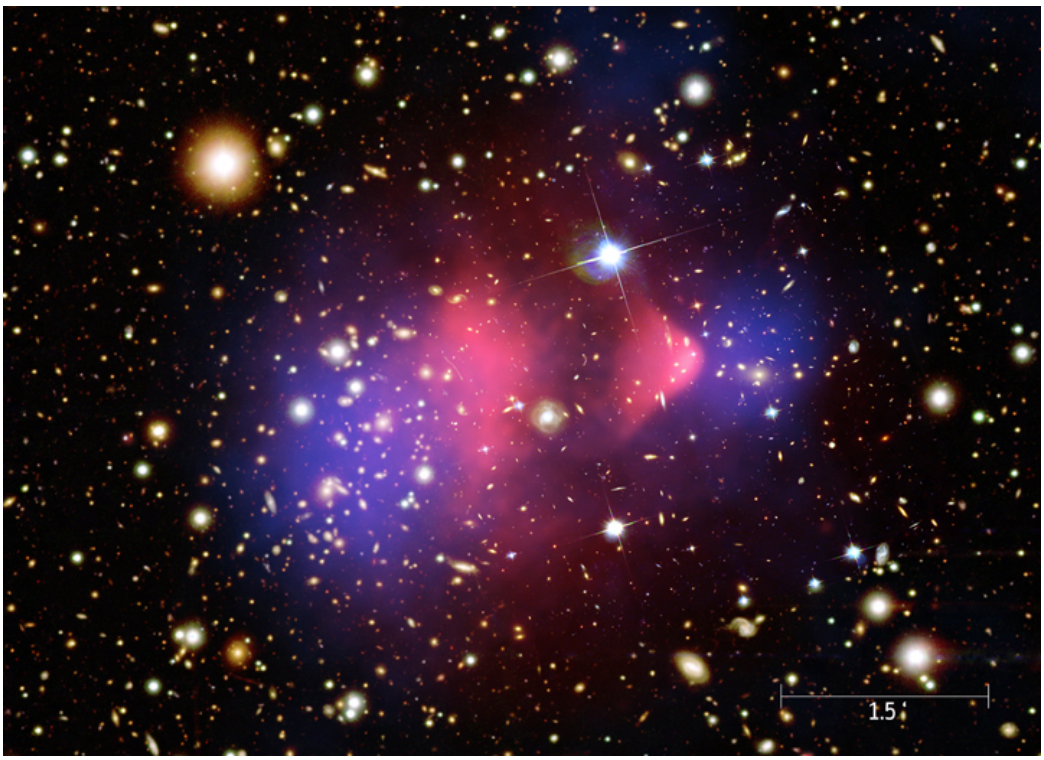

Figure 1.2: The image shows the galaxy cluster 1E 0657-56, also known as the bullet cluster. The optical image from Magellan and HST shows galaxies in orange and white. Hot gas in the cluster, which contains the bulk of the normal matter in the cluster, is shown by the Chandra X-ray Observatory image in pink. Most of the mass in the cluster is shown in blue, as measured by gravitational lensing, the distortion of background images by mass in the cluster. This mass is dominated by dark matter. The clear separation between normal matter and dark matter has not been seen before and gives the strongest evidence yet that most of the matter in the Universe is dark. Image source: NASA Chandra Observatory

expect that the luminosity function or stellar mass function which counts the number of galaxies within a given stellar mass or luminosity bin to follow halo mass function. However, there are significant differences: ΛCDM model generically predicts the slope of the mass function at low mass to be around -2 (e.g., Tinker et al., 2008), while the the slope of the observed galaxy stellar mass function (SMF) is shallower ≈ -1.3. At high mass end, both halo mass function and stellar mass function are exponentially cut-off but the halo mass function turn-over is at much larger masses, implying a lack of star formation rate at high mass halos.

Figure 1.3 shows the stellar to halo mass ratio for different halo mass from various measurements. The relation shows similar behavior to SMF where the stellar mass - halo mass relation is different between high mass and low mass halos. It also highlights how different baryonic physics impact the star formation of halos of different mass ranges. Several studies suggest that at low mass, supernova feedback suppress star formation by ejecting gas from the galaxy (Dekel & Silk, 1986; White & Frenk, 1991), while at high mass, active galactic nuclei due to supermassive black hole at the center of galaxies drive out the star forming cold gas (Silk & Rees, 1998; Croton et al., 2006). Additionally, satellite galaxies in cluster environments stop star forming due to strangulation where the galaxy can no longer accrete star forming cold gas (Balogh et al., 2000) or gas stripping due to ram pressure (Gunn & Gott, 1972; Abadi et al., 1999). Even for the star-forming galaxies, the gas in the interstellar medium only lasts over a depletion time scale of $\tau_{\rm dep} \sim M_{\rm gas}/\dot{M}_{\rm sfr}$, which is only a small fraction of the time they have been forming stars (Whitaker et al., 2012; Peeples et al., 2014; Tumlinson et al., 2017), suggesting that they must continuously accrete cold gas from the cosmic web to sustain the star formation.

Study of CGM provides an avenue to probe how galaxies acquire, eject, and recycle their gas in order to understand their star formation history. The observations of the CGM reveal a complex multiphase structure, where hot virialized gas of 10^6 K

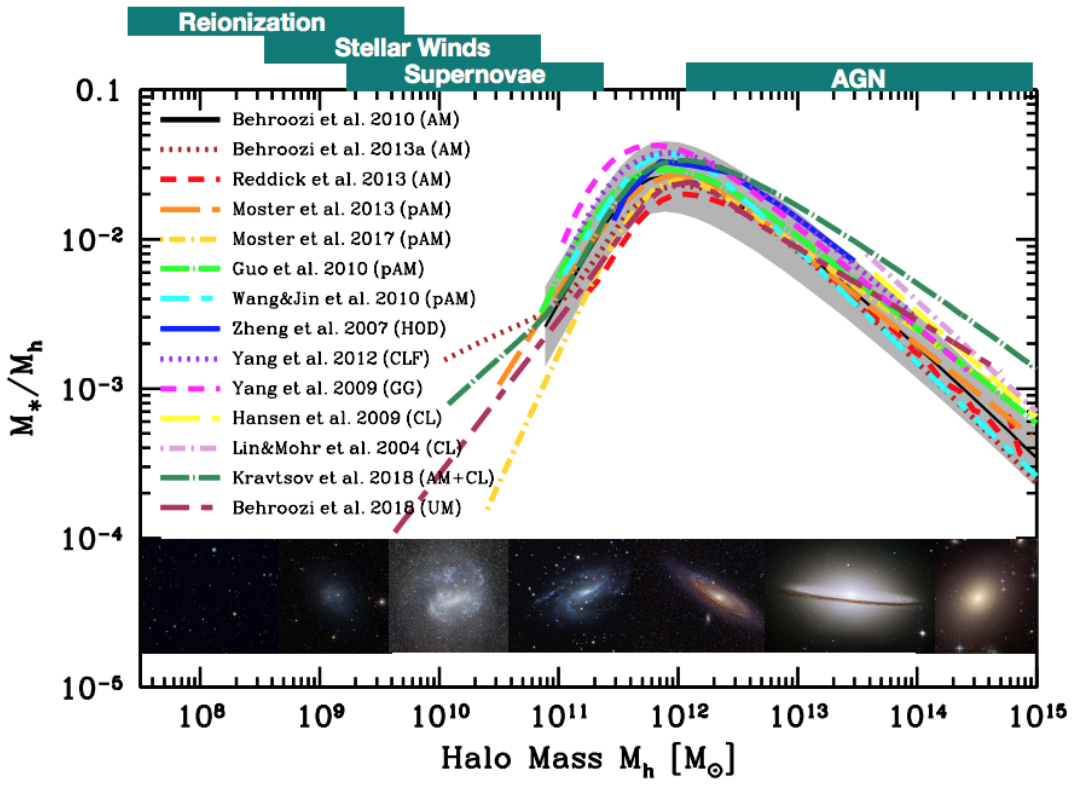

Figure 1.3: *Top panel*: galaxy stellar mass-to-halo mass ratio of central galaxies at $z = 0$. The figure shows the constraint from direct abundance matching, parametrized abundance matching, modeling halo occupation distribution or conditional luminosity function, two-point clustering, and direct measurements in groups and clusters. *Bottom panel*: example galaxies that are hosted by halos in the specified mass range. Key physical processes that may be responsible for ejecting or heating gas or suppressing star formation at those mass scales are highlighted on the top of the figure. Figure first presented in Behroozi et al. (2013d), and adapted in Wechsler & Tinker (2018).

(Anderson & Bregman, 2011; Anderson et al., 2013) exists together with the cold gas 10^4 K which are out of equilibrium or in tiny, dense clouds (Cantalupo et al., 2014; Werk et al., 2014). Understanding the origin and properties of the cold gas in CGM is critical in explaining the origin of how galaxies obtain the cold gas fuels to support the star formation process throughout cosmic time.

1.1.3 Multi-wavelength Probes of Dark Matter Halos

The next generation multi-wavelength astronomical surveys will bring new opportunities to advance our understanding of cosmology and galaxy formation. These surveys will also probe all three components of the universe: dark matter through weak-lensing such as Roman (Akeson et al., 2019), Euclid (Laureijs et al., 2011), Rubin (LSST Science Collaboration et al., 2009), galaxy through imaging and spectroscopic surveys such as Subaru Hyper Suprime-Cam (HSC, Aihara et al., 2018) and Prime Focus Spectrograph (PFS, Tamura et al., 2016), Dark Energy Science Instrument (DESI, DESI Collaboration et al., 2016), Spectro-Photometer for the History of the Universe, Epoch of Reionization, and Ices Explorer (SPHEREx, Doré et al., 2014), and baryonic gas through microwave missions measuring Sunyaev-Zeldovich (SZ) effect, such as Advanced ACT (Henderson et al., 2016), Simon Observatory (SO, Ade et al., 2019), CMB-S4 (Abazajian et al., 2016), and X-ray observatories such as eROSITA (Merloni et al., 2012), Athena (Nandra et al., 2013), and Lynx (Gaskin et al., 2019). These surveys will map out large areas of the sky expanding the area, redshift depth, and increasing the detection limit to detect the the outskirts of galaxy clusters as well as galaxies. Current spectrographs such as Cosmic Origin Spectrographs (COS, Green et al., 2012) on Hubble Space Telescope, Integral Field Units on Keck and Very Large Telescope (VLT, Ledoux et al., 2003) will continue to provide the detections of baryons through Lyman-α and other absorption lines.

These next generation surveys will not only increase the statistics of the number of halos, but also increase the resolution required to study the inner structure of the halos and low-mass galaxies. X-ray and SZ surveys along with absorption line studies will provide a wealth of information on the gas around galaxies across redshift, revealing a complex multiphase structure in order to understand the galaxy formation and evolution processes (Tumlinson et al., 2017). This allows us to probe the small scales where non-linear structure formation and baryonic physics dominates. This

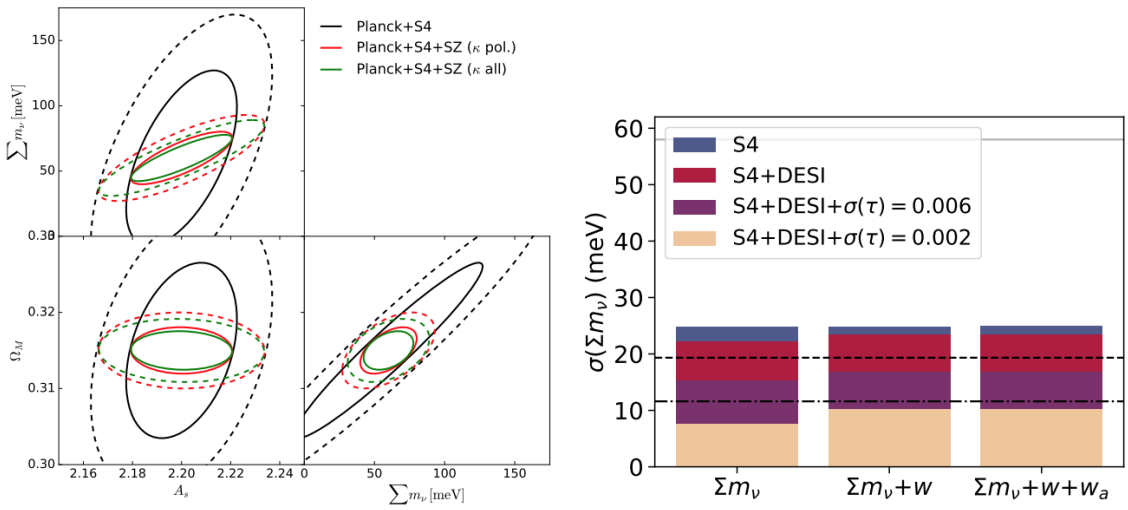

Figure 1.4: *Left panel*: Forecast of cosmological constraint on Ω_m, neutrino mass $\sum m_\nu$ and the normalization of Y-M relation combining the next generation SZ survey CMB-S4 with Planck survey priors (Louis & Alonso, 2017). *Right panel*: Error on the neutrino mass measurements when fitting for the dark energy equation of state w, w_a and neutrino mass based on CMB-S4 and DESI measurements of weak lensing mass estimate of clusters (Madhavacheril et al., 2017). The next generation survey promises to provide the cluster cosmology constraint with high precision. Figure from Pratt et al. (2019)

corresponds to improvement in cosmological constraints by a factor of 3 to 4 when small scales are included (Reid et al., 2014; Zhai et al., 2019), providing approximately the same scientific gain that would be accomplished by covering 15 times more sky. The next generation of surveys will provide competitive and independent constraints on cosmological parameters with cluster cosmology including the sum of neutrino mass and dark energy equation of state (see fig. 1.4, Pratt et al., 2019).

1.2 Structure Formation in ΛCDM Cosmology

1.2.1 Growth of Structure

The evolution of the overdensity perturbations in the ΛCDM Universe is described by the mass and momentum continuity equations and Poisson equation for pressureless

fluid to the first order as:

$$\frac{\partial \delta}{\partial t} + \frac{1}{a}\nabla.\vec{v} = 0, \tag{1.1}$$

$$\frac{\partial \vec{v}}{\partial t} + \frac{\dot{a}}{a}\vec{v} = -\frac{\nabla\phi}{a}, \tag{1.2}$$

$$\nabla^2\phi = 4\pi G\rho_m a^2\delta, \tag{1.3}$$

where δ is the overdensity perturbation, a is the expansion factor of the universe and ρ_m is the mean density of the universe. The equations can be combined into a second-order linear differential equation, which has two solutions corresponding to the growing mode δ_+ and the decaying mode δ_-. As the overdensity grows with time due to the gravitational potential, the growing mode describes the growth of the overdensity as a linear approximation:

$$\delta_+(z) \propto D(z) \propto g(z)/(1+z), \tag{1.4}$$

where $g(z)$ is a function of $\Omega_{\rm m}$ and Ω_Λ (Carroll et al., 1992).

Spherical collapse model is a simple analytical model of the formation of the dark matter halos from the overdensity and models the collapse of the infalling materials onto the halo. Assuming spherical symmetry, the motion of a mass shell follows:

$$\frac{{\rm d}^2 r}{{\rm d}t^2} = -\frac{GM}{r^2} + \frac{\Lambda r}{3}, \tag{1.5}$$

where Λ is the cosmological constant indicating the expansion due to dark energy. Around an overdense region, there is a turnaround radius, at which the outgoing velocity due to the expansion of the universe is balanced by the inflow onto the spherical overdensity. For an outgoing shell to collapse and form a halo, the model shows that a critical overdensity of $\delta_c = \rho/\langle\rho\rangle - 1 = 1.686$ is required with a weak dependence on the cosmology, which is generally ignored. The overdensity of the individual halo is

usually defined with peak-height, $\nu = \delta_c/(\sigma D(z))$ where the overdensity is measured relative to the variance of density distribution at redshift of z.

Although the spherical collapse model predicts the behavior of the collapsed material outside the halo, it does not provide a deatiled description of the non-lienar structure and dynamics of the interior of the halos. Extension of the spherical collapse model includes shell crossing, where shells that are collapsing and outgoing are allowed to cross each other (Bertschinger, 1985; Fillmore & Goldreich, 1984a; Shi, 2016a). As shells of dark matter fall in from their turnaround radius, they move radially inward to the center of the overdensity, cross the center, and splash back out. The outgoing mass shells stop and turn around again at a 'splashback' radius. At the splashback radius, a density jump appears as the mass shells splashing back out pile up at this radius.

Baryonic gas follows the initial free infall of the dark matter particles from the turnaround radius as the primordial gas is cold with negligible pressure. However, gas particles are collisional and cannot infall all the way into the center due to the pressure of the hot halo. The evolution of gas is governed by the system of differential equations involving mass, momentum, and entropy conservation:

$$\frac{\mathrm{d}\rho}{\mathrm{d}t} = -\frac{\rho}{r}\frac{\partial}{\partial r}(rv), \tag{1.6}$$

$$\frac{\mathrm{d}v}{\mathrm{d}t} = -\frac{1}{\rho}\frac{\partial p}{\partial r} - \frac{2Gm}{r}, \tag{1.7}$$

$$\frac{\mathrm{d}}{\mathrm{d}t}(p\rho^{-\gamma}) = 0, \tag{1.8}$$

$$\frac{\partial m}{\partial r} = 2\pi r\rho. \tag{1.9}$$

When the infalling gas encounters the halo gas, it is shock heated and converts most of the kinetic to thermal energy. Thus, at the shock radius, the infalling gas slows down while the temperature and pressure increases. Conservation of mass, momentum and energy dictates the discontinuity at the shock jump. Figure 1.5 shows the comparison

between the gas and dark matter infall mechanics. From the turnaround radius, both dark matter and gas particles turn around and free fall onto the halo, as the pressure of the unheated primordial gas is negligible. The infalling dark matter particles reach the halo center and splash back out. The maximum radius it can splash back out to is the splashback radius. On the other hand, the gas loses kinetic energy at the shock radius, and slows down. In the absence of non-gravitational physics such as radiative cooling and star formation, this shock radius is stable. However, in practice, radiative heat loss leads to instability and variation in the shock radius especially in the lower mass halos ($M < 10^{11} M_{\odot}$) where the gas is cooled down due to hydrogen and helium line cooling at temperature $T \approx 10^4 - 10^5 K$ (Birnboim & Dekel, 2003). For massive halos where cooling is ineffective, the splashback and shock radii coincide regardless of the mass accretion rate or baryon fraction, as long as the polytropic index is kept at $\gamma = 5/3$ (Shi, 2016b).

1.2.2 Halo Mass and Scaling Relations

The linear perturbation theory and the spherical collapse model provide a basis for analytical prediction of halo mass function and its relation to the cosmology. Press-Schechter Formalism provides an analytical halo mass function $n(M, t)$ following spherical collapse model (Press & Schechter, 1974). Assuming an initial Gaussian random overdensity field, it will grow as $\delta(x, t) = \delta(x)D(t)$ according to the linear theory. According to the spherical collapse model, the overdense region collapses to form a dark matter halo when the spherically averaged overdensity exceeds the critical threshold value, $\delta > \delta_c = 1.686$. Press-Schechter Formalism introduced the smoothed overdensity within the radius that contains mass M and postulated that the probability of having the overdensity to collapse to form the halo is the same as the mass fraction that is contained within the halo of mass M. Since the growth of the overdensity $D(t)$ is directly related to the growth of halo mass function, the abun-

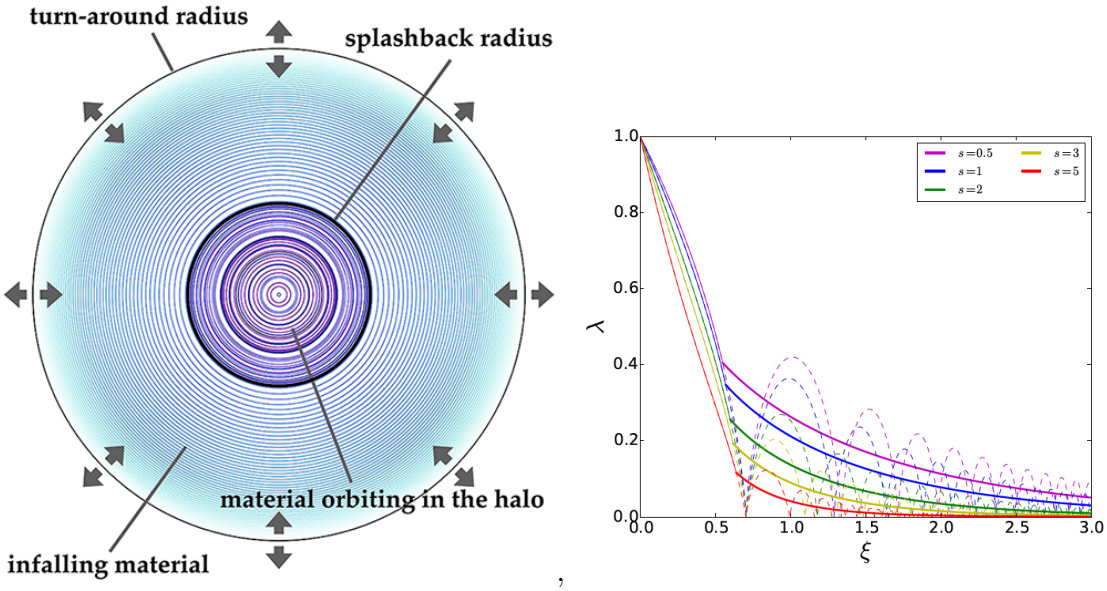

Figure 1.5: *Left panel:* A simple schematic for a spherical halo collapsing from the turnaround radius. Inside splashback radius, multiples of infalling and outgoing dark matter shells can be found. *Right panel:* The trajectory of the dark matter (dashed) and monoatmoic gas (solid) mass shells as they fall into the halo in the self-similar secondary accretion model (Shi, 2016b). The y-axis is radius scaled by turnaround radius, while the x-axis is logarithmic of time normalized by the initial collapse time. The dark matter falls into the halo and splash back out, reaching a second maximum at splashback radius. The gas, however, shocks at the shock radius and the slope in distance-time graph drops significantly as the velocity decreases. The splashback and shock radii are roughly at the same position regardless of mass accretion rate $s = d\log m/d\log a$. (Image source: http://www.benediktdiemer.com/research/splashback/)

dance of galaxy clusters and its redshift evolution offer a powerful probe of cosmology (see fig. 1.1).

In order to measure the halo mass function using observations, one must estimate the mass of individual halos. Gravitational lensing, for example, directly probes the mass distribution of dark matter halos. This general relativistic phenomenon originates when the spacetime around a massive object curves the path of the electromagnetic radiation. Strong gravitational lensing is the most spectacular phenomena caused by significant distortion in the image of the background astronomical objects when the source is well-aligned with the observer and the mass distribution. Even when the alignment is not optimal to produce strong lensing, massive galaxy clusters distort or shear the background structures via weak lensing. In optical measurements, weak lensing statistics measures the intervening mass between the source and the observer and provides a powerful tool to map the distribution of mass in the universe (Bartelmann & Schneider, 2001). Powerful statistics such as cluster mass function and power spectrum can be extracted from weak lensing surveys to constrain the cosmology (see Kilbinger, 2015, for review).

Halo mass can also be derived from other physical quantities of the intracluster medium (ICM) through scaling relations, predicted analytically by assuming self-similarity (Kaiser, 1986). The cluster radius is generally defined as the radius which encloses a region in which average density is Δ times the critical or background density. Thus,

$$M_\Delta = \frac{4\pi}{3} R_\Delta^3 \rho. \tag{1.10}$$

If the gas is roughly in hydrostatic equilibrium with the gravitational potential, then the virial theorem gives the average temperature of the gas to be

$$T_\Delta \propto \frac{M_\Delta}{R_\Delta} \propto M_\Delta^{2/3}. \tag{1.11}$$

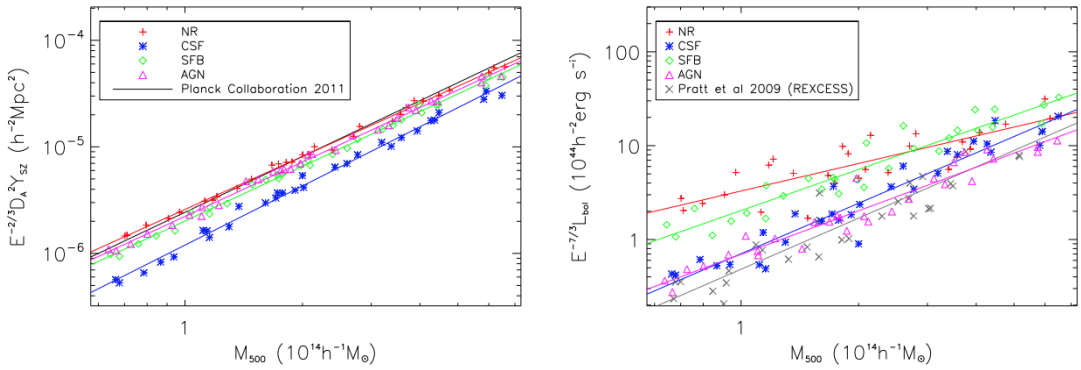

Figure 1.6: Relation between the SZ signal (left) or the X–ray luminosity (right) and the mass from the numerical simulations of Pike et al. (2014). The relations depend on the gas physics implemented in the simulation: the non-radiative model (NR, red crosses), cooling and star formation model (CSF; blue stars), supernova feedback (SFB; green diamonds) and AGN models (magenta triangles). Observational data points are from Planck Collaboration et al. (2011) (black line) and Pratt et al. (2009) (black cross). X-ray luminosity is very sensitive to the gas physics involved, and presents a large scatter as it is dominated by the core where the baryonic physics are most effective. Comparatively, the relation between Y_{SZ}–M relation is rathe tight, with slight offsets due to the baryonic physics. Figure from Pratt et al. (2019)

As the gas collapses onto dark matter halos, the gas heats up and ionizes due to shocks and adiabatic compression. The hot ionized gas emits X-ray due to thermal bremsstrahlung effect, as well as cooling lines due to recombination of hydrogen, helium and other heavier elements. The X-ray brightness strongly depends on the number density of the free electron and weakly depend on the temperature, $n_e^2 T^{1/2}$. Then the resulting integrated X-ray luminosity is $L \propto \rho^2 T^{1/2} V \propto M^{4/3}$ (Sarazin, 1986). However, as the X-ray brightness depends on density squared, it rapidly decreases with radius. Significant X-ray emission also comes from the center of the cluster due to cool cores and AGN feedback (Pratt et al., 2009). This introduces significant scatter to the luminosity-mass scaling relation as seen in fig. 1.6.

Compton scattering of CMB photons from hot electrons in galaxy clusters gives rise to secondary anisotropies in CMB, known as thermal Sunyaev-Zeldovich (tSZ) effect (Sunyaev & Zeldovich, 1970). The Compton-y parameter measures the shift in

CMB power spectrum due to the pressure of hot electrons along line-of-sight:

$$y \propto \int n_e \sigma_T \frac{k_B T}{m_e c^2} \mathrm{d}l, \tag{1.12}$$

where σ_T is the cross-sectional area for Compton scatter, n_e is the number density of free electrons, m_e is the mass of electron, and k_B is Boltzmann constant. The integrated Compton-y parameters is the integrated y in the aperture around the dark matter halo, $Y = \int \mathrm{d}\Omega\, y$. In practice, the solid angle aperture $\mathrm{d}\Omega$ is converted to area if we know the redshift. Thus, $Y \propto \int \int \mathrm{d}A \mathrm{d}l\, n_e T \propto \int \mathrm{d}V \rho T$ and the value is directly proportional to $MT \propto M^{5/3}$ (Kravtsov et al., 2006; Nagai, 2006). To derive the mass from tSZ signal, one often starts with the assumption of hydrostatic equilibrium, which describes the gas distribution in the gravitational potential well of dark matters. Halos are, however, dynamically active and out of hydrostatic equilibrium due to mergers and mass accretion, with significant turbulent non-thermal pressure support in addition to the thermal pressure (e.g., Lau et al., 2009; Nelson et al., 2012, 2014b; Shi & Komatsu, 2014; Yu et al., 2015; Green et al., 2020). Supernova and active galactic nuclei feedback also contribute suffer additional turbulence at the center of clusters (Vazza et al., 2013; Zhuravleva et al., 2014; Chadayammuri et al., 2021; Simionescu et al., 2019).

The velocity dispersion of cluster galaxies also provides an estimate of cluster masses. Specifically, by assuming that cluster galaxies are in virial equilibrium with the gravitational potential of the cluster, one infers the mass of the cluster from the velocity dispersion of its galaxies. Zwicky (1933, 1937) pioneered the method to measure the mass of the Coma Cluster. The relation between velocity dispersion of the dark matter and the cluster mass is described as :

$$\sigma_{\mathrm{DM}}(\Delta) \propto M_{\Delta}^{\alpha}, \tag{1.13}$$

where virial theorem predicts $\alpha = 1/3$. Numerical simulations have shown that the 3D velocity dispersion of dark matter particles in simulations is tightly correlated with cluster mass, with a scatter of only $\approx 4\%$ (Evrard et al., 2008). The presence of interlopers, which are not physically associated with the cluster in 3D but appear as close neighbors in redshift and in the plane of the sky, introduce additional scatters in the observed dispersion mass relation.

The velocity dispersion or rotational velocity of stars is also an important quantity in determining the mass and luminosity of galaxies. Different empirical relations exist for spiral galaxies (Tully & Fisher, 1977) and elliptical galaxies (Faber & Jackson, 1976), owing to different structures. These scaling relations provide key measurements for several properties of galaxies (e.g., Cappellari et al., 2013), as well as the primary information about the galaxy–halo connection at low masses where large samples with observable spatial statistics are not yet available (McConnachie, 2012). In fact, the scaling relations for galaxies are projections of a fundamental plane of luminosity, dispersion, and radius (Djorgovski & Davis, 1987; Bender et al., 1992; Burstein et al., 1997).

Analytical models predict well-defined relations between the mass of the halo and observable quantities. However, to achieve a percent-level accuracy needed for constraining cosmology, one must take into account the effects of still poorly understood galaxy formation physics and baryonic effects, as well as observational uncertainties such as asphericity and projection effects.

1.2.3 Cosmic Accretion into Halos from the Cosmic Webs

While the spherical halo model provides useful insight into the scaling relations of the dark matter halos and observables, the model makes a simplifying assumption that the halos are isolated and accrete smoothly and spherically symmetrically. In reality, halos grow through mergers and accretion from the large-scale cosmic web structures

(Zel'dovich, 1970; Bond et al., 1996). Halos form preferentially at the nodes where multiple filaments come together, and the accretion of dark matter and gas through filaments mainly feeds the growth of the dark matter halos (Klar & Mücket, 2012; Gheller et al., 2015). Recent simulations, for example, showed that the higher the peak-height of a halo (the more massive), the more filaments it is connected to (Codis et al., 2018), with on average 3 filaments connecting to the galaxy clusters and high redshift massive galaxies.

Massive galaxies, $M_* \sim 10^{11} M_\odot$, at high redshift, $z > 1$, are star forming galaxies with star formation rate of the order $100 M_\odot\,\mathrm{yr}^{-1}$ (Genzel et al., 2006, 2008; Förster Schreiber et al., 2006, 2009). These galaxies reside in dark matter halos with $M > 10^{12} M_\odot$, whose temperature is around $10^6\,\mathrm{K}$ based on eq. (1.11). These halos will support a stable accretion shock as the cooling time is long, and accreted gas are expected to be shocked and hot (Birnboim & Dekel, 2003). However, their star formation rates imply that almost all the gas that are accreted forms stars. Filaments feeding these galaxies carry cold, dense, narrow streams (Birnboim et al., 2016) in contrast to the filaments around galaxy clusters which are preheated due to accretion shocks (Zinger et al., 2016). If these galaxies primarily accrete gas through gas streams flowing along the cosmic filaments, the accreted gas will have shorter cooling time due to higher density, and the streams can provide efficient fuel for star formation as they carry cold gas to the central galaxy without getting shock heated (Dekel & Birnboim, 2006; Dekel et al., 2009a).

In fact, observations of CGM reveal large quantities of cold gas with spatial and kinematic properties consistent with the predictions for cold streams (e.g., Bouché et al., 2013, 2016; Steidel et al., 2000; Matsuda et al., 2006, 2011). In addition to feeding cold gas for star formation, they also play a key role in the evolution of the galactic disk. The gas streams can carry and supply angular momentum all the way to the disk (Stewart et al., 2013; Pichon et al., 2011; Kimm et al., 2011; Danovich

et al., 2015; Codis et al., 2012). They also drive turbulence and can trigger violent disk instabilities that cause the formation of giant star-forming clumps and dramatic compaction events (Dekel & Burkert, 2014; Zolotov et al., 2015; Tacchella et al., 2016b,a). Thus, the evolution of cold gas stream in CGM and the properties of gas deposited into CGM and galactic disk will be of importance in order to understand the evolution of galaxies and star formation processes in galaxies at cosmic noon.

1.3 Simulating Dark Matter and Gaseous Halos in the Cosmic Webs

Numerical simulations offer a powerful approach for modeling the formation and evolution of galaxies and galaxy clusters, while properly taking into account the details of the non-linear growth of structures and galaxy formation physics, such as radiative cooling, star formation, and feedback in a realistic cosmological setting. Over the past several decades, numerical simulations have provided significant physical insights into our understanding the structure and formation of dark matter halos in the concordance ΛCDM model (see Frenk & White, 2012; Kravtsov & Borgani, 2012; Vogelsberger et al., 2020, for reviews). There are two classes of cosmological simulations, N-body and hydrodynamical simulations. N-body simulations simplify the computation by assuming that matter consists of dark matter as the only interaction between dark matter particles is gravity. Hydrodynamical simulations model the gas dynamics by solving the fluid equations explicitly and the properties of baryons (gas and stars) with realistic cosmological growth of structures.

1.3.1 N-body Simulations

N-body simulations compute the gravitational field based on the particles in the initial condition, advance the positions and velocities by solving the Poisson equation

in discrete time steps (Hockney & Eastwood, 1981). The direct computation of the gravitational field due to the individual particles scales with $\mathcal{O}(N^2)$ for N number of particles in the simulation. To avoid the computational cost, several methods exist to simplify the calculation which will scale with $\mathcal{O}(N \log N)$. The particle-mesh method first computes density in each grid cell. The simulation then solves the Poisson equation in Fourier space to calculate the force on individual particles. The tree method divides the simulation volume into subvolumes in a tree-like structure. The simulation then calculates the forces due to particles within the same or nearby subvolume individually, while the forces due to particles in distant subvolume are approximated by the lowest order terms in a multipole expansion. Several later methods combine these into a single tree-particle-mesh method.

Figure 1.7 shows a snapshot of cosmological N-body simulation MultiDark Planck (MDPL2) simulated with L-GADGET-2 code, a version of the publicly available cosmological code GADGET-2, which uses the tree-particle-mesh method (Springel, 2005). The simulation box spans 1 Gpc/h and highlights the large scale cosmic web filaments connecting the dark matter halos together. Galaxy clusters are the most massive gravitationally bound objects that resides in the densest structures in the universe that forms at the intersection of the large-scale cosmic web structures.

The density profile of a halo in N-body simulations is well characterized by Navarro-Frenk-White profile (NFW, Navarro et al., 1996a), with a shallow slope inside the cluster that gets progressively steeper with increasing radius. The two-parameter model for the density profile is:

$$\rho(r) = \frac{\rho_0}{(r/r_s)(1 + r/r_s)^2}, \tag{1.14}$$

where r_s is the scale radius at which the density scales with radius similar to isothermal sphere, $\rho \propto r^{-2}$. The profile breaks down at inner radii, as the density approaches

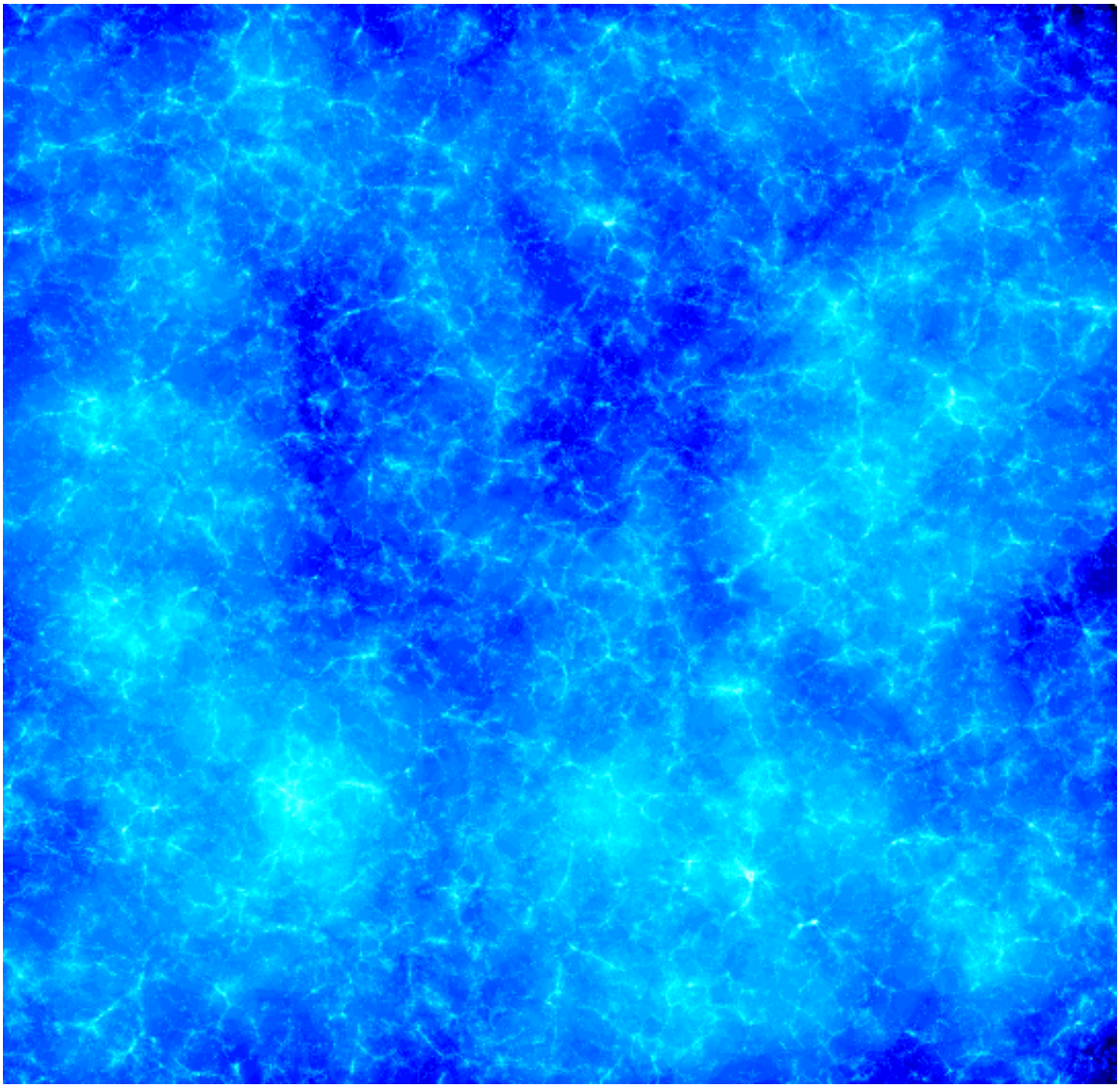

Figure 1.7: A snapshot of the MultiDark Planck (MDPL2) N-body simulation. The simulation features a large cosmic web, with millions of dark matter halos connected by filaments. The simulation box is $1Gpc/h$ and with mass resolution of $1.51 \times 10^9 M_\odot/h$. This allows us to resolve the largest mass scale clusters $10^{15} M_\odot/h$ in the universe with 10^6 particles. Image Source: Cosmosim database (Klypin et al., 2016)

infinity as the radius decreases to 0. Later studies show that Einasto profile (Einasto, 1965) fixes this issue at inner radii, where the density slope scales with radius as $\mathrm{d}\log\rho/\mathrm{d}\log r \propto r^{\alpha}$ (Navarro et al., 2004).

As the dynamics of the dark matter halos follow the gravitational potential, the density profile also specifies the velocity dispersion profile through Jeans equation:

$$\frac{1}{\rho(r)}\frac{\mathrm{d}}{\mathrm{d}r}\left[\rho(r)\sigma_r^2(r)\right] + 2\beta(r)\frac{\sigma_r^2(r)}{r} = -\frac{\mathrm{d}\Phi(r)}{\mathrm{d}r}, \tag{1.15}$$

where β is the velocity anisotropy that denotes the difference between radial and tangential velocity dispersion. Thus, the dispersion profile is increasing when the density slope is shallow, and decreasing outward when the density slope is steep (Cole & Lacey, 1996; Taylor & Navarro, 2001). In fact, the radius at which the velocity dispersion profile is maximum r_{max} correlates with the scale radius defined from NFW profile, $r_{\mathrm{max}} = 2.16 r_s$.

Extension of NFW and Einasto profiles beyond the virial radius of the halo shows that there is a radius at which density drops rapidly as predicted by the self-similar model, after which the density smoothly transitions to background density (see fig. 1.8, Diemer & Kravtsov, 2014; Adhikari et al., 2014; More et al., 2015). However in practice, the detailed analysis of individual particle trajectories in N-body simulations revealed a broad distribution in the apocenters of the splashback particle population (Diemer, 2017), and the splashback surface where the density slope is minimal is highly aspherical (Mansfield et al., 2017). Thus, the radius where the density drops sharply does not coincide with the outermost apocenters of the dark matter particles.

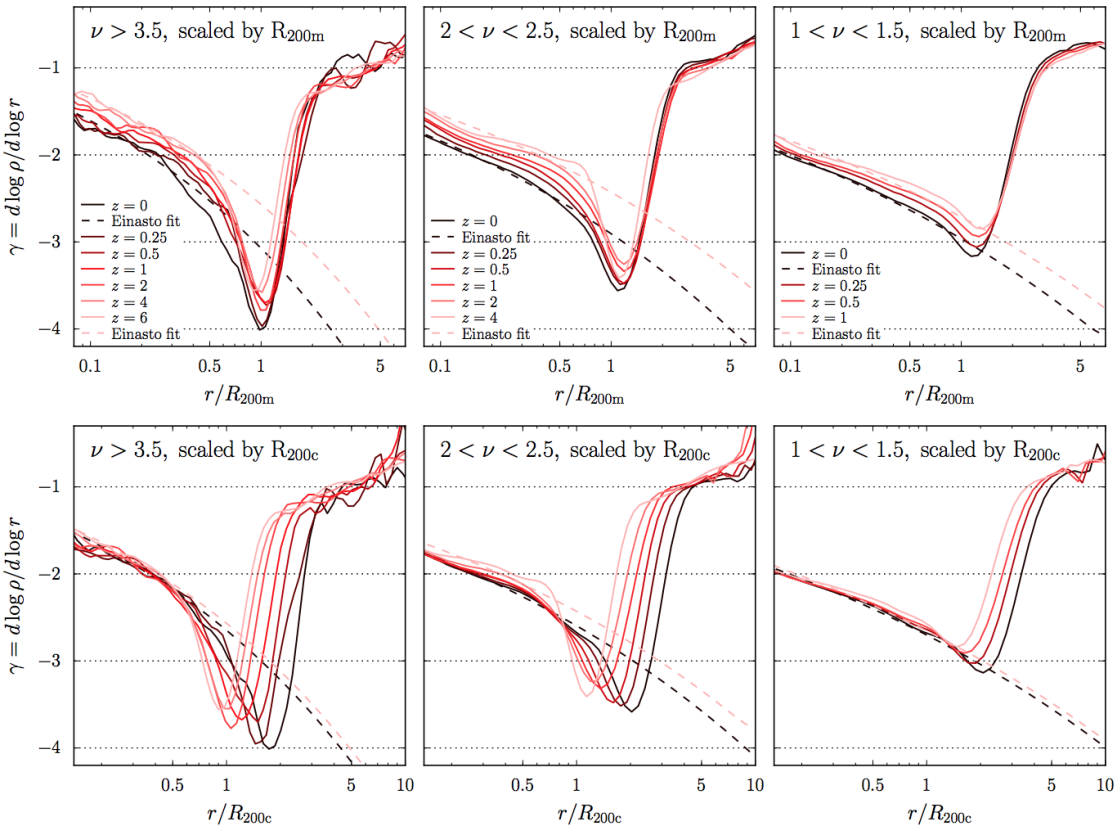

Figure 1.8: The profiles of dark matter halos in N-body simulations as measured in Diemer & Kravtsov (2014). The Einasto model provides excellent fit throughout the inner part of the halo, but breakdowns near R_{200m} as the density profile steepens. The profile smooths out to the mean matter density as the density slope becomes shallower after the splashback radius. The steepening in the density slope is predicted as the boundary of dark matter halo in self-similar secondary accretion model, and this radius is later termed splashback radius.

1.3.2 Hydrodynamic Simulations

Hydordynamic simulations predict the baryonic quantities which provide the observed signatures of galaxy clusters in X-ray and SZ as well as the galaxy formation physics, directly connecting to the dark matter halos they reside in. To treat the baryons as collisional fluids consistently, one requires hydrodynamical simulations which solve Euler's equations and other baryonic physics. There are two different classes of hydrodynamical simulations, Lagrangian method or Eulerian method. The Lagrangian method often called smooth particle hydrodynamics (SPH) tracks individual baryonic particles, where the hydrodynamical properties are smoothed quantities around each particle. In Eulerian method, the hydrodynamical properties are sampled and solved in grid or mesh cells of the simulation box.

Comparison of the hydrodynamical simulations show that both types of simulations generally agree on the properties of gas in intracluster medium except the entropy in the inner core of the clusters (Frenk et al., 1999). SPH simulations suffer from the lack of mixing (Agertz et al., 2007) and cannot resolve the shocks and discontinuity in the hydrodynamic properties as effectively (Anninos & Norman, 1994; Tasker et al., 2008). On the other hand, Eulerian codes are limited by the highest spatial resolution in the simulation. Later simulations resolve these issues by adopting pressure-entropy formalism for SPH (Hopkins, 2013) and adaptive mesh refinement technique where the resolution of the simulation follows the density of the cell (Berger & Oliger, 1984; Kravtsov et al., 1997). Moving mesh simulations combine the benefits of both methods by tracking the fluid flow as particles while the mesh grid moves along with the particle (Vogelsberger et al., 2012). The mesh defines the boundary for the hydrodynamical properties using Voronoi tessellation. Such an approach improves mixing and highlights the discontinuities better, while being able to track individual gas particles (Sembolini et al., 2016).

Several baryonic physics, such as radiative cooling, star formation, supernova and

active galactic nuclei feedback require sub-parsec scales in resolution in order to model galaxy formation physics correctly (Nagai et al., 2007; Wetzel & Nagai, 2015). For example, the modern state-of-the-art hydrodynamical simulations achieved a resolution of order hundred parsecs in a simulation box of order hundred Mpc, spanning 6 orders of magnitude (e.g., Pillepich et al., 2018; Nelson et al., 2019). This, however, does not yet cover the full dynamic range necessary to resolve all relevant length scales for modeling the physics of galaxy formation while taking into account cosmological structure formation processes. Instead, modern cosmological hydrodynamical simulations account for many baryonic physics using subgrid models: radiative cooling (Sutherland & Dopita, 1993), star formation (Katz, 1992; Springel & Hernquist, 2003), metal production and supernova feedback (Scannapieco et al., 2006), active galactic nuclei (AGN) feedback (Sijacki et al., 2007), cosmic rays (Pfrommer et al., 2007), and magnetic field (Dolag et al., 2009).

Figure 1.9 shows a snapshot of hydrodynamical simulation using an Eulerian Adaptive Refinement Tree method, where the resolution of the simulation adaptively follows the density of the simulation (Nagai et al., 2007). Baryonic physics significantly impacts the structure of the dark matter halos, especially in the inner parts of the clusters as the dark matter will respond to the changes in the potential due to baryon condensation (Gnedin et al., 2004). Specifically, baryonic physics introduces significant scatter in the scaling relations introduced in section 1.2.2. Depending on the strength of the feedback involved, gas can be pushed out from the center affecting the electron number density, pressure and thus, the X-ray luminosity and the integrated SZ signal (Pratt et al., 2009). The velocity dispersion measurements are also biased due to the galaxy number density as well as the selection with the stellar mass especially in the center of the clusters (Lau et al., 2010; Wu et al., 2013; Munari et al., 2013). Thus, cluster outskirts provide characteristics of the structure formation without the systematics from the poorly understood baryonic physics.

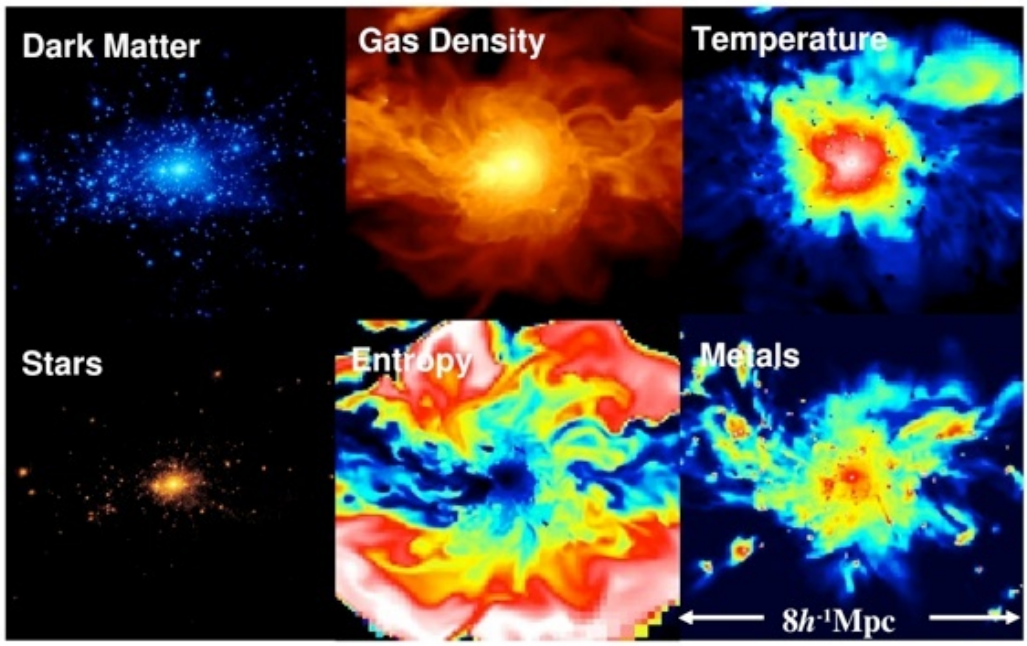

Figure 1.9: A snapshot of the adaptive refinement tree (ART) cosmological hydrodynamical simulation of galaxy clusters where the dark matter, stars, and hydrodynamic properties of gas are depicted together (Nagai et al., 2007). On the first order, stars and gas follow dark matter as they are all influenced by gravity. However, stars are more concentrated at the wells of gravitational potential than the dark matter, while the gas is more distributed. The temperature entropy map the cluster shows various shocks resulting from mergers and accretions as well as a gas stream penetrating into the cluster, a continuation of the cosmic filament. The cluster is also enriched with heavier metals, which are produced in stars, distributed into the galactic environment by supernova, and then dispersed into the intracluster medium by stripping of gas from the galaxies.

Hydrodynamical simulations also show that the most massive halos are penetrated by the gas streams, a continuation from the filaments of the cosmic web. These streams constitute the main mode of gas accretion onto the central galaxies for high-redshift galaxies and galaxy clusters (Kereš et al., 2005; Dekel & Birnboim, 2006; Dekel et al., 2009a; Ceverino et al., 2010; Danovich et al., 2012; Zinger et al., 2016). This is evident in the galaxy cluster shown in fig. 1.9, where low entropy gas stream is embedded within the high entropy shock heated halo gas. Similarly, cold, dense streams feed the high redshift galaxies $M > 10^{12} M_{\odot}$ at $z > 2$ shown in fig. 1.10, as they travel through the hot CGM towards the central galaxy. Cosmological simulations also suggest that instead of accelerating towards the halo center, the streams maintain roughly constant velocities as they inflow from the outer halo to the central galaxy (Dekel et al., 2009a; Goerdt & Ceverino, 2015). However, cosmological simulations predict different properties for the cold streams: the simulations based on the moving mesh suggest the streams dissolve at radius larger than half of virial radius $r_{\rm vir}$ (Nelson et al., 2013), while AMR and SPH simulations predict the streams remain cold and dense upto $0.25 r_{\rm vir}$ (Kereš et al., 2005; Faucher-Giguère et al., 2010). This is likely a result of the resolution of cosmological simulations only reaching a similar order of magnitude to the stream width of a few hundred pc, and hydrodynamic and other instabilities which are at play at smaller scales in disrupting the streams are not captured correctly.

1.3.3 Idealized Simulations

Idealized simulations provide high resolution of hydrodynamic simulations needed to resolve small scale physics, which the cosmological simulations either use subgrid model or fail to take into account. To resolve the small scales, idealized simulations do not include large scale cosmological accretion. Thus, these simulations aim to study the individual physical processes and their effects but will not provide the

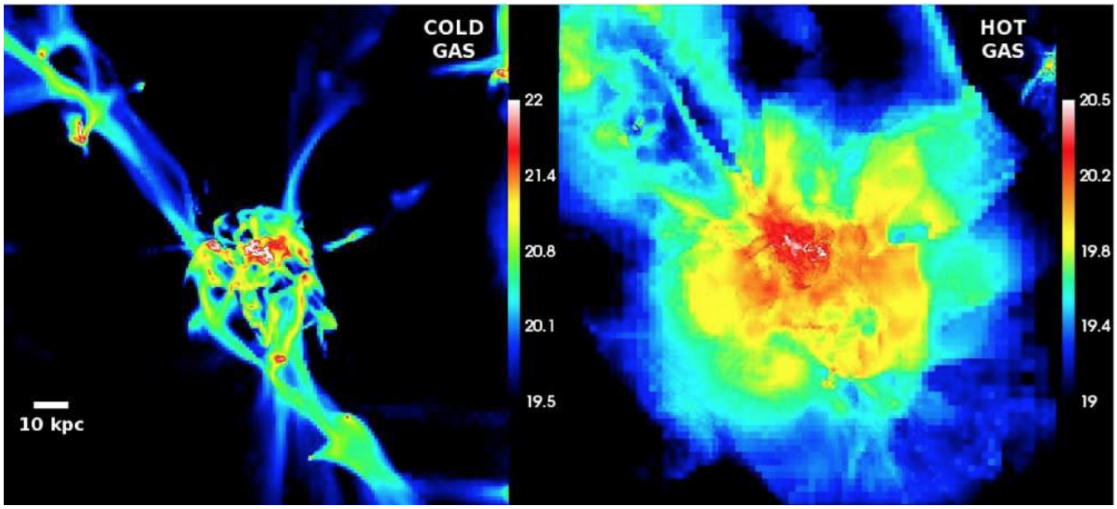

Figure 1.10: A zoom-out gas surface-density maps showing the streams feeding galaxy. *Left Panel*: cold gas ($T < 3 \times 10^4$K). *Right Panel*: hot gas ($T > 3 \times 10^4$K). The box size is 160×160 kpc, covering the whole virial sphere. The color refers to log gas surface density in units of H atoms cm^{-2}. Two major narrow streams carry the gas from well outside the virial radius to the inner 20 kpc halo core, where they break into a multi-stream turbulent core before joining the inner disc of radius 6 kpc, seen nearly edge-on at the box centre (mostly in white).

exact evolution history in the universe. For example, idealized simulations are widely used to study how physical processes, such as AGN feedback and cosmic rays, shape the properties of ICM and CGM (Guo & Oh, 2008; Gaspari et al., 2012; Gaspari & Sądowski, 2017; Li et al., 2017). As cosmological simulations do not provide enough resolution to resolve the gas stream penetrating halos for more than a few cells, one require idealized simulations to study their evolution and impact on CGM.

Idealized simulations of cold gas streams embedded within hot halo background show that they will experience Kelvin-Helmholtz instability (KHI) due to the shearing motion between the inflowing gas stream and stationary halo gas (Mandelker et al., 2016; Padnos et al., 2018; Mandelker et al., 2018). In the absence of gravity, cooling, magnetic fields and other effects, KHI will disrupt the gas stream before reaching the central galaxy for typical stream radius of $< 5\%$ of virial radius. Cosmological simulations do not resolve KHI as the typical length scales needed is much smaller

than the resolution of simulation. This may create an overestimate of the stream penetration into the halo or the difference in the properties and nature of the streams when they arrive at the central galaxy. However, self-gravity in spherical gas cloud can suppress KHI (Murray et al., 1993), while introducing additional gravitational instabilities in cylindrical gas stream (Nagasawa, 1987; Inutsuka & Miyama, 1992; Hunter et al., 1998). Cooling can either enhance or inhibit the growth rates of KHI depending on the slope of the cooling function and on the ratio of the cooling time in the fluid to the sound crossing time (Massaglia et al., 1992; Bodo et al., 1993; Vietri et al., 1997; Hardee & Stone, 1997; Xu et al., 2000). Magnetic fields can stabilize the disruptions due to gravitational instability (Nagasawa, 1987; Hunter et al., 1998), and due to KHI when magnetic field is parallel to the flow (Ferrari et al., 1981; Birkinshaw, 1990). Thus, even though the idealized simulations highlight the importance of small scale physics such as KHI on stream evolution, one need to properly take into account additional physical effects and the complex interplay between them to describe the stream evolution.

1.4 Opportunities and Challenges

Upcoming multi-wavelength astronomical surveys will provide unprecedented data to advance the halo-gas-galaxy connection in a broad mass spectrum ranging from galactic to galaxy cluster scales. Understanding astrophysics of ICM and CGM will allow us to improve our understanding of galaxy formation physics, which in turn helps us control systematic uncertainties that are currently limiting the use of dark matter halos as a cosmological probe in the era of precision cosmology. Structure formation processes leave distinct features in cluster outskirts, a boundary of dark matter and gaseous halos, while also featuring gas stream from large scale cosmic filaments penetrating the outer boundary deep into the central galaxies of the halos.

In this thesis, we will study how different types of accretion processes shape the structures and properties of the ICM and CGM, and how we can use these properties for studying cosmology and galaxy formation physics.

While the N-body simulations highlight the existence of the halo boundary as well as similar feature in the density profile to the theoretical studies, it poses a new problem as the radius which denotes the steepest point in the radial density profile does not enclose all apocenters (Diemer et al., 2017). In chapter 2, we define the boundary of dark matter halo using phase space structure. We show that the simulations deviate from the ideal spherical symmetry case presented in self-similar models, as the splashback radius defined from the density drop does not enclose all the particles, while the boundary of phase space provides better estimate of the halo boundary.

In chapter 3, we study the outer boundary of gas using shock radius in hydrodynamical simulations to show that the shock radius is also offset from the splashback radius defined from the density drop in the radial profile, but closer to the boundary of the phase space of the dark matter halo. We show that baryonic effects do not impact the shock radius and study the effects of mergers which introduce the minor offset of the shock radius from the boundary of the phase space.

Filamentary accretion directly transports gas into the inner halo, instead of shock heating primordial gas at the halo boundary. In chapter 4, we study the evolution of cold gas stream embedded within the hot halo gas under the influence of KHI and gravitational instability. We find that self-gravity either causes the stream to clump with radius similar to the stream radius when the mass per unit length is larger than critical value or stabilizes the stream from the disruption due to KHI when the mass per unit length is smaller. Further studies should highlight how the gravitational instability and KHI will interplay with other physics such as magnetic field and cooling in order to assess the evolution of gas stream in cosmological environment.

We provide the conclusions and the broader implications of our results for advancing cosmology and astrophysics in the era of multi-wavelength cosmological surveys in chapter 5.

Chapter 2

Phase Space Structure of the halo

2.1 Introduction

Over the past several decades, numerical simulations have provided significant insights into our understanding the structure and formation of dark matter halos in the concordance ΛCDM model (Frenk & White, 2012, for review). The density profile of a halo in N-body simulations is typically characterized by Navarro-Frenk-White profile (Navarro et al., 1996a) or Einasto profile (Einasto, 1965), with a shallow slope inside the cluster that gets progressively steeper with increasing radius. The velocity dispersion profile is related to the density profile of the halo through Jeans equation, and has been found to be increasing when the density slope is shallow, and decreasing outward when the density slope is steep (Cole & Lacey, 1996; Taylor & Navarro, 2001). Studies have shown that the density profile, and thus the velocity dispersion profile, reflect the initial density peaks and assembly history of the halo (Dalal et al., 2010; Ludlow et al., 2014). Recent simulations showed that halos have a sharp drop in the slope of the density profile at large radii, where the precise location of this feature is dependent on the peak height and mass accretion rate of the halo (Diemer & Kravtsov, 2014).

The simple spherical collapse model predicts that there exists the outermost physical caustic in the phase space structure of the halo (Bertschinger, 1985). The splashback radius is defined by the apocenters of the recently accreted spherical shells of particles that are at their second turnaround, and the sharp jump in the slope of the spherically symmetric density profile coincides with the caustic in the phase space (Adhikari et al., 2014). Even without perfect spherical symmetry, such a density drop can be detected in the spherically-averaged density profile in N-body simulations, and has been regarded as a physical boundary of the halo that encompasses most of the bounded particles (Diemer & Kravtsov, 2014; More et al., 2015). In practice, the detailed analysis of individual particle trajectories in N-body simulations revealed a broad distribution in the apocenters of the splashback particle population (Diemer, 2017), and the splashback surface where the density slope is minimal can be highly aspherical (Mansfield et al., 2017). This splashback surface contains most halos which have been inside the central halo, with only 1-2 per cent of flyby haloes outside of this surface (Mansfield & Kravtsov, 2020). However, the volume-averaged radius of the surface encloses only 87% of the apocenters of the particle trajectories, while the radius from the spherically averaged density profile only encompassed 75%, regardless of the mass accretion rate and mass of the halos (Diemer et al., 2017). Analysis of hydrodynamics simulations also reveals that some galaxies outside the splashback radius of a halo have been inside the halo before (Haggar et al., 2020). Consequently, halos appear to extend at least somewhat past the 'average' splashback radius defined using the density profile.

Motivated by analysis in the companion paper (Tomooka et al., 2020), in this work we set out to determine whether a detailed study of the phase space structure of dark matter halos can shed light on their bonafide outermost physical boundary. The phase space structure of a dark matter halo can be used to constrain cosmology through cluster mass measurements (Evrard et al., 2008; Munari et al., 2013; Bocquet

et al., 2015; Hamabata et al., 2019), to constrain modified gravity models (Schmidt, 2010; Lam et al., 2012; Zu et al., 2014; Mitchell et al., 2018) and to understand astrophysical processes such as assembly bias (Hearin, 2015; Xu & Zheng, 2018; Mansfield & Kravtsov, 2020). Detailed characterization of the phase space structure of dark matter halos, however, reveals that near the splashback radius, the tracers of the potential well cannot be cleanly separated into infalling and orbiting matter, which gives rise to the velocity structure of the halo, using a simple radial cut. Throughout this work, we define the orbiting population to be subhalos and halos which have experienced their first pericenter event, which marks the end of the first radial infall. Instead, the spatial distribution usually exhibits a mix of these two types of tracers. Indeed, the infalling stream may penetrate all the way into the halo center (Zu & Weinberg, 2013, hereafter ZW13). For these reason, halo models that split the density distribution into a one-halo term at small scales and a two-halo term at large scales usually break down near the edge of the halo, with differences in velocity dispersion as large as 20% (Lam et al., 2013). This difference is comparable to the changes in phase space which arise from assembly bias, and is much larger than the effects from modified gravity. Thus, proper understanding of the phase space structure of dark matter halos is needed to make reliable testable predictions for cosmology and astrophysics using galaxy surveys.

In this paper, we analyze the phase space structure of dark matter halos with the goal of understanding the transition from the orbiting to infalling region better. In particular, we identify the "edge radius" beyond which one does not find any additional orbiting structures. Specifically, we (1) characterize the phase space structure of dark matter halos in and around the edge radius, (2) show how this radius differs from the “splashback radius” defined by the steep feature of the slope of the density profile, and (3) relate this radius to the splashback radius, and interpret it as enclosing a certain percentile of splashback particles. To analyze the phase space structure of

the dark matter halos, we use the dark matter halos and subhalos from the *MDPL2* (Multi-Dark Planck) N-body simulation as tracers. Section 2.2 describes the simulations and mock catalog. We present our results in section 2.3. We summarize our findings in section 2.4.

2.2 Methodology

In this work, we analyze the *MDPL2* dark matter-only N-body simulation performed with L-GADGET-2 code, a version of the publicly available cosmological code GADGET-2 (Springel, 2005). The simulation has a box size of $1\,\mathrm{Gpc/h}$, with a force resolution of $5 - 13\,\mathrm{kpc/h}$. The mass resolution for dark matter particle is $1.51 \times 10^9 M_\odot/h$, corresponding to 3840^3 particles. It assumes the *Planck* 2013 cosmology with $\Omega_m = 0.307$, $\Omega_\Lambda = 0.693$, $\sigma_8 = 0.823$, and $H_0 = 68\,\mathrm{km(s\,Mpc)}^{-1}$. More details of the simulation can be found in Klypin et al. (2016). The halos and subhalos are identified using the Rockstar 6D phase space halo finder (Behroozi et al., 2013a), and the merger tree is built using the Consistent-Tree algorithm (Behroozi et al., 2013c). For this study, we treat the subhalos and halos around the main halos equally and are selected with a peak mass cut $M_p > 3 \times 10^{11} M_\odot/h$, which corresponds to at least 200 particles before falling onto the halos. The main central halos are selected using a mass cut $M_{200m} > 10^{14} M_\odot/h$. All analyses are performed using the stacked profiles of the central halos.

2.3 Results

2.3.1 The Orbiting & Infalling Components of Dark Matter Structures in Phase Space

To understand the phase space around halos, we study the radial and tangential velocities using dark matter halos as tracers. The velocity of the tracer with respect to the central halo is given by $\vec{v} = \vec{v}_{\rm tracer} - \vec{v}_{\rm cen}$. The radial velocity is $v_r = \vec{v} \cdot \hat{r}$ and the tangential velocity is $v_{\rm tan} = \sqrt{v^2 - v_r^2}$. Thus, the radial velocity is directional, positive for outgoing, and negative for infalling, while the tangential component is only a magnitude.

Figure 2.1 shows the phase space structure of dark matter halos, illustrated as the 2D histograms of radial and tangential velocities in 4 representative radial bins. Note that the velocities are normalized by the circular velocity at $r_{\rm 200m}$ of the halo, $v_c = \sqrt{GM_{\rm 200m}/r_{\rm 200m}}$. All other radial bins are qualitatively similar to one of the four bins shown below.

The top-left panel shows the distributions of halos in the v_r–$v_{\rm tan}$ plane for the radial bin, $r/r_{200m} = [0.5 - 0.55]$. The phase space structure at this radius is typical of halos, with approximately zero mean radial velocity. However, we can see a faint split between low and high total velocities for negative radial velocity component. The blue-dashed line, determined as the local minimum in the distribution $P(v|v_r < 0)$, denotes the valley between low and high total velocity (or kinetic energy) components. The average infall time of the high energy halos is less than a dynamical time[1], indicating that these are halos that have recently fallen into the central halo. Turning to the distribution of halos with positive radial velocities, we can see a large population of halos with large kinetic energy, similar to those in the infall stream outside blue

1. The dynamical time is the timescale for halos at $r_{\rm 200m}$ to fall into the center of halo given a typical circular velocity, $t_{\rm dyn} = r_{\rm 200m}/\sqrt{GM_{\rm 200m}/r_{\rm 200m}})$.

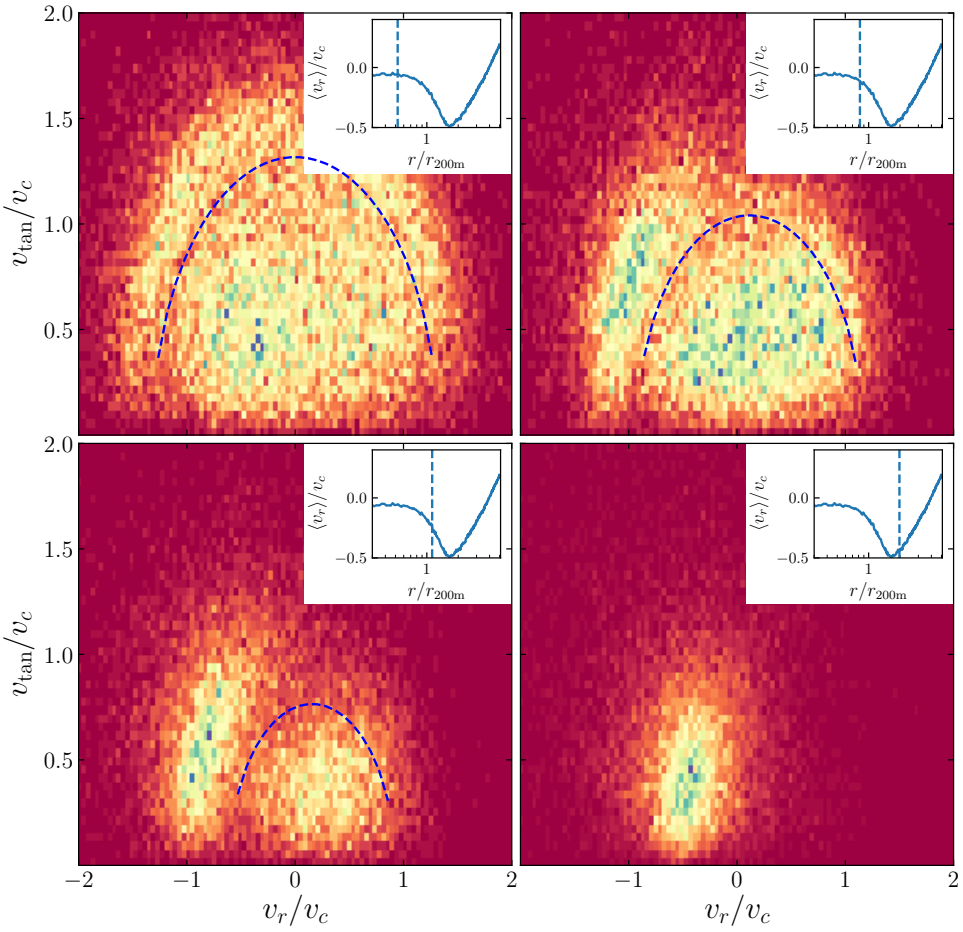

Figure 2.1: The 2D histograms of the radial and tangential velocity distribution at 4 representative radii. The top-left panel shows the inner region ($r/r_{\rm 200m} = [0.5-0.55]$) which consists of orbiting and infalling populations. The blue dashed line for $v_r < 0$ separates the two populations. The velocity structure of the splashback stream outside the blue line mirrors that of the infall stream. The top-right panel also shows a mix of orbiting and infalling halos at $r/r_{\rm 200m} = [0.8 - 0.85]$. The bottom-left panel shows similar structure outside halo, but with orbiting population less prominent at $r/r_{\rm 200m} = [1.1 - 1.15]$. The bottom-right panel at $r/r_{\rm 200m} = [1.95 - 2]$ shows an infalling region. A small panel inside each histogram shows the radial position of the histogram along with average radial velocity.

dashed line[2]. As we move radially outward in the top-right panel to $r/r_{200m} = [0.8 - 0.85]$, the splitting between the low and high velocity components for the negative radial velocity becomes more apparent. However, the "arc" of outgoing material with large velocities becomes less distinct with slightly less kinetic energy than the infall stream. These outgoing subhalos form the splashback stream, which recently fell into the central halo.

The bottom-left panel shows the result at $r/r_{200\mathrm{m}} = [1.1 - 1.15]$ and exhibits features that are quite similar to those found in the previous radial bin at $r/r_{200m} = [0.8 - 0.85]$, despite the fact that this bin is past the r_{200m} radius of the central halo. In both cases, there are two kinematically distinct populations. The first one has a slightly positive average radial velocity, indicating structures similar to the orbiting populations within the central halo. The second population has a negative radial velocity on average, corresponding to infalling halos. In addition, there is also a small population with the total velocity larger than the blue dashed line and positive radial velocity, associated with the splashback stream. Traditionally, the halos with zero radial velocity found at $r = [1.1 - 1.15]r_{200\mathrm{m}}$ are not considered subhalos of the central halo, because they lie outside most halo radius definitions (such as $r_{200\mathrm{m}}$ or $r_{200\mathrm{c}}$). However, it is clear that these halos are kinematically distinct from the infalling population, and are better thought of as subhalos associated with the central halo.

We can see in these 3 panels that in general the infall streams have the largest total velocity, followed by the splashback stream, and then the rest of the orbiting halos. The difference between infall and splashback streams is most pronounced at large radii ($r/r_{200\mathrm{m}} = [0.8 - 0.85]$ and $r/r_{200\mathrm{m}} = [1.1 - 1.15]$ in Figure 2.1), because the splashback population was accreted earlier when the halo was less massive and is also affected by dynamical friction longer compared to the infalling population. The infall and splashback streams have almost symmetric velocity distributions with

2. The line is reflected across Hubble velocity for the minimum in the distribution of $P(v|v_r < 0)$.

respect to $v_r = 0$ in the inner part of the halo ($r/r_{200\mathrm{m}} = [0.5 - 0.55]$ in Figure 2.1), because the difference in the infall time between the two populations becomes small. Orbiting halos, which fell in even earlier, have even lower kinetic energy than the splashback halos. After the first apocentric passage, orbiting subhalos form multiple caustic-like phase space structures whose kinetic energy depends on the number of pericentric passages (Sugiura et al., 2020).

Finally, the bottom-right panel of fig. 2.1 shows that the orbiting populations have disappeared by $r/r_{200\mathrm{m}} = [1.95 - 2]$, leaving behind only the infalling component. As we move further away from the central halo, the average velocity of the infalling component becomes less negative, being eventually overtaken by the Hubble flow at the turnaround radius r_{ta}. Beyond this radius, the distance between halos increases due to the expansion of the Universe.

Figure 2.2 illustrates the halos from the bottom-left panel of fig. 2.1 separated into two categories: (1) top panel: halos that have been in the central halo (the radial position of the halo is less than $r_{200\mathrm{m}}$ of the central halo) at least once in the last 2 Gyr (approximately 1 dynamical time at $z = 0$, or 1.5 dynamical time at $z = 0.36$); (2) bottom panel: halos that have not been in the central halo in the last 2 Gyr. The top panel shows that the halos that have been in the central halo are the ones responsible for creating the orbiting components of the velocity distribution. These halos have at least one pericentric passage with respect to the central halo. The escape velocity at these radii is $\approx \sqrt{2}v_c$, which means that most of these halos are bounded to central halos with highly elliptical orbits. In the bottom panel, the halos that have never been in the central halo clearly correspond to the infalling population, and have not had a pericentric passage in their history. Our results are consistent with the findings in Haggar et al. (2020), which showed that backsplash galaxies can exist outside $r_{200\mathrm{m}}$.

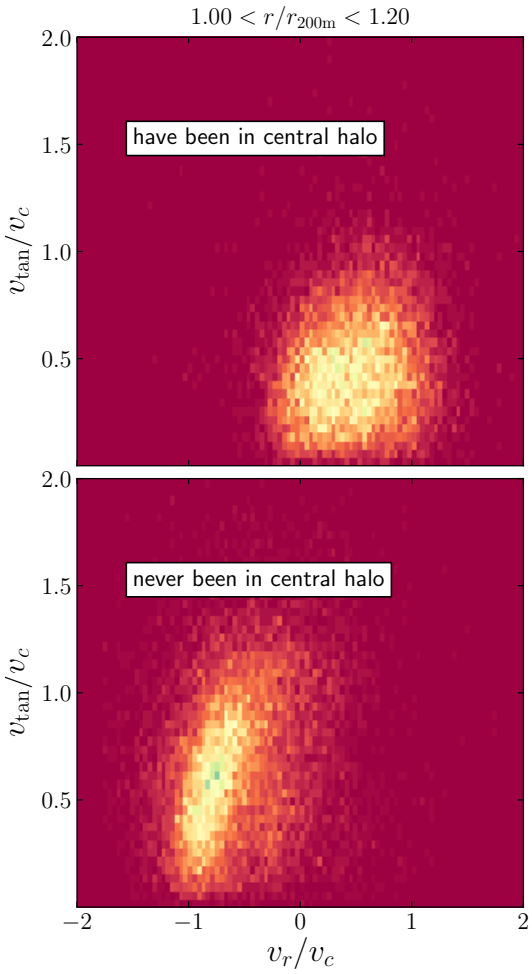

Figure 2.2: A more detailed look at the halos outside $r_{200\mathrm{m}}$, the third panel of fig. 2.1 but with slightly larger radial bin. The halos are now distinguished into halos that have been inside the central halo in the past 2 Gyr and halos that have never been in the central halo. The former constitutes a population of halos around $\langle v_r \rangle > 0$, indicating that these halos are orbiting, while the latter constitutes infalling halos with largely negative radial velocity.

2.3.2 The Edge of Dark Matter Halos

Figure 2.1 presents a simple yet compelling way of describing the phase space structure of orbiting dark matter structures around a central halo. At small radii, dark matter halos in a halo belong to one of three categories: (1) halos in approximate virial equilibrium with the central halo; (2) an infalling stream of halos; and (3) an outgoing population of splashback halos. As we move towards larger radii, the orbiting populations disappear, eventually leaving only a stream of infalling structures. In this work, we want to identify the radius $r_{\rm edge}$ which defines the transition from a mix of infall and orbiting populations to an infall only region based on the kinematics of halos.

In a previous study of the phase space structure of dark matter halos, ZW13 defined the virial extent of a halo by modeling the distribution of galaxies near a halo as a mixture of orbiting[3] and infalling galaxies. The infall stream was modeled using a skewed t-distribution, whereas the orbiting structures are modeled as a Gaussian distribution with mean of 0. However, the model fit produced a decreasing orbiting fraction in the inner part of the halo. This is in contrast to the phase space structure in the fig. 2.1, which shows the orbiting population increases toward the halo center as expected. The degree of freedom of the t-distribution also hits the upper bound, turning the t-distribution into a Gaussian. In fitting the ZW13 model to our data, we find that these peculiarities arise because the t-distribution shifts to smaller median so that it ends up describing the wide-peaked orbiting population, rather than the infalling stream in the interior of the halo (see section A.1 for details).

We find that modeling the orbiting population as a double Gaussian distribution suffices to describe all the populations adequately, thereby removing the peculiarities seen in ZW13. We also find that the unskewed t-distribution for infalling stream

3. ZW13 use the term "virialized" when referring to the orbiting population as defined in this paper.

produces a good fit for the region of interest (upto $r \lesssim 2.5 r_{200\mathrm{m}}$), with the skewed distribution only needed when we move further away from the halo. Our final model for the radial velocity distribution of halos is

$$\mathrm{PDF}(v_r, r) = f_{\mathrm{orb}}[fG(v_r, \mu, \sigma_1) + (1-f)G(v_r, \mu + \mu_d, \sigma_2)] + (1 - f_{\mathrm{orb}})t\left(\frac{v_r - \mu_{\mathrm{inf}}}{\sigma_{\mathrm{inf}}}, \nu\right), \quad (2.1)$$

where $G(x, \mu, \sigma)$ is a normalized Gaussian distribution with mean μ and standard deviation σ, and $t(x, \nu)$ is a normalized standard t-distribution with ν degree-of-freedom. f_{orb} is the fraction of orbiting halos (i.e. any substructure that has had one pericentric passage), whereas f controls the relative weight of the two Gaussians. All the parameters in eq. (2.1) depend on the radius. Thus, we fit the distribution for halos within each individual radial bin of $r/r_{200\mathrm{m}}$, by maximizing the total likelihood function ($\mathcal{L} = \sum_i \mathrm{PDF}(v_{r,i})$) using the Markov Chain Monte Carlo (MCMC) method. We set a prior to ensure that the mean radial velocity of infalling population μ_{inf} decreases monotonically, and the means of the two Gaussian populations are larger than that of t-distribution (i.e., $\mu > \mu_{\mathrm{inf}}, \mu_d > 0$). This ensures that our model utilizes the t-distribution for capturing the behavior of the infalling stream in all radii.

Figure 2.3 shows the fraction of orbiting halos as a function of radius recovered by our model. Following fig. 2.2, we defined the "true" fraction of orbiting halos as those which have had their first pericentric passages. Our model recovers the fraction of orbiting structures correctly at all radial bins. We can see that the fraction starts out at 0 at large radii, and constantly rises after $r \lesssim 1.7 - 1.8 r_{200\mathrm{m}}$. It then asymptotically approaches toward but not equal to unity as we move towards smaller radii. $f_{\mathrm{orb}}(r)$ is well fit by a slight modification to the original function used in ZW13, namely $f_{\mathrm{orb}}(r) = a \exp(-(r/r_0)^\gamma)$, where $a = 0.986$ is the asymptotic fraction as it approaches center, and $r_0 = 1.27 r_{200\mathrm{m}}$ is the radius where the fraction reaches $1/e$.

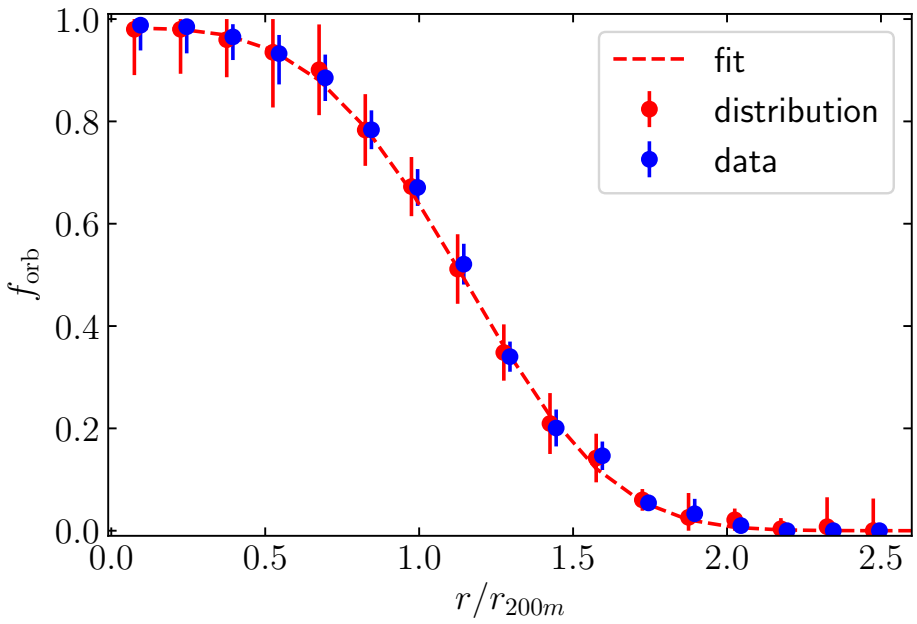

Figure 2.3: Fraction of orbiting halos, $f_{\rm orb}$, as a function of radius. The result of fitting the eq. (2.1) in different radial bins agrees with the fraction of halos which have had their first pericentric passages (offset slightly in x-axis for clarity) and describes the evolution of infalling stream vs orbiting populations.

The decreasing slope is fitted to $\gamma = 3.5$. Since the fraction of orbiting population approaches 0 as we move outward, we define the edge radius as the radius where the fraction reaches 0.01, which results in $r_{\rm edge}/r_{\rm 200m} = 1.96$.

2.3.3 Relation Between the Edge Radius and the Splashback Radius

We now compare the edge radius we have identified based on the halo kinematics to the splashback radius defined using the *SPARTA* algorithm, calculated using the fitting formula in Diemer (2017) for the median mass (and thus peak height) and mass accretion rate of the halos in each bin using COLOSSUS (Diemer, 2018). *SPARTA* identifies the splashback radius of individual particles by tracking their trajectories. The splashback radius of a particle is defined as the apocenter of the orbit at the

second turnaround. The splashback radius of the halo is defined as the radius within which a specified percentile of the particle apocenters lie. The splashback radius identified using the slope of the spherically-averaged dark matter density profile corresponds to 75 to 87-percentile of particle apocenters (Xhakaj et al., 2020), while the splashback radius defined by line-of-sight density slopes corresponds to 87-percentile (Mansfield et al., 2017). In other words, at least 13% of the particles in a halo lie outside the splashback radius identified using density profile.

Figure 2.4 illustrates the mass and redshift dependence of the ratio of $r_{\rm edge}$ and $r_{\rm sp,87\%}$. We see that this ratio ($r_{\rm edge}/r_{\rm sp,87\%}$) is approximately constant throughout the entire mass and redshift range we sampled. Since the peak-height is a function of mass and redshift, the ratio also stays constant as a function of the peak-height as well. Thus, we interpret the edge radius as a splashback radius containing specific percentiles of the apocenters of orbiting halos. Specifically, we can see that the edge radius ($r_{\rm edge}$) extends further out than the radius encompassing 87-percentile of the dark matter particles. Beyond the 87-percentile, the splashback radius defined using particle apocenters diverges quickly (Diemer, 2017). We conclude that $r_{\rm edge} = 1.6r_{\rm sp,87\%}$ provides a better definition of the boundary of halo as we can infer from our fitting function that roughly 40% of halos at $r_{\rm sp,87\%}$ are still orbiting halos. Mansfield & Kravtsov (2020) argued that the outlying halos which were originally inside the central halo are contained within an aspherical splashback surface. We note that these splashback halos should disappear after $r_{\rm edge}$, likely coinciding with the maximum radius of the splashback surface.

Figure 2.5 also shows the ratio ($r_{\rm edge}/r_{\rm sp,87\%}$) as a function of the mass accretion rate (Γ), where the mass accretion rate is defined as $\Gamma = {\rm d}\log M/{\rm d}\log a$ evaluated in the $a = [0.600 - 0.733]$ range which spans one dynamical time as defined in Diemer et al. (2017). This figure further demonstrates the constancy of the ratio ($r_{\rm edge}/r_{\rm sp,87\%}$). It has the same mass accretion rate dependence as the splashback

radius, and is again roughly a fixed multiple of $r_{\rm sp,87\%}$.

Analysis of the relative change of $r_{\rm edge}$ using different halo mass cuts also shows splashback-like behavior as seen in fig. 2.5. $r_{\rm edge}$ serves as the furthest splashback radius for all matter orbiting around the halo. When working with halos, this radius is expected to be sensitive to the effects of dynamical friction. Dynamical friction tends to increase with the mass squared, so the higher the mass of the orbiting halo, the more kinetic energy the halo will lose and the smaller the splashback radius will be Adhikari et al. (2016). Thus, $r_{\rm edge}$ decreases for a halo sample of larger M_p.

Our findings demonstrate that the average edge radius for halos generally lies around $2r_{\rm 200m}$, consistent with the extent to which backsplash or ejected halos and galaxies are found within clusters and high-mass halos (Li et al., 2013; Haggar et al., 2020; Knebe et al., 2020). However, studies focusing on the low-mass halos with $M \approx 10^{12} M_{\odot}/h$ show that ejected halos may extend past $3r_{\rm 200c} \approx 2r_{200m}$, although the fraction of ejected halos outside of this range is less than 15% (Ludlow et al., 2009; Wang et al., 2009). This radius depends on mass accretion rate in addition to mass. In particular, $r_{\rm edge}$ is related to the 87% splashback radius defined using *SPARTA* by a constant factor of ≈ 1.6, where the ratio of these two radii is independent of the mass accretion rate. As such, the steep slope of the spherically average density profile at the splashback radius, for example, occurs at a constant radius when normalized using $r_{\rm edge}$. Notably, the spatial extent of the 1-halo term extends significantly beyond the traditionally defined splashback radius, and must be taken into account when modeling the structures of dark matter halos.

2.4 Conclusions

In this work, we analyzed the phase space structure of dark matter halos using dark matter subhalos and nearby halos as tracers. Our main findings are summarized as

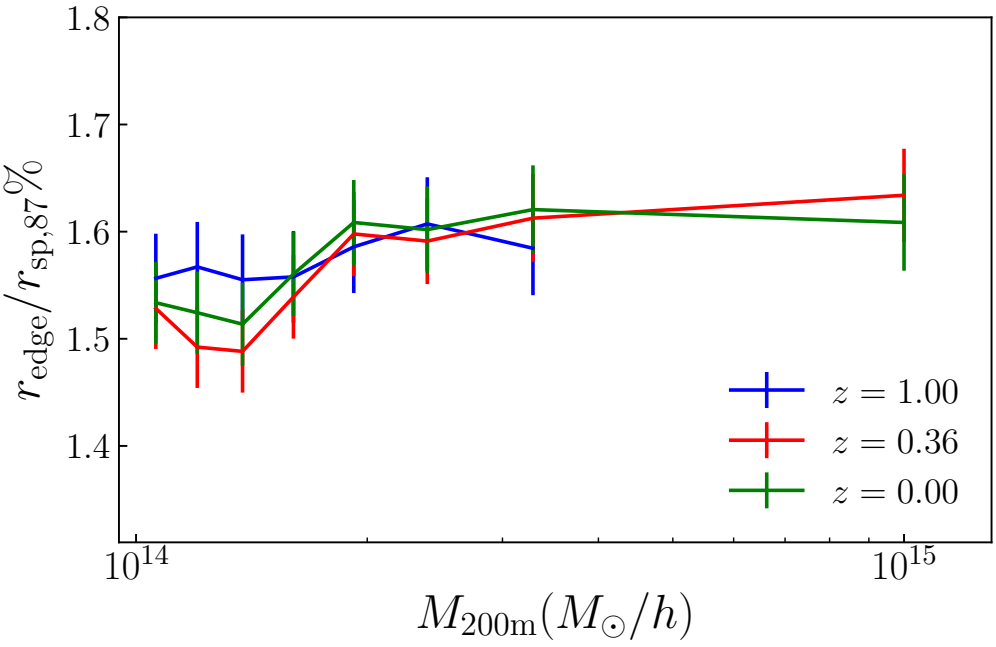

Figure 2.4: The ratio of $r_{\rm edge}$ and $r_{\rm sp,87\%}$, the splashback radius containing 87-percentile of particles from *SPARTA*, demonstrating that the edge radius has the same mass and redshift dependence as $r_{\rm sp,87\%}$.

follows:

- The phase space structure inside dark matter halos can be modeled as a mixture of halos on their first infall, a splashback stream of halos that are on their way to their first apocentric passage, and halos which have orbited the main halo at least once. We refer to the latter two halo populations as "orbiting", in that they are in an orbit around the central halo, bounded or unbounded.

- The edge of the halo can be defined by the radius ($r_{\rm edge}$), beyond which little ($< 1\%$) orbiting populations exist. Inside the edge radius ($r < r_{\rm edge}$), orbiting and infalling structures are mixed in physical space, but they are distinct in velocity space. Outside $r_{\rm edge}$ and up to the turnaround radius $r_{\rm ta}$, the halos are infalling to the central halo. Outside $r_{\rm ta}$, the halos are receding away from the central halo due to the Hubble flow.

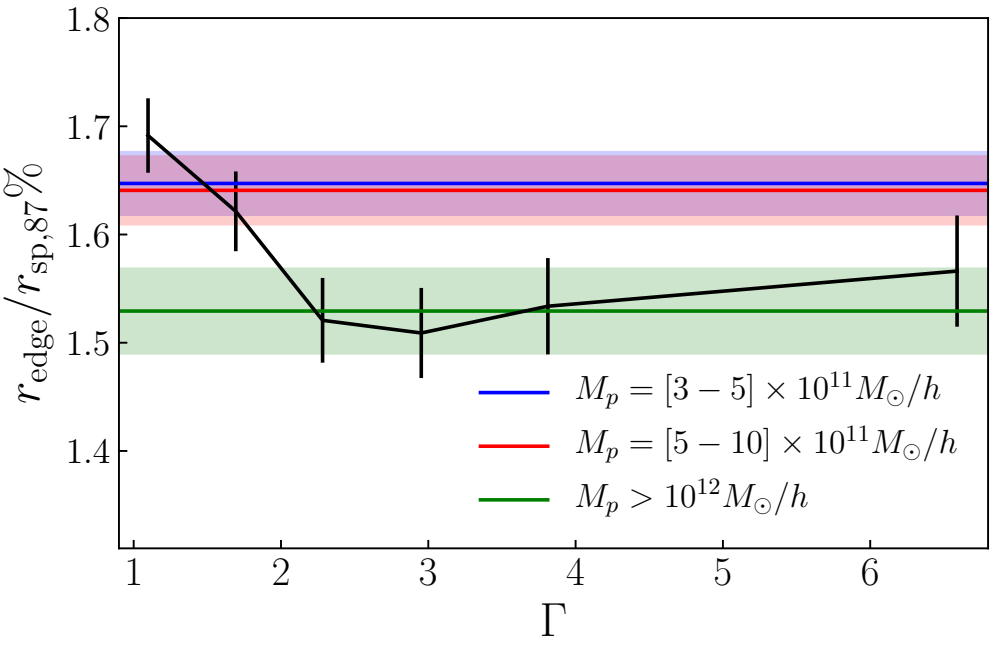

Figure 2.5: The ratio of $r_{\rm edge}$ and $r_{\rm sp,87\%}$ as a function of mass accretion rate. The two have similar mass accretion rate dependence and the ratio remains roughly constant except at very low accretion regime. The three dashed lines indicate $r_{\rm edge}$ computed using halos within different M_p bins. Higher mass halos have smaller $r_{\rm edge}$ due to dynamical friction similar to splashback radius.

- The edge radius ($r_{\rm edge}$) coincides with a fixed multiple of the splashback radius defined either using the slope of the density profile or the splashback radius containing 87-percentile of apocenters of dark matter particles. We reinterpret the edge radius $r_{\rm edge}$, which has been previously found as part of the phase space analysis in ZW13, as the radius within which all apocenters of splashback tracers lie. This is supported by the fact that it has similar mass, redshift and mass accretion rate dependence as the splashback radii.

Our results suggest a new way of defining the halo boundaries based on the phase space structure of halos around dark matter halos. The edge radius ($r_{\rm edge}$) is larger than the traditional splashback radius defined based on the slope of the dark matter density profile. Our finding is consistent with previous studies showing that the splashback radius defined based on the density slope does not encompass all the splashback particles. We show, however, that the edge radius $r_{\rm edge}$ is clearly defined in phase space, and encompasses more than 99% of all orbiting structures. That is, the edge radius ($r_{\rm edge}$) defines a real kinematic boundary for a dark matter halo. In addition, we improved upon the previous characterization of a phase space model by ZW13, by enforcing that the t-distribution used in the model corresponds to the same physical population of structures at all radii (namely infalling structures).

The improved modeling and phase space and new definition of the halo boundary will allow us to use phase space measurements of cluster galaxies for cosmology and astrophysics. In the companion paper (Tomooka et al., 2020), we present the first detection of the outer edge of galaxy clusters based on spectroscopic measurements of SDSS cluster galaxy kinematics. Our study presents the physical interpretation of the edge radius defined based on the halo kinematics and its connection to the splashback radius and its properties. In future work, we plan to investigate observational and systematic uncertainties in extracting the 3D phase space information from line-of-sight velocity measurements and test the robustness of the method used

by Tomooka et al. (2020) to infer the cluster edge radius. Such work is particularly important for measuring the phase space structures of dark matter halos accurately and precisely with the next generation spectroscopic galaxy surveys, e.g., DESI (DESI Collaboration et al., 2016) and Subaru PFS (Takada et al., 2014).

Chapter 3

Shock and Splash: Gas and Dark Matter Halo Boundaries around ΛCDM Galaxy Clusters

3.1 Introduction

In recent years, the outskirts of galaxy clusters have emerged as one of the new frontiers for cosmology and astrophysics (see Walker et al., 2019, for review). Recent theoretical advances revealed that the physical outer boundary for a dark matter (DM) halo can be defined using by the "splashback" radius based on the DM density profile drop (e.g., Diemer & Kravtsov, 2014; Adhikari et al., 2014; More et al., 2015), the aspherical splashback surface (Mansfield et al., 2017; Mansfield & Kravtsov, 2020), or the edge radius of the DM phase space structure (Aung et al., 2021), with various definitions encompass varying fraction of orbiting DM particles (Diemer et al., 2017). Observationally, the outer boundaries of the DM haloes have recently been detected using weak-lensing (e.g., Chang et al., 2018), galaxy number density (e.g., More et al., 2016; Baxter et al., 2017; Shin et al., 2019; Zürcher & More, 2019; Murata et al.,

2020) and phase space structure (Tomooka et al., 2020). Upcoming multiwavelength surveys (such as CMB-S4 in microwave and DESI, Rubin, PFS in optical) will provide unprecedented insight on the outer boundaries of massive DM haloes and promise to shed new insight into cosmology and non-linear structure formation of the Universe.

Gas accreting at cluster outskirts provides an alternative probe of cluster boundary. However, the dynamics of the collisional gas is fundamentally different from that of collisionless DM. Unlike the collisionless DM particles which orbit within the DM halos, the collisional gas is shock heated during its first infall, resulting in a high Mach number ($\mathcal{M} > 100$) cosmic accretion shock marked by the prominent entropy jump. The secondary infall model predicts that the location of the accretion shock coincides with the splashback radius (Bertschinger, 1985; Shi, 2016b). Commonly referred to as "external shock" in the literature (e.g., Miniati et al., 2000; Ryu et al., 2003; Skillman et al., 2008; Molnar et al., 2009), the accretion shock arises from the infall of low density pristine gas in the void regions onto the cluster potential (in contrast to "internal shocks" which occurs within the virialization region of DM haloes due to mergers and penetrating filaments). The external accretion shock thus defines a physical boundary of the hot collapsed gas in DM haloes, which is also dependent on their mass accretion rate (MAR) (Lau et al., 2015).

In this work we investigate the locations of shock and splashback radii by analyzing the *Omega500* hydrodynamical cosmological simulations. We find that the accretion shock radius defined using the drop in the gas entropy is larger than all definitions of the splashback radius in the literature by $20 - 100\%$, in contrast to the prediction of the self-similar models. Specifically, we find that the accretion shock radius is larger by ≈ 1.89 relative to the splashback radius and ≈ 1.2 relative to the edge radius of the DM phase space structure. Furthermore, we find that the ratios of the shock and splashback/edge radii are independent of halo mass and redshift, but dependent on their MAR.

We describe our simulations and analysis methods in §3.2. Results and discussions are presented in §3.3 and §3.4, respectively. Conclusions are summarized in §3.5.

3.2 Simulations

We analyze the clusters from the *Omega500* simulation (Nelson et al., 2014a), a high-resolution hydrodynamical simulation of a large cosmological volume with the comoving box size of $500\,h^{-1}$ Mpc. The simulation is performed using the Adaptive Refinement Tree (ART) N-body+gas-dynamics code (Kravtsov, 1999; Kravtsov et al., 2002; Rudd et al., 2008), which is an Eulerian code that uses adaptive refinement in space and time, and non-adaptive refinement in mass (Klypin et al., 2001) to achieve the dynamic ranges to resolve the cores of haloes formed in self-consistent cosmological simulations in a flat ΛCDM model with WMAP 5 years cosmological parameters: $\Omega_m = 1 - \Omega_\Lambda = 0.27$, $\Omega_b = 0.0469$, $h = 0.7$ and $\sigma_8 = 0.82$, where the Hubble constant is defined as $100\,h$ km s^{-1} Mpc^{-1} and σ_8 is the mass variance within spheres of radius $8\,h^{-1}$ Mpc.

Haloes are identified in the simulation using a spherical overdensity halo finder described in Nelson et al. (2014a). We select 65 haloes with mass $M_{500c} \geq 3 \times 10^{14}\,h^{-1}M_\odot$ at $z = 0$ and re-simulate the box with the higher resolution DM particles in regions of the selected haloes, resulting in an effective mass resolution of $1.09 \times 10^9\,h^{-1}M_\odot$, which corresponds to 2048^3 DM particles. We built the merger tree by tracking the most massive progenitors of haloes over time using the merger tree code presented in Yu et al. (2015). This is done by following the 10% most bound DM particles at each snapshot. We define the start of the merging process at the epoch when R_{500c} of the two haloes start to overlap with each other. Following Diemer &

Kravtsov (2014), we compute the MAR of DM haloes as

$$\Gamma_{200\mathrm{m}} = \frac{\log_{10} M_{200\mathrm{m}}(z) - \log_{10} M_{200\mathrm{m}}(z')}{\log_{10} a(z) - \log_{10} a(z')} \,, \tag{3.1}$$

where a is the expansion factor and $z = 0$, $z' = 0.5$ over a dynamical time as defined in Diemer et al. (2017), and $M_{200\mathrm{m}}$ is the mass enclosed within the radius $R_{200\mathrm{m}}$ such that the density enclosed is 200 times the mean density of the universe, $M_{200\mathrm{m}} = 200\rho_m \times 4\pi R^3_{200\mathrm{m}}/3$.

The simulation is performed on a uniform 512^3 grid with 8 levels of mesh refinement, implying a maximum comoving spatial resolution of $3.8\,h^{-1}\,\mathrm{kpc}$. The spatial resolution is controlled by the density of the cells, and the maximum comoving resolution is only achieved at the centre of the haloes. However, the spatial resolution near the shock radius is between $0.03\,h^{-1}\,\mathrm{Mpc}$ and $0.12\,h^{-1}\,\mathrm{Mpc}$, which is sufficient to determine the locations of the edge and shock radii (which is typically of order several Mpc in size) with the accuracy better than 5%. With a typical number density of $n_e \approx 10^{-3}\,\mathrm{cm}^{-3}$ and temperature of $T \approx 10^6\,\mathrm{K}$, the mean free path of electron is much smaller than the resolution.

Since the effects of non-gravitational baryonic physics (such as gas cooling and energy feedback from supernova and black holes) are small in cluster outskirts compared to cluster cores, we focus on analyzing the outputs of the non-radiative simulation for simplicity. For completeness, we also checked the effects of baryonic physics by comparing the results to those of runs with cooling and star formation and AGN feedback.

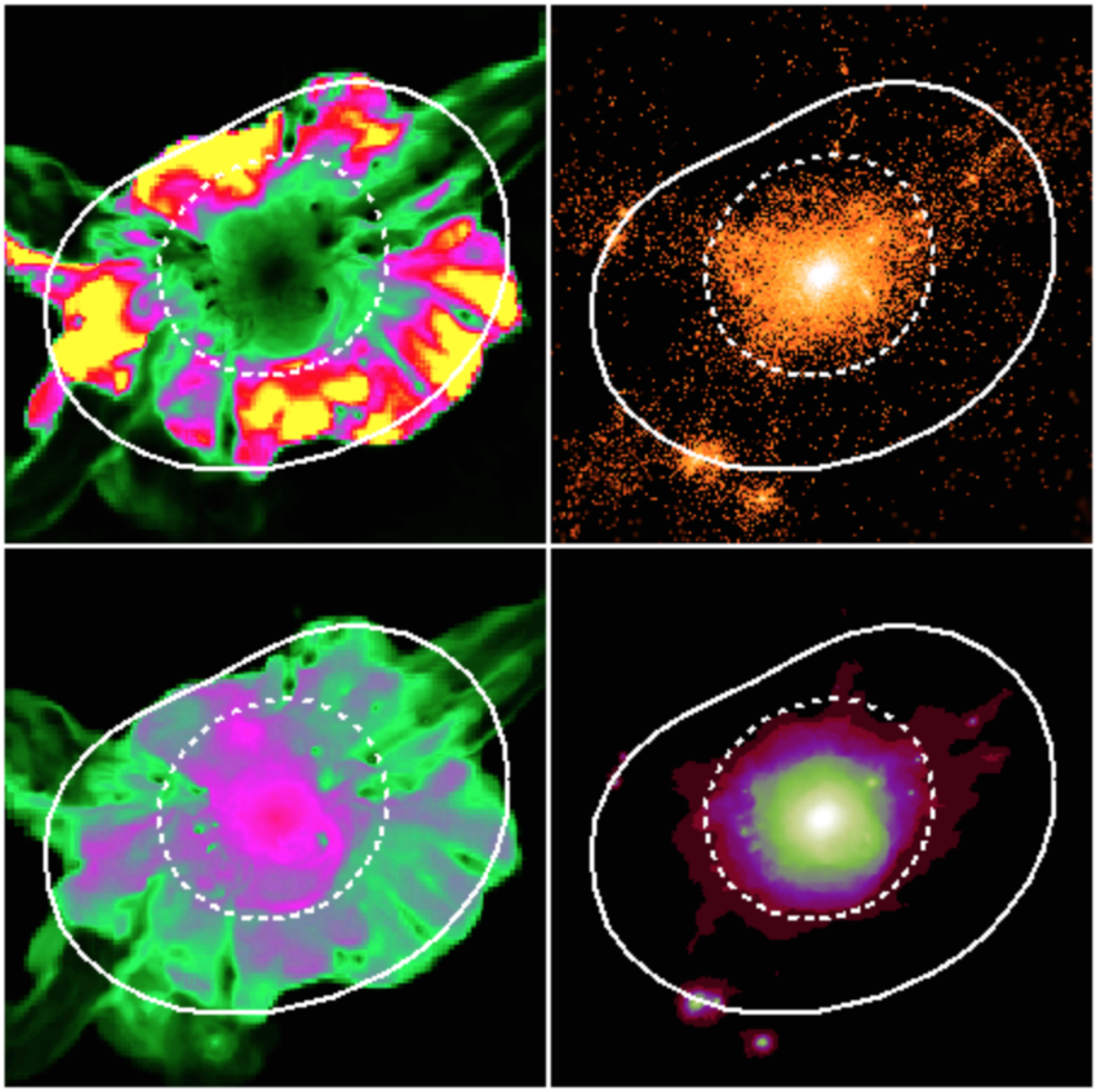

Figure 3.1: Gas entropy (top left), DM density (top right), gas temperature (bottom left) and gas pressure (bottom right) maps of the simulated cluster (CL135) extracted from the non-radiative *Omega500* hydrodynamical cosmological simulation. The images are 15.625Mpc/h wide with the projection depth of 3.90625 Mpc/h. The inner dashed lines indicate the splashback shell computed using the method from Mansfield et al. (2017), whereas the outer white lines indicate the shock shell found by the discontinuous jump in entropy as well as pressure. Note that several low-entropy gas streams have penetrated inside of the accretion shock radius along the filaments without getting shock heated.

3.3 Results

3.3.1 Identifying Splashback and Shock Surface

We determine the location of the splashback radius using the SHELLFISH code (Mansfield et al., 2017). For each halo, the code draws 10^5 random sight lines from the halo centre and samples the DM density along each line-of-sight (LOS). The splashback radius $R_{\rm sp}$ is defined as the radius of a spherical surface that encompasses the same volume as that enclosed by the surface of sharp DM density jumps in all LOS (see Mansfield et al., 2017, for more details).

We determine the accretion shock radius in a similar manner using the SHELLFISH code. Namely, we draw 786 LOS according to HEALPix (Górski et al., 2005) pixels from the halo centre and sample the gas entropy profile along each LOS. The 786 LOS chosen here corresponds to the fourth level resolution of HEALPix, and at the shock radius, each pixel corresponds to about $0.26\,h^{-2}\,{\rm Mpc}^2$, with a length resolution of $\approx 0.5\,h^{-1}\,{\rm Mpc}$, about 4 times the simulation resolution in the region. Measuring the shock radius with the fifth level resolution with 3072 LOS leads to a less than 3% difference in shock measurements.

For each LOS, we select all the gas cells that each LOS passes through, and sample the gas entropy profile along each LOS. The profile is then smoothed with a Savitzky-Golay (SG) filter with window-length of 9 equally spaced logarithmic radial bins and a polynomial order of 5; we checked that the results are robust to the variation in the parameter for SG filter (in the window-length from 5 to 11 bins) and polynomial orders (in the range of 2 to 7). We define the location of the accretion shock as the radius of the minimum in the logarithmic entropy slope. We remove LOS where the entropy jump is less than a factor of 50 (corresponding to Mach number of $\mathcal{M} \sim 20$; the results are unchanged for $\mathcal{M} = 10$ to 50), as these directions host substructures and filamentary gas streams. After these removals, the covering fraction of the shock

surface of the total spherical area is approximately 80% for all clusters. We fit Penna-Dines function with $K = 1, I = J = 2$ (corresponding to the first and second order expansion of $\cos\phi$ and $\sin\phi$ of polar angle ϕ, Penna & Dines, 2007):

$$r(\theta, \phi) = \sum_{i,j,k=0}^{I,J,K} c_{\rm ijk} \sin^{i+j}\phi \cos^{k}\phi \sin^{j}\theta \cos^{i}\theta, \tag{3.2}$$

to the shock position along each LOS and calculate the enclosed volume inside the fitted (non-spherical) surface. We then define the shock "radius" as the radius of a sphere that encompasses the same amount of volume as that enclosed within the fitted surface. We note that the total volume inside the shock radius is larger than the total volume of shock heated gas as it also includes volume of unshocked gas residing in filaments.

Figure 3.1 shows the map of one of the haloes indicating the splashback and shock shells identified using the above algorithms. The splashback shell identified encompasses the DM structure, whereas the shock shell encompasses a much larger, extended area, where the entropy and pressure shows significant decline. We also note that there are several unshocked, low-entropy gas streams that have penetrated inside of the accretion shock radius of the halo along the filaments.

3.3.2 Phase Space Structures of DM and Gas

Figure 3.2 shows phase-space densities of DM and gas for their radial velocity components as a function of radius, for a relaxed cluster (CL135) and a merging cluster (CL77), respectively. The average radial velocity of gas and DM is negative outside the shock radius ($R_{\rm sh}$) as they fall onto the cluster potential. The two trace each other as the gas pressure is low, rendering gas to behave similarly to collisionless DM. Gas infalling from the void is shock heated at the shock radius, causing gas to lose its kinetic energy into heating of the gas. Filamentary accretion can bring infalling gas

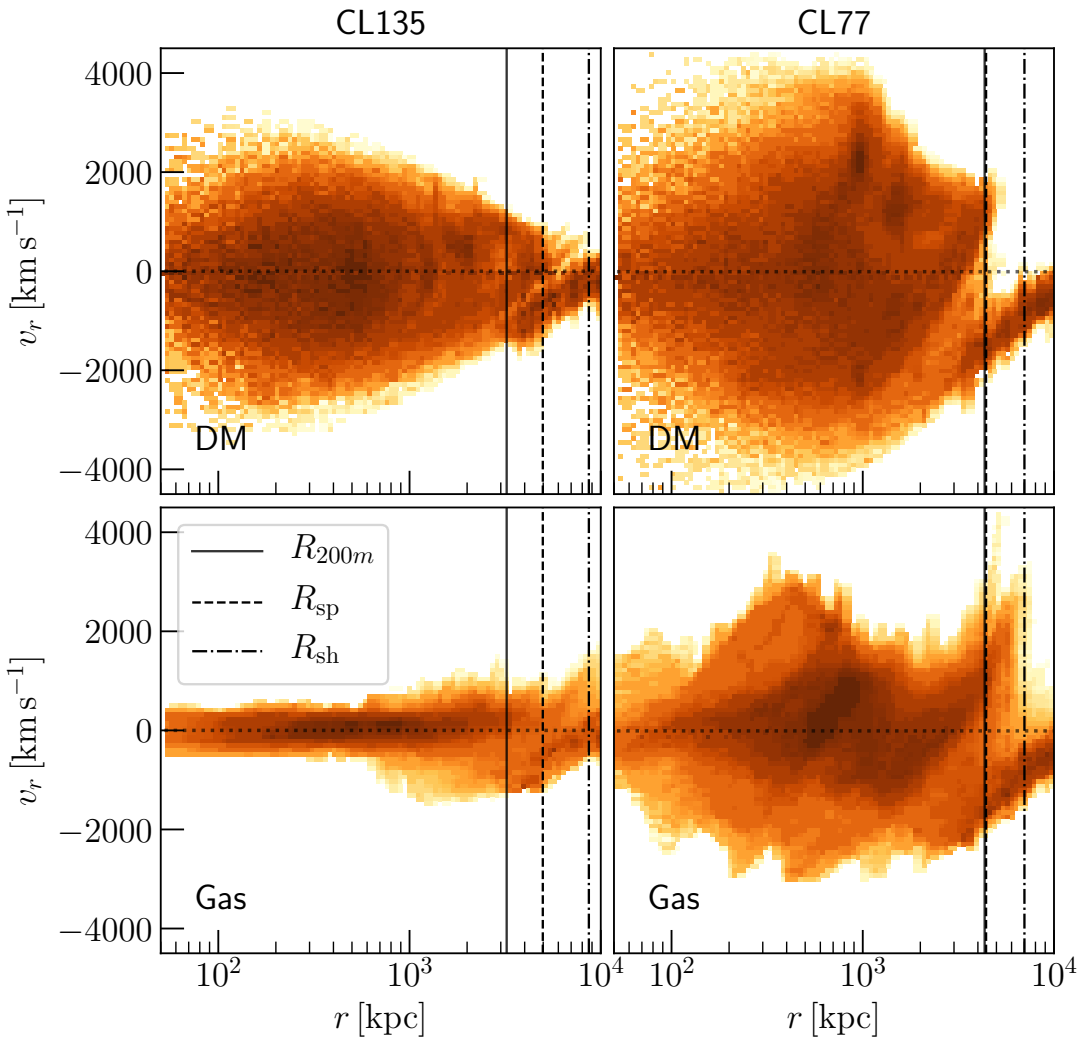

Figure 3.2: Phase-space diagrams of DM (*top* panels) and gas (*bottom* panels) for a relaxed cluster CL135 (*left* panels) with low MAR ($\Gamma = 0.5$), and a merging cluster CL77 (*right* panels) with high MAR ($\Gamma = 2.9$). The solid, dashed, dotted, and dot-dashed lines represent $R_{\rm 200m}$, $R_{\rm sp}$ (splashback radius), $R_{\rm max,sp}$ (maximum splashback radius along any line-of-sight), and $R_{\rm sh}$ (shock radius), respectively. The colour represents the relative mass fraction of DM (top panels) and gas (bottom panels), with deeper colour indicating higher mass fraction at a given radius. The phase space structure of virialized DM haloes extends past $R_{\rm sp}$, reaching nearly $R_{\rm sh}$. Gas follows DM at $r \gtrsim R_{\rm sh}$, while gas dynamics differs significantly from that of collisionless DM at $r \lesssim R_{\rm sh}$.

inside of the virialization region of the DM haloes and form shocks with small Mach number ($\mathcal{M} < 3$) before gas loses their kinetic energy. The DM particles, on the other hand, exchange energy through gravitational interactions as they orbit through the interior of the DM halo. Within the splashback radius ($R_{\rm sp}$), a DM halo exhibits a typical virialized phase-space structure, where the splashback and orbital motions of DM particles produce a dispersion with zero mean radial velocity. The phase space structure of the DM halo can extend out to radii larger than the volume-averaged splashback radius as not all particles within the splashback surface are expected to lie within the volume-averaged splashback radius $R_{\rm sp}$ due to asphericity (Mansfield et al., 2017; Diemer et al., 2017; Aung et al., 2021). Even when using $R_{\rm max,sp}$ (the maximum radius of the splashback surface defined using the Penna-Dines approximation surface), a small amount (upto 1%) of orbiting particles can still exist beyond $R_{\rm max,sp}$ (Mansfield & Kravtsov, 2020) as shown in Figure 3.2.

Due to the collisional nature of the gas, however, the phase-space distribution of gas differs significantly within the interior of the cluster. The radial velocity dispersion of gas is considerably smaller because, as the gas is shock heated through the accretion shock, where most of the gas kinetic energy is converted to thermal energy. Thus, inside $R_{\rm 200m}$, the level of gas motions inside the accretion shock remains small in absence of external disruption by mergers for CL135, while gas motions induced by mergers comprise of most of the velocity dispersion in CL77. The position of the shock radius is closer to the edge of DM phase space than the splashback radius.

3.3.3 Shock Radii Determined from Profiles

Figure 3.3 shows the spherically averaged DM density, gas density, and volume-weighed entropy and pressure profiles for two representative clusters in the sample, CL135 a relaxed cluster with low Γ, and CL77, a merging cluster with high Γ. We also overplot their splashback radii estimated from SHELLFISH $R_{\rm sp}$, and their shock

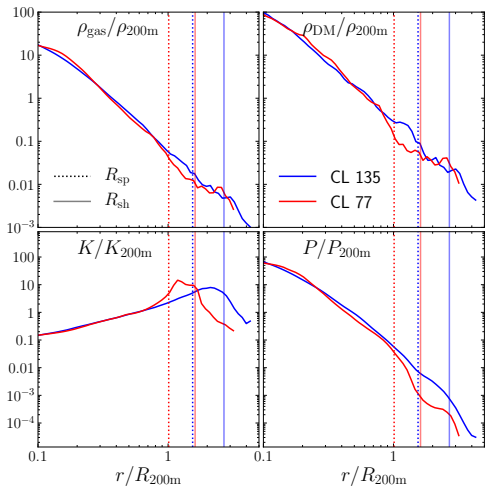

Figure 3.3: Spherically averaged gas density, DM density, volume-weighed entropy and pressure as a function of radius for the two different clusters: a relaxed cluster CL135 with low MAR ($\Gamma = 0.5$), and a merging cluster CL77 (*right* panels) with high MAR ($\Gamma = 2.9$). The vertical lines indicate splashback and shock radii based on the SHELLFISH and our method, respectively. The gas pressure and entropy profiles show significant decrease near the shock radii, while the gas density and DM density decreases at the splashback radii. The gas density slope is shallower than the DM density slope. The slower accreting halo (CL135) also has a smoother jump and larger shock and splashback radii than the fast accreting CL77.

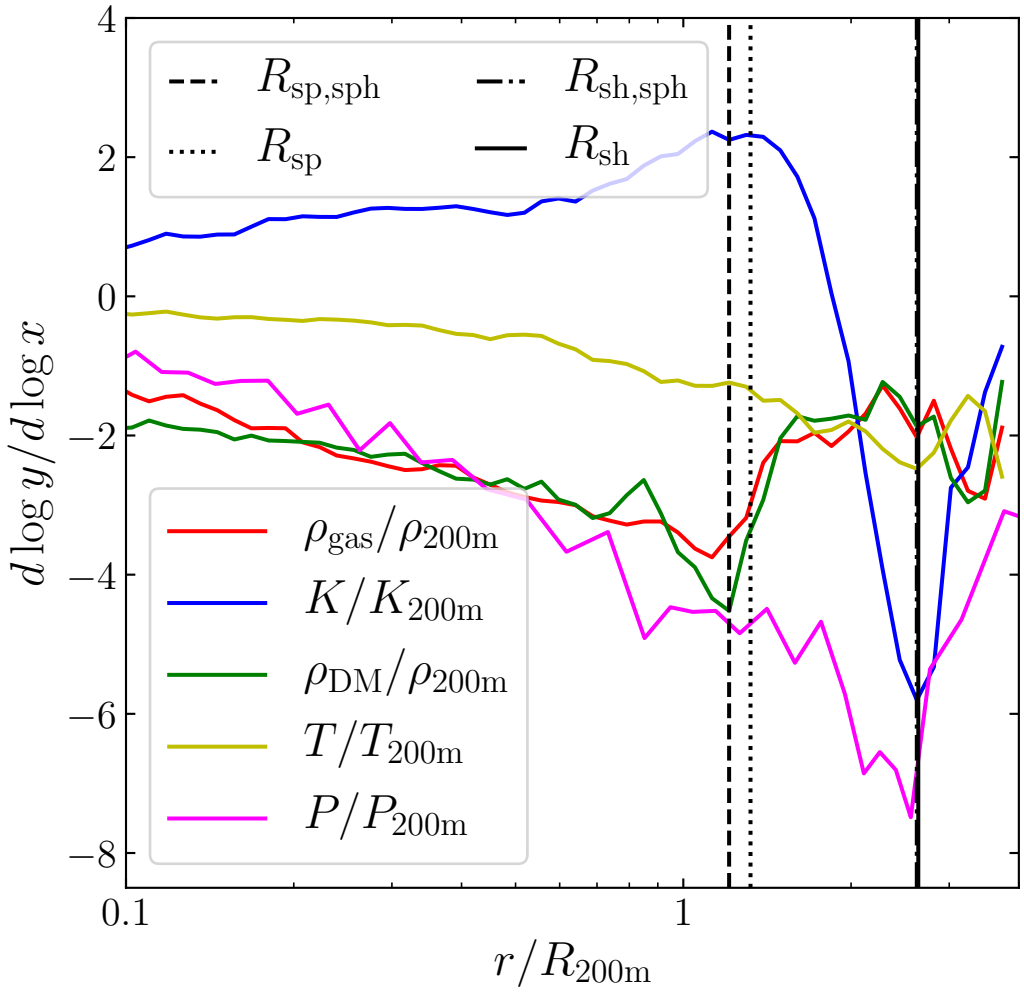

Figure 3.4: The logarithmic slope of different gas and DM median profiles as a function of radius. The radius where the minimum of gas entropy, temperature and pressure slope is defined as the shock radius $R_{\rm sh,sph}$ of the spherically averaged gas profile, denoted by dotted line. The radius where the minimum of DM density slope is defined as the splashback radius $R_{\rm sp,sph}$ of the spherically averaged profile, denoted by dashed line, and coincides with the minimum of the gas density slope.

radii from the shock surface $R_{\rm sh}$. Both $R_{\rm sp}$ and $R_{\rm sh}$ are smaller for the high Γ cluster CL77 than than the low Γ cluster CL135. In both clusters, there are sharp drops in the pressure and entropy profiles at the accretion shock, and they are particularly prominent in the high Γ cluster CL77. However, the corresponding decrease in gas density profiles are small at the accretion shock. This is because the density contrast across a shock is intrinsically smaller than their counterparts in pressure and entropy, and is capped at a maximum value of 4, as expected from the Rankine – Hugoniot shock jump condition.

Figure 3.4 shows the logarithmic slope of the spherically averaged median DM density, gas density, temperature, pressure, and entropy profiles for all clusters at $z = 0$. The entropy profile is increasing at all radii before the shock radius, and within $0.1 \leq r/R_{\rm 200m} \leq 0.6$, it is consistent with previous findings of entropy slope of 1.1 (e.g., Voit et al., 2005) as expected from self-similar cluster growth. At the shock radius, entropy decreases sharply indicating a strong shock. The shock front, however, is wider and is not as abrupt as the shock front in LOS profile due to smoothing over aspherical shock fronts and variations among clusters. The pressure profile has the minimum slope about -7 at the shock radius. Inside the shock radius, the pressure profile is also rapidly decreasing, consistent with the universal pressure profile characterized by the generalized NFW profile (e.g., Nagai et al., 2007; Arnaud et al., 2010). Similarly, the temperature profile has the minimum slope of about -2 at the shock radius.

The DM density slope follows NFW profile (Navarro et al., 1996b) closely, where the slope is -1 in the inner region and slowly decreases to -3 in outer region before hitting minimum at the splashback radius. The gas density is much flatter in inner region starting with slope of ≈ 0, but approaches NFW and follows DM profile at outer radii. In fact, gas density slope becomes minimum at DM splashback radius, while only showing mild decrease at the shock radius. The smaller decrease in density

slope at the shock radius compared to other thermodynamic quantities is expected, as the density jump for a shock wave in ideal gas is capped at 4, while there is no upper bound for the jumps in temperature, pressure or entropy.

For DM, the splashback radius identified as the steepest point in the spherically averaged density profile $R_{\rm sp,sph}$ is smaller than the splashback radius estimated from SHELLFISH $R_{\rm sp}$ (see also Mansfield et al., 2017). For the accretion shock radius, the radius computed from spherically averaged profile $R_{\rm sh,sph}$, is the same as that identified from the volume-averaged shock surface $R_{\rm sh}$.

Figure 3.5 shows the profile slopes for different Γ samples. Here the splashback and shock radii are identified as the steepest jumps in DM density and gas entropy profiles, respectively. Both radii decrease for larger Γ. The DM density slope is steeper for larger Γ, consistent with the previous result (Diemer & Kravtsov, 2014; More et al., 2015). The pressure jump is larger for larger Γ, indicating a stronger shock.

3.3.4 Offsets between Splashback and Shock Radii

Figure 3.6 shows the splashback radius $R_{\rm sp}$ normalized by the halo radius $R_{\rm 200m}$, plotted as a function of the MAR ($\Gamma_{\rm 200m}$) of haloes extracted from the non-radiative *Omega500* simulation. The splashback radius decreases with increasing MAR, confirming previous numerical (Diemer & Kravtsov, 2014; Mansfield et al., 2017) and analytic results (Adhikari et al., 2014; Shi, 2016a). The $R_{\rm sp}$ from our hydrodynamic simulation agrees well with the best-fitting relation from the DM-only simulation.

In the same panel, we show that $R_{\rm sh}/R_{\rm 200m}$ decreases with $\Gamma_{\rm 200m}$ in a similar manner to the $R_{\rm sp}$–$\Gamma_{\rm 200m}$ relation. The average ratio between the radii is $R_{\rm sh}/R_{\rm sp} = 1.89 \pm 0.16$ (based on the yellow dashed line in Figure 3.6, where the error indicates 1σ scatter) at $z = 0$, and it is only weakly dependent on MAR for the range probed here. At $z = 1$, $R_{\rm sh}/R_{\rm sp} = 2.03 \pm 0.32$, and at $z = 3$, $R_{\rm sh}/R_{\rm sp} = 2.12 \pm 0.35$ which

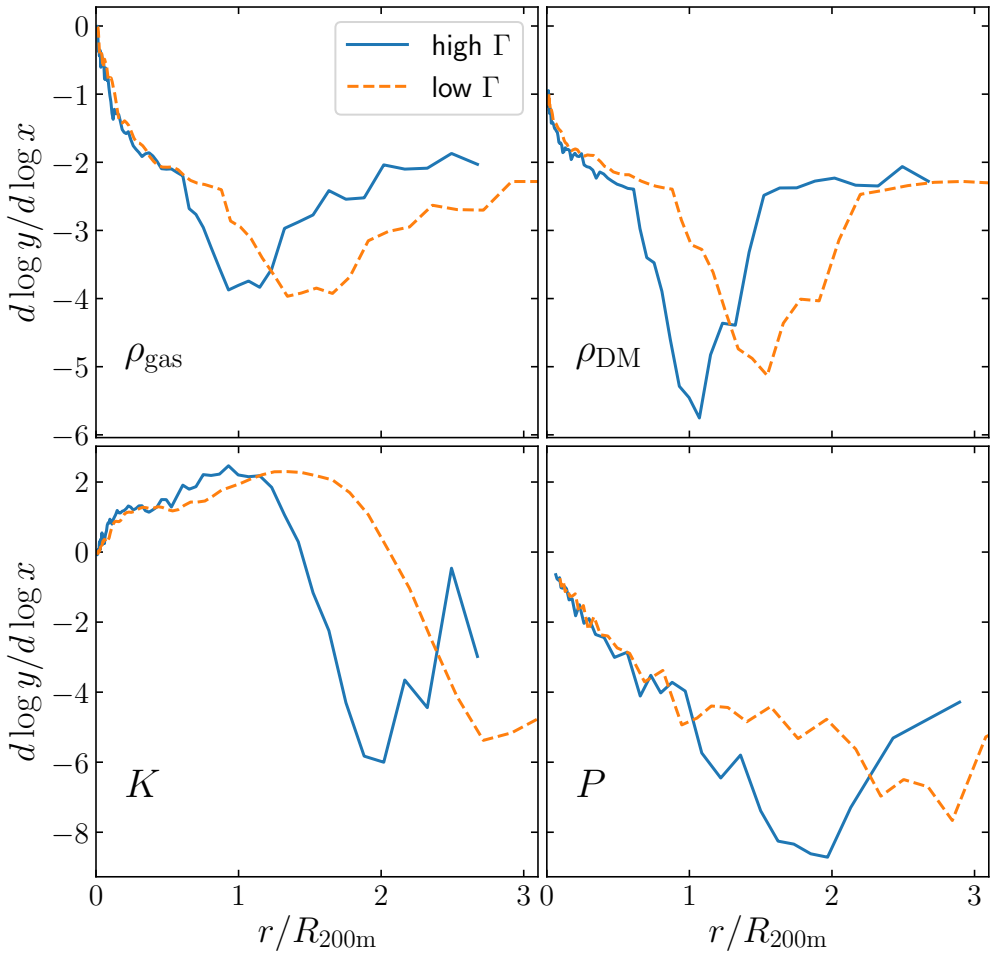

Figure 3.5: The logarithmic slope of different gas and DM median profiles for different MAR. The MAR is split at the 33 and 66-percentile of all haloes, which results in the low $\Gamma_{\rm 200m}$ sample with $\Gamma_{\rm 200m} < 1.5$ (dashed line) and high $\Gamma_{\rm 200m}$ sample with $\Gamma_{\rm 200m} > 2.7$ (solid line). The splashback radius is where the total matter (DM+gas) density slopes is the smallest, and the shock radius where the minimum of entropy and pressure slope is smaller for the higher MAR haloes.

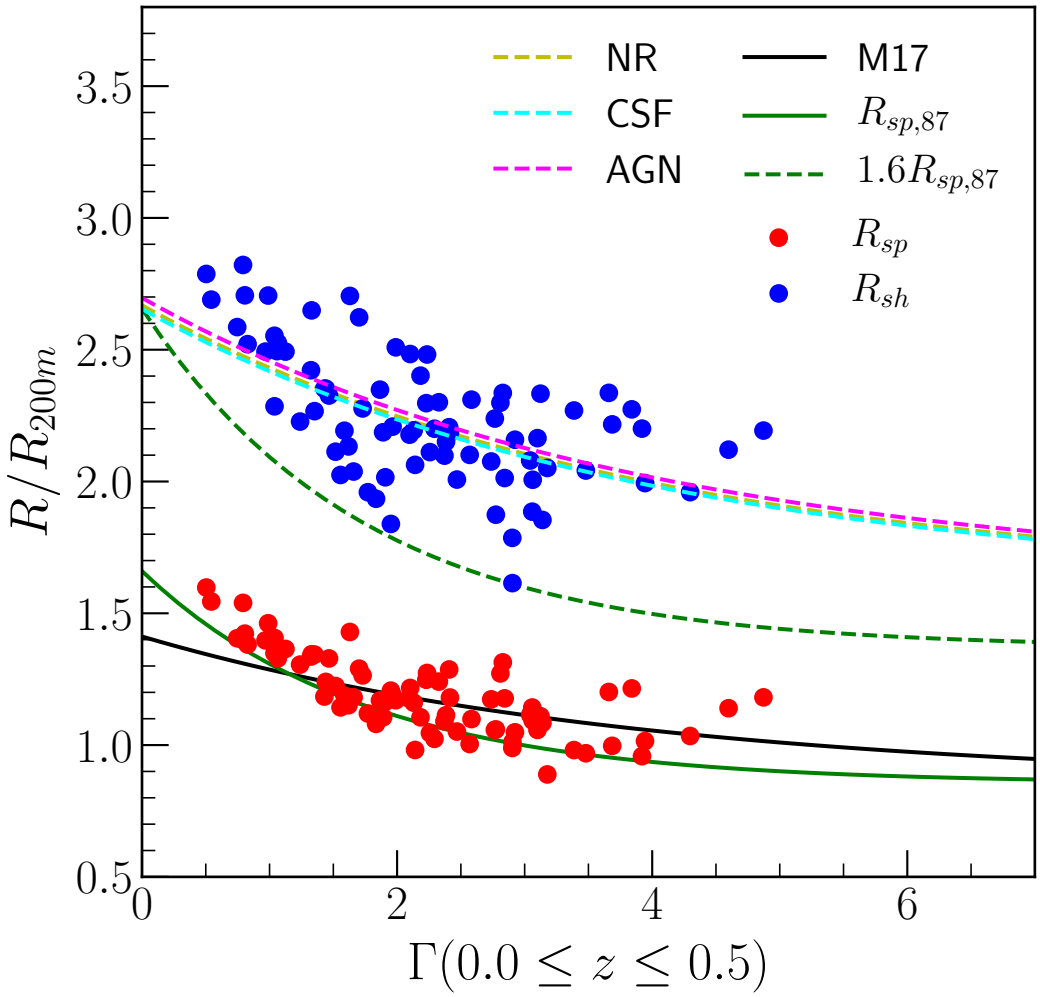

Figure 3.6: The splashback radius $R_{\rm sp}$ (red points) and the accretion shock radius $R_{\rm sh}$ (blue points), normalized by the halo radius $R_{\rm 200m}$, plotted as a function of the MAR of the cluster-size DM haloes, $\Gamma_{\rm 200m}$. The solid line is the $R_{\rm sp} - \Gamma_{\rm 200m}$ relation from DM-only cosmological simulation defined by SHELLFISH (M17, Mansfield et al., 2017) and $R_{\rm sp,87}$ computing using SPARTA (Diemer et al., 2017). The dashed lines represent the best-fitting $R_{\rm sp} - \Gamma_{\rm 200m}$ relation times the average $R_{\rm sp}/R_{\rm sp}$ ratios for three different baryonic simulations (magenta for AGN feedback simulation, cyan for cooling and star forming simulation, and yellow for non-radiative, embedded behind cyan line). Also shown is $r_{\rm edge} \approx 1.6R_{\rm sp,87}$, marking the edge of the DM phase space structure (Aung et al., 2021).

is consistent with no evolution with redshift. We also find that the scatter in $R_{\rm sh}$ is larger than that of $R_{\rm sp}$.

We repeated the same analysis for the same sets of haloes with baryonic physics that include radiative cooling and star formation, and AGN feedback. The differences in $R_{\rm sp}$ and $R_{\rm sh}$ between simulations with different baryonic physics is $\lesssim 1\%$, thus both radii remain essentially unchanged in the presence of baryonic physics.

We note that the phase space structure of the DM halo can extend out to radii larger than the splashback radius, because not all particles within the splashback surface are expected to be enclosed within the volume-averaged $R_{\rm sp}$. In fact, the splashback radius from SHELLFISH only contains about 87% of the particle apocentre (Diemer et al., 2017). The edge radius, which marks the end of DM phase space, corresponds to the radius where the fraction of orbiting subhaloes is greater than 99% (denoted as $R_{\rm sp,99}$), which is approximately 1.6 times larger than the splashback radius measured with SHELLFISH (denoted as $R_{\rm sp,87}$) (Aung et al., 2021). This edge radius lies in the region in between the accretion shock and splashback surfaces. Specifically, the ratio of the shock and edge radius is $R_{\rm sh}/1.6R_{\rm sp,87} \approx 1.2$ for $1 \leq \Gamma_{\rm 200m} \leq 4$, indicating that the shock radius is about 20% larger than the edge radius, on average.

3.3.5 Shapes of Shock and Splashback Shells

In practice, DM splashback and accretion shock are aspherical, because haloes form through merger and accretion of materials through cosmic web of filaments that are inherently aspherical, as shown in Figure 3.1. Figure 3.7 shows the distribution of the maximum ($R_{\rm max}$) and minimum ($R_{\rm min}$) splashback and shock shells. We find that the $R_{\rm max,sh}$ and $R_{\rm min,sh}$ of the shock shell can be 1.65 times larger and 0.7 times smaller compared to the volume-averaged shock radius, respectively, while the maximum and minimum distance of the splashback shell ranges between $(0.8 - 1.42)$ times the volume-averaged splashback radius. This shows that the accretion shock shells

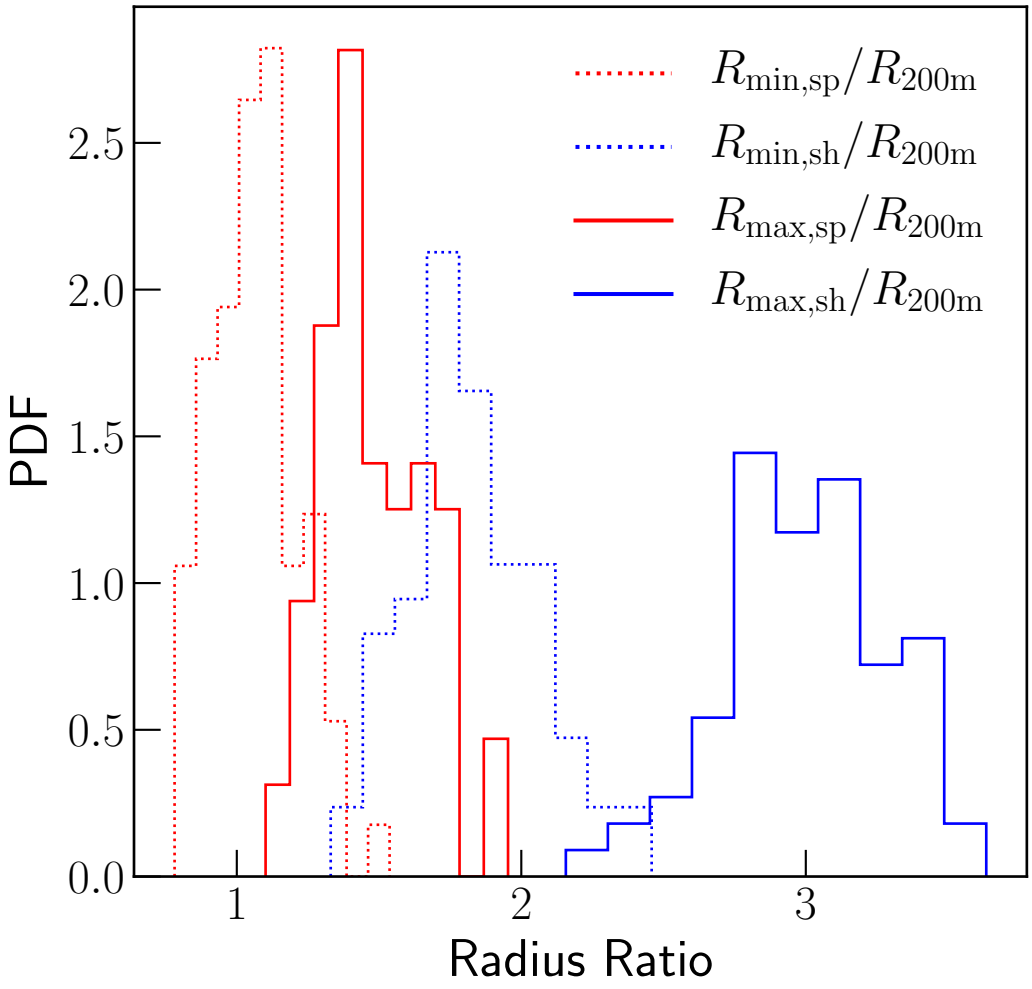

Figure 3.7: The normalized distribution of maximum (solid) and minimum (dotted) radius of shock (blue) and splashback (red) surface with respect to $R_{\rm 200m}$. The shock and splashback shells are highly aspherical, causing the maximum and minimum radius along lines-of-sight to differ by more than 65%. Note that the overlap in the distributions of the minimum shock and maximum splashback radii is due to the scatter in $R_{\rm sh}/R_{\rm sp}$ ratio. For individual haloes, the shock radius is always larger than the splashback radius along every line-of-sight.

are generally more aspherical than the splashback shells, which cause the spherically averaged gas profiles to appear smoother than the actual accretion shocks. Even though the minimum shock radii and maximum splashback radii overlap in Figure 3.7, we emphasize that the largest radius of the splashback shell is still smaller than the smallest radius of the shock shell of the same halo for the individual haloes in our sample. The minimum shock to splashback radius ratio is found in the directions perpendicular to the axis of filament and merger (see the panels in the second and third rows of Figure 3.8 where the ratio is as small as 1.06).

Major mergers are also responsible for the aspherical shapes in the accretion shock and splashback shells. Even though mergers are not directly responsible for the formation of the accretion shock, the 'run-away' shocks generated from mergers (Zhang et al., 2019) can overtake and power the accretion shock, thus affecting the shape of the accretion shock more than the shape of the DM splashback shell (see Section 3.3.6 for the impact of mergers on accretion shock radius). In Figure 3.8, we show the evolution of gas entropy (the most apparent feature in the accretion shock as seen in Figure 3.1) and DM density maps as the cluster undergoes a major merger. Before the merger, the splashback shell encompasses the two merging sub-clusters, while the accretion shock encloses the shock-heated gas associated with these two subclusters. After the merger, the splashback shell decreases rapidly as the collisionless DM of the two clusters overlap with each other. The accretion shock radius, on the other hand, decreases more slowly with time as the gas lags behind (middle two panels in Figure 3.8). Thus, towards the end of the relaxation period, the ratio of shock to splashback radii is slightly larger than that before the merger, $R_{\rm sh}/R_{\rm sp}$ by $\approx 10\%$ (bottom panel in Figure 3.8). Note that the transient internal shocks driven by mergers have much lower Mach number compared to the external accretion shock, leading to much smaller entropy jumps compared to those produced by the accretion shocks.

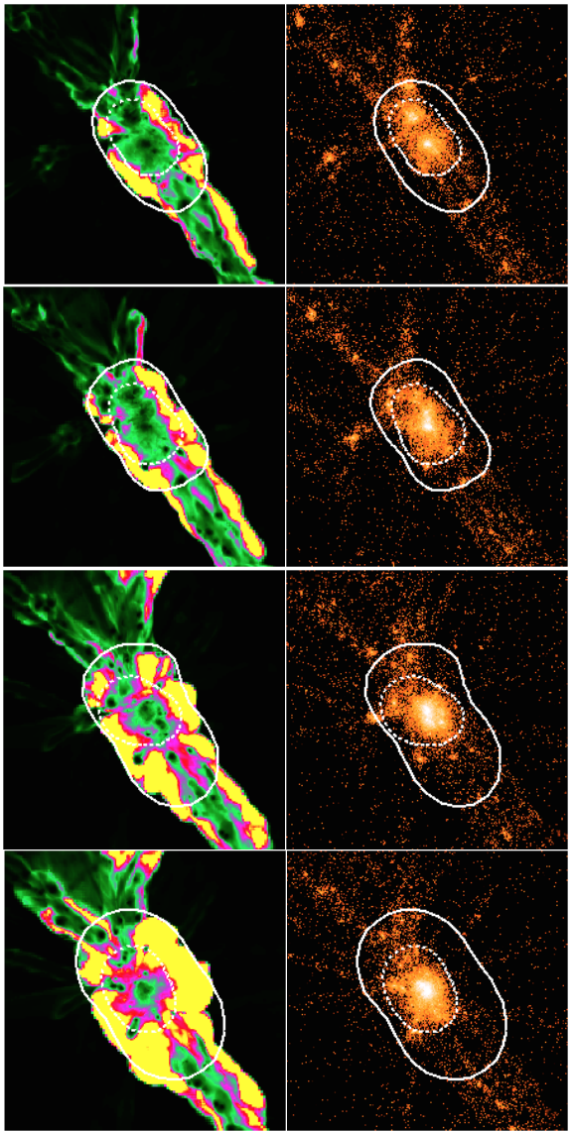

Figure 3.8: Maps of gas entropy (*left* panels) and DM (*right* panels) of a cluster (CL21) undergoing an almost equal mass (mass ratio = 0.83) merger. The solid line and the dotted line show the accretion shock and splashback shells respectively. The panels from *top* to *bottom* show the cluster at different merging stages: $t_{\rm merge} = -0.4\,{\rm Gyr}, +0.4\,{\rm Gyr}, +1.25\,{\rm Gyr}, +2\,{\rm Gyr}$, where $t_{\rm merge}$ is the merging time defined as when $R_{\rm 500c}$ of the two merging haloes first touches. During the merger, the splashback and accretion shock shells continue to evolve. After 2 Gyr, the DM splashback shell becomes more spherical, while the accretion shock is still elongated along the axis of merger and filament.

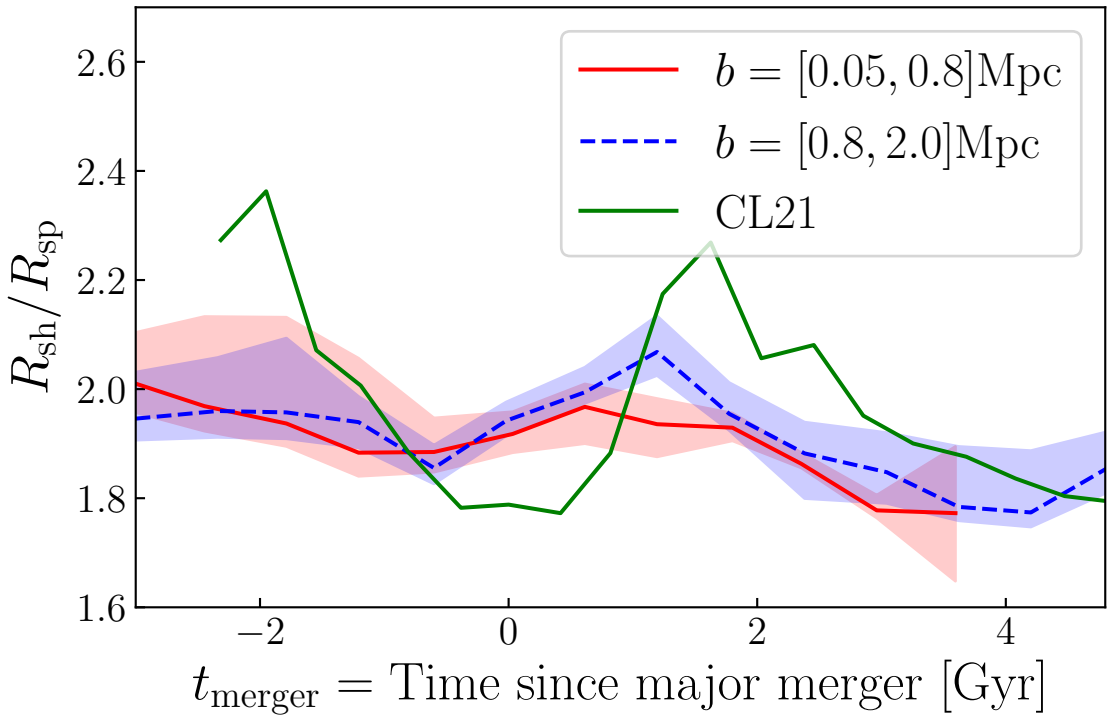

Figure 3.9: The shock to splashback radius ratio as a function of time since major merger for different impact parameters, indicated with solid and dashed lines. The lines and shaded regions indicate median and the 16-84 percentile of the ratio. The green line shows the most extreme major merger in CL21, whose gas entropy and DM density maps are shown in Figure 3.8. The $R_{\rm sh}/R_{\rm sp}$ ratios increase temporarily within $1-2\,$Gyr after major mergers, and they all stay within the range of 1.6 and 2.4 throughout the mergers.

3.3.6 Effects of Mergers on Accretion Shock Radius

Mergers can increase the accretion shock radius, boosting the ratio of the shock to splashback radii ($R_{\rm sh}/R_{\rm sp}$). A merger event can generate a merger shock in the ICM, which accelerates to outer radii through a "run-away" shock with high Mach number (Zhang et al., 2019). When a merger shock runs into the accretion shock, the merger shock accelerates the accretion shock and pushes it out temporarily, whose duration depends on the MAR of the halo and the Mach number $\mathcal{M}$ of the shock (Zhang et al., 2020). Higher MAR leads to smaller increase in the accretion shock radius. For example, for a merger shock with $\mathcal{M} = 1.5$, in a halo with low MAR of $\Gamma_{\rm 200m} = 1$, the accretion shock radius can grow to twice as predicted by self-similar model, before receding back to self-similar predicted value 3 Gyr later. However, for the same Mach number merger shock in a halo with a higher MAR of $\Gamma_{\rm 200m} = 3$, the accretion shock radius can only grow to 1.5 times the self-similar predicted shock radius, before receding back to the self-similar value after 1.5 Gyr. Physically, the higher MAR of the halo implies larger ram pressure of the infalling gas, which pushes the run-away shock farther back towards the cluster center, leading to the smaller accretion shock radius.

Figure 3.9 shows $R_{\rm sh}/R_{\rm sp}$ before and after major merger events from $z = 4$ onward for different impact parameters in the simulation, where a major merger is defined as the merger event where the mass ratio is less than 1:4. Impact parameter b is defined as the perpendicular distance between the paths of the mergers, where the direction of the path is determined by the velocities of the haloes in the last snapshot when $R_{\rm 500c}$ of two haloes do not overlap. It shows a temporary increase in $R_{\rm sh}/R_{\rm sp}$ right after the merger peaking after 1 Gyr and lasting around 2 Gyr. The average $R_{\rm sh}/R_{\rm sp}$ before and after merger remains relatively constant, but can increase by 10% within $2 - 3\,$Gyr after the merger. In extreme cases where there is equal mass merger and almost head-on collision (with the mass ratio of 0.83 and impact parameter $b = 0.49$ Mpc for

CL21), we find that after 2 Gyr of the merger the $R_{\rm sh}/R_{\rm sp}$ ratio temporarily increases up to 2.4, corresponding to an increase of about 30%, before receding back to 1.8 after 4 Gyr of the merger. In fact, the ratio ranges between 1.6 to 2.4 during mergers of all haloes in our sample.

Our results indicate that mergers cannot account for all of the offsets between the volume-averaged $R_{\rm sh}$ and $R_{\rm sp}$, which is almost a factor of 2. When undergoing major merger, the ratio of volume-averaged radii $R_{\rm sh}/R_{\rm sp}$ of CL21 remains above 1.6 before and after the merger (Figure 3.9). However, in Figure 3.8, we found the instance where the shock to splashback ratio becomes very close to 1 and rapidly increases as the merger shock propagates away from the merger axis. This indicates that whether the merger-accelerated shocks can explain the offset between the shock and splashback radii depends on which line-of-sight we choose to compare. We leave further exploration of this idea to a future work.

3.4 Discussions & Future Work

The present work focuses on the massive DM haloes where the accretion shock is growing and the cluster outskirt is not affected significantly by galaxy formation physics. However, the accretion shocks are expected to behave differently for lower-mass group and galaxy scales. Radiative cooling can significantly reduce the pressure support of the galactic haloes which can lead to the collapse of the accretion shock into the inner region (Birnboim & Dekel, 2003). In addition, at lower halo masses of $M < 10^{12} M_{\odot}$, the DM phase space structure of the orbiting halo can extend out to turnaround radii (Prada et al., 2006), which leads to much larger ratio of $R_{\rm edge}/R_{\rm 200c} \approx 4$ (Ludlow et al., 2009; Wang et al., 2009). Future studies should extend the current work to lower mass haloes. Additionally, higher mass and spatial resolution simulations will be required to resolve the shock radius of these low mass

haloes.

3.5 Conclusions

In this work, we investigate the relation between the splashback of dark matter (DM) and the accretion shock of gas in the outskirts of cluster-size DM haloes, using the *Omega500* cosmological hydrodynamical simulations. Our main findings are summarized below:

1. The accretion shock radius is located farther from the cluster centre than the DM splashback radius (Figure 3.1). The phase space structures of DM and gas follow each other outside the accretion shock where the gas thermal energy is small compared to its kinetic energy. Inside the accretion shock, gas is thermalized with relatively small radial infall velocities, while DM particles orbit with large velocity dispersion within the interior of DM haloes. The phase space structures for both the orbiting DM and the thermalized gas extend beyond DM splashback radius (Figure 3.2).

2. The ratio between the two radii depends on the definitions of the splashback and the shock radii. Specifically, the accretion shock radius defined by the entropy drop is larger than all definitions of the splashback radius in the literature. The accretion shock radius defined using the steepest drop in entropy is approximately ≈ 1.89 times larger than the splashback radius defined by the steepest slope in the DM density profile, and it is ≈ 1.2 times larger than the edge of the DM phase-space structure (Figure 3.6).

3. The accretion shock radius of gas decreases with mass accretion rate (MAR) of the halo, similar to the MAR dependence in the splashback radius (Figures 3.3 and 3.5). The resulting ratio is fairly independent of redshift and baryonic physics for the cluster-size DM haloes (Figure 3.6).

4. The gas density follows DM density at the outer radii with steepest density decrease near the DM splashback radius. The steepest decrease in other thermodynamic (temperature, pressure, and entropy) profiles, however, occurs at the location of the accretion shock (Figure 3.4). We do not find significant gas density jump in radial profiles at the accretion shock as the ratio of the post- and pre-shock density is capped at a maximum value of 4 in the strong shock limit, which is further smeared out by azimuthally averaging around aspherical shocks.

5. Mergers account for on average $\approx 10\%$, and upto 30% increase in the shock to splashback ratio for the duration of ≈ 1 Gyr right after the merger. After that, the merger-accelerated shock recedes back to the pre-merger accretion shock (Figure 3.9).

Our results have broad implications for using galaxy clusters as probes of astrophysics and cosmology. First, the apparent spatial offset between splashback and the more extended shock radii indicates that the transition boundaries between the 1-halo and 2-halo terms are different between DM and gas, leaving imprints in this transition region as probed by optical and SZ surveys. Second, the extended gas distribution beyond DM splashback must be taken into account when quantifying baryon fraction associated with DM haloes and cosmic web filaments as well as modeling galaxy quenching in the outskirts of clusters. Finally, the low density shock-heated gas between the accretion shock and the splashback radii may contribute to a significant fraction of the missing baryons and may play a role in early quenching of infalling galaxies. Although the number density and pressure near shock radius are quite low, the shock radius from stacked cluster sample will be detectable in the upcoming SZ surveys such as CMB-S4 (Baxter et al., 2021). Investigating the differential dynamics of collisionless DM and collisional gas in the outskirts of galaxy clusters will be important for using the edges of galaxy clusters as laboratories for cosmology and

astrophysics in the era of multi-wavelength cosmological surveys.

Chapter 4

Kelvin-Helmholtz Instability in Self-Gravitating Streams

4.1 Introduction

Filamentary structures are present across many astrophysical scales, from Mpc to sub-pc. On the largest scales, structure formation occurs in the "cosmic web", a network of sheets and filaments that connect dark matter haloes (Zel'dovich, 1970; Bond et al., 1996; Springel et al., 2005), and is also evident in the distributions of galaxies (e.g., Colless et al., 2003; Tegmark et al., 2004; Huchra et al., 2005). Intergalactic gas cools and condenses towards the centres of the dark matter filaments, forming a network of baryon-dominated intergalactic gas streams (Dekel & Birnboim, 2006; Birnboim et al., 2016). There have been several recent attempts to model such streams self-gravitating Mpc-scale gaseous cylinders, which seems consistent with cosmological simulations (Harford et al., 2008; Harford & Hamilton, 2011; Freundlich et al., 2014; Mandelker et al., 2018).

At the nodes of the cosmic web, the most massive haloes reside at the intersection of several filaments and are penetrated by the gas streams residing at their centres.

These streams constitute the main mode of gas accretion onto the central galaxies (Kereš et al., 2005; Dekel et al., 2009a; Danovich et al., 2012; Zinger et al., 2016). At redshifts $z \gtrsim 2$, simulations suggest that streams feeding galactic haloes remain dense and cold, with temperatures of $\sim 10^4\,\mathrm{K}$, as they travel through the hot circumgalactic medium (CGM) towards the central galaxy (Kereš et al., 2005; Dekel & Birnboim, 2006; Ocvirk et al., 2008; Dekel et al., 2009a; Ceverino et al., 2010; Faucher-Giguère et al., 2011; van de Voort et al., 2011, though see also Nelson et al., 2013, 2016). The filamentary structure in such systems can thus be maintained down to scales of tens of kpc around galaxies (though see below), where it has been suggested that they may fragment due to gravitational instability (hereafter GI; Dekel et al., 2009b; Genel et al., 2012; Mandelker et al., 2018). While these cold circumgalactic streams are difficult to directly detect, recent observations have revealed massive extended cold components in the CGM of high-redshift galaxies, whose spatial and kinematic properties are consistent with predictions for cold streams (Bouché et al., 2013, 2016; Prochaska et al., 2014; Cantalupo et al., 2014; Martin et al., 2014a,b; Borisova et al., 2016; Fumagalli et al., 2017; Leclercq et al., 2017; Arrigoni Battaia et al., 2018).

Within galactic discs, spiral arms have been modeled as one dimensional filaments whose gravitational fragmentation leads to the formation of giant molecular clouds (GMCs) or star-forming clumps (Inoue & Yoshida, 2018). Within individual GMCs, *Herschel* observations of star forming regions reveal a multi-scale network of filamentary structures and dense cores aligned with them like beads on a string (André et al., 2010; Jackson et al., 2010; Arzoumanian et al., 2011; Kirk et al., 2013; Palmeirim et al., 2013). This has led to the suggestion that turbulence-driven formation of filaments in the interstellar medium (ISM) is the first step towards core and star-formation (Molinari et al., 2010; André et al., 2010, 2014), a connection which had been speculated for some time (e.g., Schneider & Elmegreen, 1979; Larson, 1985). In this scenario, the densest filaments with widths of order $\sim 0.1\,\mathrm{pc}$ (Arzoumanian

et al., 2011; Hennebelle & André, 2013) collapse due to GI and lead to the formation of dense cores where star-formation occurs. Simulations of molecular clouds in the ISM reveal similar multi-scale filamentary structures, arising from a variety of mechanisms such as turbulence, gravitational collapse of larger structures, thermal instabilities, or colliding flows (e.g., Padoan et al., 2001; Banerjee et al., 2009; Gómez & Vázquez-Semadeni, 2014; Moeckel & Burkert, 2015; Smith et al., 2016).

Studies of the structure and stability of self-gravitating filaments have a long history, mostly in the context of star-formation in ISM filaments. Early analytic work investigated the stability of an infinite incompressible cylinder with and without an axial magnetic field (Chandrasekhar & Fermi, 1953), a compressible yet still homogeneous infinite cylinder (Ostriker, 1964b), a homogeneous stream of finite radius (Mikhaĭlovskiĭ & Fridman, 1972; Fridman & Poliachenko, 1984), and a uniformly rotating isothermal cylinder (Hansen et al., 1976). Hydrostatic equilibrium of a self-gravitating isothermal cylinder is only possible if its mass per unit length (hereafter line-mass) is less than a critical value which depends only on its temperature (Ostriker, 1964a; see eq. (4.3) below). For non-isothermal filaments, the critical line-mass is similar (§4.3.1). Filaments with line-mass larger than the critical value must collapse radially. For line-masses smaller than the critical value, a hydrostatic solution exists, but is unstable to long wavelength axisymmetric perturbations. The fastest growing wavelength is roughly eight times radius of the stream, $\lambda \sim 8R_{\rm s}$ (Nagasawa, 1987, hereafter N87), resulting in stream fragmentation as described in more detail below. A collapsing filament with a line mass slightly exceeding the critical value, as may eventually be the case for a filament growing via radial accretion, is also unstable to axisymmetric perturbations and will fragment at a similar wavelength to the hydrostatic case (Inutsuka & Miyama, 1992). Both cases eventually lead to the formation of bound clumps with masses of order the local Jeans mass (Clarke et al., 2016, 2017). However, if the line-mass greatly exceeds the critical value the filament

collapses towards its axis without fragmenting (Inutsuka & Miyama, 1992). On scales smaller than the filament radius, the local stability criterion reduces to the classical Jeans criterion, even in the presence of rotation (Freundlich et al., 2014). This implies that such local collapse is only possible if the filament is larger than its Jeans length.

N87 studied the stability of a self-gravitating isothermal cylinder with line-mass below the critical value, pressure confined by a low density external medium. He found that the system is always unstable to long-wavelength axisymmetric perturbations even at low values of the line-mass. Similarly, Hunter et al. (1998, hereafter H98) found that a self-gravitating cylinder which is pressure confined by an external medium, with a density discontinuity at the boundary, is always unstable to long-wavelength axisymmetric perturbations. These results are contrary to the spherical case, where a hydrostatic sphere with mass below the critical Bonner-Ebert mass (Ebert, 1955; Bonnor, 1956) is stable against gravitational collapse. We elaborate further on these two studies in §4.2.1.

In addition to GI, cylindrical streams or jets are susceptible to Kelvin-Helmholtz Instability (KHI) whenever there is a shearing motion between the stream and its surroundings. Numerous authors have studied KHI in cylinders, typically focusing on light or equidense jets meant to represent protostellar or AGN jets (e.g., Birkinshaw, 1984; Payne & Cohn, 1985; Hardee et al., 1995; Bassett & Woodward, 1995; Bodo et al., 1998; Bogey et al., 2011). Several authors have also addressed the effects of magnetic fields and/or radiative cooling on KHI in cylindrical jets (Ferrari et al., 1981; Massaglia et al., 1992; Micono et al., 2000; Xu et al., 2000). However, none of the aforementioned studies accounted for the self-gravity of the gas, as this is expected to be negligible for the systems being considered, namely jets from young stars or AGN. It has also been noted that tidally disrupted streams, resulting from stars tidally destroyed by black holes, may also experience KHI (Bonnerot et al., 2016). Recently, in a series of several papers, Mandelker et al. (2016); Padnos et al. (2018);

and Mandelker et al. (2019) (hereafter M16, P18 and M19, respectively) presented a detailed study of KHI, without self-gravity or radiative cooling, in a dense supersonic cylinder representing the cold circumgalactic streams feeding high redshift galaxies. These can be up to 100 times denser than their surroundings. They found that KHI can be important in the evolution of such streams, leading to significant deceleration and energy dissipation, and in certain cases to total stream disruption in the CGM. We elaborate further on these studies in §4.2.2.

Clearly, extensive work has been done studying separately the effects of GI and of KHI in filaments and streams. While the evolution of KHI in a self-gravitating fluid has been studied in planar (Hunter et al., 1997, hereafter H97) and spherical geometry (Murray et al., 1993, hereafter M93), we are unaware of any such work in cylindrical geometry. Since the evolution of KHI in cylindrical geometry is qualitatively different than in planar geometry (M19, and references therein), while GI in cylinders is qualitatively different than in spheres (e.g., N87; H98), it is worth explicitly studying the combined effects of KHI and self-gravity in cylindrical systems, which is the focus of this paper.

This has important astrophysical implications as well, as there are several filamentary systems where both effects are likely to be important. For instance, it has been shown that the cold circumgalactic streams are likely gravitationally unstable in the inner haloes of massive galaxies at high redshift, potentially resulting in star formation and even globular cluster formation along the streams in the CGM (Mandelker et al., 2018). This may explain recent *ALMA* observations of dense star-forming gas at distances of tens of kpc away from a massive galaxy at $z \sim 3.5$, which does not appear to be associated with the galaxy or any of its satellites (Ginolfi et al., 2017). Additionally, filaments in GMCs in the ISM occasionally exhibit shearing flows with respect to their background (Hily-Blant & Falgarone, 2009; Federrath et al., 2016; Kruijssen et al., 2019), suggesting that KHI may be important in their evolution.

The rest of this paper is organised as follows. In §4.2, we review the current theoretical understanding of GI and KHI in pressure-confined cylinders, and present predictions for how the two may behave in unison. In §4.3, we describe a suite of numerical simulations used to study GI and KHI in cylinders. In §4.4 we present the results of our numerical analysis and compare these to our analytical predictions. In §4.5 we discuss our results and their astrophysical applications, present caveats to our analysis and outline future work. Finally, we summarise our main conclusions in §4.6.

4.2 Theory of instabilities

In this section we briefly review the existing theory of GI (§4.2.1) and KHI (§4.2.2) in pressure confined cylinders. We then make new predictions for how the two effects may be combined in cylindrical systems (§4.2.3, to be tested using numerical simulations in §4.4), and compare these to previous results of a combined analysis in spherical systems (§4.2.4).

4.2.1 Gravitational instability

We focus here on the results of N87 and H98, as these are the most relevant for our current analysis. These studies both focus on the stability of a self-gravitating cylinder with finite radius and line-mass below the critical value for hydrostatic equilibrium, pressure confined by a uniform external medium.

N87 consider an isothermal cylinder initially in hydrostatic equilibrium, with the density profile

$$\rho(r) = \rho_{\rm c}\left[1+\frac{1}{8}\left(\frac{r}{H}\right)^2\right]^{-2}, \quad H = \frac{c_s}{\sqrt{4\pi G\rho_{\rm c}}}, \tag{4.1}$$

(Ostriker, 1964a). $\rho_{\rm c}$ is the central density of the cylinder, H is its scale height, $c_{\rm s}$ is the isothermal sound speed, and G is the gravitation constant. The line-mass of such

a cylinder out to radius R_s is

$$\Lambda = \int_0^{R_\mathrm{s}} 2\pi r \rho(r)\ \mathrm{d}r. \tag{4.2}$$

For $R_\mathrm{s} = \infty$, this yields the critical line-mass for hydrostatic equilibrium (Ostriker, 1964a),

$$\Lambda_{\mathrm{cr,\,iso}} = 2c_\mathrm{s}^2/G. \tag{4.3}$$

An equilibrium initial condition is only possible for $\Lambda \leq \Lambda_{\mathrm{cr,iso}}$. For a cylinder truncated at a finite radius R_s, the density and line mass profiles at $r < R_\mathrm{s}$ are still given by eqs. (4.1) and (4.2). Thus, the ratio of the cylinder's line-mass to the critical line-mass is related to the ratio of the cylinder's radius to its scale height,

$$\frac{\Lambda}{\Lambda_{\mathrm{cr,\,iso}}} = \left[1 + 8\left(\frac{H}{R_\mathrm{s}}\right)^2\right]^{-1}. \tag{4.4}$$

Increasing the central density, ρ_c, or decreasing the temperature and thus the sound speed, c_s, reduces the scale height, H. For a fixed stream radius, R_s, this results in an increase of the ratio $\Lambda/\Lambda_{\mathrm{cr,\,iso}}$.

In terms of the external pressure confining the truncated cylinder, pressure equilibrium at the boundary dictates that

$$P_\mathrm{ext} = P(R_\mathrm{s}) = c_\mathrm{s}^2 \rho(R_\mathrm{s}) = c_\mathrm{s}^2 \rho_\mathrm{c}\left[1 + \frac{R_\mathrm{s}^2}{8H^2}\right]^{-2}. \tag{4.5}$$

Inserting this into eq. (4.4) yields

$$\frac{\Lambda}{\Lambda_{\mathrm{cr,\,iso}}} = 1 - \frac{P_\mathrm{ext}}{\rho_\mathrm{c} c_\mathrm{s}^2}. \tag{4.6}$$

This shows that for a given temperature and external pressure, a cylinder can have any line mass from 0 to $\Lambda_{\mathrm{cr,\,iso}}$, by decreasing the central density from $\rho_\mathrm{c} = P_\mathrm{ext}/c_\mathrm{s}^2$ to

0. The critical line-mass therefore does not depend on the external pressure. This is fundamentally different from the spherical case where the maximal mass for which a hydrostatic equilibrium solution exists depends on the external pressure. This is the Bonnor-Ebert mass,

$$M_{\rm BE} = 1.18 \frac{c_{\rm s}^4}{P_{\rm ext}^{1/2} G^{3/2}} \tag{4.7}$$

(Ebert, 1955; Bonnor, 1956). For further comparison of the structure and properties of self-gravitating cylinders and spheres confined by external pressure, see Fischera & Martin (2012). For the remainder of our analysis we will use the scale-height, H, and the stream radius, $R_{\rm s}$, rather than the external pressure.

N87 analyzed perturbations about hydrostatic equilibrium in a cylinder with radius $R_{\rm s}$, pressure confined by an external medium with constant pressure and effectively zero density, $\rho_{\rm ext} << \rho(R_{\rm s})$. The dispersion relation was numerically evaluated for several values of $\Lambda/\Lambda_{\rm cr,\,iso}$. All cases were found to be stable to non-axisymmetric modes. For axisymmetric modes, the system was found to be unstable at long wavelengths, with longitudinal wavenumber $k < k_{\rm cr}$. The system attains a maximal growth rate, $\omega_{\rm max}$, at a finite wavenumber, $k_{\rm max}$, hereafter the fastest growing mode, and then stabilises again at infinite wavelengths, $\omega \rightarrow 0$ as $k \rightarrow 0$. This is unlike the spherical Jeans instability where the growth rate diverges as $k \rightarrow 0$. There is no closed analytic expression for $k_{\rm cr}$, $k_{\rm max}$ or $\omega_{\rm max}$ for the general case, but it is useful to consider two limiting cases.

In the limit $\Lambda \rightarrow \Lambda_{\rm cr,\,iso}$, equivalent to $R_{\rm s} >> H$ (eq. 4.4), the solution converges to that of an infinite cylinder. In this case, one obtains $k_{cr} \simeq 0.56 H^{-1}$, $k_{\rm max} \simeq 0.28 H^{-1}$, and $\omega_{\rm max} \simeq 0.60 \left(4 G \rho_{\rm c}\right)^{1/2}$. For comparison, the free-fall time of a cylinder with average density $< \rho >= \Lambda/(\pi R_{\rm s}^2)$ is

$$t_{\rm ff} = (4G < \rho >)^{-1/2}. \tag{4.8}$$

For an isothermal cylinder with radius $R_{\rm s}$,

$$< \rho >= \rho_{\rm c} \left(1 - \frac{\Lambda}{\Lambda_{\rm cr,\,iso}} \right) = \rho_{\rm c} \left(1 + \frac{R_{\rm s}^2}{8H^2} \right)^{-1}. \tag{4.9}$$

For $\Lambda = 0.90\Lambda_{\rm cr,\,iso}$, we thus have $R_{\rm s} \simeq 8.5H$ and $\omega_{\rm max}/t_{\rm ff}^{-1} \simeq 1.9$. For larger values of Λ the ratio $\omega_{\rm max}/t_{\rm ff}^{-1}$ increases.

In the opposite limit, when $\Lambda << \Lambda_{\rm cr,\,iso}$ or $R_{\rm s} << H$, the density is roughly constant within $R_{\rm s}$ and the solution converges to that of an incompressible cylinder, first studied by Chandrasekhar & Fermi (1953). The dispersion relation for an incompressible cylinder is given by[1]

$$\frac{\omega^2}{4\pi G\rho} = -\frac{xI_1}{I_0} \left[K_0 I_0 - \frac{1}{2} \right], \tag{4.10}$$

where $I_\nu(x)$ and $K_\nu(x)$ are modified Bessel functions of the first and second kind of order ν, evaluated at the argument $x = kR_{\rm s}$. This yields $k_{cr} \simeq 1.1R_{\rm s}^{-1}$, $k_{max} \simeq 0.6R_{\rm s}^{-1}$, and $\omega_{\rm max} \simeq 0.4t_{\rm ff}^{-1}$.

To summarise, the shortest unstable wavelength is $\lambda_{\rm cr} = 2\pi/k_{\rm cr} \sim 4\pi H$ and $2\pi R_{\rm s}$ in the limits $\Lambda \to \Lambda_{\rm cr,\,iso}$ and $\Lambda << \Lambda_{\rm cr,\,iso}$ respectively. In all cases, the most unstable mode occurs at $\lambda_{\rm max} \sim 2\lambda_{\rm cr}$, while $\omega_{\rm max}/t_{\rm ff}^{-1}$ is within a factor ~ 2 of unity. Note that since in the latter limit $R_{\rm s} << H$, we arrive at the somewhat counterintuitive result that for smaller values of the line-mass the shortest and most unstable wavelengths are much shorter. As noted by N87, the instability manifests itself in different ways in these two limits. For large values of the line-mass the system is unstable to body-modes which are maximal near the stream axis and are similar to the classic Jeans instability. On the other hand, for small values of the line-mass the instability is dominated by surface modes, which are maximal near the stream interface and lead

1. Note that there is a minus sign missing from the corresponding equation (4.10) in N87.

to its deformation. In the non-linear regime, these two modes of instability lead to different shapes and orientations of collapsed clumps within the stream (Heigl et al., 2018b).

H98 generalised this analysis by allowing for a finite background density, $\rho_{\rm b}$, confining the stream. However, they assumed a constant stream density, $\rho_{\rm s}$, rather than an isothermal profile. Their scenario is thus analogous to the limit $\Lambda << \Lambda_{\rm cr,\,iso}$ from N87. H98 derive the following dispersion relation[2]

$$\frac{\omega^2}{4\pi G\bar{\rho}} = -\left[\frac{x(\rho_{\rm s}-\rho_{\rm b})^2 I_0 K_0}{\bar{\rho}^2} - \frac{x\rho_{\rm s}(\rho_{\rm s}-\rho_{\rm b})}{2\bar{\rho}^2}\right] \times \left[\frac{\rho_{\rm s} I_0}{\bar{\rho} I_1} + \frac{\rho_{\rm b} K_0}{\bar{\rho} K_1}\right]^{-1}, \tag{4.11}$$

where $\bar{\rho} = 0.5(\rho_{\rm s}+\rho_{\rm b})$, and $I_\nu(x)$ and $K_\nu(x)$ are again modified Bessel functions with $x = kR_s$. This converges to eq. (4.10) in the limit $\rho_{\rm b} \to 0$.

From eq. (4.11), the condition for instability is

$$I_0 K_0 > \frac{1}{2\left(1-\delta^{-1}\right)}, \tag{4.12}$$

where $\delta = \rho_{\rm s}/\rho_{\rm b}$ is the density contrast between the stream and the background. If $\delta < 1$, such that the background is denser than the stream, the system is unstable at all wavelengths due to Rayleigh-Taylor instability (RTI). If $\delta > 1$, such that the stream is denser than the background, the system is unstable at long wavelengths, i.e. small values of the argument of the Bessel functions on the left-hand side of eq. (4.12), $x = kR_{\rm s}$. Furthermore, H98 find that the instability always manifests itself as a surface mode, leading to the deformation of the stream-background interface, similar to the conclusion of N87 for the low line-mass case. For $\delta \to \infty$, corresponding to $\rho_{\rm b} \to 0$, the system is unstable for $k < k_{\rm cr} \simeq 1.07 R_{\rm s}^{-1}$, as for eq. (4.10). For $\delta = 1$

2. This is equivalent to equation (68) from H98 using the identity $I_0(x)K_1(x) + I_1(x)K_0(x) = 1/x$.

such that there is no density discontinuity at the interface, $k_{\rm cr} = 0$ and the system is stable for all finite wavelengths. This highlights the fact that this is an interface instability, caused by a density discontinuity between the stream and the background. For $\delta = 4,\ 10,\ 100$, we have $k_{\rm cr}R_{\rm s} \simeq 0.79,\ 0.96,\ 1.06$. The maximal growth rate for these cases is $\omega_{\rm max}/t_{\rm ff}^{-1} \simeq 0.26,\ 0.36,\ 0.43$.

H98 also note that in the case of a dense sphere pressure confined by a lower density background, the analogous surface mode is always stable, in agreement with the known fact that spheres less massive than the Bonner-Ebert mass are stable. However, in planar geometry, such as a dense slab pressure confined by a lower density background, a similar surface instability exists above a critical wavelength (H97).

The GI surface modes can be thought of as RTI analogues, induced by the self-gravity of the fluid rather than by an external gravitational field. An intuitive explanation was offered by H97 for the planar case, and can be adapted to cylindrical geometry as follows. Consider a dense cylinder with constant density $\rho_{\rm s}$ pressure confined by a background medium with constant density $\rho_{\rm b} < \rho_{\rm s}$. Such a system is stable to classical RTI. Now consider an axisymmetric perturbation to the interface of the cylinder with longitudinal wavelength λ. In some region, say $0 < z < \lambda/2$, there is an outward distortion of the interface, $\xi(z)$, which results in a mass excess just outside the original interface, proportional to $(\rho_{\rm s} - \rho_{\rm b})\xi(z)$. Through Poisson's equation, this leads to a more negative gravitational potential in this region, resulting in a perturbation $\Phi_1 < 0$ to the initial potential. As the fluid is incompressible and at rest, Bernoulli's equation tells us that $P + \rho\Phi = $ const along any streamline in either fluid, where P is the pressure. In the incompressible limit, where $\rho = $ const in each fluid, this implies that $P_{1,{\rm s}} = -\rho_{\rm s}\Phi_1$ and $P_{1,{\rm b}} = -\rho_{\rm b}\Phi_1$, where $P_{1,{\rm s}}$ and $P_{1,{\rm b}}$ are the perturbations to the pressure in the stream and the background respectively, on either side of the interface. Since $\rho_{\rm s} > \rho_{\rm b}$ and $\Phi_1 < 0$, we have that $P_{1,{\rm s}} > P_{1,{\rm b}}$, so the pressure in the stream just inside the interface is larger than the pressure in the

background just outside the interface, causing the perturbation to continue growing.

This instability only manifests at long wavelengths, when the mass excess leading to the perturbation of the potential is large enough to overcome the stabilizing effect of RT modes induced by the unperturbed potential. As noted above, the shortest unstable wavelength for cylinders is $\sim 2\pi R_{\rm s} \sim 6.3R_{\rm s}$ (eq. 4.12). By contrast, the longest available wavelength on the surface of a sphere corresponds to the $l = 2$ spherical harmonic, since the $l = 0$ mode represents global expansion or contraction of the sphere while the $l = 1$ mode represents a rigid displacement. The wavenumber associated with the $l = 2$ mode is $k = [l(l + 1)]^{1/2}/R_{\rm s} \sim 2.5/R_{\rm s}$, corresponding to a wavelength of $\lambda \sim 2.6R_{\rm s}$. This is too short for GI surface modes to overcome RT stabilization, which is why there are no GI surface modes for spherical systems (H98).

4.2.2 KH Instability

KHI arises from shearing motion between the interfaces of two fluids, leading to efficient mixing and smoothing out the initial contact discontinuity. We focus here on the recent results of M19, who analysed the non-linear evolution of KHI in a dense 3d cylinder streaming through a static background, expanding on earlier work by M16 and P18. The system is characterised by two dimensionless parameters, the Mach number of the stream velocity with respect to the background sound speed, $M_{\rm b} = V_{\rm s}/c_{\rm b}$, and the density contrast of the stream and the background, $\delta = \rho_{\rm s}/\rho_{\rm b}$. M19 analytically derived timescales for the non-linear mixing of the two fluids and eventual disruption of the stream, as well as for stream deceleration and the loss of bulk kinetic energy, as a function of these two parameters.

We begin by noting that, similar to the dichotomy between surface modes and body modes in GI (N87), there are two modes of KHI. The nature of the instability depends primarily on the ratio of the stream velocity to the sum of the two sound

speeds,

$$M_{\rm tot} = \frac{V_{\rm s}}{c_{\rm s} + c_{\rm b}}. \tag{4.13}$$

If $M_{\rm tot} < 1$, the instability is dominated by surface modes. These are concentrated at the interface between the fluids, and lead to the growth of a shear layer which expands into both fluids. Within the expanding shear layer a highly turbulent medium develops, efficiently mixing the two fluids. Surface modes can have any longitudinal wavenumber[3], k, and any azimuthal wavenumber, m, representing the number of azimuthal nodes along the stream-background interface. $m = 0$ corresponds to axisymmetric perturbations, $m = 1$ to helical perturbations, and $m \geq 2$ to more complicated fluting modes. Low order m modes with wavelengths of order $R_{\rm s}$ dominate the early non-linear evolution of the instability, as their eddies reach the largest amplitudes before they break, but the shear layer between the fluids quickly develops into a highly turbulent mixing zone with no discernible symmetry.

The shear layer separating the fluids expands self-similarly through vortex mergers. Independent of the initial perturbation spectrum, the width of the shear layer, h, evolves as

$$h = \alpha V_{\rm s} t \tag{4.14}$$

where α is a dimensionless growth rate that depends primarily on $M_{\rm tot}$, and is typically in the range $\alpha \sim 0.05 - 0.25$ (P18; M19).

The shear layer penetrates asymmetrically into the stream and background due to their different densities. The penetration depth of the shear layer in either medium can be derived from conservation of mass and momentum in the shear layer, and are given by (P18; M19):

$$h_{\rm s} = \frac{\alpha V_{\rm s} t}{1 + \sqrt{\delta}}, \quad h_{\rm b} = \frac{\sqrt{\delta}\alpha V_{\rm s} t}{1 + \sqrt{\delta}}. \tag{4.15}$$

3. So long as the wavelength, $\lambda = 2\pi/k$, is larger than the width of the transition region between the two fluids.

Stream disruption occurs when the shear layer encompasses the entire stream, namely when $h_{\rm s} = R_{\rm s}$. This occurs at time

$$t_{\rm dis} = \frac{\left(1+\sqrt{\delta}\right) R_{\rm s}}{\alpha V_{\rm s}}. \tag{4.16}$$

The contact discontinuity effectively disappears before the stream is completely disrupted, once the full width of the shear layer is of order the stream radius, namely $h = R_{\rm s}$. This occurs at time

$$t_{\rm shear} = \frac{R_{\rm s}}{\alpha V_{\rm s}}. \tag{4.17}$$

As the shear layer expands into the background, it entrains background mass. This causes the stream to decelerate as its initial momentum is distributed over more mass. As shown by M19, the stream velocity as a function of time is well fit by

$$V_{\rm s}(t) = \frac{V_{\rm s,0}}{1 + t/t_{\rm dec}}, \tag{4.18}$$

where $V_{\rm s,0}$ is the initial velocity of the stream, and

$$t_{\rm dec} = \frac{\left(1+\sqrt{\delta}\right)\left(\sqrt{1+\delta}-1\right)}{\alpha\sqrt{\delta}} \frac{R_{\rm s}}{V_{\rm s,0}}, \tag{4.19}$$

is the time when the background mass entrained in the shear layer equals the initial stream mass, such that momentum conservation implies the velocity is half its initial value.

An empirical expression for the dimensionless shear layer growth rate, α, was proposed by Dimotakis (1991),

$$\alpha \simeq 0.21 \times \left[0.8 \exp\left(-3M_{\rm tot}^2\right) + 0.2\right]. \tag{4.20}$$

M19 found eq. (4.20) to be a good fit to shear layer growth in simulations of 2d slabs, regardless of whether one measures h, $h_{\rm s}$, or $h_{\rm b}$. However, they found that $h_{\rm s}$ expanded more rapidly in 3d cylinders due to an enhanced eddy interaction rate near the stream axis. This yielded α values $\sim 50\%$ larger than eq. (4.20) when measuring $h_{\rm s}$ and using eq. (4.15). On the other hand, $h_{\rm b}$ was found to expand at a similar rate in 2d and 3d so long as $h_{\rm b} \lesssim 2R_{\rm s}$. Since the shear layer width is dominated by $h_{\rm b}$ for $\delta > 1$, we use eq. (4.20) together with eq. (4.17) to evaluate the time when the contact discontinuity is destroyed.

Once $h_{\rm b} \gtrsim 2R_{\rm s}$, its growth rate is reduced by roughly half, due to a turbulent cascade to small scales which removes energy from the largest eddies driving the expansion. For $\delta > 8$, this occurs before the stream reaches half its initial velocity (eqs. 4.18-4.20). M19 found that in these cases, a good fit to the velocity evolution of streams can be obtained simply by using 0.5α in eq. (4.19) with α taken from eq. (4.20).

When $M_{\rm tot} > 1$, surface modes of low azimuthal order (low values of m) stabilise[4]. The nature of the instability then depends on the width of the initial transition region between the fluids (which is likely set by transport processes such as viscosity and thermal conduction). If this is relatively narrow, the instability becomes dominated by high-m surface modes, and the above description, summarised in eqs. (4.14)-(4.19), remains valid, with $\alpha \sim 0.05$ according to eq. (4.20). However, if the initial transition region is wide, of order $\gtrsim 0.25R_{\rm s}$ or larger, high-m surface modes are also stable and the instability becomes dominated by body modes. These do not result in shear layer growth but rather in the global deformation of the stream into a helical, $m = 1$, shape with a characteristic wavelength of $\sim 10R_{\rm s}$ and an amplitude of $\gtrsim R_{\rm s}$. The timescale for this to occur depends on the initial perturbation amplitude and

4. The formal condition for stabilization of $m = 0$, 1 surface modes is $M_{\rm b} > (1+\delta^{-1/3})^{3/2}$, similar to $M_{\rm tot} > 1$.

spectrum, though it is almost always longer than the timescale for stream disruption by surface modes when these are unstable. Following the formation of the sinusoid, small scale turbulence develops near its peaks and leads to stream disruption within roughly one stream sound crossing time. Interestingly M19 find that eqs. (4.18)-(4.19) are a good description of stream deceleration due to body modes as well, despite the different processes involved.

We will hereafter ignore KHI body modes, and assume that KHI is dominated by surface modes of some order m for all Mach numbers. If KHI surface modes are suppressed by a large initial transition region, then GI surface modes will also likely be suppressed, based on the analysis of H97 and H98.

4.2.3 Combined treatment

We now wish to combine the above two processes, and discuss the evolution of a pressure-confined self-gravitating cylinder undergoing KHI. In addition to $M_{\rm b}$ and δ, a third parameter is required to describe such a system, namely the line-mass of the cylinder in units of the critical line-mass for hydrostatic equilibrium, $\mu \equiv \Lambda/\Lambda_{\rm cr}$. We begin by making the assumption, to be justified below, that any coupling between GI and KHI in the linear regime is relatively small, such that the region of parameter space where each process results in instability is unchanged, and the linear growth rates are only mildly altered. Under this assumption, it is clear from §4.2.1 and §4.2.2 that for all values of $(M_{\rm b}, \delta, \mu)$, the system is unstable over some wavelength range. We assume that the initial perturbation spectrum spans this range.

GI enhances density contrasts and leads to the formation of long-lived collapsed clumps, while KHI smooths the interface between the fluids and dilutes the mean density of the stream. The question is which process will win. The timescale for GI is the inverse growth rate of the fastest growing mode discussed in §4.2.1, $t_{\rm max} \equiv \omega_{\rm max}^{-1}$. At low values of μ, GI is dominated by surface modes (N87), which require the

presence of a contact discontinuity (H98). Thus, the timescale for KHI to prevent gravitational collapse is $t_{\rm shear}$ (eq. 4.17), the timescale for nonlinear KHI to destroy the contact discontinuity. On the other hand, for high values of μ, GI is dominated by body modes which are unrelated to the contact discontinuity (N87). In this case, the relevant timescale for KHI to prevent collapse is $t_{\rm dis}$ (eq. 4.16), the timescale for nonlinear KHI to disrupt the stream itself.

Since $t_{\rm shear} < t_{\rm dis}$ for all $\delta > 1$, we distinguish between three regimes. If $t_{\rm max} < t_{\rm shear} < t_{\rm dis}$, we expect GI to win and the stream to fragment into long-lived clumps. If $t_{\rm shear} < t_{\rm dis} < t_{\rm max}$, we expect KHI to win and disrupt the stream by mixing it into the background. We hereafter refer to this process as "shredding the stream". In the intermediate case where $t_{\rm shear} < t_{\rm max} < t_{\rm dis}$, the outcome may depend on the value of μ. If μ is small, such that GI is dominated by surface modes, then we expect KHI to win and shred the stream since $t_{\rm shear} < t_{\rm max}$. On the other hand, if μ is large such that GI is dominated by body modes, GI may still win and lead to stream fragmentation and the formation of bound clumps, since $t_{\rm max} < t_{\rm dis}$. However, this is uncertain, since the shear layer will penetrate somewhat into the stream within $t_{\rm max}$, reducing the effective line-mass of the unperturbed (non-turbulent) region. If this is reduced below the threshold for GI body modes to be effective, KHI may still win and suppress clump formation.

Since $t_{\rm max} \propto \rho_{\rm c}^{-1/2} \propto \mu^{-1/2}$, as μ is increased at fixed $(M_{\rm b}, \delta)$, $t_{\rm max}$ decreases while $t_{\rm shear}$ (and $t_{\rm dis}$) remain constant. Thus, for each $(M_{\rm b}, \delta)$ there exists a critical value of μ, $\mu_{\rm cr} \equiv \mu_{\rm cr}(M_{\rm b}, \delta)$, such that $t_{\rm max} < t_{\rm shear}$ for $\mu > \mu_{\rm cr}$ (see Fig. 4.5 in §4.4.1 below). Therefore, GI will win and lead to stream fragmentation and clump formation whenever $\mu > \mu_{\rm cr}$. If $\mu_{\rm cr}$ is small enough to be in the regime where GI is dominated by surface modes, then KHI will win and shred the stream for $\mu < \mu_{\rm cr}$. On the other hand, if $\mu_{\rm cr}$ is in the regime where GI is dominated by body modes, the fate of the stream at $\mu < \mu_{\rm cr}$ depends on the ratio of $t_{\rm max}$ to $t_{\rm dis}$.

At first glance, it may seem inconsistent to compare a linear timescale for GI, $t_{\rm max} = \omega_{\rm max}^{-1}$, to a nonlinear timescale for KHI, $t_{\rm shear}$ or $t_{\rm dis}$. While $t_{\rm max}$ is formally the timescale for the growth of linear perturbations, once density perturbations grow the free-fall times become ever shorter and the collapse accelerates. Full collapse is thus dominated by the linear growth time. On the other hand, KHI tends to saturate following the linear phase, because it is driven by the presence of a contact discontinuity which is destroyed by the instability. Continued growth in the nonlinear regime is dominated by the merger of eddies within the shear layer on timescales of $t_{\rm shear}$ and $t_{\rm dis}$, as described in §4.2.2.

The above discussion notwithstanding, one may ask whether density fluctuations within the stream induced by KHI can trigger local gravitational collapse when $\mu < \mu_{\rm cr}$. Note that this is different than the global fragmentation of the stream induced by GI. Such local collapse can occur in filaments on scales larger than the spherical Jeans length, $\lambda_{\rm J} = [\pi c_{\rm s}^2/(G\rho)]^{1/2}$, but smaller than the stream radius, $R_{\rm s}$ (Freundlich et al., 2014). This implies that this is only possible if $\lambda_{\rm J} < R_{\rm s}$. A lower limit to the Jeans length is obtained by inserting $\rho = \rho_{\rm c}$, the density along the stream axis. This yields $\lambda_{\rm J} = 2\pi H$, with H given by eq. (4.1). The condition that $\lambda_{\rm J} < R_{\rm s}$ thus implies that $R_{\rm s} >> H$, so GI is dominated by body modes (N87). We conclude that KHI induced density fluctuations can only trigger local gravitational collapse if $\mu < \mu_{\rm cr}$ but GI is still dominated by body modes.

We must now justify our initial ansatz that the linear coupling between GI and KHI does not fundamentally alter the instability region of parameter space. We rely here on the analysis of H97, who derived the dispersion relation of a self-gravitating system undergoing KHI in the vortex sheet limit, i.e. two semi-infinite fluids separated by a single, planar interface. In their derivation they made the simplifying assumption that the gravitational field in the unperturbed system was weak compared to the perturbed forces induced by both pressure and potential perturbations.

This is equivalent to assuming that the wavelengths are much shorter than the gravitational scale-height of the unperturbed system, which itself is equivalent to assuming constant density and pressure in both fluids. The resulting dispersion relation contains terms associated with KHI, RTI, and surface mode GI. We refer the reader to H97 for the expression and its derivation. Relevant to our discussion is the fact that the coupling between self-gravity and shearing motions does not modify the stability region of the system, only mildly affects the linear growth rates of KH modes at short to intermediate wavelengths, and does not suppress GI surface modes at long wavelengths. Deriving an analogous dispersion relation for cylinders is beyond the scope of this paper. Rather, we assume that the same conclusions hold for cylindrical systems, in particular because KHI in cylinders is even more unstable than for planar vortex sheets (M16; M19). The validity of this assumption and our subsequent analysis will be tested with numerical simulations in §4.4.

4.2.4 Comparison to the Spherical Case

It is worth comparing our analysis to that of M93, who addressed the question of when self-gravity would prevent KHI from disrupting a cold, dense spherical cloud moving through a hot, dilute background. They assumed that the cloud was pressure confined by the background fluid, and that its mass was less than the Bonnor-Ebert mass, making it gravitationally stable and in hydrostatic equilibrium. In this case, unlike for self-gravitating cylinders, there is no GI, and the only effect of the self-gravity is to induce RT modes at the cloud surface. Since the cloud is denser than the background, these RT modes can counteract the KHI and stabilise the system, due to the restoring buoyancy force. They showed this by considering the combined dispersion relation of KHI and RTI in the incompressible limit,

$$\omega^2 = -\frac{\rho_{\rm s}\rho_{\rm b}}{(\rho_{\rm s}+\rho_{\rm b})^2}V^2k^2 + \frac{\rho_{\rm s}-\rho_{\rm b}}{\rho_{\rm s}+\rho_{\rm b}}kg, \tag{4.21}$$

where V is the velocity of the cloud in the static background and g is the gravitational acceleration at its surface. This implies that KHI is stable for all wavelengths greater than

$$\lambda_{\rm max} = \frac{2\pi\rho_{\rm s}\rho_{\rm b}V^2}{(\rho_{\rm s}^2 - \rho_{\rm b}^2)\, g}. \tag{4.22}$$

M93 then assumed that KHI would only disrupt the cloud if $\lambda_{\rm max} > R_{\rm cl}$, the cloud radius. This was based on the assumption that KHI surface modes saturate at an amplitude comparable to their wavelength, thus neglecting the subsequent shear layer growth. This assumption together with $g = GM_{\rm cl}/R_{\rm cl}^2$ and $M_{\rm cl} = (4\pi/3)\rho_{\rm cl}R_{\rm cl}^3$ results in a minimum mass for self-gravity to stabilise the sphere against KHI. For velocities of order the background sound speed, the critical mass is of order the Bonnor-Ebert mass, $M_{\rm BE}$. Such a system is thus always unstable, either to KHI at $M_{\rm cl} < M_{\rm BE}$ or to global gravitational collapse at $M_{\rm cl} > M_{\rm BE}$.

Our main prediction for the cylindrical case is qualitatively similar. We predict that a self-gravitating stream will always be unstable either to KHI at $\mu < \mu_{\rm cr}$ or to GI at $\mu > \mu_{\rm cr}$, depending on whether the timescale for GI, $t_{\rm max}$, is longer or shorter than the timescale for KHI to destroy the contact discontinuity, $t_{\rm shear}$, and/or the stream itself, $t_{\rm dis}$. However, unlike M93, we do not rely on a similar criterion of gravity stabilizing wavelengths longer than $R_{\rm s}$. First of all, unlike in spherical systems, self-gravity actually destabilises cylinders at long wavelengths (N87; H98; §4.2.1). Furthermore, even if KHI is stable for wavelengths longer than $R_{\rm s}$ in the linear regime, it can still lead to stream disruption in the nonlinear regime by shear layer growth caused by initially shorter wavelength perturbations.

4.3 Numerical Methods

In this section we describe the details of our simulation code and setup, as well as our analysis method. We use the Eulerian AMR code `RAMSES` (Teyssier, 2002), with

a piecewise-linear reconstruction using the MonCen slope limiter (van Leer, 1977), an HLLC approximate Riemann solver (Toro et al., 1994), and a multi-grid Poisson solver.

4.3.1 Hydrostatic Cylinders

Unlike the isothermal cylinder described in §4.2.1, there is no closed analytic expression for the density profile of an isentropic cylinder in hydrostatic equilibrium, so this must be evaluated numerically. We briefly review here how this is done, beginning with the equilibrium solution of an isolated cylinder following Ostriker (1964a). The equation of hydrostatic equilibrium,

$$\vec{\nabla} P = -\rho \vec{\nabla} \Phi, \tag{4.23}$$

is solved together with Poisson's equation

$$\nabla^2 \Phi = 4\pi G \rho, \tag{4.24}$$

and an isentropic equation of state (EoS),

$$P = K \rho^{\gamma}, \tag{4.25}$$

where we assumed K to be constant and the adiabatic index of ideal monoatomic gas, $\gamma = 5/3$, throughout. These equations can be combined to yield

$$\frac{1}{r} \frac{\partial}{\partial r} \left[\frac{r}{\rho} \frac{\partial \left(K \rho^{\gamma} \right)}{\partial r} \right] = -4\pi G \rho, \tag{4.26}$$

with the boundary conditions

$$\rho(r=0)=\rho_{\rm c}, \quad \left.\frac{\partial\rho}{\partial r}\right|_{r=0}=0. \tag{4.27}$$

Eqs. (4.26)-(4.27) can be cast into unitless form by defining $y=\rho/\rho_{\rm c}$ and $x=r/H$, with

$$H^2=\frac{c_{\rm s,0}^2}{(\gamma-1)4\pi G\rho_{\rm c}}, \tag{4.28}$$

the scale radius of the cylinder, where $c_{\rm s,0}^2=\gamma P_{\rm c}/\rho_{\rm c}=\gamma K\rho_{\rm c}^{\gamma-1}$ is the sound speed along the filament axis, with $P_{\rm c}=P(r=0)$ the pressure along the filament axis. The resulting equation is

$$\frac{1}{x}\frac{\partial}{\partial x}\left(x\frac{\partial y^{\gamma-1}}{\partial x}\right)=-y, \quad y(0)=1, \quad \left.\frac{\partial y}{\partial x}\right|_0=0. \tag{4.29}$$

Analytic solutions exist only for $\gamma=1$ (isothermal cylinder), $\gamma=2$, and $\gamma=\infty$ (incompressible cylinder) (Ostriker, 1964a). For other values of γ eq. (4.29) must be solved numerically.

While the isothermal cylinder discussed in §4.2.1 extends to $r=\infty$, all cases with $\gamma>1$ have a finite radius, $R_{\rm equ}$, defined as the radius where the density profile first reaches $\rho=0$ (Ostriker, 1964a). We can thus generalise the notion introduced in §4.2.1 of a critical line-mass above which hydrostatic equilibrium is not possible

$$\Lambda_{\rm cr}=\frac{c_{\rm s,0}^2}{2(\gamma-1)G}\int_0^{R_{\rm equ}/H} y(x)\times x\ {\rm d}x=a\frac{c_{\rm s,0}^2}{G}, \tag{4.30}$$

where $y(x)$ is the solution to eq. (4.29). The factor a on the right-hand-side of eq. (4.30) depends on the EoS. For $\gamma=5/3$, $R_{\rm equ}\simeq 2.648H$, the half-mass radius is $R_{1/2}\simeq 1.168H$, and $a\simeq 0.796$. For comparison, an isothermal cylinder has $R_{1/2}\simeq 2.828H$, with H defined in eq. (4.1), and $a=2$ (eq. 4.3). In Fig. 4.1 we show the normalised equilibrium density and line-mass profiles of an isolated, isentropic,

$\gamma = 5/3$ cylinder.

Equilibrium profiles with $\Lambda < \Lambda_{\rm cr}$ can be constructed for cylinders pressure confined by an external medium and truncated at some radius $R_{\rm s} < R_{\rm equ}$. In Fig. 4.2 we show the stream radius, $R_{\rm s}/H$, as a function of $\mu = \Lambda/\Lambda_{\rm cr}$. For $\mu = 0$, 1 we have $R_{\rm s} = 0$, $R_{\rm equ}$ respectively. For $\mu = 0.5$ we have $R_{\rm s} = R_{1/2} \simeq 1.17H$. We adopt model units where $G = \rho_{\rm c} = 1$ and $R_{\rm s} = 1/32$. For a given value of μ, we can obtain H in model units from Fig. 4.2 and then eq. (4.28) can be used to obtain $c_{\rm s,0} = (8\pi/3)^{1/2}H$ and $P_{\rm c} = K_{\rm s} = 3c_{\rm s,0}^2/5$. Note that the stream and the background fluid have different entropy, and hence different values of K.

In addition to μ, the system is defined by

$$\delta_{\rm c} = \frac{\rho_{\rm c}}{\rho(R_{\rm s}^+)}, \tag{4.31}$$

the ratio of the density along the stream axis to the background density just outside the stream. For a given μ and $\delta_{\rm c}$ we may evaluate the density contrast between the stream and background on either side of the interface,

$$\delta = \frac{\rho(R_{\rm s}^-)}{\rho(R_{\rm s}^+)} = \delta_{\rm c}\frac{\rho(R_{\rm s}^-)}{\rho_{\rm c}}. \tag{4.32}$$

We show the ratio $\rho(R_{\rm s}^-)/\rho_{\rm c} = \delta/\delta_{\rm c}$ as a function of μ in Fig. 4.2. For $\mu = 0.1$, 0.5, 0.9 we have $\delta/\delta_{\rm c} \simeq 0.92$, 0.58, 0.18 respectively.

To construct equilibrium profiles for pressure confined cylinders with given values of μ and $\delta_{\rm c}$, we first evaluate $R_{\rm s}/H$ and δ from Fig. 4.2. We then solve eq. (4.29) separately for $r < R_{\rm s}$ and $r > R_{\rm s}$. For $r < R_{\rm s}$, the boundary conditions are $y(0) = 1$, and $\mathrm{d}y/\mathrm{d}x|_0 = 0$, and the profile is unchanged from the isolated cylinder. For $r > R_{\rm s}$, the boundary conditions are given in terms of the pressure, rather than the density. Specifically, the pressure is continuous at the interface, $P(R_{\rm s}^-) = P(R_{\rm s}^+)$, while the

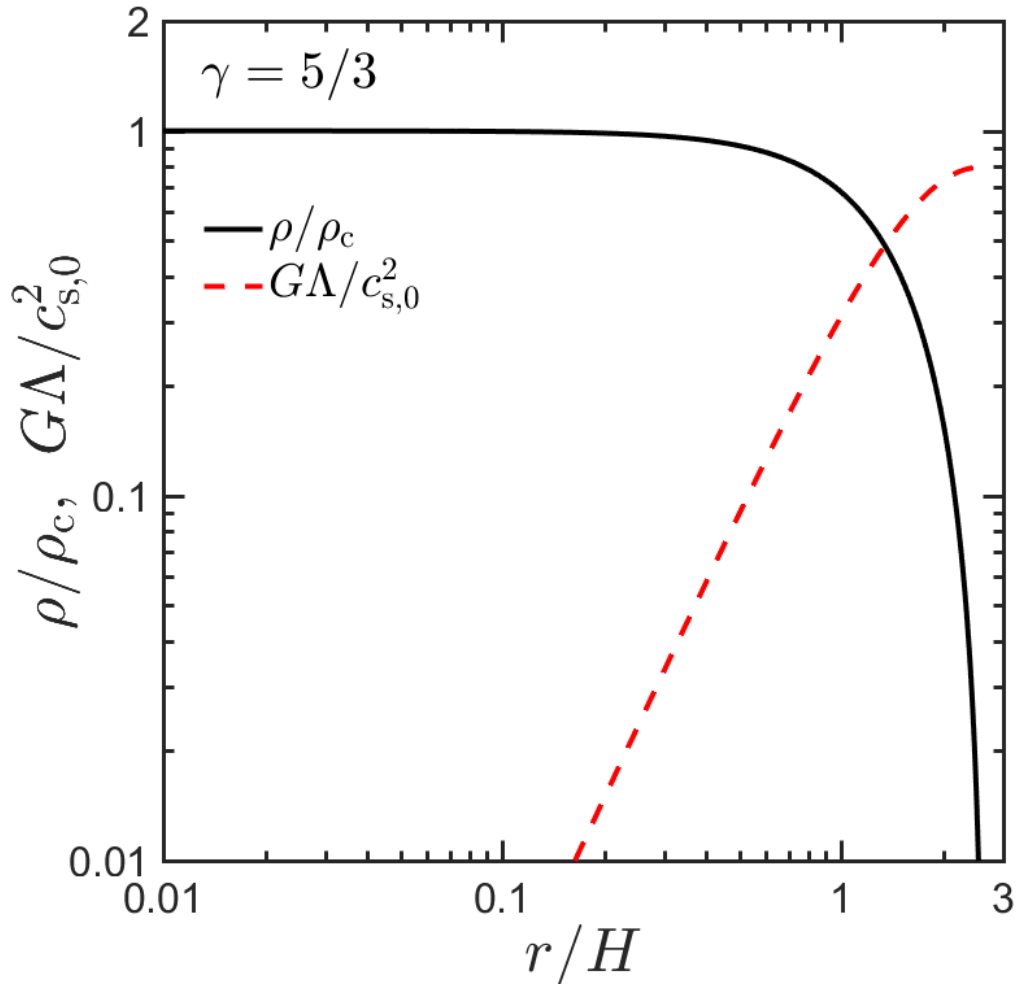

Figure 4.1: Normalised density and line-mass profiles for a self-gravitating, isentropic cylinder with $\gamma = 5/3$. The radial coordinate has been normalised by H given in eq. (4.28), the density (solid black line) has been normalised by its central value, and the line-mass (dashed red line) has been normalised by $c^2_{\rm s,0}/G$ following eq. (4.30). The cylinder has a finite radius $R_{\rm equ} \simeq 2.65H$, and a finite line-mass equal to $\Lambda_{\rm cr} \simeq 0.80c^2_{\rm s,0}/G$. The half-mass radius of the cylinder is $R_{1/2} \simeq 1.17H$.

pressure gradient is discontinuous, with

$$\frac{\mathrm{d}P/\mathrm{d}R|_{R_\mathrm{s}^-}}{\mathrm{d}P/\mathrm{d}R|_{R_\mathrm{s}^+}} = \frac{\rho(R_\mathrm{s}^-)}{\rho(R_\mathrm{s}^+)} = \left(\frac{K(R_\mathrm{s}^+)}{K(R_\mathrm{s}^-)}\right)^{1/\gamma} = \delta, \tag{4.33}$$

which follows from eq. (4.23).

Fig. 4.3 shows the resulting density and pressure profiles for $\mu = 0.1$ and 0.9. For $\mu = 0.1$ the density and pressure are nearly constant in either medium, while for $\mu = 0.9$ there are strong gradients within the stream.

4.3.2 Initial Conditions

Simulation Domain & Boundary Conditions

The simulation domain is a cube of side $L = 1$, extending from -0.5 to 0.5 in all directions. We hereafter adopt the standard cylindrical coordinates, (r, φ, z). The axis of our cylindrical stream is placed along the z axis, at $r = 0$, and we adopt a stream radius of $R_\mathrm{s} = 1/32$. The stream fluid occupies the region $r < R_\mathrm{s}$ while the background fluid occupies the rest of the domain. The equation of state (EoS) of both fluids is that of an ideal monoatomic gas with adiabatic index $\gamma = 5/3$.

We use periodic boundary conditions at $z = \pm 0.5$, and zero force boundary conditions, often called outflow boundary conditions, at $x = \pm 0.5$ and $y = \pm 0.5$, such that gas crossing the boundary is lost from the simulation domain. At these boundaries, the gradients of density and velocity are set to 0, while the pressure gradient is taken from the hydrostatic profile computed following §4.3.1. The potential at the boundary is set to be that at the outer edge of an isolated and infinitely long cylinder with total mass M, equal to the total mass in the simulation domain, $\Phi(r) = 2G(M/L)\ln(r)$ with $r = (x^2 + y^2)^{1/2}$ on the boundary. We note that this does not produce perfect equilibrium due to fitting a cylindrical profile in a cubic box. However, we find that our configuration is extremely stable in simulations with no initial perturbations and

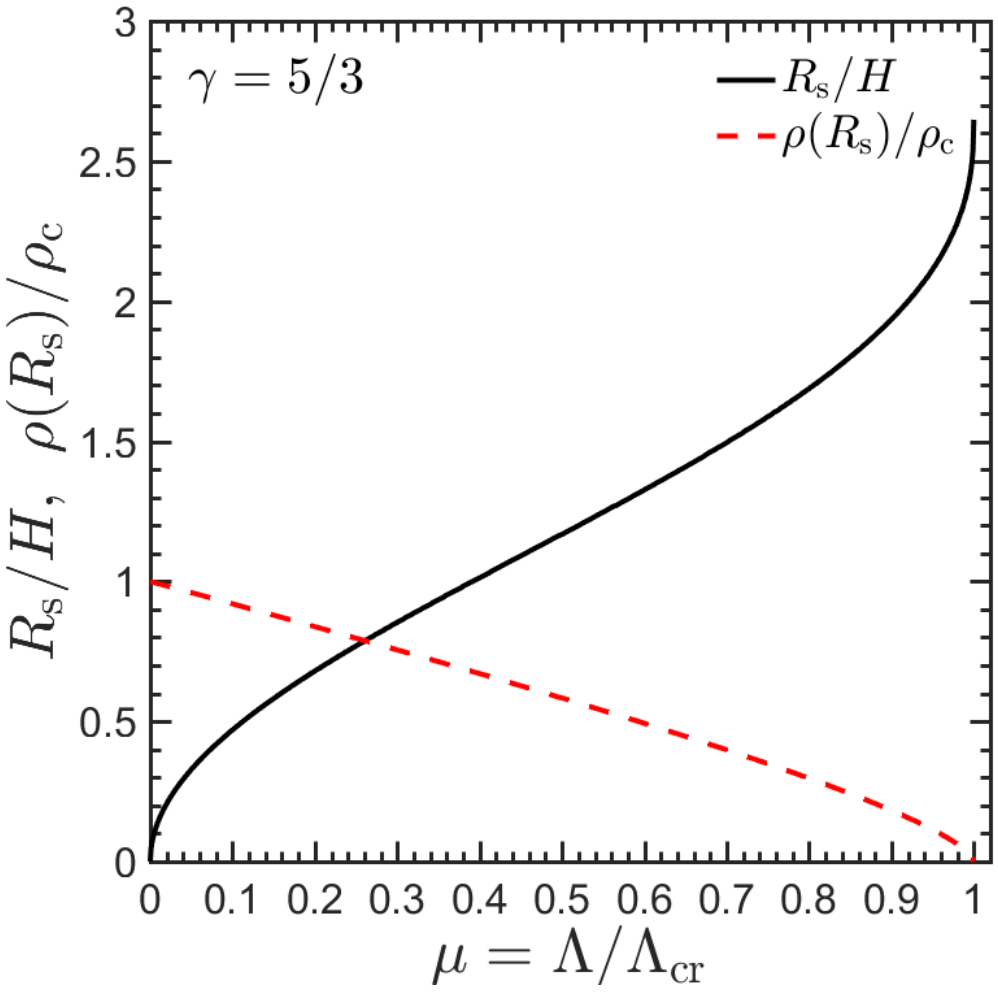

Figure 4.2: Properties of a truncated $\gamma = 5/3$ cylinder in hydrostatic equilibrium. The x-axis shows the line-mass divided by the critical line-mass, $\mu = \Lambda/\Lambda_{cr}$. On the y-axis we show the stream radius, R_s, divided by the scale radius, H (eq. 4.28, black solid line), and the density at the stream radius divided by the central density, $\rho(R_s^-)/\rho_c$ (red dashed line).

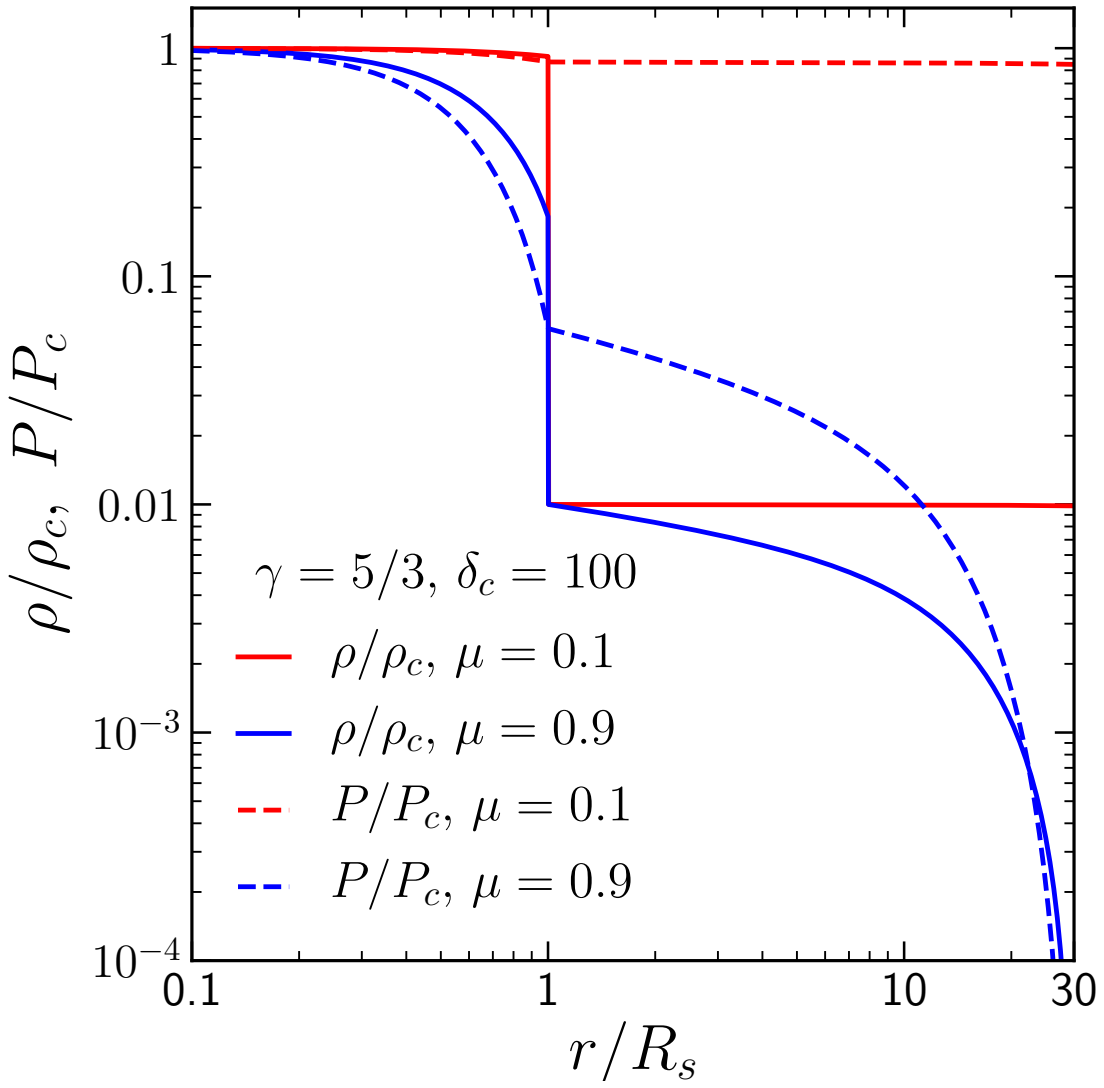

Figure 4.3: Equilibrium density and pressure profiles of pressure confined cylinders with two different values of the stream line-mass, $\mu = 0.9$ (in blue) and $\mu = 0.1$ (in red). The solid (dashed) lines show the density (pressure) profiles. All cases correspond to $\delta_{\rm c} = 100$ and $\gamma = 5/3$. For $\mu = 0.1$, $\rho(R_{\rm s}^-) \simeq 0.92\rho_{\rm c}$ (Fig. 4.2) and the density and pressure are nearly constant in both the stream and background. For $\mu = 0.9$, $\rho(R_{\rm s}^-) \simeq 0.18\rho_{\rm c}$ (Fig. 4.2), and there are strong density and pressure gradients within the stream.

no shear flow, exhibiting $\lesssim 3\%$ change in the density and pressure profiles after 4 stream free-fall times.

Smoothing the Discontinuity

As noted by many previous studies of KHI, the presence of a sharp discontinuity at the interface of two fluids leads to numerical perturbations on the grid scale. These grow faster than the intended perturbations in the linear regime, and may dominate the instability at late times depending on their amplitude. Furthermore, since smaller scales grow more rapidly in the linear regime, these numerical perturbations become more severe as the resolution is increased, preventing convergence of the solution. To alleviate this issue, we smooth the velocity and density around the interfaces using the ramp function proposed by Robertson et al. (2010), also used by M16, P18, and M19. Specifically, we normalise each quantity in the stream and the background by its value at $R_{\rm s}$, denoted $f_{\rm s}$ and $f_{\rm b}$ respectively. We then smooth between these values using

$$f(r) = f_{\rm b} + (f_{\rm s} - f_{\rm b}) \times \mathcal{R}(r), \tag{4.34}$$

$$\mathcal{R}(r) = \frac{1}{2}\left[1 - \tanh\left(\frac{r - R_{\rm s}}{\sigma}\right)\right], \tag{4.35}$$

and multiply the normalised profiles in either medium by $f(r)$. The parameter σ determines the width of the transition zone. The function $\mathcal{R}(r)$ transitions from 0.05 to 0.95 over a full width of $\sim 3\sigma$ in $(r - R_{\rm s})$. We adopt $\sigma = R_{\rm s}/32$ for all of our simulations, which is sufficient to suppress artificial perturbations with small longitudinal wavelength, while still allowing azimuthal modes with $m \lesssim 12$ to grow (M19).

Perturbations

The stream is initialised with velocity $\vec{v_s} = M_{\rm b} c_{\rm b} \hat{z}$, where $c_b = [\gamma P(R_{\rm s}^+)/\rho(R_{\rm s}^+)]^{1/2}$ is the sound speed at the outer boundary of the stream. The background gas is initialised at rest, with velocity to $\vec{v_b} = 0$.

We then perturb our simulations with a random realization of periodic perturbations in the radial component of the velocity, $v_{\rm r} = v_{\rm x}{\rm cos}(\varphi) + v_{\rm y}{\rm sin}(\varphi)$, as in M19. In practice, we perturb the Cartesian components of the velocity,

$$v_{\rm x}^{\rm pert}(r,\varphi,z) = \sum_{j=1}^{N_{\rm pert}} v_{0,j}\, \cos\left(k_j z + m_j \varphi + \phi_j\right) \times \exp\left[-\frac{(r-R_{\rm s})^2}{2\sigma_{\rm pert}^2}\right] \cos\left(\varphi\right)\ , \tag{4.36}$$

$$v_{\rm y}^{\rm pert}(r,\varphi,z) = \sum_{j=1}^{N_{\rm pert}} v_{0,j}\, \cos\left(k_j z + m_j \varphi + \phi_j\right) \times \exp\left[-\frac{(r-R_{\rm s})^2}{2\sigma_{\rm pert}^2}\right] \sin\left(\varphi\right)\ . \tag{4.37}$$

The velocity perturbations are localised on the stream-background interface, with a penetration depth set by the parameter $\sigma_{\rm pert}$. We set $\sigma_{\rm pert} = R_{\rm s}/16$ in all of our simulations, as in M19. To comply with periodic boundary conditions, all wavelengths were harmonics of the box length, $k_j = 2\pi n_j$, where n_j is an integer, corresponding to a wavelength $\lambda_j = 1/n_j$. In each simulation, we include all wavenumbers in the range $n_j = 2 - 64$, corresponding to all available wavelengths in the range $R_{\rm s}/2 - 16R_{\rm s}$. Each perturbation mode is also assigned a symmetry mode, represented by the index m_j in eqs. (4.36) and (4.37), and discussed in §4.2.2. As in M19, we only consider $m = 0, 1$. For each wavenumber k_j we include both an $m = 0$ mode and an $m = 1$ mode. This results in a total of $N_{\rm pert} = 2 \times 63 = 126$ modes per simulation. Each mode is then given a random phase $\phi_j \in [0, 2\pi)$. The stochastic variability from changing the random phases was extremely small, as shown in P18 and M19. The amplitude of each mode, $v_{0,j}$, was identical, with the rms amplitude normalised to $0.01 c_{\rm s}$.

Resolution and Refinement Scheme

We used a statically refined grid with resolution decreasing away from the stream axis. The highest resolution region is $\max(|x|, |y|) < 3R_{\rm s}$, with cell size $\Delta = 2^{-10}$. For $R_{\rm s} = 1/32$ this corresponds to 64 cells per stream diameter. The cell size increases by a factor of 2 every $3R_{\rm s}$ in the x and y-directions, up to a maximal cell size of 2^{-6}. The resolution is uniform along the z direction, parallel to the stream axis. For uniform density cylinders, KHI surface modes are converged at this resolution (M19). We also ran two cases with a factor 2 higher resolution (128 cells per stream diameter) in order to test convergence of our results for self-gravitating streams. As described in §4.4.2 and §4.4.3, we find that the majority of our results are indeed converged.

Simulations Without Self-Gravity

In addition to the simulations of self-gravitating cylinders described above, we performed several simulations without self-gravity for comparison, hereafter our "no-gravity" simulations. In the no-gravity simulations, the boundary conditions at $x = \pm 0.5$ and $y = \pm 0.5$ are simply zero gradients in all fluid variables, including the pressure. These were then initialised with the same density profiles as the corresponding self-gravitating streams, but with constant pressure throughout the simulation domain, since there is no gravitational field. We set the pressure to be the same as the pressure at the stream boundary in the corresponding self-gravity simulations, $P_{\rm no-gravity}(r) = P_{\rm self-gravity}(R_{\rm s})$. This allows us to separate the effects of the density profile from those of self-gravity on the evolution of KHI.

4.3.3 Tracing the Two Fluids

Following P18 and M19, we use a passive scalar field, $\psi(r, \varphi, z, t)$, to track the growth of the shear layer and the mixing of the two fluids. Initially, $\psi = 1$ and 0 at $r < R_{\rm s}$

and $r > R_{\rm s}$ respectively, and is then smoothed using eqs. (4.34)-(4.35). During the simulation, ψ is advected with the flow such that the density of stream-fluid in each cell is $\rho_{\rm s} = \psi\rho$, where ρ is the total density in the cell.

The volume-weighted average radial profile of the passive scalar is given by

$$\overline{\psi}(r,t) = \frac{\int_{-L/2}^{L/2}\int_{0}^{2\pi}\psi_{(r,\varphi,z,t)}r\ \mathrm{d}\varphi\,\mathrm{d}z}{2\pi r L}. \tag{4.38}$$

The resulting profile is monotonic (neglecting small fluctuations on the grid scale) and can be used to define the edges of the shear layer around the stream interface, $r(\overline{\psi} = \epsilon)$ on the background side and $r(\overline{\psi} = 1-\epsilon)$ on the stream side, where ϵ is an arbitrary threshold. We set $\epsilon = 0.04$ following M19, though our results are not strongly dependent on this choice. The background-side thickness of the shear layer is then defined as

$$h_{\rm b} \equiv \mathrm{max_r} r(\overline{\psi} = \epsilon) - R_{\rm s}, \tag{4.39}$$

while the stream-side thickness is defined as

$$h_{\rm s} \equiv R_{\rm s} - \mathrm{min_r} r(\overline{\psi} = 1-\epsilon). \tag{4.40}$$

While $h_{\rm b}$ as defined in eq. (4.39) is always well defined, at late times the perturbed region encompasses the entire stream and $\overline{\psi}(r=0) < 1-\epsilon$. In this case, we define $h_{\rm s} = R_{\rm s}$. The total width of the perturbed region is given by $h \equiv h_{\rm b} + h_{\rm s}$.

4.4 Results

In this section we present the results of our numerical simulations. In §4.4.1, we examine when the combined evolution of GI and KHI leads to the formation of long-lived clumps or to stream shredding, and compare to our theoretical predictions. In

§4.4.2 and §4.4.3, we discuss the late time evolution of the system in the cases when KHI and GI dominate, respectively.

4.4.1 KHI vs GI

As detailed in §4.2.3, we predict that a dense, self-gravitating filament shearing against a dilute background will either fragment into long-lived, bound clumps due to GI, or disrupt and mix into the background due to KHI, depending on the ratio of their respective timescales. The timescale for GI, $t_{\rm max}(\mu, \delta_{\rm c})$, is well approximated by eq. (4.11) (see the Appendix §A.2). The timescales for KHI are $t_{\rm shear}(M_{\rm b}, \delta_{\rm c})$ (eq. 4.17) or $t_{\rm dis} = (1+\delta^{1/2})t_{\rm shear}$ (eq. 4.16). For given values of $(M_{\rm b}, \delta_{\rm c})$ there is a critical line mass ratio, $\mu_{\rm cr}$, such that for $\mu > \mu_{\rm cr}$, $t_{\rm max} < t_{\rm shear}$ and GI will dominate. If $\mu_{\rm cr}$ is small enough to be in the regime where GI is dominated by surface modes, then KHI will dominate for $\mu < \mu_{\rm cr}$. However, if $\mu_{\rm cr}$ is in the regime where GI is dominated by body modes, then the fate of the stream when $\mu < \mu_{\rm cr}$ depends also on the ratio of $t_{\rm max}$ to $t_{\rm dis}$.

Solid curves in Fig. 4.4 show the ratio $t_{\rm max}/t_{\rm shear}$ as a function of μ for $(M_{\rm b}, \delta_{\rm c}) = (1.0, 100)$, $(1.0, 6.7)$, $(2.5, 100)$, and $(6.0, 100)$. The corresponding values of $\mu_{\rm cr}$ are ~ 0.36, 0.28, 0.62, and 0.96. Note the very weak dependence of $t_{\rm max}/t_{\rm shear}$ on $\delta_{\rm c}$ for $M_{\rm b} = 1$, since $t_{\rm max}$ depends weakly on $\delta_{\rm c}$ for $\delta_c \gtrsim 4$, while $t_{\rm shear}$ depends weakly on $\delta_{\rm c}$ only through $\alpha(M_{\rm tot})$ (eq. 4.20). The dependence of $t_{\rm max}/t_{\rm shear}$ on $M_{\rm b}$ is much stronger, since $t_{\rm shear}$ decreases roughly linearly with $M_{\rm b}$.

In Fig. 4.5 we show $\mu_{\rm cr}$ as a function of $M_{\rm b}$ and $\delta_{\rm c}$. The general trend is the same as inferred from Fig. 4.4, namely $\mu_{\rm cr}$ increases strongly with $M_{\rm b}$ and has only a slight tendency to increase with $\delta_{\rm c}$. The exception is a narrow strip near $M_{\rm b} \sim (1-2)$ where $\mu_{\rm cr}$ decreases with $M_{\rm b}$. In this region, the increase of $t_{\rm shear}$ due to decreasing α is stronger than the decrease in $t_{\rm shear}$ due to increasing V, leading to a net increase in $t_{\rm shear}$ with $M_{\rm b}$ and thus a net decrease in $\mu_{\rm cr}$. For density contrasts $\delta_{\rm c} \lesssim 100$, $\mu_{\rm cr} > 0.5$

only for supersonic flows with $M_{\rm b} \gtrsim 2.5$. This implies that for massive streams, KHI can only overcome GI for highly supersonic flows (recall that the Mach number of the flow with respect to the sound speed in the stream is $\sim \delta^{1/2} M_{\rm b}$). In this regime, KHI is dominated by high-order azimuthal surface modes (see §4.2.2), which have a short eddy turnover time leading to rapid shear layer growth.

Consider, for example, $\delta_{\rm c} \sim 30$. $\mu_{\rm cr}$ increases from $\mu_{\rm cr} << 1$ at $M_{\rm b} << 1$ towards $\mu_{\rm cr} \gtrsim 0.3$ at $M_{\rm b} \sim 0.6$, then decreases to $\mu_{\rm cr} \lesssim 0.2$ at $M_{\rm b} \sim 1.2$, before strongly increasing at $M_{\rm b} >> 1$. Thus, as $M_{\rm b}$ is increased from $\lesssim 0.2$ to $\gtrsim 2$ for $\delta_{\rm c} \sim 30$ and $\mu \sim 0.25$, the stream fluctuates from being dominated by GI, to KHI, to GI, to KHI. The high $M_{\rm b}$ KHI regime is dominated by surface modes with high azimuthal wavenumber. While these modes are always unstable, at lower Mach numbers they tend to be sub-dominant compared to axisymmetric or helical modes, with $m = 0, 1$ (M19).

To test our predictions, we performed a series of simulations with the same combinations of $(M_{\rm b}, \delta_{\rm c})$ as shown in Fig. 4.4, and different values of μ. For $(M_{\rm b}, \delta_{\rm c}) = (1.0, 100)$, we performed nine simulations spanning the line-mass range $\mu = 0.1,\ 0.2,\ ...,\ 0.9$. For the other combinations of $(M_{\rm b}, \delta_{\rm c})$, we performed three to four simulations each, with μ spanning a small region around the predicted $\mu_{\rm cr}$. The full list of simulations is presented in Table 4.1, along with several relevant parameters. The stream sound crossing time[5], $t_{\rm sc}$, is defined as

$$t_{\rm sc} = 2 \int_0^{R_s} 1/c_s(r) dr, \tag{4.41}$$

where $c_{\rm s}(r) = (\gamma P(r)/\rho(r))^{1/2}$ is the sound speed at radius r.

The markers in Fig. 4.4 indicate for each of our simulations whether or not the

5. The sound crossing times listed in Table 4.1 refer to the self-gravity simulations only. In the no-gravity runs at $r < R_{\rm s}$, $\rho_{\rm no-gravity}(r) = \rho_{\rm gravity}(r)$ while $P_{\rm no-gravity}(r) = P_{\rm gravity}(R_{\rm s}) < P_{\rm gravity}(r)$. This results in a lower sound speed at each $r < R_{\rm s}$, and hence a longer sound crossing time.

μ	M_b	δ_c	δ	$t_{\rm max}$	$t_{\rm shear}$	$t_{\rm dis}$	$t_{\rm sc}$	λ_{cr}
0.1	1	100	92	2.39	1.34	14.15	0.64	5.95
0.2	1	100	84	2.46	2.01	20.43	0.90	5.95
0.3	1	100	76	2.54	2.65	25.65	1.11	5.95
0.4	1	100	67	2.63	3.32	30.51	1.28	5.95
0.5	1	100	58	2.76	4.09	35.38	1.44	5.98
0.6	1	100	49	2.93	5.06	40.62	1.58	5.98
0.7	1	100	40	3.18	6.39	46.77	1.73	6.02
0.8	1	100	30	3.60	8.52	55.01	1.88	6.09
0.9	1	100	18	4.56	13.20	69.68	2.06	6.23
0.1	1	6.7	6.2	3.21	2.00	6.97	0.64	7.02
0.2	1	6.7	5.6	3.41	3.04	10.26	0.90	7.16
0.3	1	6.7	5.1	3.66	4.07	13.22	1.11	7.36
0.5	2.5	100	58	2.76	2.27	19.57	1.44	5.98
0.6	2.5	100	49	2.93	2.84	22.77	1.58	5.98
0.7	2.5	100	40	3.18	3.65	26.71	1.73	6.02
0.9	2.5	100	18	4.56	8.22	43.40	2.06	6.23
0.7	6	100	40	3.18	1.52	11.13	1.73	6.02
0.8	6	100	30	3.60	2.09	13.47	1.88	6.09
0.9	6	100	18	4.56	3.43	18.09	2.06	6.23

Table 4.1: Parameters of simulations used for studying the evolution of streams undergoing both GI and KHI. The first three columns list the control parameters, namely the line-mass ratio μ, Mach number $M_{\rm b}$, and the ratio of central density to background density at the stream boundary $\delta_{\rm c}$. The remaining six columns list derived parameters: the ratio of stream to background density on either side of the interface, δ, the GI time scale, $t_{\rm max}$, the timescale for KHI to destroy the contact discontinuity, $t_{\rm shear}$, the timescale for KHI to destroy the entire stream, $t_{\rm dis}$, the stream sound crossing time, $t_{\rm sc}$, and the shortest unstable wavelength for GI, $\lambda_{\rm cr}$. All timescales are in units of the stream free-fall time, $t_{\rm ff}$, while $\lambda_{\rm cr}$ is in units of the stream radius, $R_{\rm s}$. For all cases, the fastest growing wavelength for GI is $\lambda_{\rm max} \lesssim 2\lambda_{\rm cr}$.

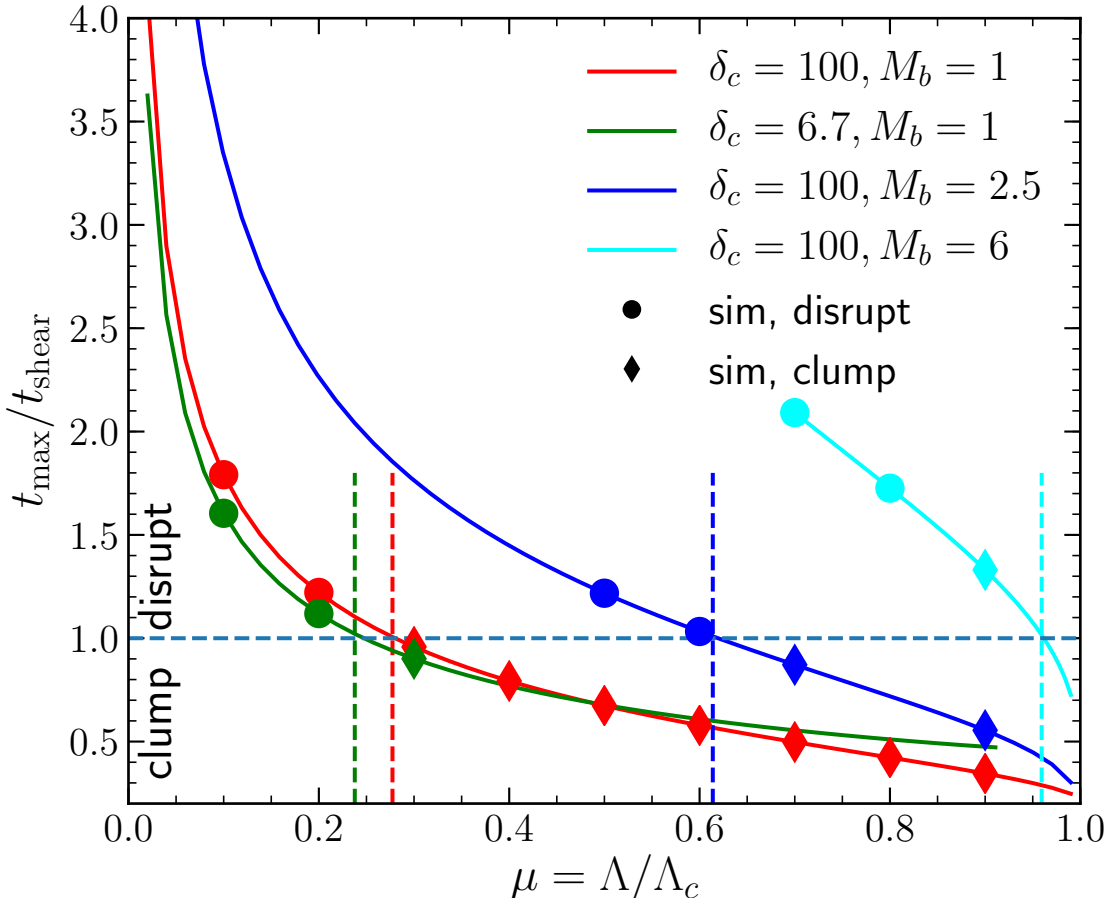

Figure 4.4: Clump formation versus stream disruption according to our model, and in simulations. The solid lines show the ratio of the timescales for GI to form clumps, $t_{\rm max}$, and for KHI to destroy the contact discontinuity, $t_{\rm shear}$, as a function of the line-mass ratio, μ. Different colours show different values of the Mach number and central density contrast, $M_{\rm b}$ and $\delta_{\rm c}$. Our model predicts that when this ratio is less than 1, marked by the horizontal dashed line, the stream should fragment and form clumps, while a ratio larger than one implies stream disruption by KHI. The transition occurs at a critical line-mass ratio, $\mu_{\rm cr} \sim 0.28$, 0.36, 0.62, and 0.96 for $(M_{\rm b}, \delta_{\rm c}) = (1.0, 6.7)$, $(1.0, 100)$, $(2.5, 100)$, and $(6.0, 100)$ respectively. The markers show simulation results, where circles indicate cases where the stream was disrupted by KHI and diamonds indicate cases where the stream fragmented to form clumps. Nearly all our simulations agree with our model, with circles lying above the dashed line and diamonds below it. The one exception is $(M_{\rm b}, \delta_{\rm c}, \mu) = (6.0, 100, 0.9)$, which is dominated by GI body modes rather than surface modes, and forms clumps despite $\mu_{\rm cr}$ 0.96.

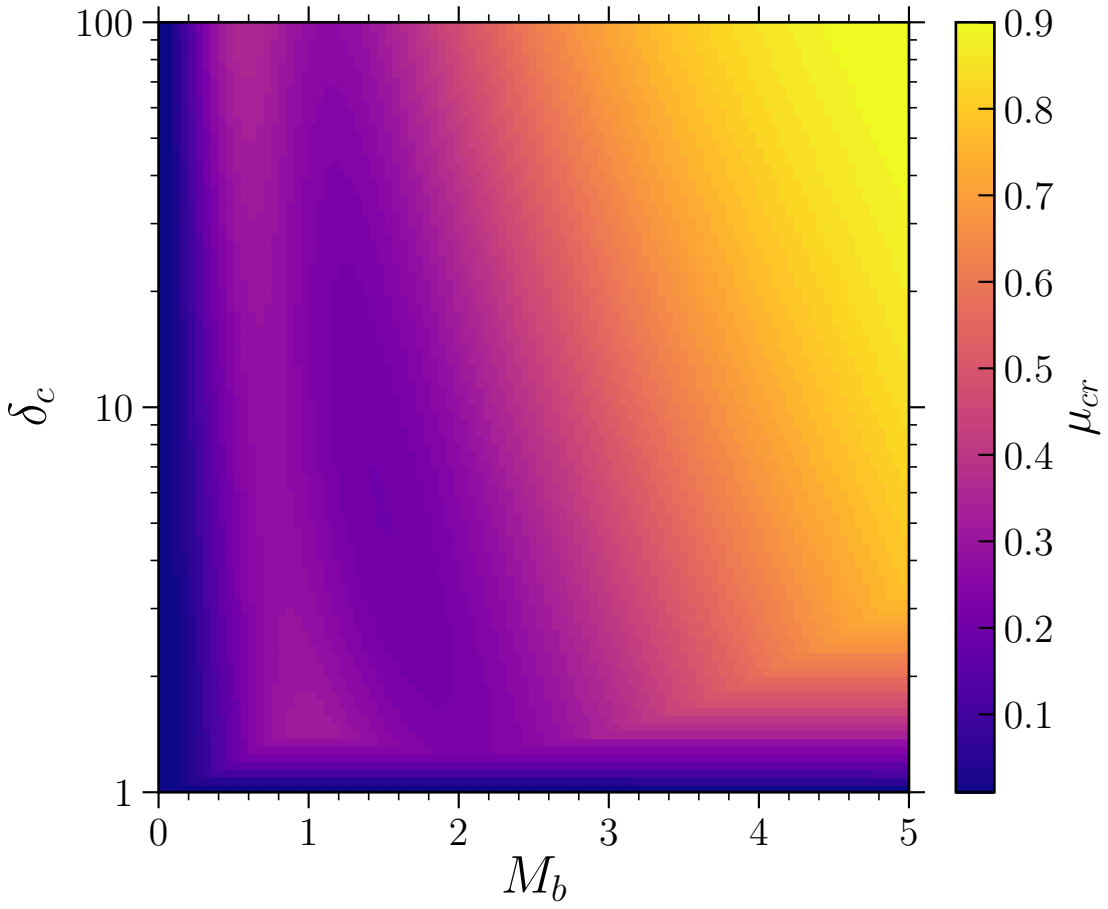

Figure 4.5: Critical line-mass ratio, $\mu_{\rm cr}$, for which $t_{\rm max}/t_{\rm shear} = 1$, as a function of $M_{\rm b}$ and $\delta_{\rm c}$. For $\mu > \mu_{\rm cr}$, the stream will eventually fragment into clumps, while for $\mu < \mu_{\rm cr}$ KHI will disrupt the stream before fragmentation occurs. $\mu_{\rm cr}$ tends to increase with $M_{\rm b}$, except for a narrow strip near $M_{\rm b} \sim 1.5$, and with $\delta_{\rm c}$, though the dependence on $\delta_{\rm c}$ is much weaker. For $\delta_{\rm c} \lesssim 100$, $\mu_{\rm cr} > 0.5$ only for $M_{\rm b} \gtrsim 2.5$, suggesting that for large line-masses KHI can only overcome GI for very supersonic flows which are dominated by high-order azimuthal modes.

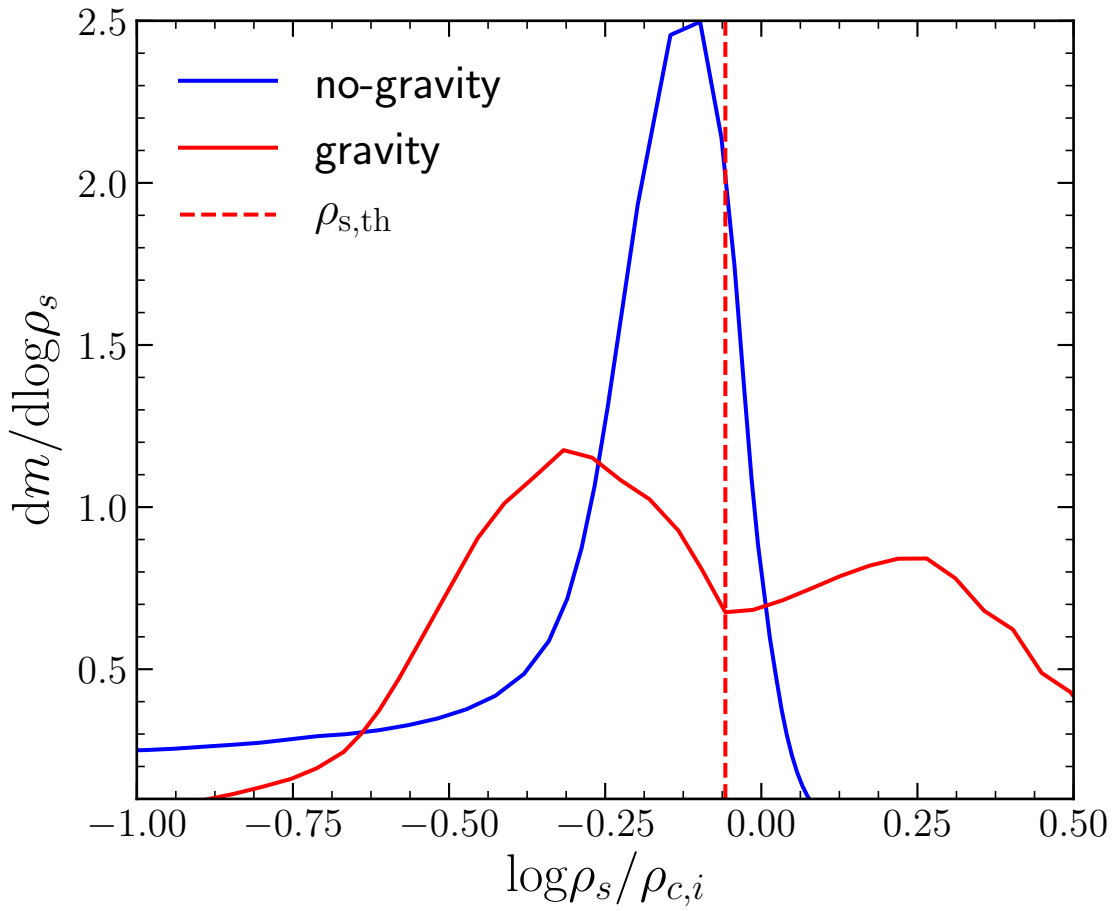

Figure 4.6: Clump identification in the simulations. We show the PDFs of stream density, $\rho_{\rm s} = \psi\rho$, at $t = 8t_{sc}$ for the no-gravity (blue) and gravity (red) simulations with $(M_{\rm b}, \delta_{\rm c}, \mu) = (1, 100, 0.9)$. While the no-gravity simulation exhibits a unimodal, roughly lognormal, PDF, the gravity simulation is bi-modal. Cells with densities higher than the break, $\rho_{\rm s,th}$ marked by the vertical dashed line, are associated with collapsed clumps.

stream has fragmented into long-lived collapsed clumps. To identify such clumps, we examine the PDF of stream fluid density, $\rho_{\rm s} = \psi\rho$. If the density distribution is a result of pure turbulence, we expect it to have a roughly lognormal shape. If, however, the highest density regions have collapsed due to gravity, we expect a break in the PDF at high densities (e.g., Vázquez-Semadeni et al., 2008; Elmegreen, 2011; Hopkins et al., 2012; Federrath & Banerjee, 2015). An example is shown in Fig. 4.6, where we show the density PDFs for the gravity and no-gravity simulations with $(M_{\rm b}, \delta_{\rm c}, \mu) = (1.0, 100, 0.9)$ at $t = 8t_{\rm sc}$. While the no-gravity simulation has a unimodal PDF which is roughly lognormal except at the lowest densities, the gravity simulation produces a bi-modal PDF, and we associate all cells with densities larger than the break density, $\rho_{\rm s,th}$, as being in clumps. As discussed in §4.4.3 below, these clumps are indeed long-lived. If a simulation never exhibits a similar break in the density PDF we determine that this simulation has not formed any clumps. In particular, isolated high density regions produced in no-gravity simulations at late times (see Figs. 4.7 and 4.11 below) are not clumps, but rather transient features associated with the high-density part of a turbulent PDF.

All of our simulations with $\mu > \mu_{\rm cr}(M_{\rm b}, \delta_{\rm c})$ form gravitating clumps, as predicted by our model. Furthermore, for $M_{\rm b} = 1, 2.5$, when $\mu_{\rm cr} \lesssim 0.63$, streams in simulations with $\mu < \mu_{\rm cr}(M_{\rm b}, \delta_{\rm c})$ are disrupted by KHI and mixed into the background before forming bound clumps, as predicted by our model. In these cases, GI is dominated by surface modes, so the comparison of $t_{\rm max}$ and $t_{\rm shear}$ is justified. On the other hand, for $M_{\rm b} = 6.0$, $\mu_{\rm cr} = 0.96$ is in the body mode regime for GI, and our simulation with $\mu = 0.9$ fragments into bound clumps, as discussed in §4.2.3. However, in this same regime we find that streams with $\mu = 0.8$ and 0.7 are disrupted by KHI and do not form bound clumps. So the effect of GI body modes is to lower $\mu_{\rm cr}$ from ~ 0.96 to ~ 0.85.

Overall, we conclude that our model adequately predicts the fate of streams under

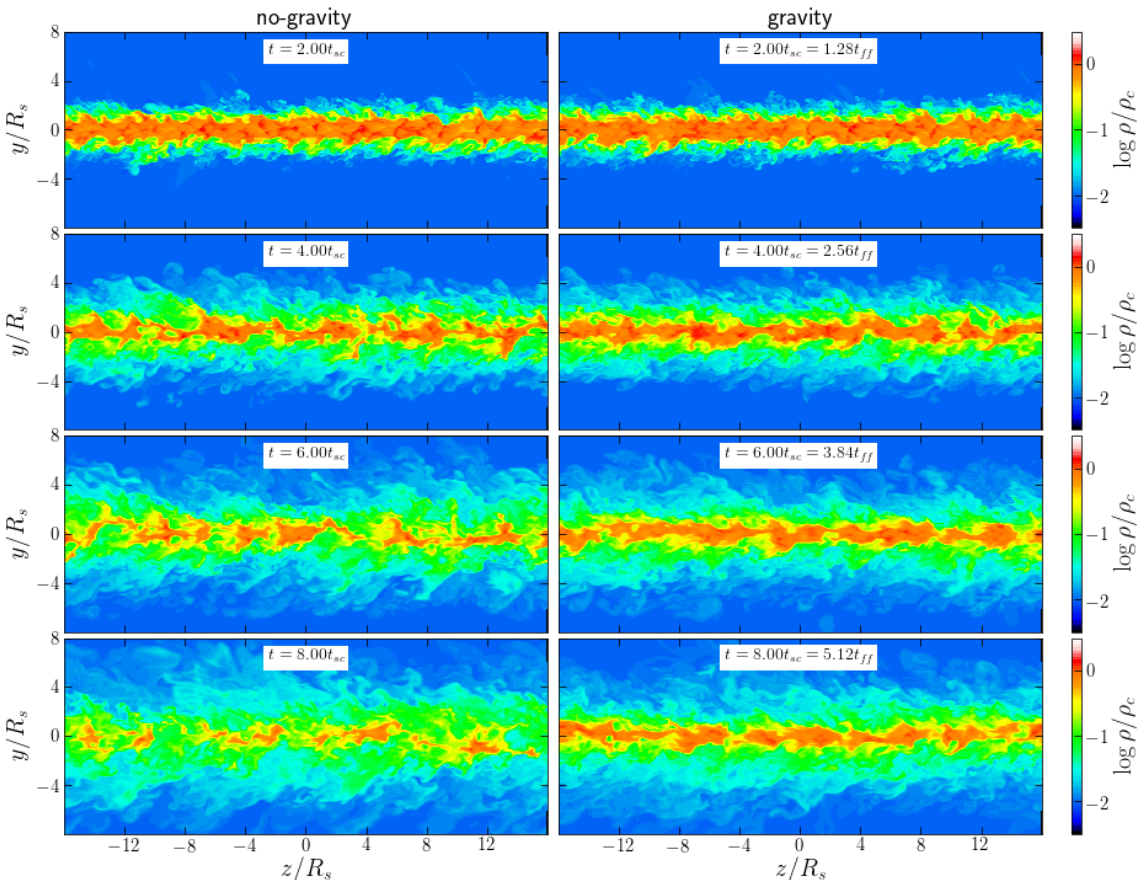

Figure 4.7: Evolution of streams with $\mu < \mu_{\rm cr}$ undergoing KHI. Shown are snapshots of density normalised by the initial density along the stream axis, $\rho_{\rm c}$, in a slice through the yz plane showing an "edge-on" view of the cylinder. The two columns show simulations with $(M_{\rm b}, \delta_{\rm c}, \mu) = (1.0, 100, 0.1)$ run without self-gravity (left) and with self-gravity (right). The snapshot times in units of the stream sound crossing time, $t_{\rm sc}$, are listed in each panel. The evolution with and without gravity is very similar up until $t \sim 5t_{\rm sc}$ and shows the formation of a turbulent shear layer penetrating into the stream and background and mixing the two fluids. At later times, the penetration of the shear layer into the background continues similarly, though self-gravity reduces the penetration into the stream, leaving more high density material near the stream axis.

the combined effects of KHI and GI when GI surface modes dominate. When GI body modes dominate, the actual value of $\mu_{\rm cr}$ is $\sim 10\%$ lower than our prediction, since the relevant timescale for KHI to prevent clump formation is no longer $t_{\rm shear}$. In the next two sections, we turn to studying the evolution of streams and clumps in the regime where each instability dominates.

4.4.2 Stream Disruption due to KHI

We here examine the evolution of streams with $\mu < \mu_{\rm cr}(M_{\rm b}, \delta_{\rm c})$, where KHI dominates over GI and prevents the formation of long-lived collapsed clumps. Specifically, we examine whether the self-gravity of the gas, while unable to completely overcome the KHI, affects its evolution in any way.

Figure 4.7 shows the evolution of streams with $(M_{\rm b}, \delta_{\rm c}, \mu) = (1.0, 100, 0.1)$, with and without self-gravity. At early times, $t \lesssim 4t_{\rm sc}$, the evolution in the two cases is extremely similar, and the shear layer seems to expand at roughly the same rate, mixing the two fluids and diluting the stream density. At later times, $t \gtrsim 6t_{\rm sc}$, while the expansion of the shear layer into the background continues similarly in both simulations, the penetration into the stream has stalled in the gravity run. The self-gravity of the stream thus seems to partly shield its inner core from mixing and disruption. As we will show below, this is due to restoring buoyancy forces caused by the stream's gravitational field.

We examine this more quantitatively in Fig. 4.8, where we compare the evolution of $h_{\rm b}$ and $h_{\rm s}$, the penetration of the shear layer into the background and stream respectively (eq. 4.15), in gravity and no-gravity simulations with $\mu < \mu_{\rm cr}(M_{\rm b}, \delta_{\rm c})$. Focusing on the top panel, we see that $h_{\rm b}$ evolves similarly with and without self-gravity, and is consistent with the results of M19. During the first sound crossing time, $h_{\rm b}$ remains roughly constant as the initial velocity perturbations trigger perturbations in the stream-background interface associated with growing eigenmodes of the system.

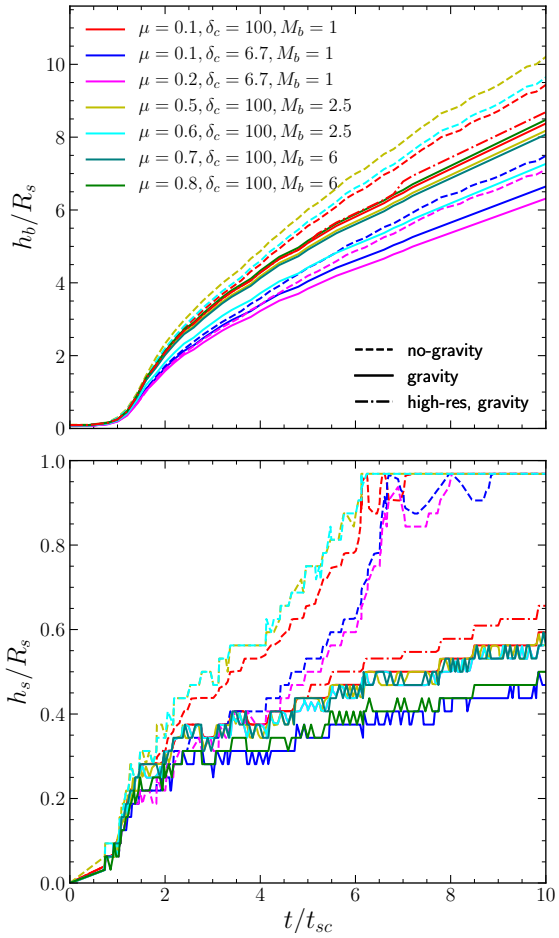

Figure 4.8: Shear layer growth in simulations dominated by KHI, with $\mu < \mu_{\rm cr}(M_{\rm b}, \delta_{\rm c})$. We show the penetration depth of the shear layer into the background, $h_{\rm b}$ (top), and into the stream, $h_{\rm s}$ (bottom). These have been normalised by the stream radius, $R_{\rm s}$, while time on the x-axis has been normalised by the stream sound crossing time, $t_{\rm sc}$. In each panel, solid lines show our fiducial simulations with self-gravity, while dashed lines show our no-gravity simulations. Different colours mark different combinations of $(M_{\rm b}, \delta_{\rm c}, \mu)$. The dot-dashed red line in each panel shows results from a simulation with $(M_{\rm b}, \delta_{\rm c}, \mu) = (1.0, 100, 0.1)$ and twice higher resolution. The penetration of the shear layer into the background proceeds similarly in simulations with and without gravity, while the penetration into the stream is qualitatively different with and without gravity. Without gravity, the shear layer consumes the entire stream at $t \sim t_{\rm dis}$ (eq. 4.16). However, with self-gravity $h_{\rm s} \sim (0.3 - 0.4) R_{\rm s}$ at this time, regardless of μ, likely caused by buoyancy stabilizing the inner stream.

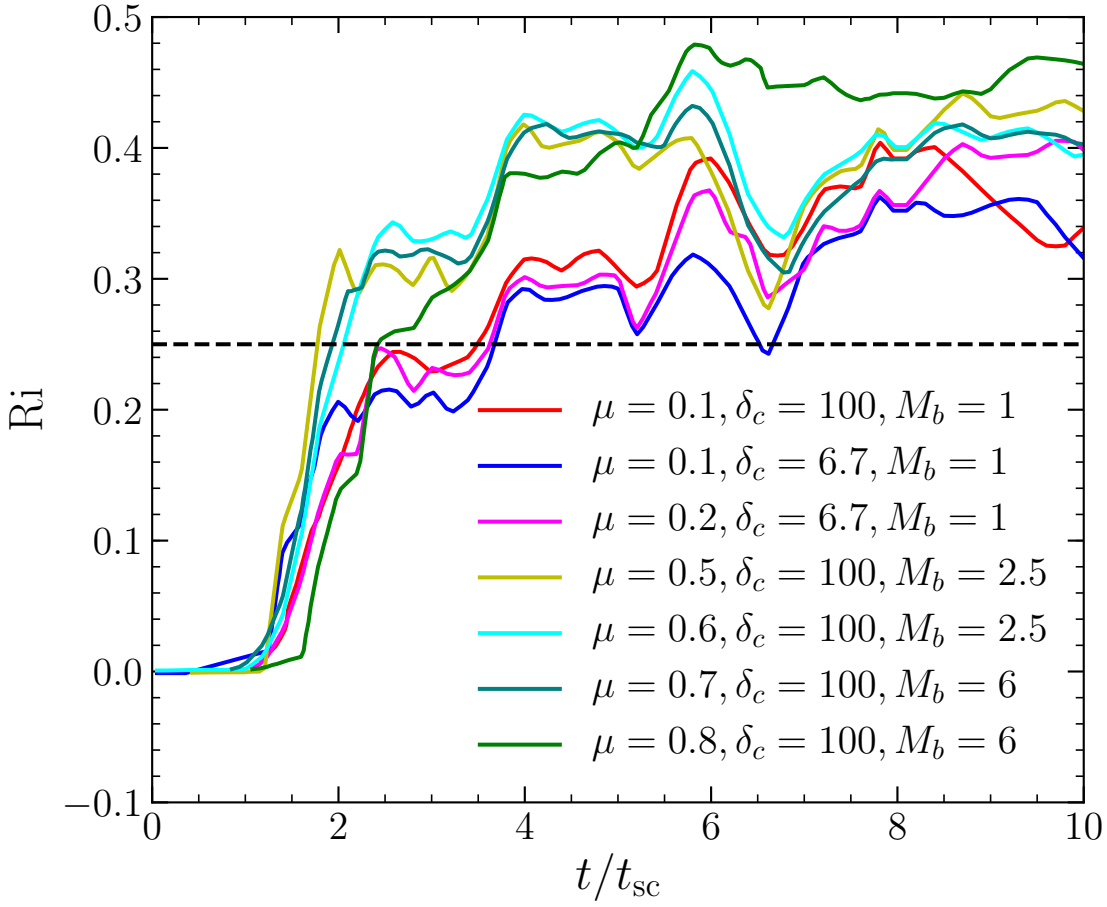

Figure 4.9: Evolution of mass-weighed Richardson number Ri within the shear layer $[R_{\rm s} - h_{\rm s}(t)] < r < R_{\rm s}$ over time. Value of Ri $< 1/4$ indicates that the buoyant force from gravity cannot stop mixing, resulting in quick growth of shear layer h_s at early times. At late times when Ri $> 1/4$, the growth of shear layer slows down due to less mixing.

Following this phase, $h_{\rm b}$ grows approximately linearly following eq. (4.15) until it reaches $h_{\rm b} \sim 2R_{\rm s}$. Up until this point, the gravity and no-gravity runs are nearly indistinguishable. Following this, the growth rate of $h_{\rm b}$ is reduced by roughly half in both cases, as the developing turbulent cascade transfers power from the largest scales driving the expansion to smaller scales (M19). During this phase, the growth rate of $h_{\rm b}$ is reduced in the gravity simulations, by $\sim 25\%$ for $\mu = (0.5 - 0.6)$ and $\sim 12\%$ for $\mu = (0.1 - 0.2)$. Overall, we find that the self-gravity of the stream has a relatively minor effect on the growth of $h_{\rm b}$.

On the other hand, as inferred from Fig. 4.7, there is a qualitative difference in the evolution of $h_{\rm s}$, shown in the bottom panel of Fig. 4.8. For the first $\sim 2t_{\rm sc}$, until $h_{\rm s} \sim 0.3R_{\rm s}$, the gravity and no-gravity runs evolve similarly. After this, the growth rate in the gravity runs is a factor ~ 3 smaller than in the no-gravity runs. In the latter, the shear layer reaches $h_{\rm s}/R_{\rm s} = 1$ and consumes the entire stream at $t \sim t_{\rm dis}$ (eq. 4.16), and the evolution is similar to that seen in M19 (see their figure B1). However, in the runs with self-gravity, $h_{\rm s} \sim (0.3 - 0.4)R_{\rm s}$ at this time, and does not exceed $\sim 0.5R_{\rm s}$ at $t = 10t_{\rm sc}$. This is consistent with the visual impression in Fig. 4.7, where the density remains high in the interior of the self-gravitating stream even after the non-gravitating stream has been completely diluted. Although the growth rate of $h_{\rm s}$ does not depend on μ, there appears to be a tendency for more penetration for larger $\delta_{\rm c}$.

We propose that the stalling of $h_{\rm s}$ is due to restoring buoyancy forces in the stream interior. This can be seen by considering the Richardson number, $\mathrm{Ri} = [N_{\rm BV}/(\mathrm{d}u/\mathrm{d}r)]^2$, where $\mathrm{d}u/\mathrm{d}r$ is the gradient of longitudinal velocity inside the shear layer, and $N_{\rm BV}$ is the Brunt-Vaisälä frequency,

$$N_{\rm BV} = \left[\frac{g}{\gamma}\frac{\partial \ln K}{\partial r}\right]^{1/2}, \tag{4.42}$$

with $g(r)$ the magnitude of the gravitational field, γ the adiabatic index, $K(r) = P(r)\rho^{-\gamma}(r)$ the entropy profile of the gas. Note that K is piecewise constant in our initial conditions, with a non-zero gradient only at the stream-background interface. However, as the shear layer expands, mixing between the fluids creates a non-zero entropy gradient throughout the shear layer. Had our initial conditions been such that the initial stream was not isentropic, this may have increased $N_{\rm BV}$ and Ri in the stream interior.

For a 2d plane-parallel system in a constant external gravitational field, it can be shown that a sufficient (but not necessary) criterion for buoyancy to stabilize the system against shearing induced mixing is that Ri > 0.25 (Miles, 1961; Howard, 1961). While our situation is more complex in that the geometry is cylindrical and the gravitational field is due to self-gravity rather than an external field[6], we may use this as a benchmark to asses the role of buoyancy in stabilizing the inner stream. In Fig. 4.9 we show the mass weighed average of Ri within the shear layer, $[R_{\rm s} - h_{\rm s}(t)] < r < R_{\rm s}$, as a function of time. In all simulations, Ri $<<$ 1 at early times, and crosses Ri $= 0.25$ at $t \sim (2-3)t_{\rm sc}$, corresponding to the sharp decline in the growth rate of $h_{\rm s}$. Further growth of Ri is rather slow and it does not exceed Ri $\sim (0.3 - 0.4)$. We find very similar behaviour when evaluating Ri locally at the inner boundary of the shear layer, $r = [R_{\rm s} - h_{\rm s}(t)]$. This supports our assertion that buoyancy stabilizes the inner stream and slows the growth of $h_{\rm s}$, significantly delaying stream disruption.

In Fig. 4.10 we show the deceleration of streams in simulations with and without gravity. We show the centre of mass velocity of the stream fluid, i.e. weighted by the passive scalar ψ, normalised by its initial value, $V_{\rm i}$, as a function of time normalised by the predicted decelration timescale, $t_{\rm dec}$ (eq. 4.19). The time axis has been shifted to begin at t_0, the time when the stream velocity reaches 98% of its initial value. In all

6. To our knowledge, no analogous criterion exists for the stability of self-gravitating flows or for cylindrical flows. Deriving such a criterion is beyond the scope of this paper.

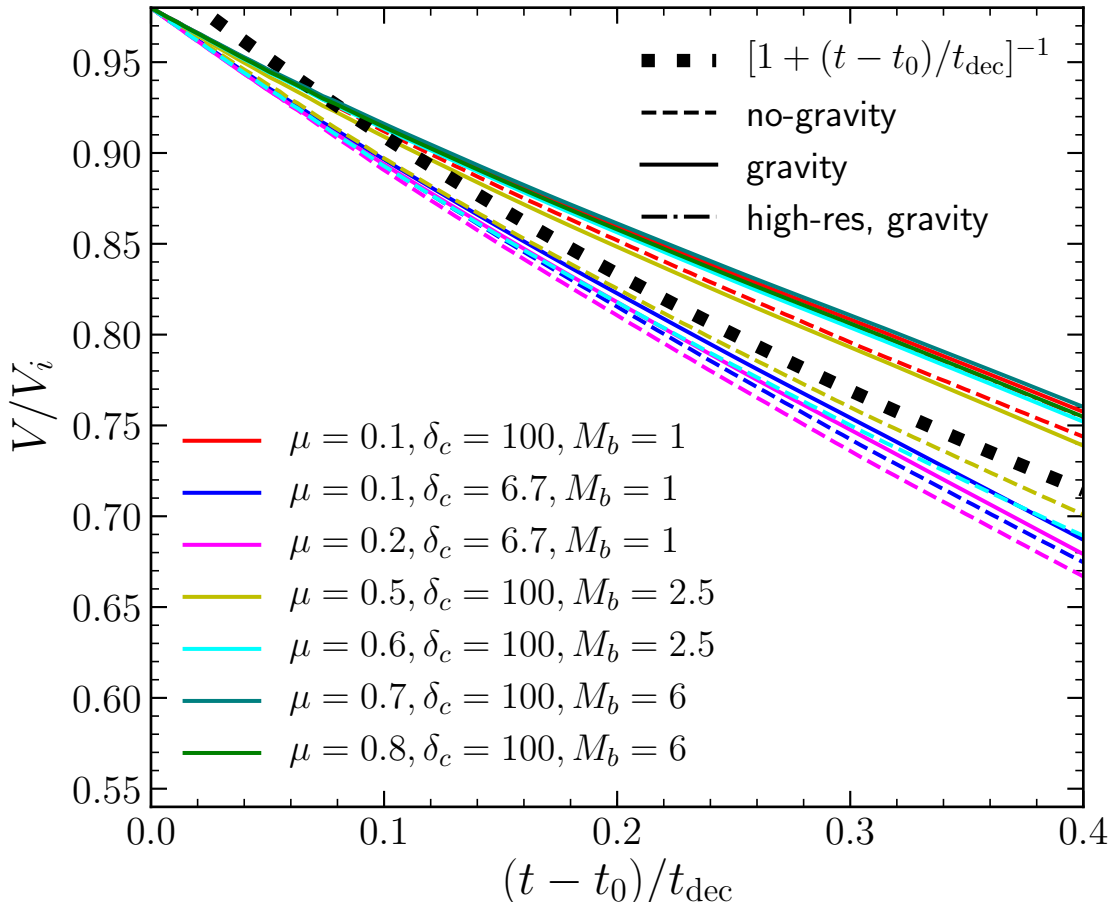

Figure 4.10: Stream deceleration due to KHI. We show the centre of mass velocity of the stream fluid normalised by its initial value, as a function of time normalised by the predicted deceleration timescale, $t_{\rm dec}$ (eq. 4.19). The time axis has been set to zero at t_0, the time when the stream velocity is 98% of its initial value. Solid (dashed) lines show simulations with (without) gravity, as in Fig. 4.8. The thick green dotted line shows the prediction for the deceleration rate due to KHI by M19 (eq. 4.18). The simulations with and without gravity behave similarly and closely follow the predicted deceleration rate. This is consistent with the similar behaviour of $h_{\rm b}$, since the deceleration is primarily driven by entrainment of background material by the shear layer.

cases, $t_0 \sim t_{\rm sc}$. The gravity and no-gravity simulations behave similarly, and both are well fit by the theoretical prediction (eq. 4.18). This was expected given the similarity between the evolution of $h_{\rm b}$ in the gravity and no-gravity simulations (Fig. 4.8), since KHI-induced deceleration is primarily driven by entrainment of background material in the shear layer (P18,M19), not affected by buoyancy in the stream.

We ran the $(M_{\rm b}, \delta_{\rm c}, \mu) = (1.0, 100, 0.1)$ simulation with a factor two higher spatial resolution throughout the simulation domain. The results of this simulation are shown in Figs. 4.8 and 4.10. The evolution of $h_{\rm b}$ and stream velocity, V, are nearly indistinguishable from our fiducial resolution. The penetration of the shear layer into the stream is slightly enhanced, with $h_{\rm s} \sim 10\%$ larger in the high-resolution run at $t \sim 8t_{\rm sc}$. This is still significantly less than the no-gravity simulation, supporting our conclusion that self-gravity significantly suppresses shear layer growth inside the stream.

4.4.3 Stream Fragmentation due to GI

We here examine the evolution of streams undergoing GI in our simulations, and in particular the properties of clumps formed within them. Regardless of whether GI is dominated by surface or body modes in the linear regime, the end result is always expected to be the collapse of dense, long-lived clumps along the stream axis (N87, H98, Heigl et al., 2016, 2018b).

Figure 4.11 shows the evolution of three simulations, each with $(M_{\rm b}, \delta_{\rm c}) = (1.0, 100)$. The left-hand column shows the no-gravity simulation with $\mu = 0.9$, while the centre and right-hand columns show the gravity simulations with $\mu = 0.9$ and 0.4, respectively. By $t = 2t_{\rm sc}$, the non-gravitating stream has developed a well defined shear layer which has penetrated into both the background and the stream, inducing a turbulent mixing zone and diluting the stream density. Meanwhile, the interior of the stream shows numerous density fluctuations caused by turbulence and shocks, with

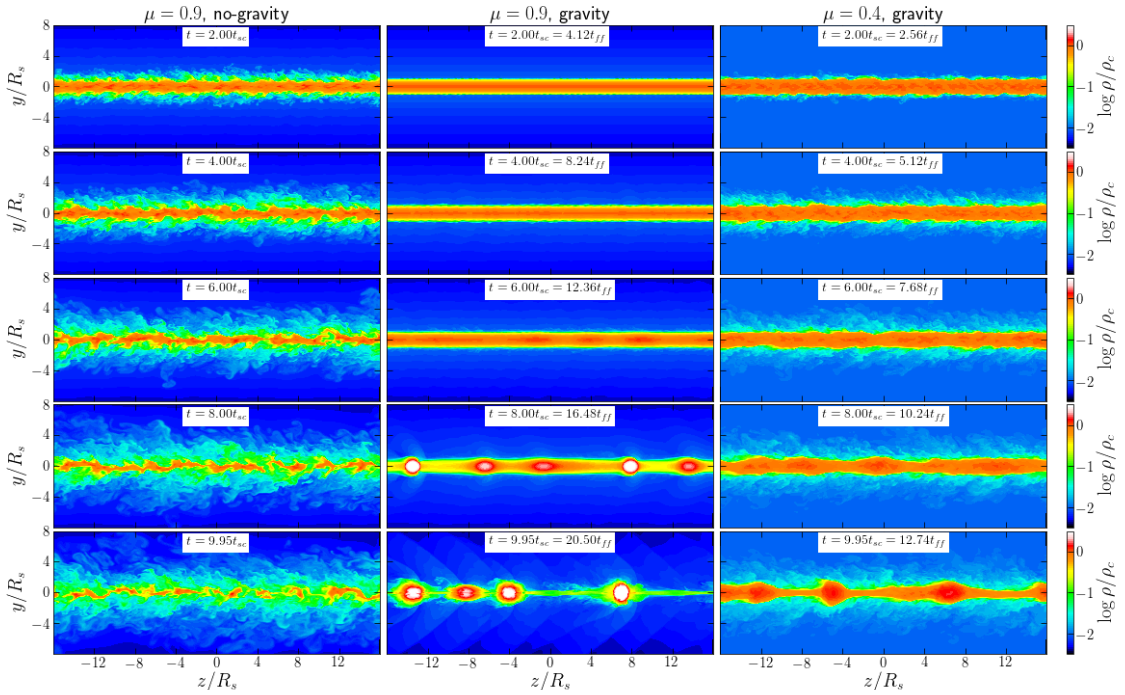

Figure 4.11: Same as Fig. 4.7, but for simulations with $\mu > \mu_{\rm cr}$. The three columns represent three different simulations, each with $(M_{\rm b}, \delta_{\rm c}) = (1.0, 100)$. The left-hand column shows the no-gravity simulation with $\mu = 0.9$, while the centre and right-hand columns show the gravity simulations with $\mu = 0.9$ and 0.4 respectively. The snapshot times in units of the stream sound crossing time, $t_{\rm sc}$, and free-fall time, $t_{\rm ff}$, are listed in each panel. At $t \sim 2t_{\rm sc}$, a turbulent shear layer has developed in the non-gravitating simulation and the gravitating simulation with $\mu = 0.4$, while the gravitating simulation with $\mu = 0.9$ appears unperturbed. At later times, the shear layer consumes the non-gravitating stream as expected for KHI, while GI takes over in both simulations with gravity, resulting in dense clumps along the stream axis by $t \sim 10t_{\rm sc}$. These clumps are separated by $\sim 6.5R_{\rm s}$, consistent with the shortest unstable mode predicted by H98 (see text).

overdensities of up to $\gtrsim 1.5$ times the unperturbed density. At later times the shear layer continues to grow, reaching $h_{\rm s} \sim 0.4 R_{\rm s}$ at $t \sim 4 t_{\rm sc}$, when the fraction of unmixed fluid in the stream, with $\psi > 0.96$, is $\sim 50\%$. This is very similar to the no-gravity simulation shown in the left-hand column of Fig. 4.7, and is consistent with the evolution of KHI in a constant density stream with $\delta = 100$ (M19, figure B1), showing that the steep density profile associated with $\mu = 0.9$ does not qualitatively alter the evolution.

Comparing to the corresponding self-gravitating stream, we see that the initial KHI has been suppressed by the introduction of gravity. At $t = 4 t_{\rm sc}$, the stream appears relatively unperturbed, with no shear layer and only minor density perturbations. The fraction of unmixed fluid in the stream is 77%. By $t \sim 6 t_{\rm sc}$, small density perturbations can be seen along the stream axis, with a wavelength of $\sim 6.5 R_{\rm s}$, slightly larger than the shortest unstable wavelength for GI predicted by H98[7] (Table 4.1). These density peaks are associated with an axisymmetric distortion of the stream-background interface, despite the fact the the initial perturbations had an equal mix of axisymmetric ($m = 0$) and helical ($m = 1$) modes. As described in §4.2.1 and §4.2.2, GI is unstable only to $m = 0$ modes, while the dominant KHI mode at late times has either a long-wavelength and $m = 1$ or a short wavelength and $m > 1$. This supports the fact that these density perturbations were not amplified by nonlinear KHI, but rather by GI. By $t \sim 8 t_{\rm sc}$, these density perturbations have evolved into five dense clumps along the box length of $32 R_{\rm s}$, two of which merge by $t \sim 10 t_{\rm sc}$.

The evolution of the lower line-mass stream, with $\mu = 0.4$, is different. Despite being in the regime where GI dominates over KHI (Fig. 4.4), at early times the evolution appears dominated by KHI. By $t \sim 4 t_{\rm sc}$, a shear layer has developed around the stream, turbulent density fluctuations are visible, and the fraction of unmixed fluid

7. While the fastest growing mode in this case is $\lambda_{\rm max} \sim 11 R_{\rm s}$, corresponding to 3 clumps, the growth rate at $\sim 6.5 R_{\rm s}$ is only 0.85 times the growth rate at $\lambda_{\rm max}$, and the resulting power spectrum is roughly flat in the range $\lambda \sim (6.5 - 12) R_{\rm s}$.

in the stream is 65%. This is because the ratio $t_{\rm max}/t_{\rm shear}$ is larger and closer to 1, allowing KHI to develop further before GI takes over. However, by $t \sim 6t_{\rm sc}$, GI has begun to dominate, developing an axisymmetric pattern in the stream-background interface associated with density perturbations along the stream axis, characteristic of GI but not of nonlinear KHI. By $t \sim 8t_{\rm sc}$, five proto-clumps are visible along the stream axis, consistent with the predicted $\lambda_{\rm cr}$. Two of these clumps merge by $t \sim 10t_{\rm sc}$, leaving four large clumps. Assymptotically, for both $\mu = 0.4$ and 0.9, the spacing between clumps is predicted to be $\lambda_{\rm max} \sim 11R_{\rm s}$, the fastest growing GI mode, corresponding to 3 clumps across $32R_{\rm s}$.

To study the properties of clumps in the simulations, we first select all cells with stream density greater than the break in the PDF of the corresponding snapshot, $\rho_{\rm s,th}$ (Fig. 4.6). We then group together neighbouring cells above this threshold, removing groups containing fewer than 30 cells to avoid spurious density fluctuations. Varying $\rho_{\rm s,th}$ by 0.1 dex, or using ρ rather than $\rho_{\rm s}$, does not change the number of identified clumps, changes the clump masses by $\lesssim 20\%$, and the other clump properties discussed below by $\lesssim 10\%$.

Figure 4.12 shows several properties of clumps identified in our simulations as a function of time, where $t = 0$ is set to the first timestep where clumps have been identified. We show the clump mass, $M_{\rm c}$, the turbulent Mach number within the clumps, $\mathcal{M}_{\rm turb} = \sigma_{\rm turb}/c_{\rm s}$, and the clump virial parameter, defined as

$$\alpha_{\rm vir} = \frac{5(\sigma_{\rm turb}^2 + c_s^2)R}{3GM}, \tag{4.43}$$

where the factor 5/3 comes from assuming a constant density profile inside the clump. If $\alpha_{\rm vir} \sim 1$, the clump is in virial equilibrium, while $\alpha_{\rm vir} < 1$ implies the clump is collapsing and $\alpha_{\rm vir} > 1$ implies it is unbound. For each property we display the average over all clumps identified in a given snapshot, typically four to five clumps.

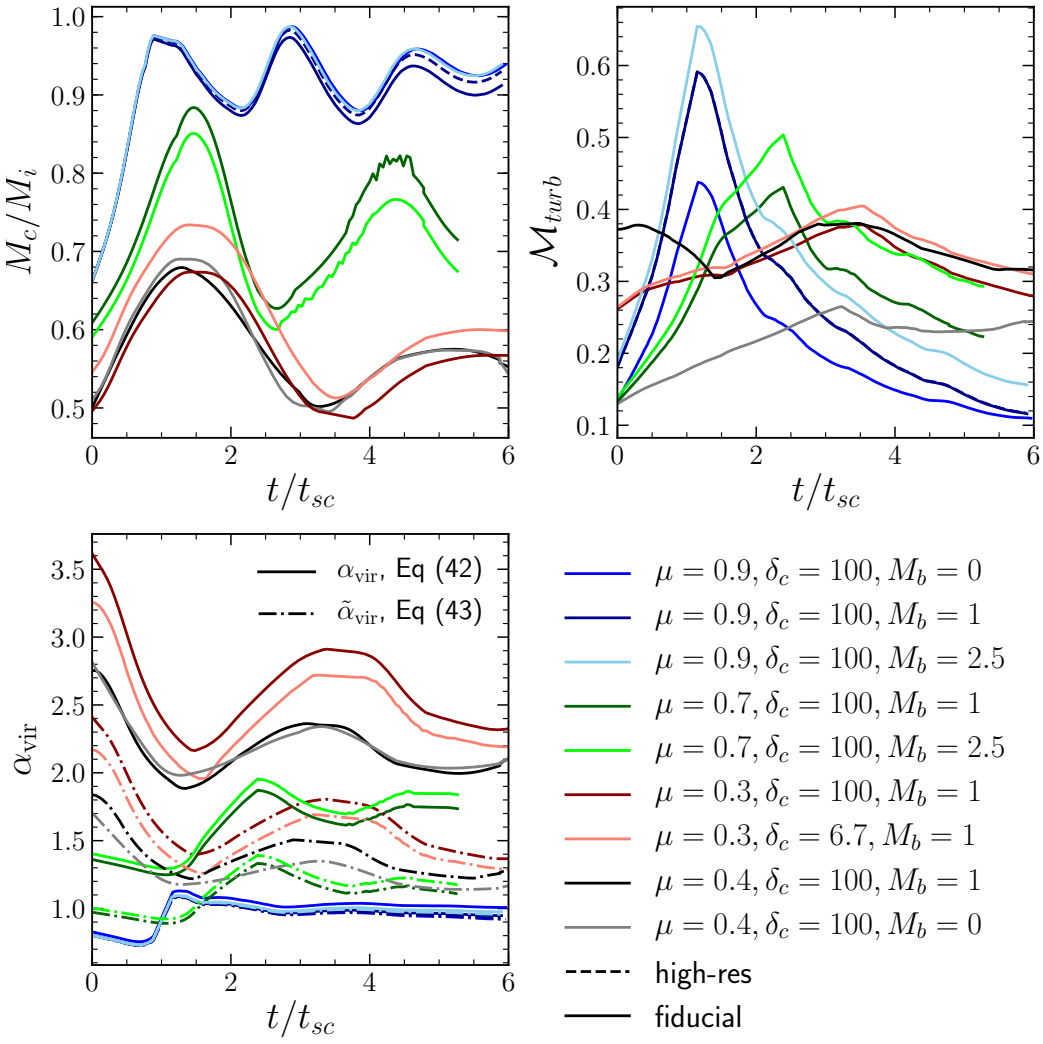

Figure 4.12: Evolution of clump properties, each shown as a function of time since clumps are first detected. Different coloured solid lines show different simulations as indicated in the legend. For clarity, we show results from only a few simulations bracketing the range of stream parameters examined, and thus the range of resulting clump properties. The dashed line in each panel shows the results of a simulation with $(M_{\rm b}, \delta_{\rm c}, \mu) = (1.0, 100, 0.9)$ and twice higher resolution than the fiducial value. *Top-left panel:* clump mass normalised by the average initial stream mass per clump, $M_{\rm i} = M_{\rm stream}/N_{\rm clump}$. *Top-right panel:* turbulent Mach number. *Bottom-left panel:* clump virial parameter, with solid (dash-dotted) lines representing the virial parameter without (with) accounting for the external pressure (eqs. 4.43 and 4.44 respectively). Clumps forming in higher line-mass streams are more massive, have lower turbulent Mach numbers and lower virial parameters, though the dependence on $M_{\rm b}$ or $\delta_{\rm c}$ is extremely weak. For $\mu = 0.9$, roughly 90% of the initial stream mass winds up in clumps, which following collapse are in approximate virial equilibrium. For $\mu = 0.3$, only $\lesssim 50\%$ of the initial stream mass is in clumps, which are primarily confined by external pressure.

Following the initial collapse when the clump mass grows significantly, it tends to saturate at a well defined value despite some oscillations. These oscillations, on the order of $\sim 10-20\%$, are due in part to our density threshold for clump cells, which is recalibrated at each snapshot. We have normalised the mass in Fig. 4.12 by $M_i = M_{\rm stream}/N_{\rm clump}$, where $N_{\rm clump}$ is the number of clumps in the stream and $M_{\rm stream} = \pi R_{\rm s}^2 L\overline{\rho_{\rm s}}$ is the initial stream mass with $\overline{\rho_{\rm s}}$ the mean density in the stream. $M_{\rm i}$ is thus the typical clump mass one would expect if the entire initial stream fragments into clumps. We find that $M_{\rm c}/M_{\rm i}$ increases with μ, rising from $\sim (0.4-0.9)$ for $\mu = (0.3-0.9)$, independent of $M_{\rm b}$ or $\delta_{\rm c}$.

The spherical Jeans mass obtained using the average properties in the initial stream is $M_{\rm J} = (\pi^{5/2}/6)\overline{c_{\rm s}}^3 G^{-3/2}\overline{\rho_{\rm s}}^{-1/2}$. For $N_{\rm clumps} = 4$ and $L = 32R_{\rm s}$ we obtain $M_{\rm i}/M_{\rm J} \sim 0.14(t_{\rm sc}/t_{\rm ff})^3$, with $t_{\rm sc} \simeq 2R_{\rm s}/\overline{c_{\rm s}}$ and $t_{\rm ff} = (4G\overline{\rho_{\rm s}})^{-1/2}$. This corresponds to $M_{\rm i}/M_{\rm J} \sim (0.2-1.2)$ for $\mu = (0.3-0.9)$ (Table 4.1), yielding clump masses $M_{\rm c} \sim (0.1-1)M_{\rm J}$. For small μ, when the density profile in the initial stream is roughly constant, the Bonnor-Ebert mass (eq. 4.7) is $M_{\rm BE} \sim 0.5M_{\rm J}$. In general, $M_{\rm BE} > M_{\rm c}$ for $\mu < 1$.

The turbulent Mach number increases by a factor of ~ 3 as μ is decreased from 0.9 to 0.3. However, in all cases $\mathcal{M}_{\rm turb}$ is $\lesssim 0.3$ asymptotically, and does not exceed ~ 0.6 during the initial collapse of the clump. Turbulent support is thus negligible compared to thermal pressure. The clump virial parameter increases from $\alpha_{\rm vir} \sim 1$ for $\mu = 0.9$, consistent with $M_{\rm c}/M_{\rm J} \sim 1$ in this case, to $\alpha_{\rm vir} \sim 2.3$ for $\mu = 0.3$.

The additional support for clumps in simulations with lower values of μ comes from the external pressure, which also played a larger role in confining the initial stream. This can be seen by considering the full virial parameter including the surface pressure term (e.g., Krumholz, 2015, Chapter 6). We approximate this as

$$\tilde{\alpha}_{\rm vir} = \frac{5(\sigma_{\rm turb}^2 + c_s^2 - \gamma P_{\rm ext}/\rho)R}{3GM}. \tag{4.44}$$

This is shown by dot-dashed lines in the rightmost panel of Fig. 4.12. For $\mu = 0.9$, the external pressure is negligible and the two virial parameters are nearly identical. However, for $\mu = 0.3$, $\tilde{\alpha}_{\rm vir} \sim 1.4$, indicating that the clumps in this case are primarily confined by external pressure. While this is still larger than 1, eq. (4.44) is only an approximation, assuming a spherical clump with constant density and uniform external pressure. Properly accounting for the density profile within the clump tends to reduce the virial parameter compared to eqs. (4.43)-(4.44) (e.g., Mandelker et al., 2017). Given this, a value of $\tilde{\alpha}_{\rm vir} \sim 1.4$ is indicative of the clumps being in approximate virial equilibrium due to a combination of gravitational and pressure confinement.

Contrary to the strong dependence of clump properties on μ, their dependence on $(M_{\rm b}, \delta_{\rm c})$ at fixed μ is extremely weak. $M_{\rm c}$ and $\alpha_{\rm vir}$ vary by only a few percent as $\delta_{\rm c}$ varies from $6.7 - 100$ or $M_{\rm b}$ from $1 - 2.5$. Furthermore, clumps formed in simulations of pure GI, with $(M_{\rm b}, \delta_{\rm c}) = (0, 100)$ (see the Appendix §A.2), have masses only $\sim 10\%$ larger than those in simulations with $M_{\rm b} = 1$ for both $\mu = 0.9$ and 0.4. We conclude that once GI dominates over KHI and leads to clump formation, KHI has little effect on the resulting clump properties even if μ only slightly exceeds $\mu_{\rm cr}$.

To check convergence, we repeated the $(M_{\rm b}, \delta_{\rm c}, \mu) = (1.0, 100, 0.9)$ simulation with a factor two higher spatial resolution, and show the results in Fig. 4.12. No significant change was found in the number of clumps, their formation time, or their properties. The clump mass increases by $\lesssim 4\%$, while $\mathcal{M}_{\rm turb}$ and $\alpha_{\rm vir}$ are unchanged. We conclude that our fiducial resolution is sufficient to resolve the stream fragmentation and resulting clumps.

In summary, clumps forming in higher line-mass streams are more massive, have lower turbulent Mach numbers and lower virial parameters. This is primarily due to the larger degree of external pressure support for low line-mass streams present in the initial conditions, with a small contribution from enhanced mixing and dilution

in lower line-mass streams caused by more efficient KHI. At fixed μ, the variation of clump properties with $M_{\rm b}$ and $\delta_{\rm c}$ is very small. For $\mu = 0.9$, roughly 90% of the initial stream mass winds up in clumps, which following collapse are in approximate virial equilibrium at the thermal Jeans scale. For $\mu = 0.3$, only $\lesssim 50\%$ of the initial stream mass is in clumps, the rest having mixed into the background due to KHI. The collapsed clumps have $M_{\rm c} \sim (0.1 - 0.2) M_{\rm J}$, and are confined by external pressure. In all cases, the turbulent pressure in the collapsed clumps is negligible, with turbulent Mach numbers $\sim (0.1 - 0.3)$ for $\mu = (0.9 - 0.3)$.

4.5 Discussion

4.5.1 Astrophysical Applications

Our results on the combined evolution of KHI and GI in self-gravitating filaments have several astrophysical implications. In this section, we highlight potential applications for studies of star-forming filaments in the ISM and for cold streams feeding massive galaxies at high redshift.

High-z Intergalactic Streams

Massive galaxies with baryonic masses $\gtrsim 10^{11} {\rm M}_{\odot}$ at $z \sim (1 - 4)$ reside in halos with virial masses $M_{\rm vir} \gtrsim 10^{12} {\rm M}_{\odot}$. The CGM of these galaxies is thought to contain hot gas with $T \gtrsim 10^6\,{\rm K}$ in approximate hydrostatic equilibrium. However, the star-formation rates measured in these galaxies of $\gtrsim 100\, M_{\odot}\,{\rm yr}^{-1}$ is significantly larger than expected from the cooling of the hot CGM, and their prevalence exceeds that expected from mergers (Dekel et al., 2009a). As outlined in §4.1, such galaxies are fed by cold, $T \sim 10^4\,{\rm K}$ gas streams from the cosmic web, which efficiently penetrate the hot halo all the way to the central galaxy (Kereš et al., 2005; Dekel & Birnboim, 2006; Ocvirk et al., 2008; Dekel et al., 2009a; Ceverino et al., 2010; Faucher-Giguère

et al., 2011; van de Voort et al., 2011). The shearing against the hot CGM makes these streams susceptible to KHI. This has motivated several detailed studies of KHI in such systems, with $\delta \sim (30 - 100)$ and $M_{\rm b} \sim (0.5 - 2)$ (M16; P18; M19). As cosmological simulations lack the spatial resolution to properly resolve KHI in the streams, these studies have been idealized, accounting thus far only for non-radiative hydrodynamics without gravity.

These studies find that sufficiently narrow streams, with $R_{\rm s}/R_{\rm v} \lesssim (0.005 - 0.05)$ where $R_{\rm v}$ is the halo virial radius, will disrupt in the CGM before reaching the central galaxy. The threshold value of $R_{\rm s}$ depends on $(M_{\rm b}, \delta)$. However, our results suggest that in a certain regime of parameter space, self-gravity may stabilize streams and halt their disruption. Even if the line mass is very low compared to the critical value, $\mu \sim 0.1$, we find that buoyancy can prevent the shear layer from penetrating the inner stream (Figs. 4.7 and 4.8). For $\delta = 100$, we find that the penetration rate of the shear layer into the stream is reduced by a factor of $\gtrsim 3$ when self-gravity is included (Fig. 4.8). This implies that the previous estimates of the upper limit on the radius of streams that can disrupt in the CGM should be reduced by a similar factor, namely $R_{\rm s}/R_{\rm v} \lesssim (0.0015 - 0.015)$. Very narrow streams may thus survive the journey to the central galaxy, though they are likely to reach it somewhat wider and more diluted than they began.

M19 also found that typical streams can significantly decelerate in the CGM, dissipating $\sim (10 - 50)\%$ of their bulk kinetic energy before the central galaxy. If this energy is subsequently radiated away, it can significantly contribute to the Lyα emission observed in the CGM of massive high-z galaxies. Our results show that the self-gravity of the gas is unlikely to alter this conclusion, because the deceleration rates and the entrainment of background mass are unaffected (Figs. 4.8 and 4.10).

Other studies have suggested that at higher redshift, $z \gtrsim 5$, the streams feeding massive galaxies may be gravitationally unstable, with $\mu \sim 1$ (Mandelker et al., 2018).

These authors speculated that such streams could gravitationally fragment while still in the halo, and that this could lead to the formation of metal-poor globular clusters and stars directly in the halos of high-z galaxies. While this study did not account for KHI in the streams, our results suggest that this is unlikely to affect their conclusions, since for $\mu \sim 1$ and $M_{\rm b} \sim 1$, GI is unaffected by KHI (Figs. 4.11 and 4.12). We note that for cosmic web filaments far from haloes, only GI operates as no shear is expected.

ISM Filaments

As outlined in §3.1, numerous filametary structures are observed in the ISM, in particular in star-forming regions such as giant molecular clouds. While much attention has been payed to the gravitational stability and fragmentation of such filaments, these studies do not consider KHI induced by shearing motions between the filament and its surroundings. This is despite the fact that strong shearing motions and even signatures of KHI have been detected in molecular clouds and around filaments (e.g., Rodriguez-Franco et al., 1992; Berné et al., 2010; Berné & Matsumoto, 2012). Numerical simulations of molecular clouds in the central molecular zone have also revealed strong shearing motions which generate turbulence and reduce the SFR by a factor of ~ 7 compared to nearby clouds (Federrath et al., 2016). It is thus important to consider how KHI might affect the fragmentation of ISM filaments.

We note that in this case, the shearing motion is thought to be due to a background "wind" flowing across a roughly static filament, rather than a stream flowing through a static background. However, due to Galilean invariance, these two scenarios should behave identically.

The regions surrounding ISM filaments are often extremely turbulent, with turbulent Mach numbers of order 10 or higher, and the filaments themselves are often supervirial, with $\mu \gtrsim 1$. This is obviously very different from our initial conditions of a smooth filament in hydrostatic equilibrium (see §4.5.2). However, subvirial fil-

aments with $\mu < 1$ have been observed (Henshaw et al., 2016; Hacar et al., 2018, and references therein; Orkisz et al., 2019). In some cases, these low line-mass filaments host pre-stellar cores which are at least partly supported by external pressure (Kirk et al., 2017; Seo et al., 2018), consistent with GI in filaments with $\mu_{\rm cr} < \mu < 1$ (Fig. 4.12). If μ is known, this will constrain $\mu_{\rm cr}$, which in turn can be used to place constraints on the properties of the confining medium, and in particular on $M_{\rm b}$, the velocity of the shear flow between the filament and the background (Fig. 4.5).

Tidal Disruption Events

Stars that wander too close to a supermassive black hole, such as found in the centres of most massive galaxies, can be disrupted by the strong tidal forces exerted by the black hole (Rees, 1988). Following the disruption, the stellar debris often evolves into a gas stream which partly accretes onto the black hole producing a luminous flare. Following their formation, the tidal shear of the black hole renders these streams gravitationally stable, so bound clumps are unlikely to form along the stream. Furthermore, the streams can be treated as approximately in hydrostatic equilibrium in the cylindrically-radial direction (Coughlin & Nixon, 2015; Coughlin et al., 2016b,a). Recently, it has been argued that interactions between the debris stream and the ambient tenuous gas near the galactic centre can render such streams unstable to KHI, with nominal disruption times shorter than the infall timescale of the stream onto the black hole (Bonnerot et al., 2016). If true, this would significantly reduce the expected luminosity of the accretion flare. However, as we have shown, even in weakly self-gravitating streams, total stream disruption is significantly delayed due to buoyancy within the stream. This would mean that KHI in the streams below $\mu_{\rm cr}$ will be stopped by buoyancy, and the decrease in the flare-luminosity predicted by Bonnerot et al. (2016) may be overestimated. Such a scenario can be tested with dedicated simulations.

4.5.2 Caveats and Additional Physical Effects

While our analysis has focused on elucidating the interplay between KHI and GI in filaments, applications of our results to astrophysical scenarios require careful consideration of additional physical processes that have not yet been taken into account. These include the assumed isentropic initial conditions and lack of radiative cooling, the assumption of line mass ratios $\mu < 1$ and hydrostatic equilibrium in the initial conditions, the lack of magnetic fields, and (in the case of cold streams feeding massive galaxies at high redshift) the lack of a dark matter component to the gravitational potential. In this section, we speculate as to the possible effects of these processes, all of which will be explored in future work.

Radiative cooling is clearly very important for both ISM filaments and intergalactic gas streams. Both of these are expected to have cooling times much shorter than their sound crossing times, which is why they are often modeled as isothermal. Radiative cooling can either enhance or suppress KHI in the linear regime, depending on the slope of the cooling function and on the ratio of the cooling time in each fluid to the sound crossing time (Massaglia et al., 1992; Bodo et al., 1993; Vietri et al., 1997; Hardee & Stone, 1997; Xu et al., 2000). However, when these ratios are either much larger or much smaller than unity, the linear growth rates are similar to the adiabatic case at longitudinal wavelengths $\lambda \gtrsim R_{\rm s}$ (Mandelker et al., in prep.). Even in this case, cooling can substantially alter the nonlinear evolution of KHI (Vietri et al., 1997; Stone et al., 1997; Xu et al., 2000; Micono et al., 2000), though the net effect again depends on details of the cooling function and the stream parameters. Some authors have found that cooling leads to more violent disruption of the stream (Stone et al., 1997; Xu et al., 2000), while others have found that it prevents stream disruption by limiting the penetration of the shear layer into the stream (Vietri et al., 1997; Micono et al., 2000). If shear layer growth is suppressed and the contact discontinuity maintained, then $t_{\rm shear}$ will increase and $\mu_{\rm cr}$ will decrease (Fig. 4.4). Thus,

the regime where GI dominates over KHI will expand. Furthermore, it is also found that KHI in a cooling medium leads to much larger density fluctuations, and to the formation of dense knots and filaments inside the stream. These are likely to further enhance GI and filament fragmentation. Cooling is also likely to allow the clumps to collapse to higher densities and reach lower temperatures, thus decreasing their Jeans mass and leading to further fragmentation and collapse.

Magnetic fields are likely to be dynamically important in ISM filaments. This can have a stabilizing effect on GI, especially when $\mu < 1$ (e.g., N87, H98), and also on KHI, where magnetic fields parallel to the flow have been found to stabilise high-m modes and suppress shear layer growth (Ferrari et al., 1981; Birkinshaw, 1990). It is therefore unclear what the net effect will be in terms of the competition between these two processes, and this will likely depend sensitively on the properties of the field. For intergalactic gas streams at high redshift, magnetic fields are likely dynamically unimportant (e.g., Bagchi et al., 2002). Nevertheless, they may significantly weaken thermal conductivity and viscosity, which will influence the width of the shear layer (M19) and thus affect the instability. All these effects should be accounted for simultaneously in future work.

When considering intergalactic gas streams, we must also account for the contribution of the host dark matter filament to the gravitational potential. To our knowledge, the gravitational stability of a gas stream embedded in a dark matter filament has not been studied. The dark matter may stabilise the stream by making it more buoyant, or it may destabilise the stream by increasing the inward radial gravitational force, thus requiring non-thermal turbulent motions to support the stream against radial collapse. This may also suppress KHI by further limiting shear layer growth and stream disruption (see Figs. 4.7-4.8). The central dark matter halo into which the streams are flowing will also affect their evolution. The central potential focuses the stream into a conical shape with its radius decreasing towards the halo

centre, $R_{\rm s} \propto r$. (Dekel et al., 2009a; van de Voort & Schaye, 2012). This decreases the KHI timescales, which are proportional to $R_{\rm s}$ (eqs. 4.16-4.17). However, this focusing also increases the stream density, with $\rho \propto R_{\rm s}^{-2} \propto r^{-2}$, resulting in a decrease of the free-fall time, $t_{\rm ff} \propto \rho^{-1/2} \propto r$. Since $t_{\rm max} \propto t_{\rm ff}$, the ratio $t_{\rm max}/t_{\rm shear}$ is unlikely to vary significantly throughout the halo, as is the critical line-mass ratio, $\mu_{\rm cr}$. However, this must be studied in more detail, as must the effect of gravitational acceleration towards the halo centre on the evolution of KHI and GI in intergalactic cold streams.

Throughout our analysis, we assumed that filaments began in hydrostatic equilibrium, and without any internal non-thermal support such as turbulence or vorticity. This is unlikely to be the case for either ISM filaments or intergalactic streams. Theoretical studies of GI in ISM filaments growing self-consistently via radial accretion have shown that turbulence builds up inside the stream with Mach numbers of order unity and contributes to its support (Heitsch, 2013; Clarke et al., 2016, 2017; Heigl et al., 2018a). Despite this, the filament was found to fragment when its line mass reached the critical value for hydrostatic equilibrium, namely at $\mu \gtrsim 1$, in a similar manner to the $\mu < 1$ filaments considered here, leading to the formation of Jeans-scale clumps (Clarke et al., 2016, 2017). It is unclear how these results will change in the presence of KHI. Likewise, it has been suggested that accretion onto cosmic gas streams from the intergalactic medium creates specific profiles (Fillmore & Goldreich, 1984b; Birnboim et al., 2016), induces roughly sonic turbulence (Mandelker et al., 2018) and vorticity (Codis et al., 2012, 2015; Laigle et al., 2015), and grows streams to $\mu > 1$ (Mandelker et al., 2018). Such non-equilibrium effects must be considered in order to describe stream evolution.

4.6 Summary and Conclusions

Self-gravitating gaseous filaments are ubiquitous in astrophysics, from sub-pc filaments within the interstellar medium, to Mpc scale streams feeding galaxies along the cosmic web. As such, they may be subject to gravitational instability (GI), which leads to stream fragmentation and to the formation of long-lived, collapsed clumps along the stream axis. In many cases, such filaments are also susceptible to Kelvin-Helmholtz Instability (KHI) due to a shear flow against a confining background medium, which acts to mix the filament with the background fluid via a turbulent shear layer. Motivated by this, we have performed the first ever study of the evolution of a self-gravitating filament or stream undergoing KHI, using simple analytic models and hydrodynamic simulations. Such a system is characterised by three dimensionless parameters: the Mach number of the stream with respect to the sound speed in the (static) background, $M_{\rm b}$, the ratio of the central density in the stream to the background density outside the stream, $\delta_{\rm c}$, and the ratio of the mass-per-unit-length (line-mass) of the stream to the maximal line-mass for which initial hydrostatic equilibrium is possible, μ. The current analysis is restricted to filaments with $\mu < 1$ initially in hydrostatic equilibrium. Our main results can be summarised as follows:

1. The competition between GI and KHI is governed by the ratio of the timescale for linear growth of the fastest growing GI mode, $t_{\rm max}$, and the relevant nonlinear KHI timescale. When GI is dominated by surface modes, this is the time for the KHI-induced shear layer to expand to a size comparable to the stream radius and destroy the initial contact discontinuity, $t_{\rm shear}$. If $t_{\rm max}/t_{\rm shear} < 1$, GI causes the stream to fragment into long-lived clumps and suppresses mixing with the background medium. Likewise, if $t_{\rm max}/t_{\rm shear} > 1$, KHI mixes the stream with the background medium, dilutes its density and suppresses clump formation

(Fig. 4.4). Regardless, the stream is always unstable. When GI is dominated by body modes, clumps may form even when $t_{\rm max}$ is slightly longer than $t_{\rm shear}$, since the contact discontinuity no longer plays a role in GI.

2. The timescale criterion can be rephrased as a criterion on the line-mass ratio μ. If this is smaller than a critical value which depends on the Mach number and density contrast, $\mu_{\rm cr}(M_{\rm b}, \delta_{\rm c})$, then KHI will win and mix the stream and background. However, if $\mu > \mu_{\rm cr}(M_{\rm b}, \delta_{\rm c})$, the stream will fragment into long-lived, bound clumps. $\mu_{\rm cr}$ increases strongly with $M_{\rm b}$, and has a weak tendency to increase with $\delta_{\rm c}$ (Fig. 4.5). For $M_{\rm b} \lesssim 2.5$ we have $\mu_{\rm cr} \lesssim 0.5$. At larger Mach numbers, when KHI is dominated by high-order azimuthal surface modes, $\mu_{\rm cr} \lesssim 0.9$. In practice, values of $\mu_{\rm cr} > 0.9$ are not relevant, as GI body modes will cause clump formation even if $\mu \lesssim \mu_{\rm cr}$.

3. When $\mu < \mu_{\rm cr}$, the evolution of KHI outside the stream boundary is similar to the case of a non-gravitating uniform density stream, studied in detail by Mandelker et al. (2019). Self-gravity slows the expansion of the shear layer into the background by less than 20% for large μ, and significantly less than that for smaller μ (Fig. 4.8). Consequently, the stream deceleration due to entrainment of background mass in the shear layer is also unaffected, and follows the analytical prediction (Fig. 4.10).

4. However, gravity does qualitatively affect the penetration of the shear layer into the stream. At $t \gtrsim (2-3)t_{\rm sc}$, the penetration rate of the shear layer into the stream is slowed by a factor of $\gtrsim 3$ compared to the no-gravity case (Fig. 4.8). This is due to restoring buoyancy forces in the stream interior, corresponding to values of the Richardson number, Ri > 0.25 (Fig. 4.9). This significantly slows the final disruption of the stream by KHI, as a dense central core remains partly shielded against mixing (Fig. 4.7).

5. The clumps that form by GI when $\mu > \mu_{\rm cr}$ are largely unaffected by KHI. They are typically less massive than the Jeans mass, and supported partially by external pressure. However, as $\mu \to 1$ the clumps approach the Jeans mass and the external pressure support becomes negligible. In all cases, the internal turbulent motions are subsonic and turbulent pressure support is negligible, though the turbulent Mach number increases towards lower μ (Fig. 4.12). KHI seems to have a minor effect on the clump properties, which are largely insensitive to the Mach number of the flow, even in the static limit, $M_{\rm b} = 0$.

6. Our finding that self-gravity may shield the inner core of filaments from disruption by KHI, implies that recent studies of KHI in gas streams feeding massive galaxies at high-z may have overestimated the disruption of these streams in the CGM. However, the dissipation and deceleration rates should not be affected. Additionally, our finding that GI induced fragmentation only occurs when $\mu > \mu_{\rm cr}(M_{\rm b}, \delta_{\rm c})$ can be used to place constraints on the properties and kinematics of the confining medium surrounding low mass filaments in the ISM. However, in order to properly address these phenomena, additional physics such as radiative cooling, magnetic fields, external gravitational potential, and non-thermal turbulent motions, will have to be added to our models.

Chapter 5

Conclusions

5.1 Summary of Key Results

One of the new frontiers for studying the structure formation and cosmology lies in understanding the dark matter-gas-galaxy connection with highlights on the physics of ICM and CGM. The upcoming multi-wavelength cosmological surveys promise to provide unprecedented insights into the physical properties of dark matter, gas, and galaxies, ranging from the core to the outer most boundary of dark matter halos and opening up a new investigation of the transition region from the virialized region in the interior of the halos to the low-density cosmic webs. Cosmic accretion plays an important role in shaping the observable properties in the outskirts of dark matter and gaseous halos as well as fueling galaxy formation by feeding gas directly into the central region of the dark matter halos from the cosmic webs. In my thesis, I combine cosmological and idealized simulations to model both the small scale astrophysics and the cosmological structure formation processes and their connection to CGM and ICM. My main results are summarized as follows:

- In chapter 2, we modeled the distribution of the kinematically distinct infalling and orbiting populations of subhalos and halos using MDPL2 N-body simula-

tion. We showed that the two are mixed spatially all the way to $r_{\rm edge}$, which extends past the splashback radius defined by the drop in the spherically averaged density profile. This edge radius can be interpreted as a radius which contains a fixed fraction of the apocenters of dark matter particles. Our results highlighted the possibility of measuring the outer boundary of a dark matter halo using its phase space structure and provide a firm theoretical foundation to the satellite galaxy model used to characterize where the phase space distribution of SDSS redMaPPer clusters (Tomooka et al., 2020).

- In chapter 3, we investigated the locations of the outer boundaries of dark matter and gas around cluster-size dark matter haloes, by analyzing a sample of 65 massive dark matter halos extracted from the *Omega500* zoom-in hydrodynamical cosmological simulations. We showed that the location of accretion shock is offset from that of the dark matter splashback radius, contrary to the prediction of the self-similar models. The accretion shock radius is larger than all definitions of the splashback radius in the literature by $20\% - 100\%$. The accretion shock radius defined using the steepest drop in the entropy and pressure profiles is approximately 1.89 times larger than the splashback radius defined by the steepest slope in the dark matter density profile, and it is ≈ 1.2 times larger than the edge of the dark matter phase-space structure. We discussed implications of our results for multi-wavelength studies of galaxy clusters.

- In chapter 4, we studied the nonlinear evolution of KHI in pressure-confined self-gravitating gas streams initially in hydrostatic equilibrium, using analytic models and hydrodynamic simulations, not including radiative cooling. We derived a critical line-mass, or mass per unit length, as a function of the stream Mach number and density contrast with respect to the background, $\mu_{\rm cr}(M_{\rm b}, \delta_{\rm c}) \leq 1$, where $\mu = 1$ is normalized to the maximal line mass for which initial hydrostatic

equilibrium is possible. For $\mu < \mu_{\rm cr}$, KHI dominates the stream evolution. A turbulent shear layer expands into the background and leads to stream deceleration at a similar rate to the non-gravitating case. However, with gravity, penetration of the shear layer into the stream is halted at roughly half the initial stream radius by stabilizing buoyancy forces, significantly delaying total stream disruption. Streams with $\mu_{\rm cr} < \mu \leq 1$ fragment and form round, long-lived clumps by gravitational instability (GI), with typical separations roughly 8 times the stream radius, similar to the case without KHI. When KHI is still somewhat effective, these clumps are below the spherical Jeans mass and are partially confined by external pressure, but they approach the Jeans mass as $\mu \to 1$ and GI dominates. We discussed potential applications of our results to streams feeding galaxies at high redshift, filaments in the ISM, and streams resulting from tidal disruption of stars near the centres of massive galaxies.

5.2 Future Research Directions & Prospects

My research represents one of the first work for understanding the physics of galaxy and cluster formation. Below, I outline several future research directions and prospects for advancing this work further in the coming years, with highlights on new sciences that will be enabled by combing computational modeling and big data from large astronomical surveys.

5.2.1 Precision Modeling of the Phase Space Structure of the Dark Matter Halo

Our results open the path to accurately modeling the projected phase space structure of the dark matter halos as the orbiting, infalling and interloping galaxies will have different kinematics. By applying such models to the measurements of line-of-sight ve-

locities of galaxies from future spectroscopic surveys (such as DESI, PFS, SPHEREx), one can significantly improve the dynamical mass estimates of galaxy clusters as well as cosmological constraints e.g., on modified gravity and Hubble parameter.

Dynamical Mass Calibration: Dynamical distinct orbiting, infalling and interloping galaxies will produce distinct distributions in the projected phase space structure of dark matter halos. Accurate modeling of these populations will allow us to measure dynamical mass without interlopers, one of the key systematics in dynamical mass calibration. There are several sources of systematics that will introduce bias in the velocity dispersion profiles and dispersion-radius relations calibrated from the N-body simulations. The interaction of the galaxies and the cluster environment introduces velocity bias due to baryonic effects. Studies of galaxies in hydrodynamic simulations show that there is radial dependent velocity bias (Lau et al., 2010; Wu et al., 2013). Selection effects on galaxies also introduce bias as dark matter mass of the galaxies gradually decrease due to tidal stripping while the stellar mass remain relatively constant (Ye et al., 2017; Armitage et al., 2017). Even though we expect that the impact of the baryonic effects and cluster environments will be small for infalling galaxies, detailed characterization of the impact of baryonic effects on the velocity biases of infalling and orbiting galaxies will allow us to quantify the robustness in using velocity dispersion as a proxy for the edge radius measurements. In addition, velocity dispersion-mass relation has a weak dependence on cosmology (Evrard et al., 2008). Quantifying the effects of cosmology and astrophysics on dispersion-radius and dispersion-mass relation is a key important step to utilize the phase space and edge radius as a cosmological probe.

Cluster selection based on optical richness biases the splashback radii measurements based on galaxy density profiles because the cluster selection algorithm uses the galaxy number density to select clusters, which is the same signal the splashback feature is measured on (Zu et al., 2017; Busch & White, 2017). Thus, we expect

smaller bias by using different mass proxies for cluster selection, such as X-ray and SZ catalogs. Further studies should calibrate the exact systematic uncertainties introduced by different selection functions in details to estimate the impact on the dynamical measurements.

Modified Gravity: While the ΛCDM model of the universe provides several predictions which are confirmed, the lack of direct detection of dark matter and dark energy prompts alternative proposals. One such alternative model to ΛCDM model is to modify the gravity from general relativity on large scales instead of introducing the dark energy Λ. Such modified gravity models should match the observed large scale signatures for cosmic expansion while simplifying to general relativity on small scales to account for the observations in the solar system. To match the observations on both scales, these models utilize non-linear screening mechanisms so that the gravitational force will revert back to the general relativity on small scales such as the solar system (e.g., chameleon screening in $f(R)$ gravity (Hu & Sawicki, 2007) and Vainshtein screening in GDP model, (Dvali et al., 2000)). The stronger gravitational force in the modified gravity enhances the velocities of the infalling objects around the clusters. Thus, the phase space of the cluster outskirts provide important signatures of the modified gravity (see fig. 5.1, Lam et al., 2012; Zu et al., 2014). By comparing the cluster masses measured directly through lensing to those measured from dynamical estimates as the two masses will differ in many modified gravity models compared to GR, one can constrain the modified gravity models (Zhang et al., 2007; Reyes et al., 2010). Modified gravity also causes differences in the splashback features in halo density profiles at the cluster outskirts as the splashback radius is a direct consequence of the infall mechanisms (Adhikari et al., 2018). However, these measurements have large systematic uncertainties compared to the effect of modified gravity as the presence of interlopers biases the dynamical mass estimates, while the splashback feature in the observed clusters depend strongly on cluster selection func-

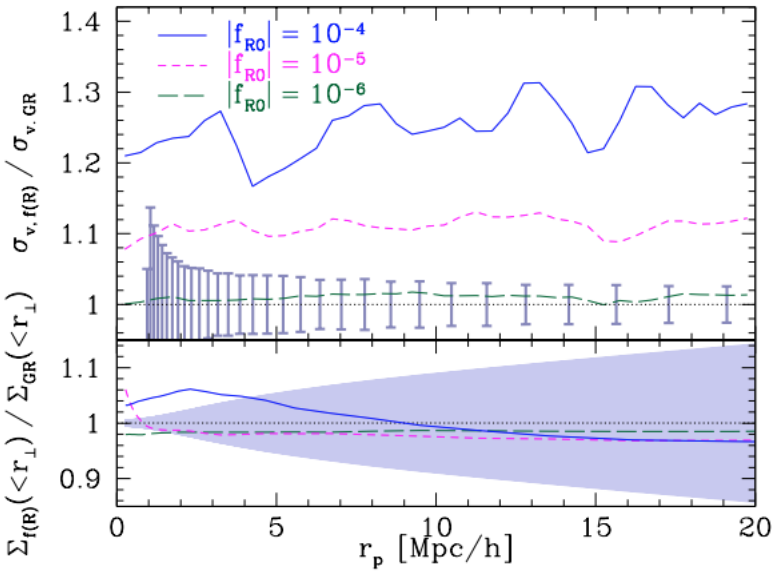

Figure 5.1: *Upper panel:* Ratio of the velocity dispersion along the line of sight measured around halos with $M_{200\mathrm{m}} > 10^{14} M_\odot/h$ in f(R) simulations to that measured around halos of the same mass in ΛCDM simulations. The error bars are estimated from the simulations for a spectroscopic survey of 2000 sq. degrees. *Lower panel:* Ratio of the enclosed projected mass profiles of the same halos in f(R) and ΛCDM simulations. This is approximately what stacked lensing would measure. The shaded region indicates the range of statistical uncertainties for an imaging survey of the same area. Image source: Lam et al. (2012)

tions. Our improved phase model will provide us unbiased measurements of infall velocity distributions and dynamical mass estimates needed to constrain modified gravity. The shock feature in gas will also provide us an independent constraint to the splashback feature to account for systematic uncertainties.

Hubble Constant: Recent analysis has shown that the next generation of spectroscopic survey, DESI, can obtain highly precise measurement of Hubble constant with a statistical uncertainty of $< 1.3\%$ (Wagoner et al., 2021). Figure 5.2 shows the resulting confidence contours for the matter density and Hubble parameter possible from DESI. This level of precision is easily sufficient for resolving the $\approx 9\%$ difference between the Hubble constant estimate from the Planck and SH0ES collaborations. The estimation of Hubble parameter requires precise determination of the distance–velocity disper-

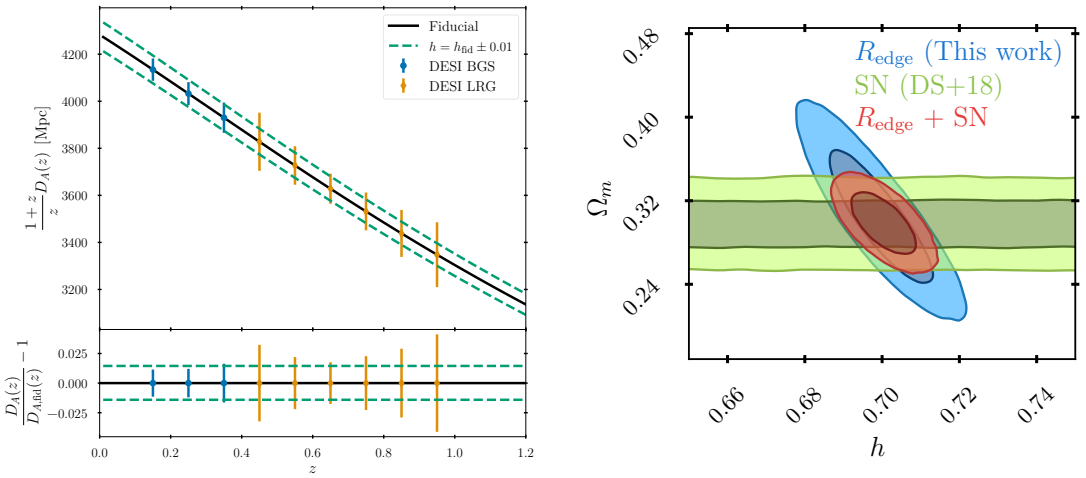

Figure 5.2: *Left Panel:* Forecasted Hubble diagram using the DESI spectroscopic data set (Wagoner et al., 2021). Blue and orange points are derived using galaxies from the Bright Galaxy Survey and Luminous Red Galaxy samples respectively. The solid line is our fiducial model, whereas the parallel dashed green lines correspond to changing the Hubble constant by $\Delta h = 0.01$. The bottom panel shows the residuals of the best fit model, from which it is immediately evident that DESI can constrain the Hubble parameter with high precision. *Right Panel:* 68% and 95% confidence contours in the $\Omega_{\rm m}$ and h plane, as constrained by the Hubble diagram in the left panel assuming a flat ΛCDM model. Including the prior on the matter density parameter $\Omega_{\rm m}$ from the Pantheon supernova sample (Scolnic et al., 2018) significantly improves the constraint on the Hubble parameter, from $h = 0.700 \pm 0.009$ to $h = 0.700 \pm 0.005$. Note that the central values in this forecast are arbitrary.

sion scaling relation from the simulations. Further work should carefully calibrate the cosmological and astrophysical dependence of dispersion-radius scaling relation in order to assess the accuracy to which Hubble constant can be measured.

5.2.2 The Physics of Penetrating Gas Streams in CGM

CGM provides a laboratory to study the inflow and outflow of gas, the origin of the multiphase structure and the star formation history of the galaxies. Gas streams penetrating the CGM can carry the cold gas from the cosmic filaments to fuel the star formation in central galaxy at high redshift galaxies and produce observed properties of CGM. However, current idealized simulations only take into account a small subset

of properties actually in play. Cooling in spherical gas clouds can extend the survival time of cool clouds travelling through a hot background due to condensation of hot gas onto the cloud tail (Gronke & Oh, 2018, 2020). Similarly, follow up study on cold gas stream in hot halo gas using idealized simulations show that cooling can extend the penetration depth of cold streams feeding galaxies if the cooling time in shear layer is shorter than the time for shear layer to grow (Mandelker et al., 2020a). Analytical predictions in Mandelker et al. (2020b) also show that the radiative energy from the cold stream can power the Lyman-α blobs with luminosity $> 10^{43}\mathrm{erg\,s^{-1}}$, observed in CGM (Cantalupo et al., 2019). While these studies provide promising results, there are several missing physical effects in order to fully understand the role of gas streams on the physics of CGM and star formation.

- **Cooling and self-gravity:** Initial analytical estimates show that self-gravity can lead to the collapse and fragmentation of streams, within a virial crossing time thus leading to star-formation within the CGM (Mandelker et al., 2018). Detailed studies of self-gravity on the stream reveal that there are weak-gravity regimes where the self-gravity can stabilise the stream against KHI limiting the maximum mixing layer in the stream to half the stream radius, while in strong-gravity regime, the stream collapses and fragments into clumps. Cooling of gas will lead the clumps to collapse further potentially leading to star-formation in these fragmented clumps. Detailed studies of the combined effects of the cooling and gravity will illuminate the details of the stability criterion of the stream under cooling and self-gravity, the properties of the clumps formed, and potentially provide theoretical grounds for globular clusters as well as clumps and overdensities observed in Lyman-α nebulae.

- **Magnetic Field:** The addition of magnetic field can suppress growth of mixing layer (Ferrari et al., 1981) as well as stabilise the effects of self-gravity by adding external pressure support (Nagasawa, 1987). Thus, it is unclear what the net

effect of magnetic field will be in terms of the competition between KHI and self-gravity. Step-by-step studies of the effects of magnetic field by running simulations of magnetic field+cooling, magnetic field+self-gravity, and all three effects combined will illuminate how magnetic fields affect the stream stability and clump formation process and how it interacts with different instabilities.

- **Halo Potential:** The gravitational potential of the halo the stream is penetrating not only accelerates the infalling gas, but also provides a pressure gradient in the CGM. As a result, the infalling stream will get narrower as the gravitational potential is deeper, significantly changing the stream geometry. Such effort to simulate the stream under halo potential is currently underway. The simulation will be combined together with magnetic field, cooling, and self-gravity with the eventual goal of accurately modeling the gas stream in CGM, while the step-by-step process in adding one process at a time allows us to pinpoint what physics are at play in the final evolution of the col gas stream.

While idealized simulations cold gas streams reveal a wealth of insights into the evolution of the stream, understanding the star formation and the connection to the physics of CGM require simulations where cold gas streams directly interact with CGM. Latest advancement in technologies allow us to resolve the cooling length and KHI necessary to study the gas streams in CGM in cosmological simulations (e.g., van de Voort et al., 2019). Using cosmological simulations which can resolve the physical processes studied in idealized simulations, one should study (1) the properties of clumps formed from the fragmentation of stream, and how it can impact star formation and formation of dark matter less clumps, (2) the momentum and kinetic energy of the stream as they reach the galactic disk, and how much angular momentum and turbulence they can deposit, and (3) the radiative energy loss and the comparison to the observed Lyman-α emissions.

5.2.3 Modeling the Dark Matter and Gaseous Halos for Multi-wavelength Surveys

Our studies define the halo boundary and the lack of baryonic effects on them. However, baryonic effects significantly impact the measurements of the inner structure of the clusters and galaxies. Recent measurements of lensing signal probing the underlying density profile also show that the observed signal is lower than what is expected from halo models (Leauthaud et al., 2017). The tension can be either due to baryonic effects and other systematics or provide a basis for new physics. This opens up the possibility of constraining the baryonic effects with tSZ measurements in order to constrain the systematics on weak lensing signal (Amodeo et al., 2021). In addition, cross-correlation between tSZ and WL signal is a powerful tool for constraining cosmology and astrophysics (e.g., Van Waerbeke et al., 2014; Hill & Spergel, 2014; Osato et al., 2018, 2020). Cross-correlation analysis allows us to probe large-scale structure controlled by underlying cosmology and gravity as well as small-scale influenced by baryonic physics together to improve the cosmology constraint by a factor of 3 to 4 (Reid et al., 2014; Zhai et al., 2019). Future surveys will have better detection limits increasing the number of low-mass halos forming a significant part of the cross-correlation signal (Hojjati et al., 2015) and increased resolution allowing us to probe smaller scales where baryonic physics such as feedback of active galactic nuclei(AGN) and supernova can affect not only the gas but also the dark matter WL signal (Semboloni et al., 2011; Huang et al., 2019).

Probing dark matter halos with combined multi-wavelength data through cross-correlation requires a consistent model of gas and dark matter. The models start by parametrizing the dark matter and gas profiles for the virialized halo, 1-halo term (e.g., Komatsu & Seljak, 2001; Shaw et al., 2010; Flender et al., 2017). The model extends to large scale by adding a 2-halo term, which assumes that any additional dark matter and gas found outside the primary halo are due to other halos of different

masses distributed in the space. Our result provides a natural boundary for the transition between 1-halo and 2-halo term (Garcia et al., 2020). Future studies should focus on (1) taking into account the baryonic effects on dark matter profiles, which in turn affect the small scale power spectrum (Schneider & Teyssier, 2015; Schneider et al., 2019), and (2) extending to aspherical models of the halo to account for the effects of triaxiality (Chen et al., 2019).

Appendix A

A.1 Radial Velocity Distribution

The previous model of the dark matter phase space structure by ZW13 uses the combination of a Gaussian distribution and a t-distribution to model both the radial and tangential velocities[1]:

$$\mathrm{PDF}(v_r, r) = f_{\mathrm{orb}} G(v_r, \mu, \sigma_1) + (1 - f_{\mathrm{orb}}) t\left(\frac{v_r - \mu_{\mathrm{inf}}}{\sigma_{\mathrm{inf}}}, \nu\right). \tag{A.1}$$

Figure A.1 shows the distribution of radial velocity in the radial bin of $r = [0.6 - 0.7]r_{200\mathrm{m}}$, along with our fits as well as ZW13 model. We find that the ZW13 model fails to capture the infall stream under the t-distribution. Instead, there exists an extra second Gaussian component with a negative radial velocity. If this component is not properly taken into account, it causes underestimation of the orbiting fraction inside the halo.

Figure A.2 shows the radial dependence of the various parameters obtained by fitting our new model described in eq. (2.1) to the radial velocity distribution of subhalos. The orbiting parameters also vary monotonically with radius. Specifically, the difference between the mean of two distributions disappears as it approaches

1. ZW13 uses skewed t-distribution. However, the skewness disappears in the innermost radii, where the orbiting fraction of ZW13 and our model disagrees. Hence, a normal t-distribution suffices.

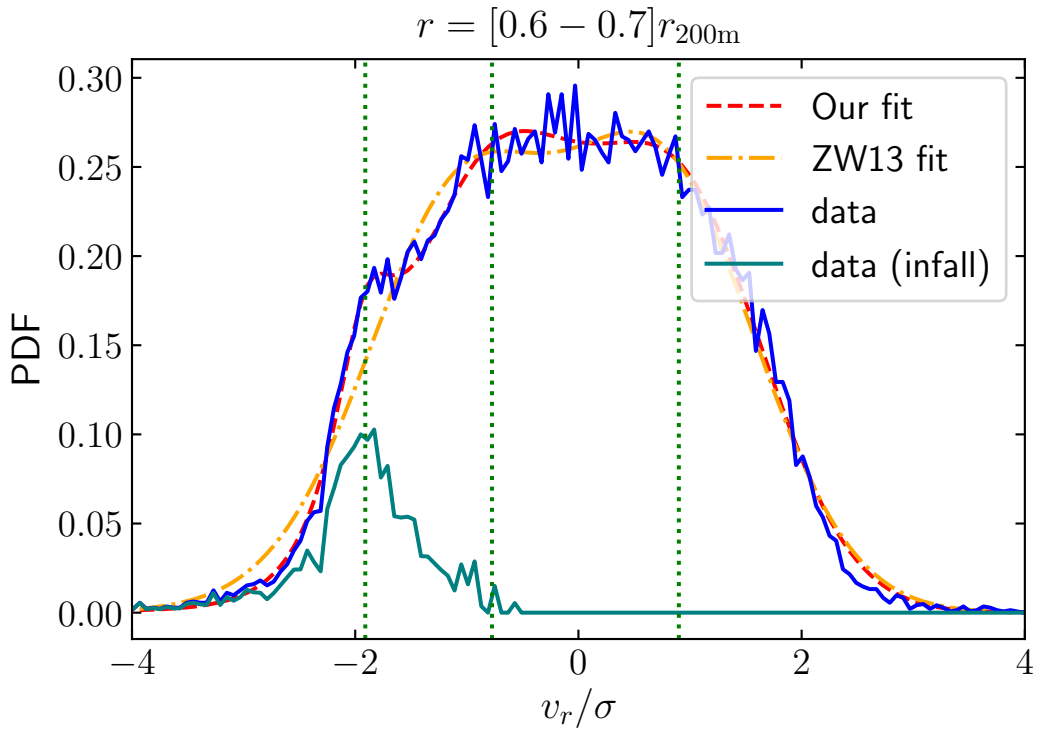

Figure A.1: The distribution of radial velocities of all subhalos for the radial bin of $r = [0.6 - 0.7]r_{200\mathrm{m}}$ and of infalling subhalos, which have not had a pericentric passage. Our best-fit model based on the eq. (2.1) is indicated with the red-dashed curve. The vertical lines indicate 3 means of the distributions, with the leftmost line indicating the infalling stream, while the other two indicate the means of orbiting Gaussian components. Employing ZW13 model with varying mean for Gaussian fails to capture the infall stream using the t-distribution.

the edge radius. The median of the infalling distribution decreases monotonically as enforced, while the scale parameter is approximately constant. We found that the fitted degree of freedom $\nu \approx 2.2$ is approximately the same outside the halo, but starts to gradually increase at $r \lesssim 1.5r_{200\mathrm{m}}$ and hits the upper bound of the prior at $r \lesssim 0.5r_{200\mathrm{m}}$. Our results agree with ZW13 outside the halo, which is expected as the only difference in our model is the distribution of the orbiting population. However, inside the halo, the degree of freedom ν approaches ∞, and the distribution becomes Gaussian at smaller radii than the radius ZW13 model predicts. Our model accurately captures the phase space structure associated with the infalling stream.

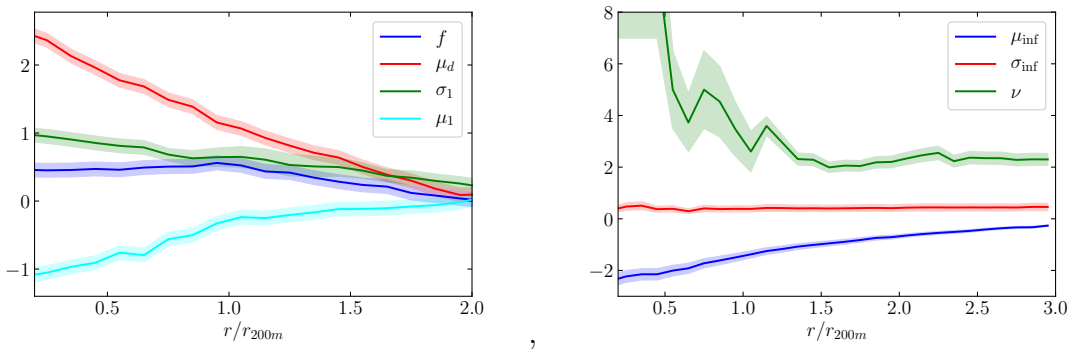

Figure A.2: The radial dependence of the fitted parameters based on the two Gaussians *(top panel)* and the t-distribution *(bottom panel)*. The parameter σ_2 is skipped for clarity in the figure and is approximately the same as σ_1. The error band is the standard deviation of the MCMC posterior.

A.2 GI Growth Rates and Surface Vs Body Modes

For an incompressible pressure-confined cylinder, the linear growth-time of the fastest growing GI mode is given by eq. (4.11), based on H98. In our case, however, the stream is highly compressible and its density can be far from constant (Fig. 4.3), so it is unclear whether eq. (4.11) remains valid. On the other hand, for isothermal cylinders confined by a zero density background, the ratio $t_{\rm max}/t_{\rm ff}$ does not vary much with line-mass (N87). If the same is true for a non-isothermal cylinder confined by an arbitrary density background, then eq. (4.11) may also apply to our case. To test this, we performed simulations with self-gravity but without shear flow, $M_b = 0$, and with a single perturbation wavelength, $\lambda = 1/4 = 8R_{\rm s}$. We examined two different values of the line-mass, $\mu = 0.4$ and 0.9, with $\delta_{\rm c} = 100$. Based on the analysis of N87, the former is expected to be unstable to surface modes, while the latter to body modes.

Fig. A.3 shows the perturbation amplitude as a function of time, measured in each simulation at both the surface of the stream and along its axis. The former is defined

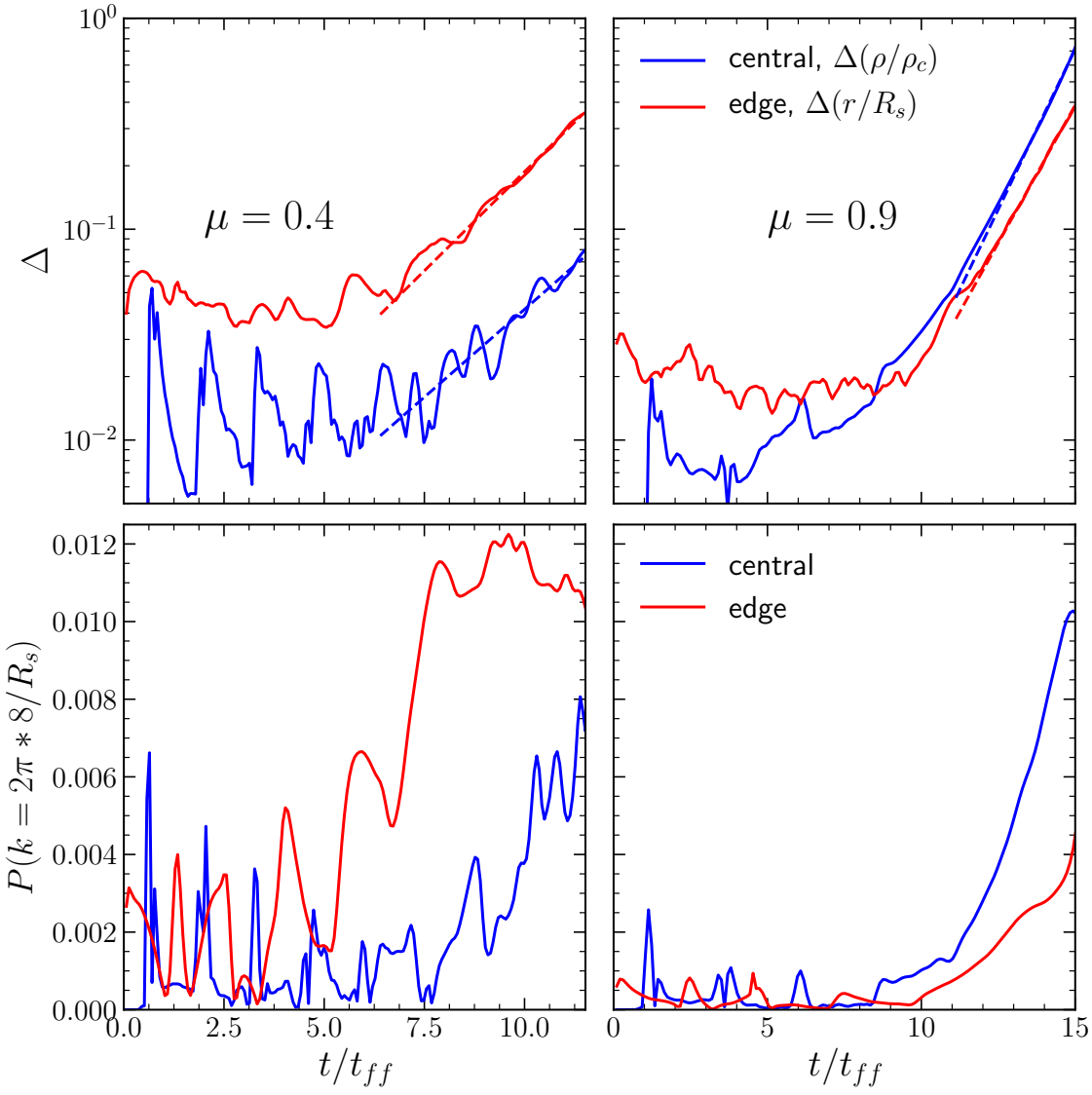

Figure A.3: Growth of a single wavelength perturbation, $k = 2\pi \times 8/R_s$, due to GI in simulations with line-mass $\mu = 0.4$ (left) and 0.9 (right). *Top panels:* the perturbation amplitude Δ, measured as the rms density fluctuations along the stream axis (blue lines, eq. (A.2)) or as the deformation of the stream-background interface (red lines, eq. (A.3)). Both definitions yield similar evolution. After a perturbation sound crossing time, the perturbations grow exponentially, with best fit exponential growth rates, shown by dashed lines, within $\lesssim 10\%$ of those predicted by H98. *Bottom panels:* the power of the density perturbation at the perturbed wavelength, $\lambda = 8R_s$, measured along the stream axis (blue lines) and near the stream edge (red lines). For $\mu = 0.4$ (0.9) perturbations near the edge (centre) contain more power and grow faster. This is consistent with $\mu = 0.4$ (0.9) being a surface (body) mode.

by the deformation of the stream-background interface,

$$\Delta\left(r/R_s\right) = \left(\max - \min\right)\left(r/R_s\right), \tag{A.2}$$

where r specifies the radius at which the tracer variable $\psi = 0.5$. For the perturbation along the stream axis we use the density

$$\Delta\left(\rho/\rho_c\right) = \mathrm{rms}\left[\rho(t, r=0)/\rho_c - 1\right]. \tag{A.3}$$

As can be seen in the top panels of Fig. A.3, these two measurements of the perturbation amplitude yield similar growth rates. At $t \lesssim 7t_{\rm ff}$, the perturbation amplitude is roughly constant. This is approximately four times the stream sound crossing time, $t_{\rm sc} \propto 2R_{\rm s}/c_{\rm s}$ (see eq. 4.41 and Table 4.1), which is the sound crossing time of the perturbation wavelength, $\lambda = 8R_{\rm s}$. This is the coherence time of the perturbation, during which the initial velocity perturbation is converted into a growing eigenmode of the system (see M16 and M19 for a discussion of a similar phenomenon in KHI). At later times the perturbation amplitude is well fit by $\Delta \propto \exp\left(\omega t\right)$. The best fit growth rates are $\omega_{\rm fit} \approx 0.96\omega_{\rm Hunter}$ for $\mu = 0.4$, and $\omega_{\rm fit} \approx 0.90\omega_{\rm Hunter}$ for $\mu = 0.9$, where the profile deviates further from the constant density assumption in H98. We conclude that the growth time for GI can be approximated by the H98 dispersion relation even for large values of the line-mass, μ.

The bottom panels compare the 1-D power spectra of density perturbations along the stream axis, at $r = 0$, and near its edge, at $r \lesssim R_{\rm s}$. We show here the power measured at the wavelength $8R_s$, but note that the results are nearly identical when showing the total power, as power at all other scales is small. For $\mu = 0.4$, the power near the stream edge is larger, while the opposite is true for $\mu = 0.9$, consistent with these two simulations corresponding to surface and body modes, respectively.

Bibliography

Abadi M. G., Moore B., Bower R. G., 1999, Ram pressure stripping of spiral galaxies in clusters, Monthly Notices of the Royal Astronomical Society, 308, 947

Abazajian K. N., et al., 2016, CMB-S4 Science Book, First Edition, arXiv e-prints, p. arXiv:1610.02743

Ade P., et al., 2019, The Simons Observatory: science goals and forecasts, Journal of Cosmology and Astroparticle Physics, 2019, 056

Adhikari S., Dalal N., Chamberlain R. T., 2014, Splashback in accreting dark matter halos, Journal of Cosmology and Astroparticle Physics, 11, 19

Adhikari S., Dalal N., Clampitt J., 2016, Observing dynamical friction in galaxy clusters, Journal of Cosmology and Astroparticle Physics, 2016, 022

Adhikari S., Sakstein J., Jain B., Dalal N., Li B., 2018, Splashback in galaxy clusters as a probe of cosmic expansion and gravity, Journal of Cosmology and Astroparticle Physics, 2018, 033

Agertz O., et al., 2007, Fundamental differences between SPH and grid methods, Monthly Notices of the Royal Astronomical Society, 380, 963

Aihara H., et al., 2018, The Hyper Suprime-Cam SSP Survey: Overview and survey design, Publications of the Astronomical Society of Japan, 70, S4

Akeson R., et al., 2019, The Wide Field Infrared Survey Telescope: 100 Hubbles for the 2020s, arXiv e-prints, p. arXiv:1902.05569

Allen S. W., Schmidt R. W., Fabian A. C., 2002, Cosmological constraints from the X-ray gas mass fraction in relaxed lensing clusters observed with Chandra, Monthly Notices of the Royal Astronomical Society, 334, L11

Allen S. W., Schmidt R. W., Ebeling H., Fabian A. C., van Speybroeck L., 2004, Constraints on dark energy from Chandra observations of the largest relaxed galaxy clusters, Monthly Notices of the Royal Astronomical Society, 353, 457

Amodeo S., et al., 2021, Atacama Cosmology Telescope: Modeling the gas thermodynamics in BOSS CMASS galaxies from kinematic and thermal Sunyaev-Zel'dovich measurements, Physical Review D, 103, 063514

Anderson M. E., Bregman J. N., 2011, Detection of a Hot Gaseous Halo around the Giant Spiral Galaxy NGC 1961, Astrophysical Journal, 737, 22

Anderson M. E., Bregman J. N., Dai X., 2013, Extended Hot Halos around Isolated Galaxies Observed in the ROSAT All-Sky Survey, Astrophysical Journal, 762, 106

André P., et al., 2010, From filamentary clouds to prestellar cores to the stellar IMF: Initial highlights from the Herschel Gould Belt Survey, Astronomy and Astrophysics, 518, L102

André P., Di Francesco J., Ward-Thompson D., Inutsuka S.-I., Pudritz R. E., Pineda J. E., 2014, From Filamentary Networks to Dense Cores in Molecular Clouds: Toward a New Paradigm for Star Formation, Protostars and Planets VI, pp 27–51

Anninos W. Y., Norman M. J., 1994, Nonlinear Hydrodynamics of Cosmological Sheets. I. Numerical Techniques and Tests, Astrophysical Journal, 429, 434

Armitage T. J., Barnes D. J., Kay S. T., Bahé Y. M., Dalla Vecchia C., Crain R. A., Theuns T., 2017, The Cluster-EAGLE project: velocity bias and the velocity dispersion - mass relation of cluster galaxies, preprint, (arXiv:1708.00508)

Arnaud M., Pratt G. W., Piffaretti R., Böhringer H., Croston J. H., Pointecouteau E., 2010, The universal galaxy cluster pressure profile from a representative sample of nearby systems (REXCESS) and the Y_{SZ} - M_{500} relation, Astronomy and Astrophysics, 517, A92

Arrigoni Battaia F., Prochaska J. X., Hennawi J. F., Obreja A., Buck T., Cantalupo S., Dutton A. A., Macciò A. V., 2018, Inspiraling halo accretion mapped in Ly α emission around a z $\sim$ 3 quasar, Monthly Notices of the Royal Astronomical Society, 473, 3907

Arzoumanian D., et al., 2011, Characterizing interstellar filaments with Herschel in IC 5146, Astronomy and Astrophysics, 529, L6

Aung H., Nagai D., Rozo E., García R., 2021, The phase-space structure of dark matter haloes, Monthly Notices of the Royal Astronomical Society, 502, 1041

Bagchi J., Ensslin T. A., Miniati F., Stalin C. S., Singh M., Raychaudhury S., Humeshkar N. B., 2002, Evidence for shock acceleration and intergalactic magnetic fields in a large-scale filament of galaxies ZwCl 2341.1+0000, New Astronomy, 7, 249

Balogh M. L., Navarro J. F., Morris S. L., 2000, The Origin of Star Formation Gradients in Rich Galaxy Clusters, Astrophysical Journal, 540, 113

Banerjee R., Vázquez-Semadeni E., Hennebelle P., Klessen R. S., 2009, Clump morphology and evolution in MHD simulations of molecular cloud formation, Monthly Notices of the Royal Astronomical Society, 398, 1082

Bartelmann M., Schneider P., 2001, Weak gravitational lensing, Physics Reports, 340, 291

Bassett G. M., Woodward P. R., 1995, Simulation of the instability of Mach 2 and Mach 4 gaseous jets in two and three dimensions, Astrophysical Journal, 441, 582

Battaglia N., et al., 2019, Probing Feedback in Galaxy Formation with Millimeter-wave Observations, Bulletin of the American Astronomical Society, 51, 297

Baxter E., et al., 2017, The Halo Boundary of Galaxy Clusters in the SDSS, Astrophysical Journal, 841, 18

Baxter E. J., Adhikari S., Vega-Ferrero J., Cui W., Chang C., Jain B., Knebe A., 2021, Shocks in the stacked Sunyaev-Zel'dovich profiles of clusters I: Analysis with the Three Hundred Simulations, Monthly Notices of the Royal Astronomical Society,

Behroozi P. S., Wechsler R. H., Wu H.-Y., 2013a, The ROCKSTAR Phase-space Temporal Halo Finder and the Velocity Offsets of Cluster Cores, Astrophysical Journal, 762, 109

Behroozi P. S., Wechsler R. H., Conroy C., 2013b, On the Lack of Evolution in Galaxy Star Formation Efficiency, Astrophysical Journal, Letters, 762, L31

Behroozi P. S., Wechsler R. H., Wu H.-Y., Busha M. T., Klypin A. A., Primack J. R., 2013c, Gravitationally Consistent Halo Catalogs and Merger Trees for Precision Cosmology, Astrophysical Journal, 763, 18

Behroozi P. S., Wechsler R. H., Conroy C., 2013d, The Average Star Formation Histories of Galaxies in Dark Matter Halos from z = 0-8, Astrophysical Journal, 770, 57

Bender R., Burstein D., Faber S. M., 1992, Dynamically Hot Galaxies. I. Structural Properties, Astrophysical Journal, 399, 462

Berger M. J., Oliger J., 1984, Adaptive Mesh Refinement for Hyperbolic Partial Differential Equations, Journal of Computational Physics, 53, 484

Berné O., Matsumoto Y., 2012, The Kelvin-Helmholtz Instability in Orion: A Source of Turbulence and Chemical Mixing, Astrophysical Journal, Letters, 761, L4

Berné O., Marcelino N., Cernicharo J., 2010, Waves on the surface of the Orion molecular cloud, Nature, 466, 947

Bertone G., Hooper D., 2018, History of dark matter, Reviews of Modern Physics, 90, 045002

Bertschinger E., 1985, Self-similar secondary infall and accretion in an Einstein-de Sitter universe, Astrophysical Journal, Supplement, 58, 39

Birkinshaw M., 1984, The Kelvin-Helmholtz instability for relativistic particle beams. I - Stability analyses in the time and space domains for vortex-sheet flows, Monthly Notices of the Royal Astronomical Society, 208, 887

Birkinshaw M., 1990, The Stability of Jets. in Beams and Jets in Astrophysics, ed. P.A. Hughes, Cambridge University Press, Chapter 6.

Birnboim Y., Dekel A., 2003, Virial shocks in galactic haloes?, Monthly Notices of the Royal Astronomical Society, 345, 349

Birnboim Y., Padnos D., Zinger E., 2016, The Hydrodynamic Stability of Gaseous Cosmic Filaments, Astrophysical Journal, Letters, 832, L4

Bocquet S., et al., 2015, Mass Calibration and Cosmological Analysis of the SPT-SZ Galaxy Cluster Sample Using Velocity Dispersion σ_v and X-Ray Y $_X$ Measurements, Astrophysical Journal, 799, 214

Bodo G., Massaglia S., Rossi P., Trussoni E., Ferrari A., 1993, Kelvin-Helmholtz instabilities in radiating flows, Physics of Fluids, 5, 405

Bodo G., Rossi P., Massaglia S., Ferrari A., Malagoli A., Rosner R., 1998, Three-dimensional simulations of jets, Astronomy and Astrophysics, 333, 1117

Bogey C., Marsden O., Bailly C., 2011, Large-eddy simulation of the flow and acoustic fields of a Reynolds number 10^5 subsonic jet with tripped exit boundary layers, Physics of Fluids, 23, 035104

Bond J. R., Kofman L., Pogosyan D., 1996, How filaments of galaxies are woven into the cosmic web, Nature, 380, 603

Bonnerot C., Rossi E. M., Lodato G., 2016, Bad prospects for the detection of giant stars' tidal disruption: effect of the ambient medium on bound debris, Monthly Notices of the Royal Astronomical Society, 458, 3324

Bonnor W. B., 1956, Boyle's Law and gravitational instability, Monthly Notices of the Royal Astronomical Society, 116, 351

Borisova E., et al., 2016, Ubiquitous Giant Lyα Nebulae around the Brightest Quasars at z $\sim$ 3.5 Revealed with MUSE, Astrophysical Journal, 831, 39

Bouché N., Murphy M. T., Kacprzak G. G., Péroux C., Contini T., Martin C. L., Dessauges-Zavadsky M., 2013, Signatures of Cool Gas Fueling a Star-Forming Galaxy at Redshift 2.3, Science, 341, 50

Bouché N., et al., 2016, Possible Signatures of a Cold-flow Disk from MUSE Using a z $\sim$ 1 Galaxy-Quasar Pair toward SDSS J1422-0001, Astrophysical Journal, 820, 121

Burstein D., Bender R., Faber S., Nolthenius R., 1997, Global Relationships Among the Physical Properties of Stellar Systems., Astronomical Journal, 114, 1365

Busch P., White S. D. M., 2017, Assembly bias and splashback in galaxy clusters, Monthly Notices of the Royal Astronomical Society, 470, 4767

Cantalupo S., Arrigoni-Battaia F., Prochaska J. X., Hennawi J. F., Madau P., 2014, A cosmic web filament revealed in Lyman-α emission around a luminous high-redshift quasar, Nature, 506, 63

Cantalupo S., et al., 2019, The large- and small-scale properties of the intergalactic gas in the Slug Ly α nebula revealed by MUSE He II emission observations, Monthly Notices of the Royal Astronomical Society, 483, 5188

Cappellari M., et al., 2013, The ATLAS^{3D} project - XX. Mass-size and mass-σ distributions of early-type galaxies: bulge fraction drives kinematics, mass-to-light ratio, molecular gas fraction and stellar initial mass function, Monthly Notices of the Royal Astronomical Society, 432, 1862

Carroll S. M., Press W. H., Turner E. L., 1992, The cosmological constant., Annual Review of Astronomy and Astrophysics, 30, 499

Ceverino D., Dekel A., Bournaud F., 2010, High-redshift clumpy discs and bulges in cosmological simulations, Monthly Notices of the Royal Astronomical Society, 404, 2151

Chadayammuri U., Tremmel M., Nagai D., Babul A., Quinn T., 2021, Fountains and storms: the effects of AGN feedback and mergers on the evolution of the intracluster medium in the ROMULUSC simulation, Monthly Notices of the Royal Astronomical Society,

Chandrasekhar S., Fermi E., 1953, Problems of Gravitational Stability in the Presence of a Magnetic Field., Astrophysical Journal, 118, 116

Chang C., et al., 2018, The Splashback Feature around DES Galaxy Clusters: Galaxy Density and Weak Lensing Profiles, Astrophysical Journal, 864, 83

Chen H., Avestruz C., Kravtsov A. V., Lau E. T., Nagai D., 2019, Imprints of mass accretion history on the shape of the intracluster medium and the T_X-M relation, Monthly Notices of the Royal Astronomical Society, 490, 2380

Clarke S. D., Whitworth A. P., Hubber D. A., 2016, Perturbation growth in accreting filaments, Monthly Notices of the Royal Astronomical Society, 458, 319

Clarke S. D., Whitworth A. P., Duarte-Cabral A., Hubber D. A., 2017, Filamentary fragmentation in a turbulent medium, Monthly Notices of the Royal Astronomical Society, 468, 2489

Codis S., Pichon C., Devriendt J., Slyz A., Pogosyan D., Dubois Y., Sousbie T., 2012, Connecting the cosmic web to the spin of dark haloes: implications for galaxy formation, Monthly Notices of the Royal Astronomical Society, 427, 3320

Codis S., Pichon C., Pogosyan D., 2015, Spin alignments within the cosmic web: a theory of constrained tidal torques near filaments, Monthly Notices of the Royal Astronomical Society, 452, 3369

Codis S., Pogosyan D., Pichon C., 2018, On the connectivity of the cosmic web: theory and implications for cosmology and galaxy formation, Monthly Notices of the Royal Astronomical Society, 479, 973

Cole S., Lacey C., 1996, The structure of dark matter haloes in hierarchical clustering models, Monthly Notices of the Royal Astronomical Society, 281, 716

Colless M., et al., 2003, VizieR Online Data Catalog: The 2dF Galaxy Redshift Survey 100k Data Release (2dFGRS Team, 2001), VizieR Online Data Catalog, 7226

Coughlin E. R., Nixon C., 2015, Variability in Tidal Disruption Events: Gravitationally Unstable Streams, Astrophysical Journal, Letters, 808, L11

Coughlin E. R., Nixon C., Begelman M. C., Armitage P. J., Price D. J., 2016a, Post-periapsis pancakes: sustenance for self-gravity in tidal disruption events, Monthly Notices of the Royal Astronomical Society, 455, 3612

Coughlin E. R., Nixon C., Begelman M. C., Armitage P. J., 2016b, On the structure of tidally disrupted stellar debris streams, Monthly Notices of the Royal Astronomical Society, 459, 3089

Croton D. J., et al., 2006, The many lives of active galactic nuclei: cooling flows, black holes and the luminosities and colours of galaxies, Monthly Notices of the Royal Astronomical Society, 365, 11

DESI Collaboration et al., 2016, The DESI Experiment Part I: Science,Targeting, and Survey Design, preprint, (arXiv:1611.00036)

Dalal N., Lithwick Y., Kuhlen M., 2010, The Origin of Dark Matter Halo Profiles, arXiv e-prints, p. arXiv:1010.2539

Danovich M., Dekel A., Hahn O., Teyssier R., 2012, Coplanar streams, pancakes and angular-momentum exchange in high-z disc galaxies, Monthly Notices of the Royal Astronomical Society, 422, 1732

Danovich M., Dekel A., Hahn O., Ceverino D., Primack J., 2015, Four phases of angular-momentum buildup in high-z galaxies: from cosmic-web streams through an extended ring to disc and bulge, Monthly Notices of the Royal Astronomical Society, 449, 2087

Dekel A., Birnboim Y., 2006, Galaxy bimodality due to cold flows and shock heating, Monthly Notices of the Royal Astronomical Society, 368, 2

Dekel A., Burkert A., 2014, Wet disc contraction to galactic blue nuggets and quenching to red nuggets, Monthly Notices of the Royal Astronomical Society, 438, 1870

Dekel A., Silk J., 1986, The origin of dwarf galaxies, cold dark matter, and biased galaxy formation, Astrophysical Journal, 303, 39

Dekel A., et al., 2009a, Cold streams in early massive hot haloes as the main mode of galaxy formation, Nature, 457, 451

Dekel A., Sari R., Ceverino D., 2009b, Formation of Massive Galaxies at High Redshift: Cold Streams, Clumpy Disks, and Compact Spheroids, Astrophysical Journal, 703, 785

Diemer B., 2017, The Splashback Radius of Halos from Particle Dynamics. I. The SPARTA Algorithm, Astrophysical Journal, Supplement, 231, 5

Diemer B., 2018, COLOSSUS: A Python Toolkit for Cosmology, Large-scale Structure, and Dark Matter Halos, Astrophysical Journal, Supplement, 239, 35

Diemer B., Kravtsov A. V., 2014, Dependence of the Outer Density Profiles of Halos on Their Mass Accretion Rate, Astrophysical Journal, 789, 1

Diemer B., Mansfield P., Kravtsov A. V., More S., 2017, The Splashback Radius of Halos from Particle Dynamics. II. Dependence on Mass, Accretion Rate, Redshift, and Cosmology, Astrophysical Journal, 843, 140

Dimotakis P. E., 1991, Turbulent free shear layer mixing and combustion, Turbulent free shear layer mixing and combustion. Tech. rep.

Djorgovski S., Davis M., 1987, Fundamental Properties of Elliptical Galaxies, Astrophysical Journal, 313, 59

Dolag K., Borgani S., Murante G., Springel V., 2009, Substructures in hydrodynamical cluster simulations, Monthly Notices of the Royal Astronomical Society, 399, 497

Doré O., et al., 2014, Cosmology with the SPHEREX All-Sky Spectral Survey, arXiv e-prints, p. arXiv:1412.4872

Dvali G., Gabadadze G., Porrati M., 2000, 4D gravity on a brane in 5D Minkowski space, Physics Letters B, 485, 208

Ebert R., 1955, Über die Verdichtung von H I-Gebieten. Mit 5 Textabbildungen, Z. Astrophys., 37, 217

Einasto J., 1965, On the Construction of a Composite Model for the Galaxy and on the Determination of the System of Galactic Parameters, Trudy Astrofizicheskogo Instituta Alma-Ata, 5, 87

Elmegreen B. G., 2011, On the Initial Conditions for Star Formation and the Initial Mass Function, Astrophysical Journal, 731, 61

Evrard A. E., et al., 2008, Virial Scaling of Massive Dark Matter Halos: Why Clusters Prefer a High Normalization Cosmology, Astrophysical Journal, 672, 122

Faber S. M., Jackson R. E., 1976, Velocity dispersions and mass-to-light ratios for elliptical galaxies., Astrophysical Journal, 204, 668

Faucher-Giguère C.-A., Kereš D., Dijkstra M., Hernquist L., Zaldarriaga M., 2010, Lyα Cooling Emission from Galaxy Formation, Astrophysical Journal, 725, 633

Faucher-Giguère C.-A., Kereš D., Ma C.-P., 2011, The baryonic assembly of dark matter haloes, Monthly Notices of the Royal Astronomical Society, 417, 2982

Federrath C., Banerjee S., 2015, The density structure and star formation rate of non-isothermal polytropic turbulence, Monthly Notices of the Royal Astronomical Society, 448, 3297

Federrath C., et al., 2016, The Link between Turbulence, Magnetic Fields, Filaments, and Star Formation in the Central Molecular Zone Cloud G0.253+0.016, Astrophysical Journal, 832, 143

Ferrari A., Trussoni E., Zaninetti L., 1981, Magnetohydrodynamic Kelvin-Helmholtz instabilities in astrophysics. II Cylindrical boundary layer in vortex sheet approximation, Monthly Notices of the Royal Astronomical Society, 196, 1051

Fillmore J. A., Goldreich P., 1984a, Self-similar gravitational collapse in an expanding universe, Astrophysical Journal, 281, 1

Fillmore J. A., Goldreich P., 1984b, Self-similar gravitational collapse in an expanding universe, Astrophysical Journal, 281, 1

Fischera J., Martin P. G., 2012, Physical properties of interstellar filaments, Astronomy and Astrophysics, 542, A77

Flender S., Nagai D., McDonald M., 2017, Constraints on the Optical Depth of Galaxy Groups and Clusters, Astrophysical Journal, 837, 124

Förster Schreiber N. M., et al., 2006, SINFONI Integral Field Spectroscopy of z ~2 UV-selected Galaxies: Rotation Curves and Dynamical Evolution, Astrophysical Journal, 645, 1062

Förster Schreiber N. M., et al., 2009, The SINS Survey: SINFONI Integral Field Spectroscopy of z ~2 Star-forming Galaxies, Astrophysical Journal, 706, 1364

Frenk C. S., White S. D. M., 2012, Dark matter and cosmic structure, Annalen der Physik, 524, 507

Frenk C. S., et al., 1999, The Santa Barbara Cluster Comparison Project: A Comparison of Cosmological Hydrodynamics Solutions, Astrophysical Journal, 525, 554

Freundlich J., Jog C. J., Combes F., 2014, Local stability of a gravitating filament: a dispersion relation, Astronomy and Astrophysics, 564, A7

Fridman A. M., Poliachenko V. L., 1984, Physics of gravitating systems. II - Nonlinear collective processes: Nonlinear waves, solitons, collisionless shocks, turbulence. Astrophysical applications. in New York, Springer-Verlag, 1984, 367 p. Translation.

Fumagalli M., et al., 2017, Witnessing galaxy assembly in an extended z∼3 structure, Monthly Notices of the Royal Astronomical Society, 471, 3686

Garcia R., Rozo E., Becker M. R., More S., 2020, A Redefinition of the Halo Boundary Leads to a Simple yet Accurate Halo Model of Large Scale Structure, arXiv e-prints, p. arXiv:2006.12751

Gaskin J. A., et al., 2019, Lynx X-Ray Observatory: an overview, Journal of Astronomical Telescopes, Instruments, and Systems, 5, 021001

Gaspari M., Sądowski A., 2017, Unifying the Micro and Macro Properties of AGN Feeding and Feedback, Astrophysical Journal, 837, 149

Gaspari M., Ruszkowski M., Sharma P., 2012, Cause and Effect of Feedback: Multiphase Gas in Cluster Cores Heated by AGN Jets, Astrophysical Journal, 746, 94

Genel S., Dekel A., Cacciato M., 2012, On the effect of cosmological inflow on turbulence and instability in galactic discs, Monthly Notices of the Royal Astronomical Society, p. 3466

Genzel R., Tacconi L. J., Eisenhauer F., Förster Schreiber N. M., Cimatti A., Daddi E., Bouché N., et al., 2006, The rapid formation of a large rotating disk galaxy three billion years after the Big Bang, Nature, 442, 786

Genzel R., et al., 2008, From Rings to Bulges: Evidence for Rapid Secular Galaxy Evolution at z ~2 from Integral Field Spectroscopy in the SINS Survey, Astrophysical Journal, 687, 59

Gheller C., Vazza F., Favre J., Brüggen M., 2015, Properties of cosmological filaments extracted from Eulerian simulations, Monthly Notices of the Royal Astronomical Society, 453, 1164

Ginolfi M., et al., 2017, Molecular gas on large circumgalactic scales at z = 3.47, Monthly Notices of the Royal Astronomical Society, 468, 3468

Gnedin O. Y., Kravtsov A. V., Klypin A. A., Nagai D., 2004, Response of Dark Matter Halos to Condensation of Baryons: Cosmological Simulations and Improved Adiabatic Contraction Model, Astrophysical Journal, 616, 16

Goerdt T., Ceverino D., 2015, Inflow velocities of cold flows streaming into massive galaxies at high redshifts, Monthly Notices of the Royal Astronomical Society, 450, 3359

Gómez G. C., Vázquez-Semadeni E., 2014, Filaments in Simulations of Molecular Cloud Formation, Astrophysical Journal, 791, 124

Górski K. M., Hivon E., Banday A. J., Wandelt B. D., Hansen F. K., Reinecke M., Bartelmann M., 2005, HEALPix: A Framework for High-Resolution Discretization and Fast Analysis of Data Distributed on the Sphere, Astrophysical Journal, 622, 759

Green J. C., et al., 2012, The Cosmic Origins Spectrograph, Astrophysical Journal, 744, 60

Green S. B., Aung H., Nagai D., van den Bosch F. C., 2020, Scatter in Sunyaev-Zel'dovich effect scaling relations explained by inter-cluster variance in mass accretion histories, Monthly Notices of the Royal Astronomical Society,

Gronke M., Oh S. P., 2018, The growth and entrainment of cold gas in a hot wind, Monthly Notices of the Royal Astronomical Society, 480, L111

Gronke M., Oh S. P., 2020, How cold gas continuously entrains mass and momentum from a hot wind, Monthly Notices of the Royal Astronomical Society, 492, 1970

Gunn J. E., Gott III J. R., 1972, On the Infall of Matter Into Clusters of Galaxies and Some Effects on Their Evolution, Astrophysical Journal, 176, 1

Guo F., Oh S. P., 2008, Feedback heating by cosmic rays in clusters of galaxies, Monthly Notices of the Royal Astronomical Society, 384, 251

Hacar A., Tafalla M., Forbrich J., Alves J., Meingast S., Grossschedl J., Teixeira P. S., 2018, An ALMA study of the Orion Integral Filament. I. Evidence for narrow fibers in a massive cloud, Astronomy and Astrophysics, 610, A77

Haggar R., Gray M. E., Pearce F. R., Knebe A., Cui W., Mostoghiu R., Yepes G., 2020, The Three Hundred Project: Backsplash galaxies in simulations of clusters, Monthly Notices of the Royal Astronomical Society, p. 277

Hamabata A., Oguri M., Nishimichi T., 2019, Constraining cluster masses from the stacked phase space distribution at large radii, Monthly Notices of the Royal Astronomical Society, 489, 1344

Hansen C. J., Aizenman M. L., Ross R. L., 1976, The Equilibrium and Stability of Uniformly Rotating, Isothermal Gas Cylinders, Astrophysical Journal, 207, 736

Hardee P. E., Stone J. M., 1997, The Stability of Radiatively Cooling Jets I. Linear Analysis, Astrophysical Journal, 483, 121

Hardee P. E., Clarke D. A., Howell D. A., 1995, The stability and collimation of three-dimensional jets, Astrophysical Journal, 441, 644

Harford A. G., Hamilton A. J. S., 2011, Intergalactic filaments as isothermal gas cylinders, Monthly Notices of the Royal Astronomical Society, 416, 2678

Harford A. G., Hamilton A. J. S., Gnedin N. Y., 2008, Intergalactic baryon-rich regions at high redshift, Monthly Notices of the Royal Astronomical Society, 389, 880

Hearin A. P., 2015, Assembly bias & redshift-space distortions: impact on cluster dynamics tests of general relativity., Monthly Notices of the Royal Astronomical Society, 451, L45

Heigl S., Burkert A., Hacar A., 2016, Non-linear dense core formation in the dark cloud L1517, Monthly Notices of the Royal Astronomical Society, 463, 4301

Heigl S., Burkert A., Gritschneder M., 2018a, Accretion-driven turbulence in filaments - I. Non-gravitational accretion, Monthly Notices of the Royal Astronomical Society, 474, 4881

Heigl S., Gritschneder M., Burkert A., 2018b, Morphology of prestellar cores in pressure-confined filaments, Monthly Notices of the Royal Astronomical Society, 481, L1

Heitsch F., 2013, Gravitational Infall onto Molecular Filaments, Astrophysical Journal, 769, 115

Henderson S. W., et al., 2016, Advanced ACTPol Cryogenic Detector Arrays and Readout, Journal of Low Temperature Physics, 184, 772

Hennebelle P., André P., 2013, Ion-neutral friction and accretion-driven turbulence in self-gravitating filaments, Astronomy and Astrophysics, 560, A68

Henshaw J. D., Longmore S. N., Kruijssen J. M. D., 2016, Seeding the Galactic Centre gas stream: gravitational instabilities set the initial conditions for the formation of protocluster clouds, Monthly Notices of the Royal Astronomical Society, 463, L122

Hill J. C., Spergel D. N., 2014, Detection of thermal SZ-CMB lensing cross-correlation in Planck nominal mission data, Journal of Cosmology and Astroparticle Physics, 2014, 030

Hily-Blant P., Falgarone E., 2009, Intermittency of interstellar turbulence: parsec-scale coherent structure of intense, velocity shear, Astronomy and Astrophysics, 500, L29

Hockney R. W., Eastwood J. W., 1981, Computer Simulation Using Particles

Hojjati A., McCarthy I. G., Harnois-Deraps J., Ma Y.-Z., Van Waerbeke L., Hinshaw G., Le Brun A. M. C., 2015, Dissecting the thermal Sunyaev-Zeldovich-gravitational lensing cross-correlation with hydrodynamical simulations, Journal of Cosmology and Astroparticle Physics, 2015, 047

Hopkins P. F., 2013, A general class of Lagrangian smoothed particle hydrodynamics methods and implications for fluid mixing problems, Monthly Notices of the Royal Astronomical Society, 428, 2840

Hopkins P. F., Kereš D., Murray N., Quataert E., Hernquist L., 2012, Stellar feedback and bulge formation in clumpy discs, Monthly Notices of the Royal Astronomical Society, 427, 968

Howard L. N., 1961, Note on a paper of john w. miles, Journal of Fluid Mechanics, 10, 509

Hu W., Sawicki I., 2007, Models of f(R) cosmic acceleration that evade solar system tests, Physical Review D, 76, 064004

Huang H.-J., Eifler T., Mandelbaum R., Dodelson S., 2019, Modelling baryonic physics in future weak lensing surveys, Monthly Notices of the Royal Astronomical Society, 488, 1652

Huchra J., et al., 2005, in Fairall A. P., Woudt P. A., eds, Astronomical Society of the Pacific Conference Series Vol. 329, Nearby Large-Scale Structures and the Zone of Avoidance. p. Fairall

Hunter Jr. J. H., Whitaker R. W., Lovelace R. V. E., 1997, Kelvin-Helmholtz and Thermal-dynamic Instabilities with Self-Gravity: A New Gravitational Interface Instability, Astrophysical Journal, 482, 852

Hunter Jr. J. H., Whitaker R. W., Lovelace R. V. E., 1998, Stability of Interfaces with Self-Gravity, Relative Flow, and B Field, Astrophysical Journal, 508, 680

Inoue S., Yoshida N., 2018, Spiral-arm instability: giant clump formation via fragmentation of a galactic spiral arm, Monthly Notices of the Royal Astronomical Society, 474, 3466

Inutsuka S.-I., Miyama S. M., 1992, Self-similar solutions and the stability of collapsing isothermal filaments, Astrophysical Journal, 388, 392

Jackson J. M., Finn S. C., Chambers E. T., Rathborne J. M., Simon R., 2010, The "Nessie" Nebula: Cluster Formation in a Filamentary Infrared Dark Cloud, Astrophysical Journal, Letters, 719, L185

Joyce A., Lombriser L., Schmidt F., 2016, Dark Energy Versus Modified Gravity, Annual Review of Nuclear and Particle Science, 66, 95

Kaiser N., 1986, Evolution and clustering of rich clusters, Monthly Notices of the Royal Astronomical Society, 222, 323

Katz N., 1992, Dissipational Galaxy Formation. II. Effects of Star Formation, Astrophysical Journal, 391, 502

Kereš D., Katz N., Weinberg D. H., Davé R., 2005, How do galaxies get their gas?, Monthly Notices of the Royal Astronomical Society, 363, 2

Kilbinger M., 2015, Cosmology with cosmic shear observations: a review, Reports on Progress in Physics, 78, 086901

Kimm T., Devriendt J., Slyz A., Pichon C., Kassin S. A., Dubois Y., 2011, The angular momentum of baryons and dark matter halos revisited, preprint, (arXiv:1106.0538)

Kirk J. M., et al., 2013, First results from the Herschel Gould Belt Survey in Taurus, Monthly Notices of the Royal Astronomical Society, 432, 1424

Kirk H., et al., 2017, The Green Bank Ammonia Survey: Dense Cores under Pressure in Orion A, Astrophysical Journal, 846, 144

Klar J. S., Mücket J. P., 2012, Filaments and sheets of the warm-hot intergalactic medium, Monthly Notices of the Royal Astronomical Society, 423, 304

Klypin A., Kravtsov A. V., Bullock J. S., Primack J. R., 2001, Resolving the Structure of Cold Dark Matter Halos, Astrophysical Journal, 554, 903

Klypin A., Yepes G., Gottlöber S., Prada F., Heß S., 2016, MultiDark simulations: the story of dark matter halo concentrations and density profiles, Monthly Notices of the Royal Astronomical Society, 457, 4340

Knebe A., et al., 2020, The Three Hundred project: shapes and radial alignment of satellite, infalling, and backsplash galaxies, Monthly Notices of the Royal Astronomical Society,

Komatsu E., Seljak U., 2001, Universal gas density and temperature profile, Monthly Notices of the Royal Astronomical Society, 327, 1353

Kravtsov A. V., 1999, PhD thesis, New Mexico State Univ.

Kravtsov A. V., Borgani S., 2012, Formation of Galaxy Clusters, Annual Review of Astronomy and Astrophysics, 50, 353

Kravtsov A. V., Klypin A. A., Khokhlov A. M., 1997, Adaptive Refinement Tree: A New High-Resolution N-Body Code for Cosmological Simulations, Astrophysical Journal, Supplement, 111, 73

Kravtsov A. V., Klypin A., Hoffman Y., 2002, Constrained Simulations of the Real Universe. II. Observational Signatures of Intergalactic Gas in the Local Supercluster Region, Astrophysical Journal, 571, 563

Kravtsov A. V., Vikhlinin A., Nagai D., 2006, A New Robust Low-Scatter X-Ray Mass Indicator for Clusters of Galaxies, Astrophysical Journal, 650, 128

Kruijssen J. M. D., et al., 2019, The dynamical evolution of molecular clouds near the Galactic Centre - II. Spatial structure and kinematics of simulated clouds, Monthly Notices of the Royal Astronomical Society, 484, 5734

Krumholz M. R., 2015, Notes on Star Formation, arXiv e-prints,

LSST Science Collaboration et al., 2009, LSST Science Book, Version 2.0, preprint, (arXiv:0912.0201)

Laigle C., et al., 2015, Swirling around filaments: are large-scale structure vortices spinning up dark haloes?, Monthly Notices of the Royal Astronomical Society, 446, 2744

Lam T. Y., Nishimichi T., Schmidt F., Takada M., 2012, Testing Gravity with the Stacked Phase Space around Galaxy Clusters, Physical Review Letters, 109, 051301

Lam T. Y., Schmidt F., Nishimichi T., Takada M., 2013, Modeling the phase-space distribution around massive halos, Physical Review D, 88, 023012

Larson R. B., 1985, Cloud fragmentation and stellar masses, Monthly Notices of the Royal Astronomical Society, 214, 379

Lau E. T., Kravtsov A. V., Nagai D., 2009, Residual Gas Motions in the Intracluster Medium and Bias in Hydrostatic Measurements of Mass Profiles of Clusters, Astrophysical Journal, 705, 1129

Lau E. T., Nagai D., Kravtsov A. V., 2010, Effects of Baryon Dissipation on the Dark Matter Virial Scaling Relation, Astrophysical Journal, 708, 1419

Lau E. T., Nagai D., Avestruz C., Nelson K., Vikhlinin A., 2015, Mass Accretion and its Effects on the Self-similarity of Gas Profiles in the Outskirts of Galaxy Clusters, Astrophysical Journal, 806, 68

Laureijs R., et al., 2011, Euclid Definition Study Report, arXiv e-prints, p. arXiv:1110.3193

Leauthaud A., et al., 2017, Lensing is low: cosmology, galaxy formation or new physics?, Monthly Notices of the Royal Astronomical Society, 467, 3024

Leclercq F., et al., 2017, The MUSE Hubble Ultra Deep Field Survey. VIII. Extended Lyman-α haloes around high-z star-forming galaxies, Astronomy and Astrophysics, 608, A8

Ledoux C., Petitjean P., Srianand R., 2003, The Very Large Telescope Ultraviolet and Visible Echelle Spectrograph survey for molecular hydrogen in high-redshift damped Lyman α systems, Monthly Notices of the Royal Astronomical Society, 346, 209

Li R., Gao L., Xie L., Guo Q., 2013, Assembly bias of dwarf-sized dark matter haloes, Monthly Notices of the Royal Astronomical Society, 435, 3592

Li Y., Ruszkowski M., Bryan G. L., 2017, AGN Heating in Simulated Cool-core Clusters, Astrophysical Journal, 847, 106

Louis T., Alonso D., 2017, Calibrating cluster number counts with CMB lensing, Physical Review D, 95, 043517

Ludlow A. D., Navarro J. F., Springel V., Jenkins A., Frenk C. S., Helmi A., 2009, The Unorthodox Orbits of Substructure Halos, Astrophysical Journal, 692, 931

Ludlow A. D., Navarro J. F., Angulo R. E., Boylan-Kolchin M., Springel V., Frenk C., White S. D. M., 2014, The mass-concentration-redshift relation of cold dark matter haloes, Monthly Notices of the Royal Astronomical Society, 441, 378

Madhavacheril M. S., Battaglia N., Miyatake H., 2017, Fundamental physics from future weak-lensing calibrated Sunyaev-Zel'dovich galaxy cluster counts, Physical Review D, 96, 103525

Mandelker N., Padnos D., Dekel A., Birnboim Y., Burkert A., Krumholz M. R., Steinberg E., 2016, Instability of supersonic cold streams feeding galaxies - I. Linear Kelvin-Helmholtz instability with body modes, Monthly Notices of the Royal Astronomical Society, 463, 3921

Mandelker N., Dekel A., Ceverino D., DeGraf C., Guo Y., Primack J., 2017, Giant clumps in simulated high- z Galaxies: properties, evolution and dependence on feedback, Monthly Notices of the Royal Astronomical Society, 464, 635

Mandelker N., van Dokkum P. G., Brodie J. P., van den Bosch F. C., Ceverino D., 2018, Cold Filamentary Accretion and the Formation of Metal-poor Globular Clusters and Halo Stars, Astrophysical Journal, 861, 148

Mandelker N., Nagai D., Aung H., Dekel A., Padnos D., Birnboim Y., 2019, Instability of supersonic cold streams feeding Galaxies - III. Kelvin-Helmholtz instability in three dimensions, Monthly Notices of the Royal Astronomical Society, 484, 1100

Mandelker N., Nagai D., Aung H., Dekel A., Birnboim Y., van den Bosch F. C., 2020a, Instability of supersonic cold streams feeding galaxies – iv. survival of radiatively cooling streams, Monthly Notices of the Royal Astronomical Society, 494, 2641–2663

Mandelker N., van den Bosch F. C., Nagai D., Dekel A., Birnboim Y., Aung H., 2020b, Lyα blobs from cold streams undergoing kelvin–helmholtz instabilities, Monthly Notices of the Royal Astronomical Society, 498, 2415–2427

Mansfield P., Kravtsov A. V., 2020, The three causes of low-mass assembly bias, Monthly Notices of the Royal Astronomical Society, 493, 4763

Mansfield P., Kravtsov A. V., Diemer B., 2017, Splashback Shells of Cold Dark Matter Halos, Astrophysical Journal, 841, 34

Mantz A. B., Allen S. W., Morris R. G., Rapetti D. A., Applegate D. E., Kelly P. L., von der Linden A., Schmidt R. W., 2014, Cosmology and astrophysics from relaxed galaxy clusters - II. Cosmological constraints, Monthly Notices of the Royal Astronomical Society, 440, 2077

Markevitch M., Gonzalez A. H., Clowe D., Vikhlinin A., Forman W., Jones C., Murray S., Tucker W., 2004, Direct Constraints on the Dark Matter Self-Interaction Cross Section from the Merging Galaxy Cluster 1E 0657-56, Astrophysical Journal, 606, 819

Martin D. C., Chang D., Matuszewski M., Morrissey P., Rahman S., Moore A., Steidel C. C., 2014a, Intergalactic Medium Emission Observations with the Cosmic

Web Imager. I. The Circum-QSO Medium of QSO 1549+19, and Evidence for a Filamentary Gas Inflow, Astrophysical Journal, 786, 106

Martin D. C., Chang D., Matuszewski M., Morrissey P., Rahman S., Moore A., Steidel C. C., Matsuda Y., 2014b, Intergalactic Medium Emission Observations with the Cosmic Web Imager. II. Discovery of Extended, Kinematically Linked Emission around SSA22 Lyα Blob 2, Astrophysical Journal, 786, 107

Massaglia S., Trussoni E., Bodo G., Rossi P., Ferrari A., 1992, Radiative unstable modes in the jets of young stellar objects, Astronomy and Astrophysics, 260, 243

Matsuda Y., Yamada T., Hayashino T., Yamauchi R., Nakamura Y., 2006, A Keck/DEIMOS Spectroscopy of Lyα Blobs at Redshift z = 3.1, Astrophysical Journal, Letters, 640, L123

Matsuda Y., et al., 2011, The Subaru Lyα blob survey: a sample of 100-kpc Lyα blobs at z= 3, Monthly Notices of the Royal Astronomical Society, 410, L13

McConnachie A. W., 2012, The Observed Properties of Dwarf Galaxies in and around the Local Group, Astronomical Journal, 144, 4

Merloni A., et al., 2012, eROSITA Science Book: Mapping the Structure of the Energetic Universe, arXiv e-prints, p. arXiv:1209.3114

Micono M., Bodo G., Massaglia S., Rossi P., Ferrari A., Rosner R., 2000, Kelvin-Helmholtz instability in three dimensional radiative jets, Astronomy and Astrophysics, 360, 795

Mikhaĭlovskiĭ A. B., Fridman A. M., 1972, Beam Instability in Gravitating Media, Soviet Journal of Experimental and Theoretical Physics, 34, 243

Miles J. W., 1961, On the stability of heterogeneous shear flows, Journal of Fluid Mechanics, 10, 496

Miniati F., Ryu D., Kang H., Jones T. W., Cen R., Ostriker J. P., 2000, Properties of Cosmic Shock Waves in Large-Scale Structure Formation, Astrophysical Journal, 542, 608

Mitchell M. A., He J.-h., Arnold C., Li B., 2018, A general framework to test gravity using galaxy clusters - I. Modelling the dynamical mass of haloes in f(R) gravity, Monthly Notices of the Royal Astronomical Society, 477, 1133

Moeckel N., Burkert A., 2015, The Formation of Filamentary Bundles in Turbulent Molecular Clouds, Astrophysical Journal, 807, 67

Molinari S., et al., 2010, Clouds, filaments, and protostars: The Herschel Hi-GAL Milky Way, Astronomy and Astrophysics, 518, L100

Molnar S. M., Hearn N., Haiman Z., Bryan G., Evrard A. E., Lake G., 2009, Accretion Shocks in Clusters of Galaxies and Their SZ Signature from Cosmological Simulations, Astrophysical Journal, 696, 1640

More S., Diemer B., Kravtsov A. V., 2015, The Splashback Radius as a Physical Halo Boundary and the Growth of Halo Mass, Astrophysical Journal, 810, 36

More S., et al., 2016, Detection of the Splashback Radius and Halo Assembly Bias of Massive Galaxy Clusters, Astrophysical Journal, 825, 39

Munari E., Biviano A., Borgani S., Murante G., Fabjan D., 2013, The relation between velocity dispersion and mass in simulated clusters of galaxies: dependence on the tracer and the baryonic physics, Monthly Notices of the Royal Astronomical Society, 430, 2638

Murata R., Sunayama T., Oguri M., More S., Nishizawa A. J., Nishimichi T., Osato K., 2020, The splashback radius of optically selected clusters with Subaru HSC

Second Public Data Release, Publications of the Astronomical Society of Japan, 72, 64

Murray S. D., White S. D. M., Blondin J. M., Lin D. N. C., 1993, Dynamical instabilities in two-phase media and the minimum masses of stellar systems, Astrophysical Journal, 407, 588

Nagai D., 2006, The Impact of Galaxy Formation on the Sunyaev-Zel'dovich Effect of Galaxy Clusters, Astrophysical Journal, 650, 538

Nagai D., Kravtsov A. V., Vikhlinin A., 2007, Effects of Galaxy Formation on Thermodynamics of the Intracluster Medium, Astrophysical Journal, 668, 1

Nagasawa M., 1987, Gravitational Instability of the Isothermal Gas Cylinder with an Axial magnetic Field, Progress of Theoretical Physics, 77, 635

Nandra K., et al., 2013, The Hot and Energetic Universe: A White Paper presenting the science theme motivating the Athena+ mission, arXiv e-prints, p. arXiv:1306.2307

Navarro J. F., Frenk C. S., White S. D. M., 1996a, The Structure of Cold Dark Matter Halos, Astrophysical Journal, 462, 563

Navarro J. F., Frenk C. S., White S. D. M., 1996b, The Structure of Cold Dark Matter Halos, Astrophysical Journal, 462, 563

Navarro J. F., et al., 2004, The inner structure of ΛCDM haloes - III. Universality and asymptotic slopes, Monthly Notices of the Royal Astronomical Society, 349, 1039

Nelson K., Rudd D. H., Shaw L., Nagai D., 2012, Evolution of the Merger-induced Hydrostatic Mass Bias in Galaxy Clusters, Astrophysical Journal, 751, 121

Nelson D., Vogelsberger M., Genel S., Sijacki D., Kereš D., Springel V., Hernquist L., 2013, Moving mesh cosmology: tracing cosmological gas accretion, Monthly Notices of the Royal Astronomical Society, 429, 3353

Nelson K., Lau E. T., Nagai D., Rudd D. H., Yu L., 2014a, Weighing Galaxy Clusters with Gas. II. On the Origin of Hydrostatic Mass Bias in ΛCDM Galaxy Clusters, Astrophysical Journal, 782, 107

Nelson K., Lau E. T., Nagai D., Rudd D. H., Yu L., 2014b, Weighing Galaxy Clusters with Gas. II. On the Origin of Hydrostatic Mass Bias in ΛCDM Galaxy Clusters, Astrophysical Journal, 782, 107

Nelson D., Genel S., Pillepich A., Vogelsberger M., Springel V., Hernquist L., 2016, Zooming in on accretion - I. The structure of halo gas, Monthly Notices of the Royal Astronomical Society, 460, 2881

Nelson D., et al., 2019, The IllustrisTNG simulations: public data release, Computational Astrophysics and Cosmology, 6, 2

Ocvirk P., Pichon C., Teyssier R., 2008, Bimodal gas accretion in the Horizon-MareNostrum galaxy formation simulation, Monthly Notices of the Royal Astronomical Society, 390, 1326

Orkisz J. H., et al., 2019, A dynamically young, gravitationally stable network of filaments in Orion B, arXiv e-prints,

Osato K., Flender S., Nagai D., Shirasaki M., Yoshida N., 2018, Investigating cluster astrophysics and cosmology with cross-correlation of the thermal Sunyaev-Zel'dovich effect and weak lensing, Monthly Notices of the Royal Astronomical Society, 475, 532

Osato K., Shirasaki M., Miyatake H., Nagai D., Yoshida N., Oguri M., Takahashi R., 2020, Cross-correlation of the thermal Sunyaev-Zel'dovich effect and weak gravitational lensing: Planck and Subaru Hyper Suprime-Cam first-year data, Monthly Notices of the Royal Astronomical Society, p. 112

Ostriker J., 1964a, The Equilibrium of Polytropic and Isothermal Cylinders., Astrophysical Journal, 140, 1056

Ostriker J., 1964b, On the Oscillations and the Stability of a Homogeneous Compressible Cylinder., Astrophysical Journal, 140, 1529

Padnos D., Mandelker N., Birnboim Y., Dekel A., Krumholz M. R., Steinberg E., 2018, Instability of supersonic cold streams feeding galaxies-II. Non-linear evolution of surface and body modes of Kelvin-Helmholtz instability, Monthly Notices of the Royal Astronomical Society, 477, 3293

Padoan P., Juvela M., Goodman A. A., Nordlund A., 2001, The Turbulent Shock Origin of Proto-Stellar Cores, Astrophysical Journal, 553, 227

Palmeirim P., et al., 2013, Herschel view of the Taurus B211/3 filament and striations: evidence of filamentary growth?, Astronomy and Astrophysics, 550, A38

Payne D. G., Cohn H., 1985, The stability of confined radio jets - The role of reflection modes, Astrophysical Journal, 291, 655

Peeples M. S., Werk J. K., Tumlinson J., Oppenheimer B. D., Prochaska J. X., Katz N., Weinberg D. H., 2014, A Budget and Accounting of Metals at z ~0: Results from the COS-Halos Survey, Astrophysical Journal, 786, 54

Penna M. A., Dines K. A., 2007, A simple method for fitting sphere-like surfaces, IEEE Transactions on Pattern Analysis and Machine Intelligence, 29, 1673

Pfrommer C., Enßlin T. A., Springel V., Jubelgas M., Dolag K., 2007, Simulating cosmic rays in clusters of galaxies - I. Effects on the Sunyaev-Zel'dovich effect and the X-ray emission, Monthly Notices of the Royal Astronomical Society, 378, 385

Pichon C., Pogosyan D., Kimm T., Slyz A., Devriendt J., Dubois Y., 2011, Rigging dark haloes: why is hierarchical galaxy formation consistent with the inside-out build-up of thin discs?, Monthly Notices of the Royal Astronomical Society, 418, 2493

Pike S. R., Kay S. T., Newton R. D. A., Thomas P. A., Jenkins A., 2014, Cosmological simulations of galaxy clusters with feedback from active galactic nuclei: profiles and scaling relations, Monthly Notices of the Royal Astronomical Society, 445, 1774

Pillepich A., Reiprich T. H., Porciani C., Borm K., Merloni A., 2018, Forecasts on dark energy from the X-ray cluster survey with eROSITA: constraints from counts and clustering, Monthly Notices of the Royal Astronomical Society, 481, 613

Planck Collaboration et al., 2011, Planck early results. XI. Calibration of the local galaxy cluster Sunyaev-Zeldovich scaling relations, Astronomy and Astrophysics, 536, A11

Planck Collaboration et al., 2020, Planck 2018 results. VI. Cosmological parameters, Astronomy and Astrophysics, 641, A6

Prada F., Klypin A. A., Simonneau E., Betancort-Rijo J., Patiri S., Gottlöber S., Sanchez-Conde M. A., 2006, How Far Do They Go? The Outer Structure of Galactic Dark Matter Halos, Astrophysical Journal, 645, 1001

Pratt G. W., Croston J. H., Arnaud M., Böhringer H., 2009, Galaxy cluster X-ray luminosity scaling relations from a representative local sample (REXCESS), Astronomy and Astrophysics, 498, 361

Pratt G. W., Arnaud M., Biviano A., Eckert D., Ettori S., Nagai D., Okabe N., Reiprich T. H., 2019, The Galaxy Cluster Mass Scale and Its Impact on Cosmological Constraints from the Cluster Population, Space Science Reviews, 215, 25

Press W. H., Schechter P., 1974, Formation of Galaxies and Clusters of Galaxies by Self-Similar Gravitational Condensation, Astrophysical Journal, 187, 425

Prochaska J. X., Lau M. W., Hennawi J. F., 2014, Quasars Probing Quasars. VII. The Pinnacle of the Cool Circumgalactic Medium Surrounds Massive z ˜ 2 Galaxies, Astrophysical Journal, 796, 140

Rees M. J., 1988, Tidal disruption of stars by black holes of 10 to the 6th-10 to the 8th solar masses in nearby galaxies, Nature, 333, 523

Reid B. A., Seo H.-J., Leauthaud A., Tinker J. L., White M., 2014, A 2.5 per cent measurement of the growth rate from small-scale redshift space clustering of SDSS-III CMASS galaxies, Monthly Notices of the Royal Astronomical Society, 444, 476

Reyes R., Mandelbaum R., Seljak U., Baldauf T., Gunn J. E., Lombriser L., Smith R. E., 2010, Confirmation of general relativity on large scales from weak lensing and galaxy velocities, Nature, 464, 256

Robertson B. E., Kravtsov A. V., Gnedin N. Y., Abel T., Rudd D. H., 2010, Computational Eulerian hydrodynamics and Galilean invariance, Monthly Notices of the Royal Astronomical Society, 401, 2463

Rodriguez-Franco A., Martin-Pintado J., Gomez-Gonzalez J., Planesas P., 1992, Large-scale interaction of the H II region and the quiescent gas in Orion A, Astronomy and Astrophysics, 264, 592

Rudd D. H., Zentner A. R., Kravtsov A. V., 2008, Effects of Baryons and Dissipation on the Matter Power Spectrum, Astrophysical Journal, 672, 19

Ryu D., Kang H., Hallman E., Jones T. W., 2003, Cosmological Shock Waves and Their Role in the Large-Scale Structure of the Universe, Astrophysical Journal, 593, 599

Sarazin C. L., 1986, X-ray emission from clusters of galaxies, Reviews of Modern Physics, 58, 1

Scannapieco C., Tissera P. B., White S. D. M., Springel V., 2006, Feedback and metal enrichment in cosmological SPH simulations - II. A multiphase model with supernova energy feedback, Monthly Notices of the Royal Astronomical Society, 371, 1125

Schmidt F., 2010, Dynamical masses in modified gravity, Physical Review D, 81, 103002

Schneider S., Elmegreen B. G., 1979, A catalog of dark globular filaments, Astrophysical Journal, Supplement, 41, 87

Schneider A., Teyssier R., 2015, A new method to quantify the effects of baryons on the matter power spectrum, Journal of Cosmology and Astroparticle Physics, 12, 049

Schneider A., Teyssier R., Stadel J., Chisari N. E., Le Brun A. M. C., Amara A., Refregier A., 2019, Quantifying baryon effects on the matter power spectrum and the weak lensing shear correlation, Journal of Cosmology and Astro-Particle Physics, 2019, 020

Scolnic D. M., et al., 2018, The Complete Light-curve Sample of Spectroscopically Confirmed SNe Ia from Pan-STARRS1 and Cosmological Constraints from the Combined Pantheon Sample, Astrophysical Journal, 859, 101

Sembolini F., et al., 2016, nIFTy galaxy cluster simulations - I. Dark matter and non-radiative models, Monthly Notices of the Royal Astronomical Society, 457, 4063

Semboloni E., Hoekstra H., Schaye J., van Daalen M. P., McCarthy I. G., 2011, Quantifying the effect of baryon physics on weak lensing tomography, Monthly Notices of the Royal Astronomical Society, 417, 2020

Seo Y. M., et al., 2018, An Ammonia Spectral Map of the L1495-B218 Filaments in the Taurus Molecular Cloud: II CCS & HC$_7$N Chemistry and Three Modes of Star Formation in the Filaments, arXiv e-prints, p. arXiv:1812.06121

Shaw L. D., Nagai D., Bhattacharya S., Lau E. T., 2010, Impact of Cluster Physics on the Sunyaev-Zel'dovich Power Spectrum, Astrophysical Journal, 725, 1452

Shi X., 2016a, The outer profile of dark matter haloes: an analytical approach, Monthly Notices of the Royal Astronomical Society, 459, 3711

Shi X., 2016b, Locations of accretion shocks around galaxy clusters and the ICM properties: insights from self-similar spherical collapse with arbitrary mass accretion rates, Monthly Notices of the Royal Astronomical Society, 461, 1804

Shi X., Komatsu E., 2014, Analytical model for non-thermal pressure in galaxy clusters, Monthly Notices of the Royal Astronomical Society, 442, 521

Shin T., et al., 2019, Measurement of the splashback feature around SZ-selected Galaxy clusters with DES, SPT, and ACT, Monthly Notices of the Royal Astronomical Society, 487, 2900

Sijacki D., Springel V., Di Matteo T., Hernquist L., 2007, A unified model for AGN feedback in cosmological simulations of structure formation, Monthly Notices of the Royal Astronomical Society, 380, 877

Silk J., Rees M. J., 1998, Quasars and galaxy formation, Astronomy and Astrophysics, 331, L1

Simionescu A., et al., 2019, Constraining Gas Motions in the Intra-Cluster Medium, Space Science Reviews, 215, 24

Skillman S. W., O'Shea B. W., Hallman E. J., Burns J. O., Norman M. L., 2008, Cosmological Shocks in Adaptive Mesh Refinement Simulations and the Acceleration of Cosmic Rays, Astrophysical Journal, 689, 1063

Smith R. J., Glover S. C. O., Klessen R. S., Fuller G. A., 2016, On the nature of star-forming filaments - II. Subfilaments and velocities, Monthly Notices of the Royal Astronomical Society, 455, 3640

Springel V., 2005, The cosmological simulation code GADGET-2, Monthly Notices of the Royal Astronomical Society, 364, 1105

Springel V., Hernquist L., 2003, Cosmological smoothed particle hydrodynamics simulations: a hybrid multiphase model for star formation, Monthly Notices of the Royal Astronomical Society, 339, 289

Springel V., et al., 2005, Simulations of the formation, evolution and clustering of galaxies and quasars, Nature, 435, 629

Steidel C. C., Adelberger K. L., Shapley A. E., Pettini M., Dickinson M., Giavalisco M., 2000, Lyα Imaging of a Proto-Cluster Region at $\langle z \rangle$=3.09, Astrophysical Journal, 532, 170

Stewart K. R., Brooks A. M., Bullock J. S., Maller A. H., Diemand J., Wadsley J., Moustakas L. A., 2013, Angular Momentum Acquisition in Galaxy Halos, Astrophysical Journal, 769, 74

Stone J. M., Xu J., Hardee P., 1997, The Stability of Radiatively Cooling Jets. 2: Nonlinear Evolution, Astrophysical Journal, 483, 136

Sugiura H., Nishimichi T., Rasera Y., Taruya A., 2020, Phase-space structure of cold dark matter haloes inside splashback: multistream flows and self-similar solution, Monthly Notices of the Royal Astronomical Society, 493, 2765

Sunyaev R. A., Zeldovich Y. B., 1970, Small-Scale Fluctuations of Relic Radiation, Astrophysics and Space Science, 7, 3

Sutherland R. S., Dopita M. A., 1993, Cooling Functions for Low-Density Astrophysical Plasmas, Astrophysical Journal, Supplement, 88, 253

Tacchella S., Dekel A., Carollo C. M., Ceverino D., DeGraf C., Lapiner S., Mandelker N., Primack Joel R., 2016a, The confinement of star-forming galaxies into a main sequence through episodes of gas compaction, depletion and replenishment, Monthly Notices of the Royal Astronomical Society, 457, 2790

Tacchella S., Dekel A., Carollo C. M., Ceverino D., DeGraf C., Lapiner S., Mandelker N., Primack J. R., 2016b, Evolution of density profiles in high-z galaxies: compaction and quenching inside-out, Monthly Notices of the Royal Astronomical Society, 458, 242

Takada M., et al., 2014, Extragalactic science, cosmology, and Galactic archaeology with the Subaru Prime Focus Spectrograph, Publications of the Astronomical Society of Japan, 66, R1

Tamura N., et al., 2016, in Evans C. J., Simard L., Takami H., eds, Society of Photo-Optical Instrumentation Engineers (SPIE) Conference Series Vol. 9908, Ground-based and Airborne Instrumentation for Astronomy VI. p. 99081M (arXiv:1608.01075), doi:10.1117/12.2232103

Tasker E. J., Brunino R., Mitchell N. L., Michielsen D., Hopton S., Pearce F. R., Bryan G. L., Theuns T., 2008, A test suite for quantitative comparison of hydrodynamic codes in astrophysics, Monthly Notices of the Royal Astronomical Society, 390, 1267

Taylor J. E., Navarro J. F., 2001, The Phase-Space Density Profiles of Cold Dark Matter Halos, Astrophysical Journal, 563, 483

Tegmark M., et al., 2004, The Three-Dimensional Power Spectrum of Galaxies from the Sloan Digital Sky Survey, Astrophysical Journal, 606, 702

Teyssier R., 2002, Cosmological hydrodynamics with adaptive mesh refinement. A new high resolution code called RAMSES, Astronomy and Astrophysics, 385, 337

Tinker J., Kravtsov A. V., Klypin A., Abazajian K., Warren M., Yepes G., Gottlöber S., Holz D. E., 2008, Toward a Halo Mass Function for Precision Cosmology: The Limits of Universality, Astrophysical Journal, 688, 709

Tomooka P., Rozo E., Wagoner E. L., Aung H., Nagai D., Safonova S., 2020, Clusters have edges: the projected phase-space structure of SDSS redMaPPer clusters, Monthly Notices of the Royal Astronomical Society, 499, 1291

Toro E. F., Spruce M., Speares W., 1994, Restoration of the contact surface in the hll-riemann solver, Shock Waves, 4, 25

Tully R. B., Fisher J. R., 1977, Reprint of 1977A&A....54..661T. A new method of determining distance to galaxies., Astronomy and Astrophysics, 500, 105

Tumlinson J., Peeples M. S., Werk J. K., 2017, The Circumgalactic Medium, Annual Review of Astronomy and Astrophysics, 55, 389

Van Waerbeke L., Hinshaw G., Murray N., 2014, Detection of warm and diffuse

baryons in large scale structure from the cross correlation of gravitational lensing and the thermal Sunyaev-Zeldovich effect, Physical Review D, 89, 023508

Vázquez-Semadeni E., González R. F., Ballesteros-Paredes J., Gazol A., Kim J., 2008, The nature of the velocity field in molecular clouds - I. The non-magnetic case, Monthly Notices of the Royal Astronomical Society, 390, 769

Vazza F., Brüggen M., Gheller C., 2013, Thermal and non-thermal traces of AGN feedback: results from cosmological AMR simulations, Monthly Notices of the Royal Astronomical Society, 428, 2366

Vietri M., Ferrara A., Miniati F., 1997, The Survival of Interstellar Clouds against Kelvin-Helmholtz Instabilities, Astrophysical Journal, 483, 262

Vikhlinin A., et al., 2009, Chandra Cluster Cosmology Project III: Cosmological Parameter Constraints, Astrophysical Journal, 692, 1060

Vogelsberger M., Zavala J., Loeb A., 2012, Subhaloes in self-interacting galactic dark matter haloes, Monthly Notices of the Royal Astronomical Society, 423, 3740

Vogelsberger M., Marinacci F., Torrey P., Puchwein E., 2020, Cosmological simulations of galaxy formation, Nature Reviews Physics, 2, 42

Voit G. M., Kay S. T., Bryan G. L., 2005, The baseline intracluster entropy profile from gravitational structure formation, Monthly Notices of the Royal Astronomical Society, 364, 909

Wagoner E. L., Rozo E., Aung H., Nagai D., 2021, Measuring Cosmological Distances Using Cluster Edges as a Standard Ruler, Monthly Notices of the Royal Astronomical Society,

Walker S., et al., 2019, The Physics of Galaxy Cluster Outskirts, Space Science Reviews, 215, 7

Wang H., Mo H. J., Jing Y. P., 2009, The distribution of ejected subhaloes and its implication for halo assembly bias, Monthly Notices of the Royal Astronomical Society, 396, 2249

Wechsler R. H., Tinker J. L., 2018, The connection between galaxies and their dark matter halos, Annual Review of Astronomy and Astrophysics, 56, 435

Werk J. K., et al., 2014, The COS-Halos Survey: Physical Conditions and Baryonic Mass in the Low-redshift Circumgalactic Medium, Astrophysical Journal, 792, 8

Wetzel A. R., Nagai D., 2015, The Physical Nature of the Cosmic Accretion of Baryons and Dark Matter into Halos and Their Galaxies, Astrophysical Journal, 808, 40

Whitaker K. E., van Dokkum P. G., Brammer G., Franx M., 2012, The Star Formation Mass Sequence Out to z = 2.5, Astrophysical Journal, Letters, 754, L29

White S. D. M., Frenk C. S., 1991, Galaxy Formation through Hierarchical Clustering, Astrophysical Journal, 379, 52

Wu H.-Y., Hahn O., Evrard A. E., Wechsler R. H., Dolag K., 2013, Virial scaling of galaxies in clusters: bright to faint is cool to hot, Monthly Notices of the Royal Astronomical Society, 436, 460

Xhakaj E., Diemer B., Leauthaud A., Wasserman A., Huang S., Luo Y., Adhikari S., Singh S., 2020, How accurately can we detect the splashback radius of dark matter haloes and its correlation with accretion rate?, Monthly Notices of the Royal Astronomical Society, 499, 3534

Xu X., Zheng Z., 2018, Dependence of halo bias and kinematics on assembly variables, Monthly Notices of the Royal Astronomical Society, 479, 1579

Xu J., Hardee P. E., Stone J. M., 2000, The Stability of Radiatively Cooled Jets in Three Dimensions, Astrophysical Journal, 543, 161

Ye J.-N., Guo H., Zheng Z., Zehavi I., 2017, Properties and Origin of Galaxy Velocity Bias in the Illustris Simulation, Astrophysical Journal, 841, 45

Yu L., Nelson K., Nagai D., 2015, The Influence of Mergers on Scatter and Evolution in Sunyaev-Zel'dovich Effect Scaling Relations, Astrophysical Journal, 807, 12

Zel'dovich Y. B., 1970, Gravitational instability: An approximate theory for large density perturbations, Astronomy and Astrophysics, 5, 84

Zhai Z., et al., 2019, The Aemulus Project. III. Emulation of the Galaxy Correlation Function, Astrophysical Journal, 874, 95

Zhang P., Liguori M., Bean R., Dodelson S., 2007, Probing Gravity at Cosmological Scales by Measurements which Test the Relationship between Gravitational Lensing and Matter Overdensity, Physical Review Letters, 99, 141302

Zhang C., Churazov E., Forman W. R., Lyskova N., 2019, Runaway merger shocks in galaxy cluster outskirts and radio relics, Monthly Notices of the Royal Astronomical Society, 488, 5259

Zhang C., Churazov E., Dolag K., Forman W. R., Zhuravleva I., 2020, Encounters of merger and accretion shocks in galaxy clusters and their effects on intracluster medium, Monthly Notices of the Royal Astronomical Society, 494, 4539

Zhuravleva I., et al., 2014, Turbulent heating in galaxy clusters brightest in X-rays, Nature, 515, 85

Zinger E., Dekel A., Birnboim Y., Kravtsov A., Nagai D., 2016, The role of penetrating gas streams in setting the dynamical state of galaxy clusters, Monthly Notices of the Royal Astronomical Society, 461, 412

Zolotov A., et al., 2015, Compaction and quenching of high-z galaxies in cosmological

simulations: blue and red nuggets, Monthly Notices of the Royal Astronomical Society, 450, 2327

Zu Y., Weinberg D. H., 2013, The redshift-space cluster-galaxy cross-correlation function - I. Modelling galaxy infall on to Millennium simulation clusters and SDSS groups, Monthly Notices of the Royal Astronomical Society, 431, 3319

Zu Y., Weinberg D. H., Jennings E., Li B., Wyman M., 2014, Galaxy infall kinematics as a test of modified gravity, Monthly Notices of the Royal Astronomical Society, 445, 1885

Zu Y., Mandelbaum R., Simet M., Rozo E., Rykoff E. S., 2017, On the level of cluster assembly bias in SDSS, Monthly Notices of the Royal Astronomical Society, 470, 551

Zürcher D., More S., 2019, The Splashback Radius of Planck SZ Clusters, Astrophysical Journal, 874, 184

Zwicky F., 1933, Die Rotverschiebung von extragalaktischen Nebeln, Helvetica Physica Acta, 6, 110

Zwicky F., 1937, On the Masses of Nebulae and of Clusters of Nebulae, Astrophysical Journal, 86, 217

van Leer B., 1977, Towards the ultimate conservative difference scheme III. Upstream-centered finite-difference schemes for ideal compressible flow, Journal of Computational Physics, 23, 263

van de Voort F., Schaye J., 2012, Properties of gas in and around galaxy haloes, Monthly Notices of the Royal Astronomical Society, 423, 2991

van de Voort F., Schaye J., Booth C. M., Haas M. R., Dalla Vecchia C., 2011, The

rates and modes of gas accretion on to galaxies and their gaseous haloes, Monthly Notices of the Royal Astronomical Society, 414, 2458

van de Voort F., Springel V., Mandelker N., van den Bosch F. C., Pakmor R., 2019, Cosmological simulations of the circumgalactic medium with 1 kpc resolution: enhanced H I column densities, Monthly Notices of the Royal Astronomical Society, 482, L85